Andean Interglacial Climate and Hydrology Over the Last 650,000 Years

by

Sarah A. Katz

A dissertation submitted in partial fulfillment
of the requirements for the degree of
Doctor of Philosophy
(Earth and Environmental Sciences)
in the University of Michigan
2024

Doctoral Committee:

Professor Naomi E. Levin, Chair
Professor Julia E. Cole
Associate Professor Andrew D. Gronewold
Associate Professor Benjamin H. Passey

Sarah A. Katz

skatzees@umich.edu

ORCID iD: 0000-0001-6084-6858

Acknowledgements

Throughout the process of writing this dissertation, I have been aided by many people who I would like to thank for their generous support.

First, thank you to my advisor, Naomi Levin, for being an excellent mentor and guiding my scientific journey with a huge amount of patience. In particular, I am exceedingly grateful for the many hours you have spent reviewing my writing. I have certainly become a better scientist through your efforts! I would also like to thank my committee members, Ben Passey, Julie Cole, and Drew Gronewold for many helpful conversations, words of advice, and interest in my research over the past years.

I would like to acknowledge research funding from the Geological Society of America, the Department of Earth and Environmental Sciences, and Rackham Graduate School. In addition to financial support, the opportunities to propose original research were invaluable for shaping the motivation and scope of my dissertation.

Navigating graduate school has only been possible with the help of our amazing department staff. Thank you especially to Anne Hudon, Chrissy Zigulis, Nathan Sadowsky, Paula Frank, Nico Spraggins, Katie Brennan, Courtney Hooper, Carla Huhn, Noah Goad, and Craig Delap.

I have been lucky to work alongside many excellent colleagues in the IsoPaleoLab throughout the years. In particular, I would like to thank the following people for generously sharing their time and advice with me: Ty Huth, Julia Kelson, Anne Fetrow, Phoebe Aron, Nick Ellis, Natalie Packard, Drake Yarian, and Kirsten Andrews. Thank you also to Naomi and Ben for fostering a welcoming, supportive lab environment.

I have also been fortunate to develop deep research collaborations outside of Michigan. Thank you to the members of the Junín research group for helping me learn where my own research fits within a larger framework of South American paleoclimate research. Thank you to Elizabeth Olsen, Dave Gillikin, Larry Edwards, Dylan Parmenter, Laura Lopera, Joe Werne, Pedro Tapia, Jungpyo Hong, and Ben Passey. Thank you also to Analucía Serrepe for help with field work in Peru in 2019. A very special thanks goes to Don Rodbell and Mark Abbott, who have been

incredibly generous with their time and enthusiasm for my research throughout all stages of my graduate career.

During my time at Michigan, I have met many amazing, smart, and kind graduate students. In particular, I am so grateful for meeting Phoebe Aron, who has been an incredible and steadfast friend. Phoebe has supported me through both personal and professional challenges, as well as celebrated my successes. I am also very grateful that I was paired with Fabian Hardy for a side-quest (i.e., teaching position) for two summers at Camp Davis. Considering that we have driven cross-country together multiple times and remain friends, I consider that a win. A special thank you to Daeun Lee, Jackie Kleinsasser, Zack Quirk, Anne Fetrow, and Eric Szymanski for your friendship!

I would also like to acknowledge the impact that both Jillian Weiner and Mark Robbins had on my time at Michigan. Jillian was an incredibly vibrant, bright young woman. From Mark, I learned much of what I know about good teaching; his warmth and kindness were unparalleled.

My scientific journey first began at Colgate University, and I would like to thank all of the faculty and students in the Geology Department, with a special thanks to William Peck and Martin Wong for your support over many years. Prior to graduate school, I was also very fortunate to work with Don Rodbell, Dave Gillikin, and Anouk Verheyden-Gillikin at Union College, where I was thrust into the worlds of South American paleoclimate and stable isotopes; this experience was pivotal and ultimately led me to pursue graduate research at Michigan.

Throughout my life, my family has supported each of my endeavors, including graduate school. Thank you to my mom, dad, and sister. In particular, my love and appreciation for the outdoors was instilled in me by my mom. Over the past few years I have also received a tremendous amount of support from my partner, Brian Peterson. Thank you for being a wonderful, kind, caring person, and for always believing that I could see this dissertation through to the end.

Table of Contents

List of Tables

List of Figures

Abstract

Land temperatures and water supply control the distribution of life on Earth and link the global water and carbon cycles to the planet's energy budget. Monsoons are at the nexus of these systems and function to transport water vapor and heat from the low latitudes towards the poles. However, the role of global climate on the position, intensity, and timing of monsoon rainfall remains poorly constrained in many regions, which together, are home to >70% of the world's population.

In this dissertation, I use sediment records from Andean lakes to reconstruct the impact of global climate on the South American summer monsoon (SASM), regional water balance, and temperature. Specifically, I use isotope ratios of carbonate sediments to compare the abundance of heavy oxygen and carbon isotopes to their light counterparts, as these data preserve information about hydroclimate conditions.

Chapter 2 is a calibration study of two new isotope techniques, clumped and triple oxygen isotopes, that were measured in modern waters and carbonates from four lakes in the Junín region of central Peru. Combining the isotope data with numerical water balance models, I show that lake water temperature and evaporation are the primary drivers of carbonate clumped and triple oxygen isotope values, respectively. Accordingly, the interpretive framework established in Chapter 2 scaffolds the paleoclimate interpretations in Chapters 3 and 4, and can also be applied to lake systems beyond the central Andes.

In Chapters 3 and 4, I develop Andean temperature and water balance records during two interglacial periods to assess how hydrologic change manifests under distinct global climate conditions. Chapter 3 examines three Holocene (11.7 ka to present) lake records from the Junín region and Chapter 4 presents data from a single lake (i.e., Lake Junín) during MIS 15 (621 to 563 ka). Clumped isotopes reveal that temperatures during the Holocene and MIS 15 were indistinguishable from the present over both interglacials. These data suggest that temperature variability in the central Andes was minimal and not a primary driver of tropical hydroclimate change during these interglacials. Conversely, triple oxygen isotopes suggest water balance (i.e.,

surface water supply) was highly variable and follows a precession pacing (~23 ka cycles) during both interglacials. These observations are likely related to changes in summertime insolation, which is a well-documented control on SASM strength over the last ~350 ka. The strong correlation between triple oxygen isotope values and insolation suggests this relationship was the main factor driving water balance variability during both the Holocene and MIS 15. The triple oxygen isotope data reported in Chapters 3 and 4 represent some of the first evidence that water balance is tightly coupled to SASM. This finding illustrates that global climate forcings (e.g., orbital configurations) can have a strong impact on regional hydroclimate, and suggests changes in the planet's energy balance would alter water availability throughout much of South America.

This dissertation represents the most extensive combined application of clumped and triple oxygen isotopes to lacustrine carbonates, to date, and contributes abundant data from modern and paleo-lake systems. Together with new numerical and conceptual models, these data illuminate a strong connection between Andean water balance, the SASM, and global climate which is explored through Chapters 2–4.

Chapter 1 Introduction

Continental temperatures and water availability are two critical factors determining habitability on our planet. As the primary source of atmospheric water vapor, the tropics are integral for the global water cycle. Large-scale atmospheric systems, such as monsoons, originate in the tropics and transport moisture and heat to the mid- and high-latitudes (Schneider et al., 2014; Mohtadi et al., 2016; IPCC, 2021). Today, over 70% of the human population lives in regions affected by monsoons (Mohtadi et al., 2016), highlighting a need to understand both the natural and anthropogenic factors that drive changes in monsoons, as well as the consequences of monsoons on continental water balance and temperature. In this dissertation, I use emerging high-precision stable isotope techniques and new conceptual frameworks to develop records of temperature and water availability in the South American tropics over the last 650,000 years during warm, interglacial periods. Specifically, I show that large changes in water availability accompany perturbations to the South American summer monsoon system (SASM) during two interglacials. These results contribute new insights into how the SASM, Andean temperatures, and water availability respond to orbital controls on global climate.

1.1 Modern South American hydroclimate and societal importance

The SASM is the primary atmospheric weather system in the South American outer-tropics (ca. 10 °S–25 °S). The SASM alternates on a seasonal cycle between a "strengthened" phase in the austral summer (December–February) and a "weakened" phase in the austral winter (June–August; Lenters and Cook, 1999; Garreaud et al., 2009; Marengo et al., 2012), and is anti-phased with monsoon systems in the northern hemisphere (Vera et al., 2006; Grimm et al., 2021). The seasonal cycles of the SASM onset and decay is related to inter-hemispheric insolation asymmetries caused by Earth's axial tilt and precession (Liu and Battisti, 2015), whereby tropical rain belts are enhanced during the summer months for each hemisphere (Schneider et al., 2014; Grimm et al., 2021).

During the austral summer, intense surface heating over the South American continent leads to the development of deep convective cells over the Amazon basin; the resulting low-pressure system strengthens easterly winds and draws moist air from the Atlantic over the continent (Lenters and Cook, 1999; Vera et al., 2006; Garreaud et al., 2009; Marengo et al., 2012; Mohtadi et al., 2016; Grimm et al., 2021). After passing through a series of convective cells, whereby moisture is recycled via evapotranspiration over the Amazon (Salati et al., 1979; Staal et al., 2018; Ampuero et al., 2020), the air masses reach the eastern Andean flank and orographic lifting causes intense rainout (Lenters and Cook, 1995), making this region among the wettest in the world (Vera et al., 2006). By contrast, during the austral winter, convective activity in the Southern hemisphere is much weaker and comparatively little rainfall occurs within the SASM domain (Garreaud et al., 2009; Marengo et al., 2012), including along the Andean flank (Vera et al., 2006; Grimm et al., 2021).

Over the past century, data from a network of weather stations across South America suggest that precipitation in the South American outer-tropics is decreasing (particularly during the wet season within the SASM domain; e.g., Silva et al., 2008), while surface temperatures, and the frequency of extreme weather events (e.g., drought, floods) have increased as a result of anthropogenic climate forcing (SENAMHI, 2009; IPCC, 2014; Pascale et al., 2019; Pabón-Caicedo et al., 2020). However, these trends are not uniform in sign across the continent and also appear to vary in magnitude spatially and through time, such that it is challenging to generalize the impact of global climate change on the tropics (e.g., SENAMHI, 2009; Pabón-Caicedo et al., 2020). These efforts are further thwarted by a low density of weather stations maintained across the continent and relatively short length of most records (i.e., a few decades or less; Garreaud et al., 2009; Marengo et al., 2012). Furthermore, model predictions of rainfall trends remain inconclusive throughout the SASM domain and model ensembles exhibit disagreement in both the magnitude and sign of future hydrologic change (SENAMHI, 2009; Solman, 2013; Pascale et al., 2019). Ultimately, these limitations in both instrumental datasets and models inhibit confident hydroclimate forecasting over the coming decades.

Global climate change will affect temperature, rainfall trends, and regional water availability across South America; information about these changes is highly relevant to local communities and is requisite for guiding adaptive strategies (SENAMHI, 2009; IPCC, 2014; Drenkhan et al., 2022). Negative consequences associated with higher surface temperatures

include increased frequency and severity of heat waves and accelerated melting of mountain glaciers in the Andes (Rabatel et al., 2013; IPCC, 2014; Vuille et al., 2018; Masiokas et al., 2020). Over the last 60 years, glaciers in Peru have declined by 40-60% (ANA, 2010; Masiokas et al., 2020) with an estimated rate of loss of ~1%/year between 2010-2016 (Drenkhan et al., 2018). Loss of glaciers would eliminate an important water source for agricultural food production, hydroelectric power generation, and human consumption (SENAMHI, 2009; ANA, 2010; IPCC, 2014; Mark et al., 2017; Vuille et al., 2018). Furthermore, rapid glacial melting is associated with hazards like rupturing of proglacial lakes and catastrophic flooding, leading to loss of human life and property (Drenkhan et al., 2019; Haeberli and Drenkhan, 2022).

Perturbations to the seasonality and/or amount of SASM precipitation would also compound Andean water instability and have cascading effects on hyper-arid urban regions, like Lima (population >11 million in 2024), which rely on water sourced from the high elevations (IPCC, 2014; Mark et al., 2017; Drenkhan et al., 2022). In addition to the consequences for human populations, reduced rainfall in the Amazon compromises forest resilience (Phillips et al., 2009; Ahlström et al., 2017). Combine with biomass reductions from deforestation (Brienen et al., 2015; Zemp et al., 2017; Staal et al., 2020; Kukla et al., 2021), loss of forests can reduce the carbon storage potential of the region, which is a major organic carbon sink (Phillips et al., 2009; Pangala et al., 2017).

The factors that drive tropical hydroclimate are fundamental to understanding how SASM and Andean regional water balance respond to global climate perturbations. In this dissertation I establish the relationship between the key components of tropical hydroclimate: temperature, water balance, and the SASM, offering new insights into why and how tropical hydroclimate perturbations occur.

1.2 South American paleo-hydroclimate

1.2.1 Our current understanding

One approach to understanding how tropical hydroclimate responds to various forcings is through development of paleoclimate records during key periods of Earth's history. What can be learned by studying records of Earth's past climate? Over the last 4.6 billion years, the Earth has experienced a wide range of climate forcings, including internal (e.g., atmospheric GHG, polar ice

cover, ocean circulation) and external (e.g., orbital parameters, solar output, volcanism) forcings (e.g., Zachos et al., 2001; NGRIP members, 2004; Lisiecki and Raymo, 2005; Jouzel et al., 2007). Paleoclimate records preserve evidence of how the planet's climate responded to different combinations of these forcings (Bradley, 1999; Ruddiman, 2007). Accordingly, climate records from periods in Earth's history that had similar forcing combinations to today are often leveraged to gain insights into our modern climate system. Of course, a caveat of this approach is that no period of Earth's history is an exact analog to the present-day climate system, partially due to the significant anthropogenic component to modern climate change. Regardless, paleoclimate records from intervals when global forcings were broadly similar to the present can still provide key insights into the connections between global and regional climate and the sensitivity of regional climate to climate change (Bradley, 1999; Harrison and Bartlein, 2012).

Often, Pleistocene interglacial cycles are thought of as close analogs to our modern climate state because many first-order climatic controls were similar to the present day, including continental configurations and topography, ocean and atmospheric circulation patterns, and sustained polar ice cover (Berger and Yin, 2012; Past Interglacials Working Group of PAGES, 2015). Following the mid-Pleistocene transition (MPT; ~1,200 to 700 ka; where 1 ka = 1,000 years) and onset of ~100 ka glacial-interglacial cycles, the planet's orbital configuration, atmospheric GHG concentrations, and the volume of Northern hemisphere ice are thought to have been the primary drivers controlling interglacial pacing and variability (Berger and Yin, 2012). Both northern hemisphere ice volume and GHG concentrations are constrained by long (>700 ka) polar ice core and marine sediment records (e.g., Lisiecki and Raymo, 2005; Jouzel et al., 2007; Loulergue et al., 2008; Bereiter et al., 2015), and orbital parameters can be reliably calculated (e.g., Laskar et al., 2004). Accordingly, close study of tropical hydroclimate records from late Pleistocene interglacials can provide insights into the sensitivity and response of the tropics to these global forcings. For this reason, Chapters 3 and 4 of this dissertation are focused on tropical hydroclimate records during two Pleistocene interglacials.

To date, South American paleoclimate research has focused primarily on the last ~350 ka which spans the last ~3 glacial-interglacial cycles (e.g., Peterson et al., 2000; Cruz et al., 2005; Fritz et al., 2007; Cheng et al., 2013; Baker and Fritz, 2015; Wang et al., 2017; Hou et al., 2020). Oxygen isotope records from speleothems (i.e., cave carbonates) collected across the continent suggests that changes in SASM strength during interglacials tracks precession on millennial

timescales and longer (see Section 1.3 for isotope explanation) (Cruz et al., 2005, 2009; Cheng et al., 2013; Burns et al., 2019). Mechanistically, these variations can be explained by the role of precession on summertime insolation, which is greatest in the Southern hemisphere at low precession (i.e., the southern hemisphere tilts towards the sun at perihelion) and leads to stronger SASM conditions (Liu and Battisti, 2015). Canonically, orbitally-paced changes in SASM strength are thought to be associated with meridional displacement of the SASM pathway north/south, however, new evidence now suggests the width of the SASM may actually expand/contract (e.g., Chiessi et al., 2021) and this remains an important subject of future research. In comparison to interglacials, a strong relationship between SASM and precession is not always observed during glacials, possibly due to increased sensitivity to millennial-scale high-latitude climate events (e.g., Kanner et al., 2012; Wang et al., 2017), though this subject also deserves additional attention.

1.2.2 Remaining questions

Paleoclimate records from the last ~350 ka provide a clear framework for guiding expectations of precession-paced SASM variability during interglacials. However, establishing whether the SASM followed the same orbital forcing during earlier interglacials or if SASM was decoupled from insolation (as during glacials) has been hindered by a lack of reliably-dated continental climate records older than 350 ka. Compared to interglacials over the last 350 ka, older interglacials might have reflected unique SASM dynamics due to specific combinations of climate forcings (e.g., Berger and Yin, 2012; Past Interglacials Working Group of PAGES, 2015). Therefore, studying SASM variability under a diverse range of global boundary conditions could provide new insights into how SASM will respond to ongoing global change (e.g., increasing atmospheric GHG concentrations; decreasing polar ice volume). These societally relevant questions motivate the development of tropical climate records that span the entirety of the late Pleistocene from the MPT to present.

The SASM is a critical aspect of South American hydroclimate, but it remains uncertain how/if changes in SASM are related to regional water balance or temperature (e.g., Wortham et al., 2017; Ward et al., 2019; Woods et al., 2020). Compared to marine temperature records, continental temperature records are relatively sparce and this bias is especially true in the tropics. In South America, a handful of temperature records from the last 20 ka suggest that Holocene temperatures in the tropics and mid-latitudes were similar to present, but were cooler by ~5°C

during the Last Glacial (e.g., Stute et al., 1995; Punyasena et al., 2008). Beyond this, we have little quantitative temperature evidence from South America and have a poor understanding of how continental temperatures in the tropics vary over time and space.

Regional water balance (i.e., the volumetric proportion of local precipitation to evaporative losses) is also difficult to address because many hydrologic records (e.g., from speleothem oxygen isotopes) reflect rainout along the SASM moisture pathway but do not necessarily reflect local rainfall amounts, particularly in the Andes (see Section 1.3; Wortham et al., 2017; Ward et al., 2019). Furthermore, speleothems in most settings are poorly suited to reflect surface hydrologic processes, such as evaporation, that modify the distribution or amount of water on a landscape (Lachniet, 2009). Accordingly, it is difficult to establish changes in regional water balance from speleothem oxygen isotope records. Therefore, developing water balance and temperature records that exist in concert with SASM records remains an important and outstanding requirement for understanding how global climate influences local environments.

When I started my PhD work, these two challenges—a lack of long tropical climate records and a murky connection between SASM, regional water balance, and continental temperature—were obstacles that plagued the South American paleoclimate community. In the remainder of this chapter, I discuss how Chapters 2–4 of this dissertation address both of these outstanding research areas by building new interglacial temperature and water balance records, and I use these records to analyze the global climate factors (e.g., orbital parameters) driving perturbations to tropical climate.

1.3 Study area and isotope background

Sediment cores from Lake Junín, Peru (11.0 °S; 76.1 °W; 4050 meters above sea level), have been used for over 40 years to study Andean hydroclimate (e.g., Hansen et al., 1984, 1994; Seltzer et al., 2000; Woods et al., 2020; Schiferl et al., 2023). Located on the westernmost SASM range, Lake Junín is a large, shallow lake (~300 km^2 surface area; 8–12 m water depth) that is highly sensitive to changes in regional water balance and hydrology (Seltzer et al., 2000; Flusche et al., 2005; Katz et al., 2023). Stable isotope analysis (i.e., carbonate $\delta^{18}O$) of sediment cores collected along the western margin of the lake seem to record changes in local water balance over the last 50 ka, which provides useful insights into a possible connection with the SASM (changes in the SASM are inferred from nearby speleothem records; Seltzer et al., 2000; Kanner et al.,

2013). However, the controls on lake carbonate $\delta^{18}O$ are complex (see below; Leng and Marshall, 2004; Horton et al., 2016; Gibson et al., 2016) and the interpretations from prior studies have not been confirmed by techniques that more directly record water balance or lake water evaporative losses.

In 2015, a 90 m sediment core was collected from the lake depocenter and represents ~700 ka of continuous sediment deposition (Hatfield et al., 2020b, 2020a; Chen et al., 2020). This record has generated significant excitement within the paleoclimate community for being one of the first well-dated tropical climate records to span numerous interglacial cycles and for recording information about Andean water cycling and high elevation temperatures. To date, research has focused on geochemical and pollen analysis, and has revealed that floral community compositions and the glacial history of the catchment follow the same 100 ka pacing as global glacial cycles (Woods et al., 2020; Rodbell et al., 2022; Schiferl et al., 2023). This suggests a link between tropical climate and global forcings was maintained over the last 700 ka (Rodbell et al., 2022). However, as both glacier extent and plant communities are sensitive to multiple factors, including water balance and temperature, it remains unclear to what extent each of these factors contributed to the overall environmental change in the region. In this dissertation, I address this question using newly developed isotope tools that are sensitive to temperature and hydrology, and apply these techniques to ancient interglacial intervals recorded at Lake Junín.

Stable isotopes are powerful paleoclimate tools because isotopes record information about hydroclimate conditions (e.g., Dansgaard, 1964; Rozanski et al., 1993; Gat, 1996) and are preserved in a variety of materials like carbonates and ice. In conventional hydrologic applications, ratios of oxygen-18 (^{18}O) to oxygen-16 (^{16}O) in a sample are measured and reported as $\delta^{18}O$ values (where, $\delta^{18}O = {}^{18}O/{}^{16}O_{sample}/ {}^{18}O/{}^{16}O_{standard} - 1$) in units of "per mille" (‰; where, $\delta^{18}O$ is multiplied by 10^3). $\delta^{18}O$ variations within hydrologic applications can be explained by mass dependent fractionation (e.g., Criss, 1999) and modern data shows that the $\delta^{18}O$ composition of precipitation ($\delta^{18}O_P$) is dominantly controlled by moisture source and Rayleigh distillation (e.g., Dansgaard, 1964; Rozanski et al., 1993; Gat, 1996), with the latter strongly influencing advected moisture. Other factors, including cloud type, convective activity, and air mass mixing can also contribute to $\delta^{18}O_P$ values (e.g., Aggarwal et al., 2016; Konecky et al., 2019), though they are typically thought to have a lesser influence. As SASM precipitation is dominantly sourced from the Atlantic Ocean and advected over the continent, Rayleigh distillation is the strongest control

on $\delta^{18}O_P$ values. Accordingly, $\delta^{18}O_P$ and SASM intensity are strongly correlated, such that $\delta^{18}O_P$ values (or geologic records that reflect $\delta^{18}O_P$) can be used to reconstruct changes in SASM intensity through time (e.g., Cruz et al., 2005; Bird et al., 2011b, 2011a; Kanner et al., 2013).

The isotopic composition of surface waters reflects local precipitation, though the surface water isotope composition can be modified, e.g., by evaporation or mixing of isotopically-distinct reservoirs (Horton et al., 2016; Kelson et al., 2022). In particular, evaporation of lake waters is well documented and can increase the $\delta^{18}O$ value of residual waters by ~>15 ‰ compared to $\delta^{18}O_P$ values (Leng and Marshall, 2004; Horton et al., 2016; Gibson et al., 2016). Carbonates precipitated from these waters (e.g., lake carbonates) preserve the isotopic composition of their formation waters, albeit with a temperature dependent offset (Leng and Marshall, 2004; Gibson et al., 2016). Accordingly, carbonate $\delta^{18}O$ ($\delta^{18}O_C$) records are commonly used in paleoclimate studies to investigate changes in continental climate and the hydrologic cycle. However, interpreting $\delta^{18}O_C$ values is often ambiguous, particularly in paleoclimate applications, because we lack clear evidence of how the individual drivers of $\delta^{18}O_C$ are expressed concurrently in the isotope record (Leng and Marshall, 2004; Gibson et al., 2016). Below, I describe how the recent advent of two additional isotope systems can aid in the interpretation of $\delta^{18}O_C$ records and ultimately contribute to more reliable paleoclimate interpretations.

In recent decades, carbonate "clumped" isotopes have become increasingly used to determine temperature during carbonate mineralization (e.g., Eiler, 2011; Huntington and Petersen, 2023). "Clumped" isotopes refers to a bond containing two heavy isotopes, typically ^{13}C–^{18}O in carbonate applications (Eiler, 2007). Based on the abundance of ^{13}C and ^{18}O in a sample (compared to ^{12}C and ^{16}O atoms), some number of random ^{13}C–^{18}O pairings is expected. However, bonds containing double substitutions (e.g., ^{13}C–^{18}O) are thermodynamically favored compared to two single substitution bonds (e.g., ^{12}C–^{18}O and ^{13}C–^{16}O; Wang et al., 2004; Ghosh et al., 2006; Schauble et al., 2006). Accordingly, the observed abundance of ^{13}C–^{18}O bonds in carbonates exceeds the random or "stochastic" abundance by a very small amount (i.e., fractions of a percent). When measured via mass spectrometry on CO_2 evolved from acid digestion of carbonates, the excess of ^{13}C–^{18}O bonds from the stochastic abundance is denoted Δ_{47} (Dennis et al., 2011). Δ_{47} is inversely proportional to formation temperature, which can be calculated from Δ_{47} using either theoretical or empirical regressions (e.g., Schauble et al., 2006; Guo et al., 2009; Kelson et al., 2017; Petersen et al., 2019). In the past two decades, clumped isotopes have been applied to a

variety of terrestrial carbonates (see Huntington and Petersen, 2023, for a recent review), including soil carbonates (e.g., Passey et al., 2010; Kelson et al., 2020), palustrine carbonates (Fetrow et al., 2022), and lake carbonates (e.g., Petryshyn et al., 2015; Ingalls et al., 2020; Santi et al., 2020). Accordingly, we use clumped isotopes of lacustrine carbonates to develop temperature records from Lake Junín and other Andean lakes.

In addition to clumped isotopes, triple oxygen isotopes are an emerging isotope proxy with potential applications towards modern and ancient hydrologic systems. While traditional oxygen isotopes ($\delta^{18}O$) only consider the two most abundant stable oxygen isotopes, triple oxygen isotopes also include the rarest stable isotope, ^{17}O (representing 0.04% of all oxygen atoms). Like $\delta^{18}O$, $\delta^{17}O$ variations are controlled by mass dependent fractionation, though only by about half the magnitude of $\delta^{18}O$ (Clayton et al., 1976; Matsuhisa et al., 1978; Bao et al., 2016). The relationship between $\delta^{18}O$ and $\delta^{17}O$ is commonly depicted as a linear relationship between $\delta'^{18}O$ and $\delta'^{17}O$ ($\delta' = \ln(\delta+1)$) and is characterized by process-specific slopes (λ values), which range from ~0.510 to 0.535 for most mass dependent processes (e.g., Young et al., 2002; Miller, 2002; Bao et al., 2016; Hayles and Killingsworth, 2022). Near the top of this range, Rayleigh distillation follows a slope ($\lambda_{Rayleigh}$) of ~0.528, close to that of water vapor–liquid water equilibrium exchange ($\lambda_{eq} = 0.529$) (Barkan and Luz, 2005; Aron et al., 2021). Taking a reference λ (λ_{ref}) value of 0.528, triple oxygen isotope measurements of waters and other geologic materials can fingerprint non-Rayleigh processes (e.g., processes with a kinetic component) such as diffusion of liquid water into a dry atmosphere as water vapor ($\lambda_{diff} = 0.5185$; Barkan and Luz, 2007), where the residual from λ_{ref} is quantified as $\Delta'^{17}O$ ($\Delta'^{17}O = 0.528*\delta'^{18}O - \delta'^{17}O$). Accordingly, $\Delta'^{17}O$ is emerging as a powerful tool for probing hydrologic processes that are difficult to address with $\delta^{18}O$ alone, including mixing and evaporation (Barkan and Luz, 2007; Aron et al., 2021; Kelson et al., 2022). In recent years, studies that systematically explore $\Delta'^{17}O$ in modern systems have begun to emerge (e.g., Luz and Barkan, 2010; Aron et al., 2021; Terzer-Wassmuth et al., 2023), although, to date, adoption in paleoclimate applications is limited (e.g., Gázquez et al., 2018; Ibarra et al., 2021; Kelson et al., 2022). In this dissertation, I present new data and conceptual models that scaffold $\Delta'^{17}O$ interpretations in lacustrine systems. I also apply $\Delta'^{17}O$ to Pleistocene lake carbonates for the first time, catapulting this tool beyond methodological development and firmly into use for paleoclimate investigations.

1.4 Dissertation chapter summaries

In this thesis, I use traditional oxygen isotopes ($\delta^{18}O$), clumped isotopes (Δ_{47}), and triple oxygen isotopes ($\Delta'^{17}O$) of lacustrine carbonates to develop temperature and hydrologic records from the tropical Andes. This work expands our understanding of how South American hydroclimate responds to global forcings. Furthermore, this dissertation represents the most comprehensive series of work to date which combines clumped and triple oxygen isotopes in carbonate lake systems, and I demonstrate the clear contributions these tools can make in paleoclimate applications. The body of this work focuses on lakes in the Junín region of central Peru and begins with a modern calibration study (Chapter 2) that is followed by studies examining two ancient interglacial periods (Chapters 3 and 4).

The purpose of Chapter 2 (published in *Earth and Planetary Science Letters*; Katz et al., 2023) is to assess the climate and hydrologic controls on the isotopic compositions of water and lake carbonates from the Lake Junín region. At the time of this study, clumped and triple oxygen isotopes were still emergent techniques and these tools had not been applied widely in modern or paleo-lacustrine applications. In this chapter, I collected and analyzed local precipitation, surface waters, and modern lake carbonates from four catchments in the Junín region. The results showed that carbonate clumped isotopes reflected local water temperatures and are a reliable continental temperature proxy. Triple oxygen isotopes closely reflect the degree of evaporative water loss from each basin, which is consistent with isotope theory. I further contextualized the triple oxygen isotope data using deterministic modeling of steady state lake isotope mass balance models (after Benson and White, 1994; Criss, 1999; Gibson et al., 2016; Herwartz et al., 2017; Passey and Ji, 2019). The model results illuminate the role of local humidity on the $\Delta'^{17}O$ composition of evaporated lake water and predict a smaller and more positive $\Delta'^{17}O$ range in humid settings than arid settings. These results are supported by the observational $\Delta'^{17}O$ data from the Junín region (the four lakes all exist within the same humid climate regime), which cover a smaller, more positive range of $\Delta'^{17}O$ values than lakes in highly arid environments (Surma et al., 2015, 2018; Herwartz et al., 2017; Passey and Ji, 2019). Despite the relatively small range of $\Delta'^{17}O$ values in the Junín region, the values at each lake track the degree of evaporative water loss and lake hydrology, indicating that lake carbonate $\Delta'^{17}O$ values can faithfully record hydrologic differences among different lakes even in humid environments. The interpretive framework for carbonate Δ_{47}

and $\Delta'^{17}O$ values presented in this chapter is applicable to lakes in the Junín region, while also accommodating lakes that span diverse global climate and hydrologic conditions. We build upon this framework in Chapters 3 and 4, and hope that other practitioners will be able to apply this approach to different study regions.

Following successful proxy calibration, in Chapters 3 and 4, I use lake carbonate clumped and triple oxygen isotopes to develop temperature and water balance histories in the Junín region from two ancient interglacial periods: the Holocene (11.7 ka to present) and Marine Isotope Stage (MIS) 15 (621 to 563 ka).

Chapter 3 (in review at *Paleoceanography and Paleoclimatology*; Katz et al. *in review*) focuses on Holocene lake records from three of the same lakes which were the focus of Chapter 2. I present temperature (Δ_{47}) and lake water evaporation records ($\Delta'^{17}O$) from the lakes and compare the results to the modern calibration study and nearby records that reflect SASM strength and local summertime insolation. These data are among the first quantitative evidence to show that regional water balance variability followed changes in SASM during the Holocene and suggests a close connection between global climate and regional hydroclimate in the Andes. In addition to the new isotope data presented in this chapter, I also use lake water steady state equations (Benson and White, 1994; Criss, 1999; Gibson et al., 2016; Herwartz et al., 2017; Passey and Ji, 2019) to estimate the proportion of evaporative water loss (compared to inputs) from the three lakes during two time slices: the early Holocene (weak SASM and high proportion of evaporation) and the late Holocene (strong SASM and low proportion of evaporation). The deterministic modeling approach that I present provides quantitative constraints on regional water balance and is an important conceptual advance which can be widely adapted to other lake systems around the world.

In Chapter 4, I present temperature (Δ_{47}) and lake water evaporation records ($\Delta'^{17}O$) from Lake Junín during an ancient interglacial, MIS 15, which occurred from 621 to 563 ka. The Lake Junín record is among the first well-dated continental climate record from South America to cover MIS 15 and provides an opportunity to explore how regional hydroclimate responded to global boundary conditions which were distinct from the Holocene. The major findings in this chapter are that changes in lake water balance track a precession pacing, highlighting that the link between water balance and SASM endured during ancient interglacials and was not only a feature of the Holocene. Interestingly, the magnitude of water balance variability during MIS 15 was larger than observed in the Holocene and suggests the occurrence of a wet, unevaporated endmember state

that was wetter than any point during the Holocene and is probably related to unique orbital factors (i.e., enhanced eccentricity) during this interglacial. In addition to the new paleoclimate insights offered by this work, this chapter represents a major contribution in the field of high precision isotope geochemistry by demonstrating that robust climate insights can be achieved from Δ_{47} and $\Delta'^{17}O$ data.

Chapter 5 concludes this dissertation; I begin by summarizing the major findings of Chapters 2–4 and I discuss how these results have advanced the fields of South American paleoclimatology and stable isotope geochemistry. I conclude with a brief reflection and a summary of the current state of the field.

1.5 References

Aggarwal, P.K., Romatschke, U., Araguas-Araguas, L., Belachew, D., Longstaffe, F.J., Berg, P., Schumacher, C., and Funk, A., 2016, Proportions of convective and stratiform precipitation revealed in water isotope ratios: Nature Geoscience, v. 9, p. 624–629, doi:10.1038/ngeo2739.

Ahlström, A., Canadell, J.G., Schurgers, G., Wu, M., Berry, J.A., Guan, K., and Jackson, R.B., 2017, Hydrologic resilience and Amazon productivity: Nature Communications, v. 8, p. 387, doi:10.1038/s41467-017-00306-z.

Ampuero, A. et al., 2020, The Forest Effects on the Isotopic Composition of Rainfall in the Northwestern Amazon Basin: Journal of Geophysical Research: Atmospheres, v. 125, doi:10.1029/2019JD031445.

ANA, 2010, Recursos Hídricos del Perú en Cifras (in Spanish): Authoridad Nacional del Agua, Oficina del Sistema Nacional de Información de Recursos Hídricos. Peru. https://hdl.handle.net/20.500.12543/211.

Aron, P.G., Levin, N.E., Beverly, E.J., Huth, T.E., Passey, B.H., Pelletier, E.M., Poulsen, C.J., Winkelstern, I.Z., and Yarian, D.A., 2021, Triple oxygen isotopes in the water cycle: Chemical Geology, v. 565, p. 1–23, doi:10.1016/j.chemgeo.2020.120026.

Baker, P.A., and Fritz, S.C., 2015, Nature and causes of Quaternary climate variation of tropical South America: Quaternary Science Reviews, v. 124, p. 31–47, doi:10.1016/j.quascirev.2015.06.011.

Bao, H., Cao, X., and Hayles, J.A., 2016, Triple Oxygen Isotopes: Fundamental Relationships and Applications: Annual Review of Earth and Planetary Sciences, v. 44, p. 463–492, doi:10.1146/annurev-earth-060115-012340.

Barkan, E., and Luz, B., 2007, Diffusivity fractionations of $H_2{}^{16}O/H_2{}^{17}O$ and $H_2{}^{16}O/H_2{}^{18}O$ in air and their implications for isotope hydrology: Rapid Communications in Mass Spectrometry, v. 21, p. 2999–3005, doi:10.1002/rcm.3180.

Barkan, E., and Luz, B., 2005, High precision measurements of $^{17}O/^{16}O$ and $^{18}O/^{16}O$ ratios in H_2O: Rapid Communications in Mass Spectrometry, v. 19, p. 3737–3742, doi:10.1002/rcm.2250.

Benson, L. V, and White, J.W.C., 1994, Stable Isotopes of Oxygen and Hydrogen in the Truckee River Pyramid Lake Surface-Water System .1. Data-Analysis and Extraction of Paleoclimatic Information: Limnology and Oceanography, v. 39, p. 344–355.

Bereiter, B., Eggleston, S., Schmitt, J., Nehrbass-Ahles, C., Stocker, T.F., Fischer, H., Kipfstuhl, S., and Chappellaz, J., 2015, Revision of the EPICA Dome C CO_2 record from 800 to 600 kyr before present: Geophysical Research Letters, v. 42, p. 542–549, doi:10.1002/2014GL061957.

Berger, A., and Yin, Q., 2012, Modelling the Past and Future Interglacials in Response to Astronomical and Greenhouse Gas Forcing, *in* The Future of the World's Climate, Elsevier, p. 437–462, doi:10.1016/B978-0-12-386917-3.00015-4.

Bird, B.W., Abbott, M.B., Rodbell, D.T., and Vuille, M., 2011a, Holocene tropical South American hydroclimate revealed from a decadally resolved lake sediment $\delta^{18}O$ record: Earth and Planetary Science Letters, v. 310, p. 192–202, doi:10.1016/J.EPSL.2011.08.040.

Bird, B.W., Abbott, M.B., Vuille, M., Rodbell, D.T., Stansell, N.D., and Rosenmeier, M.F., 2011b, A 2,300-year-long annually resolved record of the South American summer monsoon from the Peruvian Andes: Proceedings of the National Academy of Sciences, v. 108, p. 8583–8588, doi:10.1073/pnas.1003719108.

Bradley, R.S., 1999, Paleoclimatology: Reconstructing Climates of the Quaternary: Elsevier.

Brienen, R.J.W. et al., 2015, Long-term decline of the Amazon carbon sink: Nature, v. 519, p. 344–348, doi:10.1038/nature14283.

Burns, S.J., Welsh, L.K., Scroxton, N., Cheng, H., and Edwards, R.L., 2019, Millennial and orbital scale variability of the South American Monsoon during the penultimate glacial period: Scientific Reports, v. 9, p. 1234, doi:10.1038/s41598-018-37854-3.

Chen, C.Y. et al., 2020, U-Th dating of lake sediments: Lessons from the 700 ka sediment record of Lake Junín, Peru: Quaternary Science Reviews, v. 244, p. 106422, doi:10.1016/j.quascirev.2020.106422.

Cheng, H., Sinha, A., Cruz, F.W., Wang, X., Edwards, R.L., d'Horta, F.M., Ribas, C.C., Vuille, M., Stott, L.D., and Auler, A.S., 2013, Climate change patterns in Amazonia and biodiversity: Nature Communications, v. 4, p. 1411, doi:10.1038/ncomms2415.

Chiessi, C.M. et al., 2021, Mid- to Late Holocene Contraction of the Intertropical Convergence Zone Over Northeastern South America: Paleoceanography and Paleoclimatology, v. 36, doi:10.1029/2020PA003936.

Clayton, R.N., Onuma, N., and Mayeda, T.K., 1976, A classification of meteorites based on oxygen isotopes: Earth and Planetary Science Letters, v. 30, p. 10–18, doi:10.1016/0012-821X(76)90003-0.

Criss, R.E., 1999, Principles of Stable Isotope Distribution: New York, Oxford University Press, 1–254 p.

Cruz, F.W., Burns, S.J., Karmann, I., Sharp, W.D., Vuille, M., Cardoso, A.O., Ferrari, J.A., Silva Dias, P.L., and Viana, O., 2005, Insolation-driven changes in atmospheric circulation over the past 116,000 years in subtropical Brazil: Nature, v. 434, p. 63–66, doi:10.1038/nature03365.

Cruz, F.W., Vuille, M., Burns, S.J., Wang, X., Cheng, H., Werner, M., Lawrence Edwards, R., Karmann, I., Auler, A.S., and Nguyen, H., 2009, Orbitally driven east-west antiphasing of South American precipitation: Nature Geoscience, v. 2, p. 210–214, doi:10.1038/ngeo444.

Dansgaard, W., 1964, Stable isotopes in precipitation: Tellus, v. 16, p. 436–468, doi:10.3402/tellusa.v16i4.8993.

Dennis, K.J., Affek, H.P., Passey, B.H., Schrag, D.P., and Eiler, J.M., 2011, Defining an absolute reference frame for "clumped" isotope studies of CO_2: Geochimica et Cosmochimica Acta, v. 75, p. 7117–7131, doi:10.1016/j.gca.2011.09.025.

Drenkhan, F., Buytaert, W., Mackay, J.D., Barrand, N.E., Hannah, D.M., and Huggel, C., 2022, Looking beyond glaciers to understand mountain water security: Nature Sustainability, v. 6, p. 130–138, doi:10.1038/s41893-022-00996-4.

Drenkhan, F., Guardamino, L., Huggel, C., and Frey, H., 2018, Current and future glacier and lake assessment in the deglaciating Vilcanota-Urubamba basin, Peruvian Andes: Global and Planetary Change, v. 169, p. 105–118, doi:10.1016/j.gloplacha.2018.07.005.

Drenkhan, F., Huggel, C., Guardamino, L., and Haeberli, W., 2019, Managing risks and future options from new lakes in the deglaciating Andes of Peru: The example of the Vilcanota-Urubamba basin: Science of The Total Environment, v. 665, p. 465–483, doi:10.1016/j.scitotenv.2019.02.070.

Eiler, J.M., 2007, "Clumped-isotope" geochemistry-The study of naturally-occurring, multiply-substituted isotopologues: Earth and Planetary Science Letters, v. 262, p. 309–327, doi:10.1016/j.epsl.2007.08.020.

Eiler, J.M., 2011, Paleoclimate reconstruction using carbonate clumped isotope thermometry: Quaternary Science Reviews, v. 30, p. 3575–3588, doi:10.1016/j.quascirev.2011.09.001.

Fetrow, A.C., Snell, K.E., Di Fiori, R. V., Long, S.P., and Bonde, J.W., 2022, How Hot Is Too Hot? Disentangling Mid-Cretaceous Hothouse Paleoclimate From Diagenesis: Paleoceanography and Paleoclimatology, v. 37, doi:10.1029/2022PA004517.

Flusche, M.A., Seltzer, G., Rodbell, D., Siegel, D., and Samson, S., 2005, Constraining water sources and hydrologic processes from the isotopic analysis of water and dissolved strontium, Lake Junin, Peru: Journal of Hydrology, v. 312, p. 1–13, doi:10.1016/j.jhydrol.2005.02.021.

Fritz, S.C., Baker, P.A., Seltzer, G.O., Ballantyne, A., Tapia, P., Cheng, H., and Edwards, R.L., 2007, Quaternary glaciation and hydrologic variation in the South American tropics as reconstructed from the Lake Titicaca drilling project: Quaternary Research, v. 68, p. 410–420, doi:10.1016/j.yqres.2007.07.008.

Garreaud, R.D., Vuille, M., Compagnucci, R., and Marengo, J., 2009, Present-day South American climate: Palaeogeography, Palaeoclimatology, Palaeoecology, v. 281, p. 180–195, doi:10.1016/j.palaeo.2007.10.032.

Gat, J.R., 1996, Oxygen and Hydrogen Isotopes in the Hydrologic Cycle: Annual Review of Earth and Planetary Sciences, v. 24, p. 225–262, doi:10.1146/annurev.earth.24.1.225.

Gázquez, F., Morellón, M., Bauska, T., Herwartz, D., Surma, J., Moreno, A., Staubwasser, M., Valero-Garcés, B., Delgado-Huertas, A., and Hodell, D.A., 2018, Triple oxygen and hydrogen isotopes of gypsum hydration water for quantitative paleo-humidity reconstruction: Earth and Planetary Science Letters, v. 481, p. 177–188, doi:10.1016/j.epsl.2017.10.020.

Ghosh, P., Adkins, J., Affek, H., Balta, B., Guo, W., Schauble, E.A., Schrag, D., and Eiler, J.M., 2006, ^{13}C–^{18}O bonds in carbonate minerals: A new kind of paleothermometer: Geochimica et Cosmochimica Acta, v. 70, p. 1439–1456, doi:10.1016/j.gca.2005.11.014.

Gibson, J.J., Birks, S.J., and Yi, Y., 2016, Stable isotope mass balance of lakes: A contemporary perspective: Quaternary Science Reviews, v. 131, p. 316–328, doi:10.1016/j.quascirev.2015.04.013.

Grimm, A.M., Dominguez, F., Cavalcanti, I.F.A., Cavazos, T., Gan, M.A., Silva Dias, P.L., Fu, R., Castro, C., Hu, H., and Barreiro, M., 2021, South and North American Monsoons: Characteristics, Life Cycle, Variability, Modeling, and Prediction, *in* The Multiscale Global Monsoon System (4th ed.), p. 49–66, doi:10.1142/9789811216602_0005.

Guo, W., Mosenfelder, J.L., Goddard, W.A., and Eiler, J.M., 2009, Isotopic fractionations associated with phosphoric acid digestion of carbonate minerals: Insights from first-principles theoretical modeling and clumped isotope measurements: Geochimica et Cosmochimica Acta, v. 73, p. 7203–7225, doi:10.1016/j.gca.2009.05.071.

Haeberli, W., and Drenkhan, F., 2022, Future Lake Development in Deglaciating Mountain Ranges, *in* Oxford Research Encyclopedia of Natural Hazard Science, Oxford University Press, doi:10.1093/acrefore/9780199389407.013.361.

Hansen, B.C.S., Seltzer, G.O., and Wright, H.E., 1994, Late Quaternary vegetational change in the central Peruvian Andes: Palaeogeography, Palaeoclimatology, Palaeoecology, v. 109, p. 263–285, doi:10.1016/0031-0182(94)90179-1.

Hansen, B.C.S., Wright, H.E., and Bradbury, J.P., 1984, Pollen studies in the Junín area, central Peruvian Andes: Geological Society of America Bulletin, v. 95, p. 1454, doi:10.1130/0016-7606(1984)95<1454:PSITJA>2.0.CO;2.

Harrison, S.P., and Bartlein, P., 2012, Records from the Past, Lessons for the Future, *in* The Future of the World's Climate, Elsevier, p. 403–436, doi:10.1016/B978-0-12-386917-3.00014-2.

Hatfield, R.G., Stoner, J.S., Solada, K.E., Morey, A.E., Woods, A., Chen, C.Y., McGee, D., Abbott, M.B., and Rodbell, D.T., 2020a, Paleomagnetic Constraint of the Brunhes Age Sedimentary Record From Lake Junín, Peru: Frontiers in Earth Science, v. 8, p. 1–18, doi:10.3389/feart.2020.00147.

Hatfield, R.G., Woods, A., Lehmann, S.B., Weidhaas, N., Chen, C.Y., Kück, J., Pierdominici, S., Stoner, J.S., Abbott, M.B., and Rodbell, D.T., 2020b, Stratigraphic correlation and splice generation for sediments recovered from a large-lake drilling project: an example from Lake Junín, Peru: Journal of Paleolimnology, v. 63, p. 83–100, doi:10.1007/s10933-019-00098-w.

Hayles, J.A., and Killingsworth, B.A., 2022, Constraints on triple oxygen isotope kinetics: Chemical Geology, v. 589, p. 120646, doi:10.1016/j.chemgeo.2021.120646.

Herwartz, D., Surma, J., Voigt, C., Assonov, S., and Staubwasser, M., 2017, Triple oxygen isotope systematics of structurally bonded water in gypsum: Geochimica et Cosmochimica Acta, v. 209, p. 254–266, doi:10.1016/j.gca.2017.04.026.

Horton, T.W., Defliese, W.F., Tripati, A.K., and Oze, C., 2016, Evaporation induced ^{18}O and ^{13}C enrichment in lake systems: A global perspective on hydrologic balance effects: Quaternary Science Reviews, v. 131, p. 365–379, doi:10.1016/j.quascirev.2015.06.030.

Hou, A., Bahr, A., Raddatz, J., Voigt, S., Greule, M., Albuquerque, A.L., Chiessi, C.M., and Friedrich, O., 2020, Insolation and Greenhouse Gas Forcing of the South American Monsoon System Across Three Glacial-Interglacial Cycles: Geophysical Research Letters, v. 47, doi:10.1029/2020GL087948.

Huntington, K.W., and Petersen, S. V., 2023, Frontiers of Carbonate Clumped Isotope Thermometry: Annual Review of Earth and Planetary Sciences, v. 51, doi:10.1146/annurev-earth-031621-085949.

Ibarra, D.E., Kukla, T., Methner, K.A., Mulch, A., and Chamberlain, C.P., 2021, Reconstructing Past Elevations From Triple Oxygen Isotopes of Lacustrine Chert: Application to the Eocene Nevadaplano, Elko Basin, Nevada, United States: Frontiers in Earth Science, v. 9, p. 1–19, doi:10.3389/feart.2021.628868.

Ingalls, M., Frantz, C.M., Snell, K.E., and Trower, E.J., 2020, Carbonate facies-specific stable isotope data record climate, hydrology, and microbial communities in Great Salt Lake, UT: Geobiology, v. 18, p. 566–593, doi:10.1111/gbi.12386.

IPCC, 2021, Annex V: Monsoons, *in* Cherchi, A. and Turner, A. eds., Climate Change 2021 – The Physical Science Basis Contribution of Working Group I to the Sixth Assessment Report of the Intergovernmental Panel on Climate Change, Cambridge, United Kingdom and New York, NY, USA, Cambridge University Press, p. 2193–2204, doi:10.1017/9781009157896.019.

IPCC, 2014, Climate change 2014 impacts, adaptation, and vulnerability Part B: Regional aspects (V. R. Barros et al., Eds.): Cambridge, United Kingdom and New York, NY, USA, Cambridge University Press, 1–688 p., doi:10.1017/CBO9781107415386.

Jouzel, J. et al., 2007, Orbital and Millennial Antarctic Climate Variability over the Past 800,000 Years: Science, v. 317, p. 793–796, doi:10.1126/science.1141038.

Kanner, L.C., Burns, S.J., Cheng, H., and Edwards, R.L., 2012, High-Latitude Forcing of the South American Summer Monsoon During the Last Glacial: Science, v. 335, p. 570–573, doi:10.1126/science.1213397.

Kanner, L.C., Burns, S.J., Cheng, H., Edwards, R.L., and Vuille, M., 2013, High-resolution variability of the South American summer monsoon over the last seven millennia: insights from a speleothem record from the central Peruvian Andes: Quaternary Science Reviews, v. 75, p. 1–10, doi:10.1016/j.quascirev.2013.05.008.

Katz, S.A., Levin, N.E., Abbott, M.B., Rodbell, D.T., Passey, B.H., DeLuca, N.M., Larsen, D.J., and Woods, A. Holocene temperature and water stress in the Peruvian Andes: insights from lake carbonate clumped and triple oxygen isotopes: Paleoceanography and Paleoclimatology, *in review*.

Katz, S.A., Levin, N.E., Rodbell, D.T., Gillikin, D.P., Aron, P.G., Passey, B.H., Tapia, P.M., Serrepe, A.R., and Abbott, M.B., 2023, Detecting hydrologic distinctions among Andean lakes using clumped and triple oxygen isotopes: Earth and Planetary Science Letters, v. 602, p. 117927, doi:10.1016/j.epsl.2022.117927.

Kelson, J.R., Huntington, K.W., Schauer, A.J., Saenger, C., and Lechler, A.R., 2017, Toward a universal carbonate clumped isotope calibration: Diverse synthesis and preparatory methods suggest a single temperature relationship: Geochimica et Cosmochimica Acta, v. 197, p. 104–131, doi:10.1016/J.GCA.2016.10.010.

Kelson, J.R., Petersen, S. V., Niemi, N.A., Passey, B.H., and Curley, A.N., 2022, Looking upstream with clumped and triple oxygen isotopes of estuarine oyster shells in the early Eocene of California, USA: Geology, doi:10.1130/G49634.1.

Konecky, B.L., Noone, D.C., and Cobb, K.M., 2019, The Influence of Competing Hydroclimate Processes on Stable Isotope Ratios in Tropical Rainfall: Geophysical Research Letters, v. 46, p. 1622–1633, doi:10.1029/2018GL080188.

Kukla, T., Ahlström, A., Maezumi, S.Y., Chevalier, M., Lu, Z., Winnick, M.J., and Chamberlain, C.P., 2021, The resilience of Amazon tree cover to past and present drying: Global and Planetary Change, v. 202, doi:10.1016/j.gloplacha.2021.103520.

Lachniet, M.S., 2009, Climatic and environmental controls on speleothem oxygen-isotope values: Quaternary Science Reviews, v. 28, p. 412–432, doi:10.1016/j.quascirev.2008.10.021.

Laskar, J., Robutel, P., Joutel, F., Gastineau, M., Correia, A.C.M., and Levrard, B., 2004, A long-term numerical solution for the insolation quantities of the Earth: Astronomy & Astrophysics, v. 428, p. 261–285, doi:10.1051/0004-6361:20041335.

Leng, M.J., and Marshall, J.D., 2004, Palaeoclimate interpretation of stable isotope data from lake sediment archives: Quaternary Science Reviews, v. 23, p. 811–831, doi:10.1016/J.QUASCIREV.2003.06.012.

Lenters, J.D., and Cook, K.H., 1995, Simulation and Diagnosis of the Regional Summertime Precipitation Climatology of South America: Journal of Climate, v. 8, p. 2988–3005, doi:10.1175/1520-0442(1995)008<2988:SADOTR>2.0.CO;2.

Lenters, J.D., and Cook, K.H., 1999, Summertime Precipitation Variability over South America: Role of the Large-Scale Circulation: Monthly Weather Review, v. 127, p. 409–431, doi:10.1175/1520-0493(1999)127<0409:SPVOSA>2.0.CO;2.

Lisiecki, L.E., and Raymo, M.E., 2005, A Pliocene-Pleistocene stack of 57 globally distributed benthic $\delta^{18}O$ records: Paleoceanography, v. 20, doi:10.1029/2004PA001071.

Liu, X., and Battisti, D.S., 2015, The influence of orbital forcing of tropical insolation on the climate and isotopic composition of precipitation in South America: Journal of Climate, v. 28, p. 4841–4862, doi:10.1175/JCLI-D-14-00639.1.

Loulergue, L., Schilt, A., Spahni, R., Masson-Delmotte, V., Blunier, T., Lemieux, B., Barnola, J.-M., Raynaud, D., Stocker, T.F., and Chappellaz, J., 2008, Orbital and millennial-scale features of atmospheric CH_4 over the past 800,000 years: Nature, v. 453, p. 383–386, doi:10.1038/nature06950.

Luz, B., and Barkan, E., 2010, Variations of $^{17}O/^{16}O$ and $^{18}O/^{16}O$ in meteoric waters: Geochimica et Cosmochimica Acta, v. 74, p. 6276–6286, doi:10.1016/j.gca.2010.08.016.

Marengo, J.A. et al., 2012, Recent developments on the South American monsoon system: International Journal of Climatology, v. 32, p. 1–21, doi:10.1002/joc.2254.

Mark, B.G. et al., 2017, Glacier loss and hydro-social risks in the Peruvian Andes: Global and Planetary Change, v. 159, p. 61–76, doi:10.1016/j.gloplacha.2017.10.003.

Masiokas, M.H. et al., 2020, A Review of the Current State and Recent Changes of the Andean Cryosphere: Frontiers in Earth Science, v. 8, p. 1–27, doi:10.3389/feart.2020.00099.

Matsuhisa, Y., Goldsmith, J.R., and Clayton, R.N., 1978, Mechanisms of hydrothermal crystallization of quartz at 250°C and 15 kbar: Geochimica et Cosmochimica Acta, v. 42, p. 173–182, doi:10.1016/0016-7037(78)90130-8.

Miller, M.F., 2002, Isotopic fractionation and the quantification of ^{17}O anomalies in the oxygen three-isotope system: Geochimica et Cosmochimica Acta, v. 66, p. 1881–1889, doi:10.1016/S0016-7037(02)00832-3.

Mohtadi, M., Prange, M., and Steinke, S., 2016, Palaeoclimatic insights into forcing and response of monsoon rainfall: Nature, v. 533, p. 191–199, doi:10.1038/nature17450.

NGRIP members, 2004, High-resolution record of Northern Hemisphere climate extending into the last interglacial period: Nature, v. 431, p. 147–151, doi:10.1038/nature02805.

Pabón-Caicedo, J.D., Arias, P.A., Carril, A.F., Espinoza, J.C., Borrel, L.F., Goubanova, K., Lavado-Casimiro, W., Masiokas, M., Solman, S., and Villalba, R., 2020, Observed and Projected Hydroclimate Changes in the Andes: Frontiers in Earth Science, v. 8, p. 1–29, doi:10.3389/feart.2020.00061.

Pangala, S.R. et al., 2017, Large emissions from floodplain trees close the Amazon methane budget: Nature, v. 552, p. 230–234, doi:10.1038/nature24639.

Pascale, S., Carvalho, L.M.V., Adams, D.K., Castro, C.L., and Cavalcanti, I.F.A., 2019, Current and Future Variations of the Monsoons of the Americas in a Warming Climate: Current Climate Change Reports, v. 5, p. 125–144, doi:10.1007/s40641-019-00135-w.

Passey, B.H., and Ji, H., 2019, On the use of triple oxygen isotopes in lake waters and carbonates for reconstructing $\delta^{18}O$ of unevaporated precipitation: a case study from the Western United States: Earth and Planetary Science Letters, v. 518, p. 1–12, doi:10.1016/j.epsl.2019.04.026.

Past Interglacials Working Group of PAGES, 2016, Interglacials of the last 800,000 years: Reviews of Geophysics, v. 54, p. 162–219, doi:10.1002/2015RG000482.

Petersen, S.V. V. et al., 2019, Effects of Improved ^{17}O Correction on Inter-Laboratory Agreement in Clumped Isotope Calibrations, Estimates of Mineral-Specific Offsets, and Temperature Dependence of Acid Digestion Fractionation: Geochemistry, Geophysics, Geosystems, v. 20, p. 3495–3519, doi:10.1029/2018GC008127.

Peterson, L.C., Haug, G.H., Hughen, K.A., and Röhl, U., 2000, Rapid Changes in the Hydrologic Cycle of the Tropical Atlantic During the Last Glacial: Science, v. 290, p. 1947–1951, doi:10.1126/science.290.5498.1947.

Petryshyn, V.A., Lim, D., Laval, B.L., Brady, A., Slater, G., and Tripati, A.K., 2015, Reconstruction of limnology and microbialite formation conditions from carbonate clumped isotope thermometry: Geobiology, v. 13, p. 53–67, doi:10.1111/gbi.12121.

Phillips, O.L. et al., 2009, Drought Sensitivity of the Amazon Rainforest: Science, v. 323, p. 1344–1347, doi:10.1126/science.1164033.

Punyasena, S.W., Mayle, F.E., and McElwain, J.C., 2008, Quantitative estimates of glacial and Holocene temperature and precipitation change in lowland Amazonian Bolivia: Geology, v. 36, p. 667–670, doi:10.1130/G24784A.1.

Rabatel, A. et al., 2013, Current state of glaciers in the tropical Andes: A multi-century perspective on glacier evolution and climate change: Cryosphere, v. 7, p. 81–102, doi:10.5194/tc-7-81-2013.

Rodbell, D.T. et al., 2022, 700,000 years of tropical Andean glaciation: Nature, v. 607, p. 301–306, doi:10.1038/s41586-022-04873-0.

Rozanski, K., Araguás-Araguás, L., and Gonfiantini, R., 1993, Isotopic Patterns in Modern Global Precipitation, *in* Swart, P.K., Lohmann, K.C., McKenzie, J.M., and Savin, S. eds., Climate Change in Continental Isotopic Records Geophysical Monograph, Geophysical Monograph Series, v. 78, p. 1–36, doi:10.1029/GM078p0001.

Ruddiman, W.F., 2007, Earth's Climate: Past and Future: W.H. Freeman & Company.

Salati, E., Dall'Olio, A., Matsui, E., and Gat, J.R., 1979, Recycling of water in the Amazon Basin: An isotopic study: Water Resources Research, v. 15, p. 1250–1258, doi:10.1029/WR015i005p01250.

Santi, L.M., Arnold, A.J., Ibarra, D.E., Whicker, C.A., Mering, J.A., Lomarda, R.B., Lora, J.M., and Tripati, A., 2020, Clumped isotope constraints on changes in latest Pleistocene hydroclimate in the northwestern Great Basin: Lake Surprise, California: GSA Bulletin, v. 132, p. 2669–2683, doi:10.1130/B35484.1.

Schauble, E.A., Ghosh, P., and Eiler, J.M., 2006, Preferential formation of ^{13}C–^{18}O bonds in carbonate minerals, estimated using first-principles lattice dynamics: Geochimica et Cosmochimica Acta, v. 70, p. 2510–2529, doi:10.1016/j.gca.2006.02.011.

Schiferl, J. et al., 2023, A neotropical perspective on the uniqueness of the Holocene among interglacials: Nature Communications, v. 14, p. 7404, doi:10.1038/s41467-023-43231-0.

Schneider, T., Bischoff, T., and Haug, G.H., 2014, Migrations and dynamics of the intertropical convergence zone: Nature, v. 513, p. 45–53, doi:10.1038/nature13636.

Seltzer, G., Rodbell, D., and Burns, S., 2000, Isotopic evidence for late Quaternary climatic change in tropical South America: Geology, v. 28, p. 35, doi:10.1130/0091-7613(2000)28<35:IEFLQC>2.0.CO;2.

SENAMHI, 2009, Climate Scenarios for Peru to 2030: Ministry of Environment, National Metereology and Hidrology Service (SEHAMHI). Peru. https://www.senamhi.gob.pe/usr/cmn/pdf/Resumen_Nacional_Ingles.pdf (accessed February 2024).

Silva, Y., Takahashi, K., and Chávez, R., 2008, Dry and wet rainy seasons in the Mantaro river basin (Central Peruvian Andes): Advances in Geosciences, v. 14, p. 261–264, doi:10.5194/adgeo-14-261-2008.

Solman, S.A., 2013, Regional Climate Modeling over South America: A Review: Advances in Meteorology, v. 2013, p. 1–13, doi:10.1155/2013/504357.

Staal, A., Flores, B.M., Aguiar, A.P.D., Bosmans, J.H.C., Fetzer, I., and Tuinenburg, O.A., 2020, Feedback between drought and deforestation in the Amazon: Environmental Research Letters, v. 15, p. 044024, doi:10.1088/1748-9326/ab738e.

Staal, A., Tuinenburg, O.A., Bosmans, J.H.C., Holmgren, M., Van Nes, E.H., Scheffer, M., Zemp, D.C., and Dekker, S.C., 2018, Forest-rainfall cascades buffer against drought across the Amazon: Nature Climate Change, v. 8, p. 539–543, doi:10.1038/s41558-018-0177-y.

Stute, M., Forster, M., Frischkorn, H., Serejo, A., Clark, J.F., Schlosser, P., Broecker, W.S., and Bonani, G., 1995, Cooling of Tropical Brazil (5°C) During the Last Glacial Maximum: Science, v. 269, p. 379–383, doi:10.1126/science.269.5222.379.

Surma, J., Assonov, S., Bolourchi, M.J., and Staubwasser, M., 2015, Triple oxygen isotope signatures in evaporated water bodies from the Sistan Oasis, Iran: Geophysical Research Letters, v. 42, p. 8456–8462, doi:10.1002/2015GL066475.

Surma, J., Assonov, S., Herwartz, D., Voigt, C., and Staubwasser, M., 2018, The evolution of ^{17}O-excess in surface water of the arid environment during recharge and evaporation: Scientific Reports, v. 8, p. 4972, doi:10.1038/s41598-018-23151-6.

Terzer-Wassmuth, S., Araguás-Araguás, L.J., Wassenaar, L.I., and Stumpp, C., 2023, Global and local meteoric water lines for $\delta^{17}O/\delta^{18}O$ and the spatiotemporal distribution of $\Delta'^{17}O$ in Earth's precipitation: Scientific Reports, v. 13, p. 19056, doi:10.1038/s41598-023-45920-8.

Vera, C. et al., 2006, Toward a Unified View of the American Monsoon Systems: Journal of Climate, v. 19, p. 4977–5000, doi:10.1175/JCLI3896.1.

Vuille, M. et al., 2018, Rapid decline of snow and ice in the tropical Andes – Impacts, uncertainties and challenges ahead: Earth-Science Reviews, v. 176, p. 195–213, doi:http://dx.doi.org/10.1016/j.earscirev.2017.09.019.

Wang, X., Edwards, R.L., Auler, A.S., Cheng, H., Kong, X., Wang, Y., Cruz, F.W., Dorale, J.A., and Chiang, H.W., 2017, Hydroclimate changes across the Amazon lowlands over the past 45,000 years: Nature, v. 541, p. 204–207, doi:10.1038/nature20787.

Wang, Z., Schauble, E.A., and Eiler, J.M., 2004, Equilibrium thermodynamics of multiply substituted isotopologues of molecular gases: Geochimica et Cosmochimica Acta, v. 68, p. 4779–4797, doi:10.1016/j.gca.2004.05.039.

Ward, B.M., Wong, C.I., Novello, V.F., McGee, D., Santos, R. V., Silva, L.C.R., Cruz, F.W., Wang, X., Edwards, R.L., and Cheng, H., 2019, Reconstruction of Holocene coupling between the South American Monsoon System and local moisture variability from speleothem $\delta^{18}O$ and $^{87}Sr/^{86}Sr$ records: Quaternary Science Reviews, v. 210, p. 51–63, doi:10.1016/j.quascirev.2019.02.019.

Woods, A. et al., 2020, Andean drought and glacial retreat tied to Greenland warming during the last glacial period: Nature Communications, v. 11, p. 5135, doi:10.1038/s41467-020-19000-8.

Wortham, B.E., Wong, C.I., Silva, L.C.R., McGee, D., Montañez, I.P., Troy Rasbury, E., Cooper, K.M., Sharp, W.D., Glessner, J.J.G., and Santos, R. V., 2017, Assessing response of local moisture conditions in central Brazil to variability in regional monsoon intensity using speleothem 87Sr/86Sr values: Earth and Planetary Science Letters, v. 463, p. 310–322, doi:10.1016/j.epsl.2017.01.034.

Young, E.D., Galy, A., and Nagahara, H., 2002, Kinetic and equilibrium mass-dependent isotope fractionation laws in nature and their geochemical and cosmochemical significance: Geochimica et Cosmochimica Acta, v. 66, p. 1095–1104, doi:10.1016/S0016-7037(01)00832-8.

Zachos, J., Pagani, M., Sloan, L., Thomas, E., and Billups, K., 2001, Trends, Rhythms, and Aberrations in Global Climate 65 Ma to Present: Science, v. 292, p. 686–693, doi:10.1126/science.1059412.

Zemp, D.C., Schleussner, C. -F., Barbosa, H.M.J., and Rammig, A., 2017, Deforestation effects on Amazon forest resilience: Geophysical Research Letters, v. 44, p. 6182–6190, doi:10.1002/2017GL072955.

Chapter 2 Detecting Hydrologic Distinctions Among Andean Lakes Using Clumped And Triple Oxygen Isotopes[1]

2.1 Abstract

Oxygen isotope distributions from lacustrine carbonates provide insights into climate and hydrological change, but it is difficult to isolate the influences of catchment precipitation $\delta^{18}O$, water temperature, and evaporation on lacustrine carbonate $\delta^{18}O$ values. Recent work shows the potential for using a combination of clumped (Δ_{47}) and triple oxygen isotope ($\Delta'^{17}O$) measurements to identify the roles of temperature and evaporation on carbonate $\delta^{18}O$ values in lakes, allowing precipitation $\delta^{18}O$ values to be inferred and facilitating paleoclimate reconstructions. However, modern calibration of this approach has been mostly limited to arid regions with a high ratio of evaporative losses over inputs (X_E) and low relative humidity (h <0.7). Developing this tool for paleoclimate and paleoelevation reconstructions requires expanding the modern calibrations to a greater range of climatic and hydrologic conditions. We sampled four lakes in different hydrologic states under a single, high humidity climate regime (h= 0.7–0.9) in the Lake Junín region of central Peru. Clumped isotope temperatures from lake carbonates reflect water temperatures during carbonate formation. Lake hydrology is the main control on the $\Delta'^{17}O$ values of carbonates and waters: $\Delta'^{17}O$ values are lowest in the larger lakes with higher X_E when compared to smaller, headwater lakes where evaporation is minimal and $\Delta'^{17}O$ is indistinguishable from that of precipitation. Reconstructed unevaporated catchment precipitation $\delta'^{18}O$ ($\delta'^{18}O_{rucp}$) values from lake waters relies on accurate characterization of λ_{lake}, the triple oxygen isotope evaporation slope. We explore the influence of humidity on λ_{lake} using both new observations and modeled data. Accounting for local humidity improves λ_{lake} estimates, which allows for more accurate reconstructions of $\delta'^{18}O_{rucp}$. We generate a $\delta'^{18}O_{rucp}$ value of -15.2 ±2.1‰ from modern carbonates

[1] Published as Katz, S.A., Levin, N.E., Rodbell, D.T., Gillikin, D.P., Aron, P.G., Passey, B.H., Tapia, P.M., Serrepe, A.R., Abbott, M.B., (2023) Detecting hydrologic distinctions among Andean lakes using clumped and triple oxygen isotopes, Earth and Planetary Science Letters, 602, 10.1016/j.epsl.2022.117927.

and waters (n= 15) in the Lake Junín region, which is similar to amount weighted mean annual precipitation -14.1 (±2.2‰). This study illustrates that (1) $\Delta'^{17}O$ can be used to differentiate between lakes with differing X_E in humid climates, (2) lake carbonate $\Delta'^{17}O$ and $\delta^{18}O$ values can be used to evaluate the influence of evaporation on lake water $\delta^{18}O$ values in a range of climates, and (3) modeling λ_{lake} under appropriate humidity conditions improves $\delta'^{18}O_{rucp}$ estimates from lake carbonate $\Delta'^{17}O$.

2.2 Introduction

Lakes are sensitive to changes in atmospheric processes, hydrology, and climate such that lake sediments are commonly used to reconstruct past climate (Seltzer et al., 2000; Leng and Marshall, 2004; Bird et al., 2011a). Stable oxygen isotope distributions in lake carbonates are powerful paleoclimate archives because they record information about $\delta^{18}O$ values of precipitation, water temperature, and evaporation (Figure 2.1; Leng and Marshall, 2004). However, difficulty isolating the controls on lake carbonate $\delta^{18}O$ limits their efficacy in paleoclimate and paleoelevation studies (Seltzer et al., 2000; Horton et al., 2016). Recent studies address these limitations and expand the utility of lake carbonates by using clumped and triple oxygen isotopes to constrain temperature and evaporative fluxes (e.g., Huntington et al., 2015; Passey and Ji, 2019).

Advances in clumped isotope carbonate thermometry provide constraints on both the temperature and $\delta^{18}O$ values of ancient lake water (e.g., Huntington et al., 2010, 2015; Hren and Sheldon, 2012; Petryshyn et al., 2015; Horton et al., 2016). However, even with these constraints, forming interpretations about hydrology, climate, or elevation from $\delta^{18}O$ values of reconstructed formation waters ($\delta^{18}O_{rfw}$), is difficult without knowing the evaporation state of the water and its relationship to the isotopic composition of precipitation (e.g., Horton et al., 2016). High-precision triple oxygen isotope geochemistry offers a new approach for identifying the role of evaporation in lake budgets and for stripping away evaporative effects on $\delta^{18}O_{rfw}$ values (Luz and Barkan, 2010; Passey et al., 2014; Gázquez et al., 2018; Surma et al., 2018; Passey and Ji, 2019). These studies use the $\Delta'^{17}O$ parameter, which represents the deviation from a reference line (λ_{ref}) in $\delta'^{18}O$ and $\delta'^{17}O$ space (λ_{ref}= 0.528; where $\delta'^{x}O=\ln(\delta^{x}O+1)$; Figure 2.1; e.g., Luz and Barkan, 2010). Evaporation involves both equilibrium and kinetic fractionations, resulting in residual waters with

low $\Delta'^{17}O$ values, as kinetic processes follow a shallower slope than λ_{ref} (Barkan and Luz, 2005; Luz and Barkan, 2010). The magnitude of kinetic fractionation during evaporation partially depends on local humidity (Landais et al., 2006), thereby linking humidity and the evaporation slope: λ_{lake}.

Combining measurements of carbonate $\Delta'^{17}O$ and clumped isotope derived temperatures allows formation water $\Delta'^{17}O$ values ($\Delta'^{17}O_{rfw}$) to be calculated and used towards evaluating evaporative losses from lakes, (i.e., X_E the fractional loss of evaporation relative to inflowing waters; Herwartz et al., 2017; Gázquez et al., 2018; Passey and Ji, 2019). As Passey and Ji (2019) illustrate, $\Delta'^{17}O_{rfw}$ and $\delta^{18}O_{rfw}$ are related to $\Delta'^{17}O$ and $\delta^{18}O$ of unevaporated precipitation by the evaporation slope, λ_{lake}, such that $\delta^{18}O$ of unevaporated catchment precipitation ($\delta^{18}O_{rucp}$) can be reconstructed via "back projection" (Figure 2.1). Recently, the back projection approach has been applied to Eocene cherts (Ibarra et al., 2021) and bivalves (Kelson et al., 2022). This approach depends on knowledge of λ_{lake}, which has been studied in closed-basin lakes and arid environments (Surma et al., 2018; Passey and Ji, 2019) and a temperate lake (Pierchala et al., 2022), but we are not aware of a study that explores the role of humidity on λ_{lake} nor that study lakes with varying X_E within humid settings.

Here we present a dataset of the triple oxygen isotope compositions of precipitation, surface waters, and lacustrine carbonates from four lakes with different hydrological configurations in the central Peruvian Andes where relative humidity is >0.7 (Table S2.1; SENAMHI, 2022). Our data contribute to clumped isotope datasets of modern lake carbonates and fill a data gap for $\Delta'^{17}O$ and λ_{lake} from low X_E lakes in humid settings. We evaluate these data by modeling expected distributions under steady state conditions for lake water evaporation, which enables us to refine the relationship between $\Delta'^{17}O$ and λ_{lake} for humid climates.

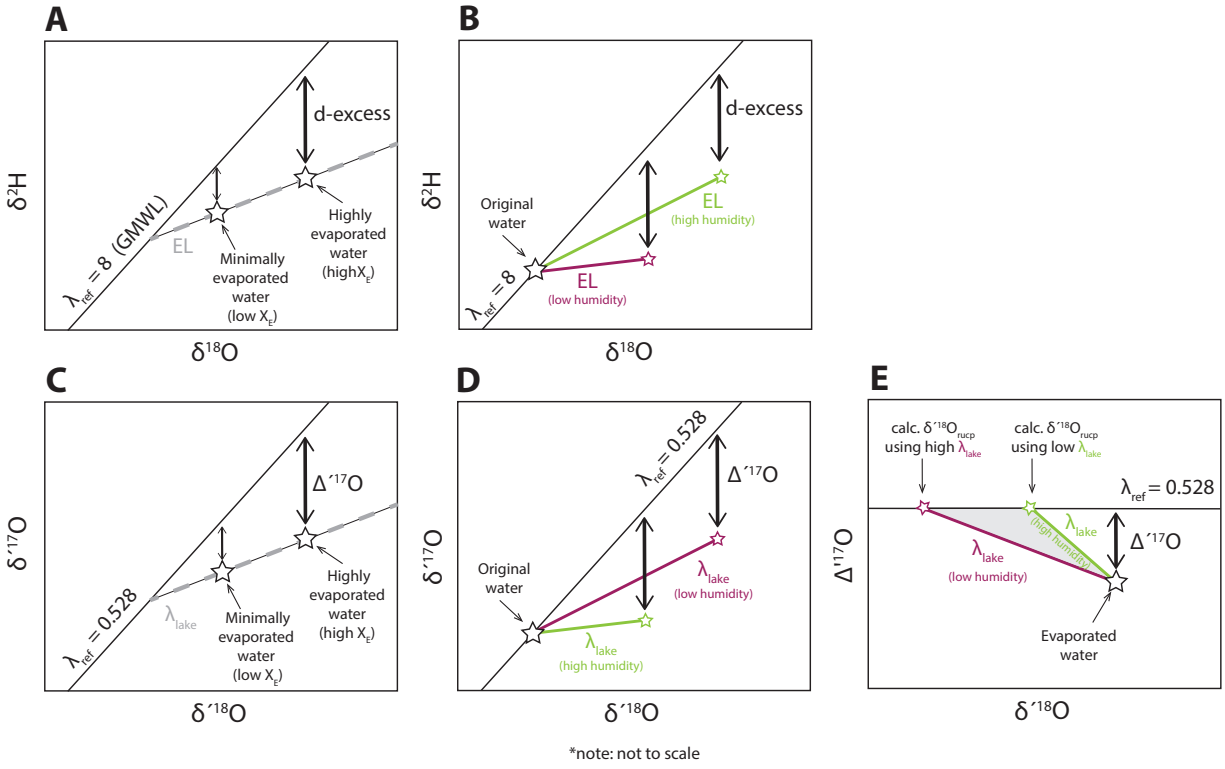

Figure 2.1: Schematics for oxygen and hydrogen isotope fractionation in waters. For $\delta^{18}O$-$\delta^{2}H$ distributions, (A) shows how evaporated waters fall along a shallower Evaporation Line (EL) slope than the Global Meteoric Water Line (GMWL) and (B) shows how the isotopic composition of evaporated waters is related to unevaporated input water; colored lines represent EL slopes under varying humidity conditions. For $\delta'^{18}O$-$\delta'^{17}O$ space, in (C) $\Delta'^{17}O$ quantifies deviations from a reference slope (λ_{ref}) along a shallower evaporation slope, λ_{lake}, and (D) shows variation in evaporation slope, λ_{lake}, under varying humidity conditions. The schematic in (E) highlights the influence of λ_{lake} (and by extension, humidity) on the calculated $\delta'^{18}O$ value of unevaporated precipitation ($\delta'^{18}O_{rucp}$). The two humidity scenarios shown in panels B, D, and E, highlight the relationships between humidity, λ_{lake}, and d-excess (B) or $\Delta'^{17}O$ (D-E). Note: not to scale.

2.3 Isotope notation

2.3.1 Oxygen and hydrogen isotopes

Isotope fractionation is described by a fractionation factor, α, where R_A and R_B represent the ratio of heavy to light isotopes of two phases or materials:

$$\alpha_{A-B} = \frac{R_A}{R_B} \quad (1)$$

In the triple oxygen isotope system, ^{18}O, ^{17}O, ^{16}O, a power law describes mass-dependent relationships between $^{18}\alpha_{A\text{-}B}$ and $^{17}\alpha_{A\text{-}B}$, which are related by a fractionation exponent, θ (Young et al., 2002):

$$^{17}\alpha_{A-B} = \left(^{18}\alpha_{A-B}\right)^{\theta} \tag{2}$$

We also use the term λ, which is mathematically equivalent to θ, for "apparent" fractionation exponents that represent a combination of multiple fractionation processes.

Conventionally, isotope ratios are reported in "delta notation":

$$\delta = \left(\frac{R_A}{R_{standard}} - 1\right) \tag{3}$$

However, isotope ratios may also be expressed in logarithmic form (Hulston and Thode, 1965):

$$\delta' = \ln\left(\frac{R_A}{R_{standard}}\right) \tag{4}$$

This "delta prime" notation is commonly used in triple oxygen isotope studies (see Miller and Pack, 2021, and references therein). In a triple oxygen isotope plot, i.e., $\delta'^{18}O$-$\delta'^{17}O$, deviations from a reference line (Figure 2.1C) are quantified using the expression for $\Delta'^{17}O$:

$$\Delta'^{17}O = \delta'^{17}O - \lambda_{ref} \times \delta'^{18}O \tag{5}$$

Frequently, $\Delta'^{17}O$ is reported in units of "per meg." The reference slope, λ_{ref}, is commonly defined as 0.528 in hydrological studies (Luz and Barkan, 2010; Aron et al., 2021a) and we follow this convention. The $\Delta'^{17}O$ term is analogous to d-excess in $\delta^{18}O$-$\delta^{2}H$ space (Figure 2.1A,B; Dansgaard, 1964):

$$\text{d-excess} = \delta^{2}H - 8 \times \delta^{18}O \tag{6}$$

2.3.2 Carbonate clumped isotopes

The abundance of multiply substituted or "clumped" isotopologues relative to a stochastic baseline is temperature-dependent in carbonates (Schauble et al., 2006; Eiler, 2007, 2011). In CO_2 derived from acid digestion of carbonates, *m/z* 47 is the most abundant clumped isotopologue. The enrichment of ^{13}C–^{18}O bonds in carbonate minerals is calculated based on simultaneous collection of *m/z* 44–49 during analysis (which inherently yields sample $^{13}C/^{12}C$ and $^{18}O/^{16}O$) and is defined as Δ_{47}, where R and R* values represent measured and stochastic isotope ratios, respectively, compared to *m/z* 44 (Wang et al., 2004; Eiler, 2011):

$$\Delta_{47} = \left[\left(\frac{\mathrm{R47}}{\mathrm{R47^*}} - 1\right) - \left(\frac{\mathrm{R46}}{\mathrm{R46^*}} - 1\right) - \left(\frac{\mathrm{R45}}{\mathrm{R45^*}} - 1\right)\right] \times 1000 \quad (7)$$

Δ_{47} values have an inverse relationship to temperature (Schauble et al., 2006; Eiler, 2007, 2011) as documented theoretically and empirically in carbonate materials (e.g., Wang et al., 2004; Petersen et al., 2019), such that it is becoming a widespread approach for determining carbonate formation temperatures. We use the term $T_{\Delta47}$ to represent reconstructed carbonate formation temperatures derived from clumped isotopes. $T_{\Delta47}$ can be used to calculate formation water values ($\delta^{18}O_{rfw}$) from carbonate $\delta^{18}O$ assuming equilibrium growth conditions (Kim and O'Neil, 1997).

2.4 Study area and materials

2.4.1 Study area

The Lake Junín region in central Peru is an intermontane plateau between the Andean Cordilleras (4000–4600 m above sea level; Figure 2.2; Table 2.1). Mean annual air temperature (MAT) is 6.5°C and annual precipitation is 900–1000 mm, with approximately 70% of rainfall from October–April (Table S2.1; SENAMHI, 2022). Mean annual potential evapotranspiration is 525–550 mm/year. Relative humidity is between 70–90% year-round, rarely falling below 70% (SENAMHI, 2022). Relative humidity normalized to lake surface temperature is >70%.

Glaciation of the Lake Junín region has resulted in many lakes that exist under the same climatic conditions but differ in size and hydrology. Jurassic–Triassic aged limestone bedrock of

the Pucarà Group leads to high bicarbonate concentrations in local surface waters and production of authigenic carbonate in many lakes (Cobbing et al., 1996; Flusche et al., 2005).

We sampled two small lakes and two larger lakes (lake surface area <10 km^2 and >10^1–10^2 km^2, respectively; Figure 2.2; Table 2.1). The smaller lakes, Pumacocha and Mehcocha, are headwater lakes in glacial valleys and have continuous inflow and outflow. Pumacocha's maximum water depth is 23.5 m, whereas at Mehcocha it is 25.5 m in the upper basin and 12.4 m in the lower basin (Bird et al., 2011b). We estimate that X_E for Pumacocha and Mehcocha is very low (X_E <0.1) and characterize them as "unevaporated," consistent with a short residence time for small, continuously overflowing lakes (e.g., Bird et al., 2011b, 2011a). The other lakes, Yanacocha and Lake Junín, have much larger watersheds. Yanacocha sits in a glacial valley with sub-basins that result in a larger lake surface area and more complex hydrology than the smaller lake systems (Figure 2.2B). Lake Junín is the largest of the four lakes sampled and sits in a fault-bounded basin, surrounded by alluvial fans. It is the second largest lake in Peru by surface area (~300 km^2), but it is shallow with a maximum water depth of 15 m (Figure 2.2B; Seltzer et al., 2000). Currently, a 4 m high dam situated downstream from the inflow/outflow regulates water level, which impacts hydrology by increasing wet season inflow and dry season outflow. We expect annual variations in X_E may be low, however we lack quantitative X_E estimates.

Table 2.1: Summary and descriptions of the locations referred to in this text.

Name	Description
Lake Junín region	The geographic area in which samples were collected (approx. 10.6−11.3°S; 75.8−76.3 °W)
Junín region	Department of Junín (Peruvian geopolitical region; approx. 10.7−12.6°S; 73.4−76.5 °W)
Junín	Town of Junín, Peru (11.15 °S; 75.00 °W)
Marcapomacocha	Town of Marcapomacocha and site of IAEA GNIP station (11.40 °S; 76.33 °W)
Pumacocha	Laguna Pumacocha watershed (10.70 °S; 76.06 °W)
Mehcocha[1]	Laguna Mehcocha watershed (11.26 °S; 76.04 °W)
Yanacocha	Laguna Yanacocha watershed (10.84 °S; 76.04 °W)
Lake Junín[2]	Lake Junín watershed (11.00 °S; 76.10 °W)

[1] The official name for this lake is Laguna Catucana, note that "Mehcocha" is an informal name.

[2] Lake Junín is also known as *Chinchaycocha* or *Chinchayqucha* in Quechua.

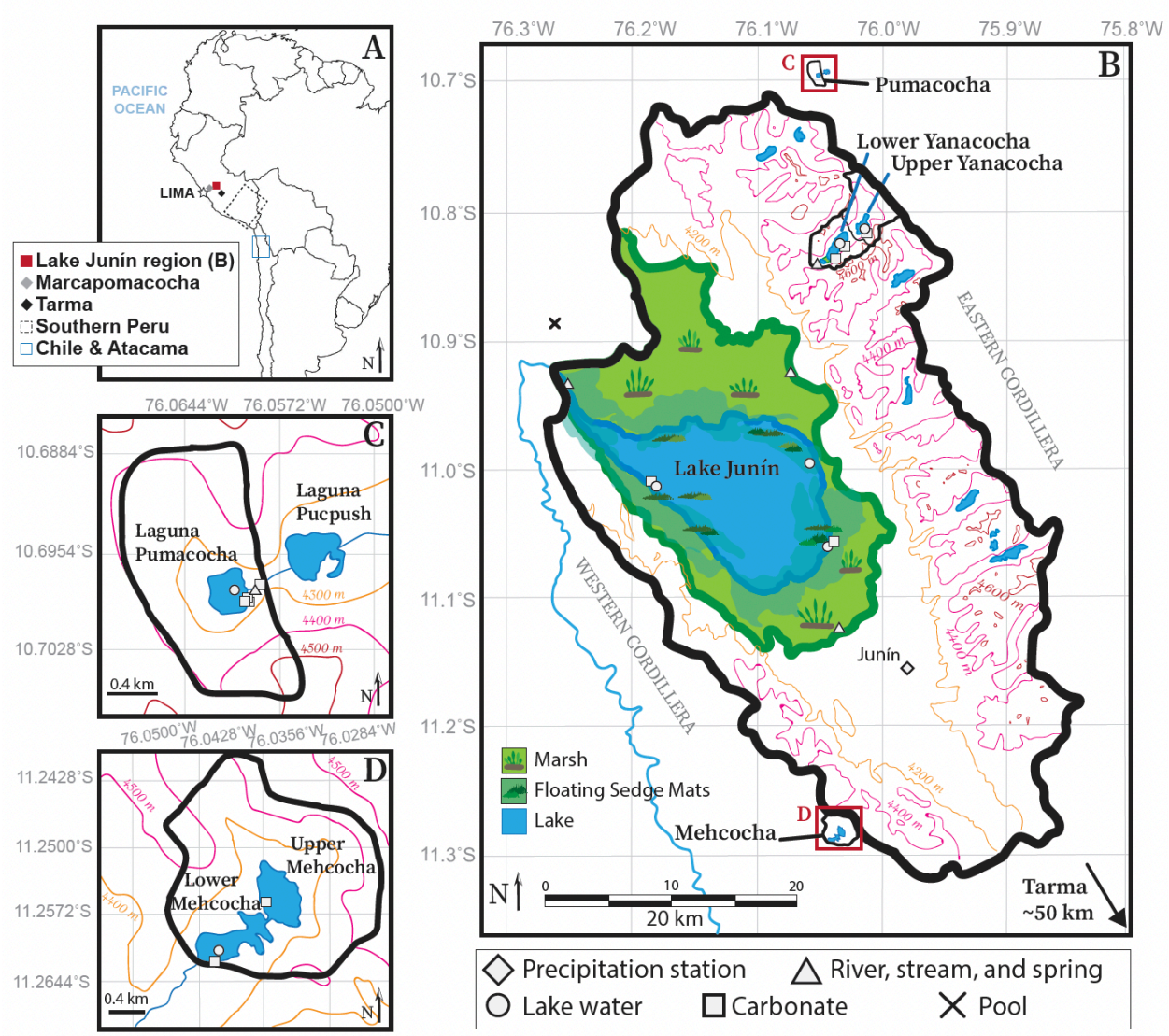

Figure 2.2: Maps of the study region. (A) Map of South America with the Lake Junín region indicated by a red box. (B) Topographic map of the Lake Junín and Yanacocha watersheds, with 200 m elevation contours. Note that the Yanacocha watershed is a glacially carved catchment located within the larger Lake Junín catchment. Red boxes indicate the locations of panels C and D. (C) Topographic map of the Pumacocha watershed (elevation contours 100 m). (D) Topographic map of the Mehcocha watershed (elevation contours 100 m). In B-D, watershed boundaries are indicated by solid black lines. The approximate locations of samples selected for $\Delta'^{17}O$ analysis are indicated for each watershed (see legend below panel B); for clarity, we do not plot the locations of all surface water samples analyzed in this study (n = 140). Coordinates for precipitation stations, water samples, and carbonates are provided in Tables S2.1–S2.2, and 2.2.

2.4.2 Sample collection

2.4.2.1 Waters

To monitor precipitation, we installed a Palmex™ rain gauge in the town of Junín (Figure 2.2). From June 2016–June 2018 monthly samples were collected by local citizens and stored in sealed 50 mL Falcon tubes (Corning #352070). Surface waters were collected in May 2016, 2017, and 2019 from various water types, including springs, streams, rivers, lakes, and isolated pools. Sampling locations are reported in Tables S2.1-S2.2.

2.4.2.2 Carbonates

In May 2019 we collected nine shallow, nearshore sediment samples, one sample from deeper, open water at Mehcocha using an Ekman box sampler, and one sample from carbonate rinds on cobbles in Pumacocha's outflow stream (Figure 2.2; Table 2.2). Stratigraphy was not preserved during collection, so bulk sediment samples represent the upper ~10 cm of the sediment-water interface. Exploring the effects of lake hydrology on carbonate Δ_{47} and $\Delta'^{17}O$ values motivated our sampling at different lakes. Given the remote field location and COVID-19 pandemic we were unable to collect additional samples. Long-term monitoring and sampling of microenvironments within lakes are logical next steps to refine Δ_{47} and $\Delta'^{17}O$ calibration studies.

We processed bulk lake sediments to concentrate authigenic carbonate by reacting samples overnight with 7% hydrogen peroxide to remove organics and wet sieving through a 63 μm mesh, retaining the <63 μm size fraction. The processed samples appear homogenous, light in color, and devoid of macroscopic shells. All geochemical analyses of lake carbonates were conducted on the <63 μm size fraction.

We collected local bedrock (Table 2.2) to characterize limestone Δ_{47} and evaluate detrital contamination in lake carbonate samples. Samples were powdered with a Dremel™ drill from fresh-cut, interior surfaces to avoid weathering surfaces.

Table 2.2. Summary of lake carbonate samples and isotope data from the Lake Junín region.

	Sample Name	Depositional Environment	Material Type	Lat. (°S)	Long. (°W)	Air Temp. (°C) [A]	Water Temp. (°C) [A]	No. rep. Δ_{47} anal.	No. rep. $\Delta'^{17}O$ anal.	$\delta^{13}C_{CaCO3}$ [B] (‰, PDB)	$\delta^{18}O_{CaCO3}$ [B] (‰, PDB)	Δ_{47} [D] (‰)	$T_{\Delta47}$ [E] (°C)	$\delta^{18}O_{rfw}$ [F] (‰, VSMOW)	$\Delta'^{17}O$ (per meg; SMOW-SLAP)	$\Delta'^{17}O_{rfw}$ [G] (per meg; VSMOW-SLAP)
Pumacocha	PE19-PUM-C007	shallow, nearshore	micrite sediment	10.6977	76.0599	-	11	3	2	-2.67 (± 0.08)	17.15 (± 0.10)	0.644 (± 0.013)	12 (± 6)	-13.6 (± 1.2)	-67 (± 6)	25
	PE19-PUM-C008	shallow, nearshore	micrite sediment	10.6977	76.0599	-	11	2	1	-2.64 (± 0.01)	17.15 (± 0.02)	0.633 (± 0.021)	16 (± 8)	-13.0 (± 1.6)	-70	20
	PE19-PUM-C021	shallow, nearshore	micrite sediment	10.6977	76.0599	-	11	-	2	-	17.02 (± 0.15)[C]	-	-	-	-77 (± 0)	15
	PE19-PUM-C133	outflow stream	rinds on cobbles	10.6976	76.0589	-	11	2	2	-3.74 (± 0.02)	17.80 (± 0.13)	0.628 (± 0.002)	17 (± 5)	-12.0 (± 1.0)	-71 (± 4)	18
Meh.	PE19-MEH-C117	deep, open water	micrite sediment	11.2618	76.0401	-	-	3	2	0.14 (± 0.09)	19.09 (± 0.13)	0.644 (± 0.017)	12 (± 6)	-11.8 (± 1.4)	-81 (± 4)	11
	PE19-MEH-C122	shallow, nearshore	micrite sediment	11.2574	76.0352	9.8	14.3	-	2	-	18.16 (± 0.61)[C]	-	-	-	-76 (± 4)	17
Yanacocha	PE19-YAN-C156	shallow, nearshore	micrite sediment	10.8495	76.0449	10.8	16.6	2	2	-0.51 (± 0.01)	21.32 (± 0.20)	0.639 (± 0.002)	14 (± 4)	-9.3 (± 1.0)	-90 (± 4)	1
	PE19-YAN-C158	shallow, nearshore	micrite sediment	10.8532	76.0506	10.6	19.4	3	2	-1.09 (± 0.05)	20.05 (± 0.10)	0.643 (± 0.016)	13 (± 6)	-10.8 (± 1.3)	-90 (± 5)	2
	PE19-YAN-C145A	shallow, nearshore	micrite sediment	10.8303	76.0209	12.6	14.2	2	2	-0.89 (± 0.02)	19.31 (± 0.10)	0.640 (± 0.004)	14 (± 5)	-11.3 (± 1.0)	-84 (± 10)	7
Junín	PE19-JUN-C163	shallow, nearshore	micrite sediment	11.0454	75.9973	13.7	24.1	3	1	-2.42 (± 0.01)	19.95 (± 0.03)	0.664 (± 0.014)	7 (± 6)	-12.1 (± 1.2)	-87	9
	PE19-JUN-C094	shallow, nearshore	micrite sediment	11.0582	76.1556	-	-	-	1	-	16.98 [C]	-	-	-	-67	28
											Average (1σ SD)		**13 (± 3)**	**-11.7 (± 1.3)**	**-78 (± 9)**	**14 (± 9)**
Bedrock	PE19-MEH-Br131A	-	whole rock bedrock	11.2623	76.0404	-	-	2	-	-2.17 (± 0.03)	25.32 (± 0.01)	0.505 (± 0.004)	61 (± 2)	-	-	-
	PE19-MEH-Br131B	-	whole rock bedrock	11.2623	76.0404	-	-	2	-	-2.34 (± 0.01)	25.15 (± 0.02)	0.513 (± 0.015)	58 (± 6)	-	-	-
	PE19-PUM-Br023A	-	whole rock bedrock	10.7206	76.0516	-	-	2	-	1.34 (± 0.01)	23.51 (± 0.05)	0.496 (± 0.01)	65 (± 5)	-	-	-
											Average (1σ SD)		**61 (± 4)**	-	-	-

[A] In-situ measurement made using a Traceable® thermocouple (VWR. #23609-232) in May 2019. Temperature measurements were collected opportunistically in the field and do not represent average conditions.
[B] Data derived from Δ_{47} analysis, except where otherwise noted.
[C] Data derived from $\Delta'^{17}O$ analysis as sample was not analyzed for Δ_{47}.
[D] Relative to the carbon dioxide equilibrium scale (CDES) of Dennis et al., (2011); the ^{17}O-correction uses "Brand parameters," (e.g. Petersen et al., 2019). See Table S2.10.
[E] Calculated from Boniface et al. (2017, Eq. 3).
[F] Calculated from carbonate $\delta^{18}O$, and Δ_{47} values generated from clumped isotope measurements. Note these values differ slightly from values calculated from triple oxygen isotopes reported in Table S2.7.
[G] Calculated from carbonate $\delta'^{18}O$, and $\Delta'^{17}O$ values generated from triple oxygen isotope measurements (Table S2.7) and Δ_{47} values (Table S2.10) generated from clumped isotope measurements. See Table S2.13 for calculations.

2.5 Analytical methods and data standardization

2.5.1 X-ray diffraction

Lake sediments and bedrock samples were analyzed on a Rigaku Ultima IV X-ray diffractometer at the University of Michigan (UM) Electron Microbeam Analysis Lab over a 15–65° angle of incidence (Table S2.3). Spectral data were corrected for background noise and normalized by relative peak intensity.

2.5.2 Isotopic measurements

2.5.2.1 $\delta^{18}O$ and $\delta^{2}H$

Waters collected in 2016 and 2017 were analyzed at Union College on a ThermoScientific Gas Bench II ($\delta^{18}O$) and TC/EA ($\delta^{2}H$) peripherals coupled to a Delta V Advantage mass spectrometer in continuous flow mode. Analytical precision was 0.02‰ for $\delta^{18}O$ and 1.0‰ for $\delta^{2}H$ based on in-run analyses of calibrated internal lab standards.

Water samples collected in 2017 and 2019 were analyzed at UM via Cavity Ring Down Spectroscopy (Picarro model L2130-i analyzer with high precision vaporizer (A0211)). Sample data were corrected using ChemCorrect™ software and standardized to the VSMOW-SLAP scale using USGS reference waters (USGS 45–47,50) and four calibrated in-house standards. Long-term instrument precision is better than 0.1‰ for $\delta^{18}O$ and 0.3‰ for $\delta^{2}H$.

Waters analyzed at both institutions were within the combined $\delta^{18}O$ and $\delta^{2}H$ uncertainty range for 94% of samples, suggesting excellent inter-laboratory agreement (Table S2.2).

2.5.2.2 Triple oxygen isotopes

Triple oxygen analyses were conducted at the UM Isotopologue Paleosciences Lab (IPL, Tables S2.4-S2.7). For carbonates, we use a three step process to convert $CaCO_3$ to an O_2 analyte following the methods of Passey et al. (2014): 1) $CaCO_3$ is digested in >100 wt% H_3PO_4 at 90°C to liberate CO_2; 2) the CO_2 is passed through a circulating loop over an Fe catalyst at 560°C in the presence of H_2 gas to transfer oxygen from the CO_2 to H_2O; 3) the H_2O is then reacted with cobalt trifluoride (CoF_3) at 360°C to produce O_2. After passing through a series of GC columns and

cryogenic traps, the purified O_2 is transferred to a Nu Perspective isotope ratio mass spectrometer where measurements of *m/z* 32–36 are made in dual inlet mode on sample and reference gases. For waters, steps 1) and 2) are bypassed and samples are injected directly into the same fluorination line as used for carbonates. The UM IPL fluorination line and mass spectrometer configuration was recently described in detail by Aron et al. (2021a), thus is not discussed further here.

Triple oxygen data are standardized to the VSMOW-SLAP scale where $\delta^{18}O_{VSMOW}$= 0.000‰, $\delta^{17}O_{VSMOW}$= 0.000‰, $\delta^{18}O_{SLAP2}$= -55.500‰, and $\delta^{17}O_{SLAP2}$= -29.6986‰ (Schoenemann et al., 2013) via multiple analyses of both VSMOW2 and SLAP2 during every analytical session. Water $\delta'^{18}O$, $\delta'^{17}O$, and $\Delta'^{17}O$ precision is 0.5‰, 0.3‰, and 9 per meg, respectively, based on the pooled standard deviation of USGS water standards run concurrently with our samples (Tables S2.8-S2.9). We normalize carbonate data to the mineral $\Delta'^{17}O$ values for IAEA-C1 reported by Wostbrock et al. (2020b) and applied a linear drift correction based on NBS19 $\Delta'^{17}O$ residuals (following Huth et al., 2022). Carbonate $\delta'^{18}O$, $\delta'^{17}O$, and $\Delta'^{17}O$ precision is 1.0‰, 0.5‰, and 7 per meg, respectively, based on the pooled standard deviation of carbonate standards run concurrently with our samples (Tables S2.8-S2.9).

2.5.2.3 Clumped isotopes

Carbonates were digested in a common acid bath (>100 wt% H_3PO_4) at 90°C following methods outlined by Passey et al. (2010). Liberated CO_2 was purified using a series of cryotraps and a GC column prior to analysis on a Nu Perspective mass spectrometer in dual inlet mode at the UM IPL. Δ_{47} values are reported (Table S2.10) relative to the carbon dioxide equilibrium scale of Dennis et al., (2011) via multiple analyses of 'heated gases' (CO_2 gases of differing $\delta^{13}C$ and $\delta^{18}O$ compositions heated at 1000°C for >2 hours offline) and 'equilibrated gases' (as above, but equilibrated with water at 30°C). ^{17}O–corrections were made using 'Brand parameters' (e.g., Petersen et al., 2019). A moving gas line scheme is used to account for temporal drift in linearity and scale compression (Passey et al., 2010). Δ_{47} analytical precision on this system is ±0.021‰, based on the long-term pooled standard deviation of carbonate standards (Table S2.9).

2.6 Results

2.6.1 X-ray diffraction

Lake carbonates (n= 5) and bedrock (n= 3) are entirely calcite based on comparison with carbonate reference spectra (Figure S2.1; Table S2.3).

2.6.2 Isotopic results

2.6.2.1 Precipitation

Junín precipitation $\delta^{18}O$ and $\delta^{2}H$ values range from -20.9‰ to -4.8‰ and -158.2‰ to -17.8‰, respectively (n= 21; Figure 2.3; Table S2.1). A subset of samples were also analyzed for triple oxygen isotopes ($\Delta'^{17}O$= 12–43 per meg; n= 5; Tables 2.3,S2.1).

We screen precipitation samples for data quality and assume samples with identical isotope values (i.e., <0.5‰ variation in $\delta^{18}O$ for consecutive months) do not reflect precipitation. These may reflect groundwater or tap sources, as also observed in other studies that employ citizen scientists (e.g., Aron et al., 2021b). Based on this criterion, we identify seven samples from the Junín dataset (Oct. 2017–April 2018) with identical isotope values; these data are included in Table S2.1 but excluded from figures and calculations.

Local meteoric water lines at Junín are: $\delta^{2}H=8.61(\pm0.08)\times\delta^{18}O+21.9(\pm1.1)$ (n= 13) and $\delta'^{17}O=0.5282(\pm0.0010)\times\delta'^{18}O+0.0333(\pm0.0170)$ (n= 5, Table S2.11). We calculated the weighted mean isotopic composition of precipitation at Junín, hereafter referred to as "amount-weighted annual precipitation." Weightings assume the same monthly rainfall amounts in 2016 and 2017 (gauge installation at Junín occurred in 2017) and are consistent with seasonal rainfall amount patterns observed regionally (Table S2.1) (SENAMHI, 2022). Amount-weighted annual precipitation $\delta^{18}O$, $\delta^{2}H$, d-excess, and $\Delta'^{17}O$ values are -14.1‰ (±2.2‰), -100.3‰ (±18.7‰), 12.8‰ (±1.3‰), and 31 per meg (±5 per meg) respectively, where uncertainty is the standard error of the weighted mean.

2.6.2.2 Surface waters

Surface water $\delta^{18}O$, $\delta^{2}H$, and d-excess values range from -16.9 to 1.5‰, -126.1 to -23.3‰, and -35.3 to 13.5‰, respectively (Figure 2.3; Table S2.2). Surface water $\Delta'^{17}O$ values range from -28 to 36 per meg (n= 16; Figures 2.3–2.4; Tables 2.3,S2.2).

Lake waters from the smaller lakes (Pumacocha, Mehcocha), springs, and rivers are isotopically similar to local precipitation while waters from larger lakes have lower $\Delta'^{17}O$ and

d-excess than precipitation (Yanacocha, Lake Junín; Figures 2.3,2.4). In the larger watersheds, we observe variability in the isotopic composition of waters and isotopic trends based on position within the catchment (similar to a "chain of lakes" scenario); inflow waters have lower $\delta^{18}O$, $\delta^{17}O$, and $\delta^{2}H$, and higher $\Delta'^{17}O$ and d-excess values than downstream lake waters and outflow streams (Figures 2.3, 2.4). Despite hydrologic modifications, the Lake Junín system follows these trends.

Considering all surface waters from the Lake Junín region together, they follow linear distributions in $\delta^{18}O$-$\delta^{2}H$ and $\delta'^{18}O$-$\delta'^{17}O$ space with lower slopes than those observed from precipitation. Regressions of surface water $\delta^{18}O$-$\delta^{2}H$ and $\delta'^{18}O$-$\delta'^{17}O$ yield evaporation lines: $\delta^{2}H=5.39(\pm0.06)\times\delta^{18}O-32.73(\pm0.82)$ and $\delta'^{17}O=0.5248(\pm0.0004)\times\delta'^{18}O-0.0208(\pm0.0044)$ (Table S2.11). We determined empirical triple oxygen isotope evaporation slopes, $\lambda_{lake}=\delta'^{17}O_{lake}-\delta'^{17}O_{precip}/\delta'^{18}O_{lake}-\delta'^{18}O_{precip}$, using the amount-weighted isotopic composition of precipitation (Table S2.12). At Lake Junín the range in observed λ_{lake} is 0.523–0.525. At Yanacocha, observed λ_{lake} ranges from 0.525 in the upper lake to 0.522 at its outlet. We did not calculate evaporation slopes for the smaller lakes, Mehcocha and Pumacocha, given the similar isotopic composition of lake water and amount-weighted annual precipitation.

Table 2.3. Summary of water isotope data from the Lake Junín region

Sample ID	Location [A]	Water Type	No. replicate $\Delta'^{17}O$ analyses	d-excess (‰)	$\delta'^{17}O$ [B] (‰)		$\delta'^{18}O$ [B] (‰)		$\Delta'^{17}O$ [B] (per meg)	
					Average	1 σ sd	Average	1 σ sd	Average	1 σ sd
J1 (6/15/2016)	Junín	Precipitation	1	9.39	-11.175	-	-21.187	-	12	-
J3 (10/15/2016)	Junín	Precipitation	2	19.02	-3.493	0.173	-6.681	0.316	35	6
J6 (1/15/2017)	Junín	Precipitation	4	11.15	-11.131	0.129	-21.163	0.253	43	9
J7 (2/15/2017)	Junín	Precipitation	2	9.05	-10.924	0.108	-20.753	0.197	34	4
J8 (4/15/2017)	Junín	Precipitation	2	12.28	-5.803	0.082	-11.042	0.151	27	2
PE19-PUM-P019	Pumacocha	Precipitation	2	13.52	-7.906	0.286	-15.016	0.570	22	15
PE19-CAR-S028	Lake Junín	Inflow stream	2	5.71	-7.845	0.019	-14.903	0.020	24	8
PE19-JUN-R063	Lake Junín	Outflow	5	-6.44	-5.448	0.104	-10.346	0.203	14	12
PE16-JUN-L016	Lake Junín	Lake	2	-15.77	-2.202	0.029	-4.159	0.059	-6	2
PE19-JUN-L090	Lake Junín	Lake	2	-0.96	-6.483	0.112	-12.326	0.219	25	4
PE19-JUN-L159	Lake Junín	Lake	3	-5.04	-5.833	0.296	-11.077	0.566	16	4
PE16-JUN-S027	Lake Junín	Isolated pool	2	-35.30	0.961	0.163	1.873	0.323	-28	7
PE16-JUN-S038	Lake Junín	River/stream	2	5.10	-7.519	0.190	-14.277	0.349	19	6
PE16-JUN-S048	Lake Junín	River/stream	2	-0.20	-6.791	0.105	-12.896	0.183	19	8
PE16-JUN-S053	Lake Junín	River/stream	2	-0.76	-6.686	0.121	-12.681	0.234	9	3
PE16-JUN-S019	Lake Junín	Spring	1	7.51	-7.445	-	-14.146	-	25	-
PE19-MEH-L116	Mehcocha	Lake	4	3.98	-6.990	0.133	-13.289	0.234	27	14
PE19-PUM-L018	Pumacocha	Lake	1	5.07	-6.864	-	-13.067	-	36	-
PE19-PUM-S016	Pumacocha	Outflow	1	5.31	-7.599	-	-14.435	-	23	-
PE19-YAN-L141	Yanacocha	Upper lake	2	-1.27	-6.195	0.009	-11.780	0.025	25	4
PE19-YAN-L155	Yanacocha	Lower lake	2	-8.69	-5.097	0.026	-9.673	0.048	10	0
PE19-YAN-S140	Yanacocha	Outflow	2	-9.28	-4.725	0.016	-8.951	0.031	1	1

[A] Sample latitudes and longitudes are given for the Junín precipitation station and surface waters in Tables S2.1 and S2.2, respectively.
[B] Data generated from triple oxygen isotope analysis and reported on the VSMOW-SLAP scale (Schoenemann et al. 2013)

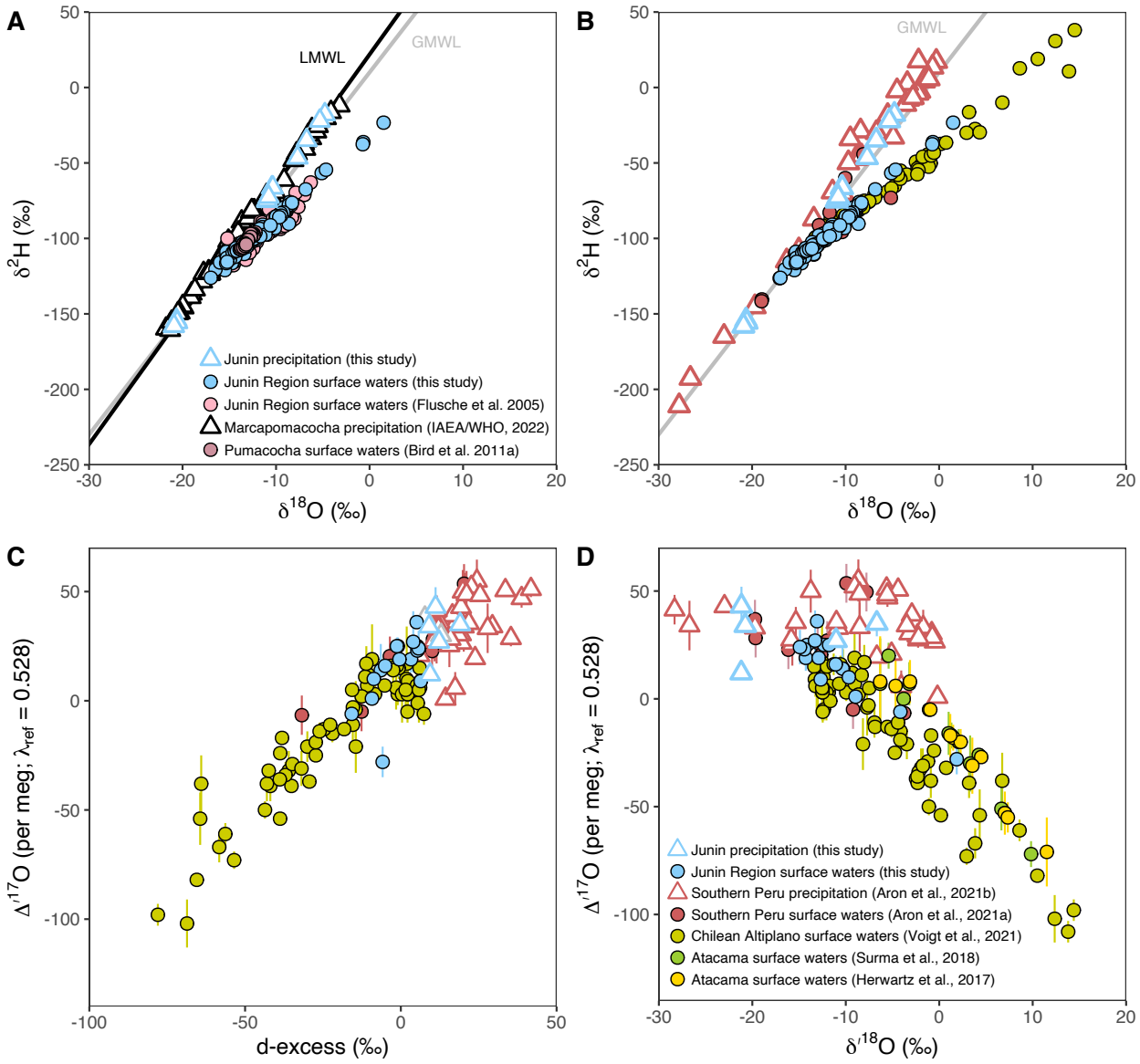

Figure 2.3: Plot of precipitation and surface water $\delta^{18}O$ and $\delta^{2}H$ values from the (A) Lake Junín region and (B) central Andes. The Global Meteoric Water Line (GMWL), $\delta^{2}H = 8*\delta^{18}O + 10$, is shown as a grey line for reference. In (A), the Local Meteoric Water Line (LMWL) for Junín precipitation ($\delta^{2}H = 8.6*\delta^{18}O + 21.9$) is shown as a black line. (C-D) Published water data from central Andean studies that report triple oxygen isotope values; the legend shown in panel D represents data plotted in panels B-D. (C) Plot of $\Delta'^{17}O$ and d-excess values. Error bars represent the 1 σ uncertainty reported in each study. (D) Plot of $\Delta'^{17}O$ versus $\delta'^{18}O$. Note that Herwartz et al. (2017) and Surma et al. (2018) did not report hydrogen isotope data, so data from those studies are only plotted in panel D.

2.6.2.3 Carbonates

We report $\delta^{18}O$, $\delta^{17}O$, $\Delta'^{17}O$, $\delta^{13}C$, and Δ_{47} data for lacustrine and bedrock carbonates in Tables 2.2, S2.7, S2.10. Carbonate $\delta^{18}O$ and $\delta^{13}C$ values generated during Δ_{47} analysis range from 17.2 to 21.3‰ (VSMOW) and -3.7 to 0.1‰ (VPDB) for lacustrine carbonates and 23.5 to 25.3‰ (VSMOW) and -2.3 to 1.3‰ (VPBD) for bedrock, respectively (Table 2.2).

Using Δ_{47} values, we calculate carbonate formation temperatures, $T_{\Delta47}$, which are 13 ±3°C (n= 8) and 61 ±4°C (n= 3) for lacustrine and bedrock carbonates respectively (Figures 2.5,S2.3; Table 2.3; Bonifacie et al., 2017). We assume equilibrium growth conditions and use the temperature-dependent equilibrium fractionation factor ($^{18}\alpha_{calcite\text{-}water}$) and $T_{\Delta47}$ to calculate reconstructed formation water $\delta^{18}O$ values ($\delta^{18}O_{rfw}$; Table 2.2; Figure 2.5C; Kim and O'Neil, 1997). Uncertainties on $T_{\Delta47}$ and $\delta^{18}O_{rfw}$ values were determined using a Monte Carlo re-sampling approach. We assume a Gaussian distribution for carbonate $\delta^{18}O$ and Δ_{47} values among sample replicates and in the slope and intercept values of the temperature-dependent transfer function (Kim and O'Neil, 1997). Unique combinations of $T_{\Delta47}$ and $\delta^{18}O_{rfw}$ values were generated (n= 10,000), from which we report the mean and 1σ standard deviation (Table S2.3, Supplemental Script 1).

The triple oxygen isotope composition of lacustrine carbonates, $\Delta'^{17}O$, range from -90 to -67 per meg (VSMOW-SLAP; Tables 2.2,S2.7). Formation water $\delta'^{18}O_{rfw}$ and $\Delta'^{17}O_{rfw}$ values calculated from $\delta^{18}O$, $\Delta'^{17}O$, $^{18}\alpha_{calcite\text{-}water}$ (derived using $T_{\Delta47}$) range from -15.1 to -9.9‰ and 1 to 28 per meg (VSMOW-SLAP, Tables 2.2,S2.13, Figures 2.4,2.5D). To determine $\Delta'^{17}O_{rfw}$, we use an equilibrium $\lambda_{calcite\text{-}water}$ value of 0.5250 (±0.0002), generated from synthetic carbonates in our lab (UM IPL) (Huth et al., 2022); this is indistinguishable to a value of 0.5249 (±0.0002) from modern bivalves also generated in our lab (Kelson et al., 2022) and is consistent with $\lambda_{calcite\text{-}water}$ values from natural and synthetic carbonates (0.5241–0.5250) compiled by Huth et al. (2022). We are not aware of any $\lambda_{calcite\text{-}water}$ values generated specifically for lacustrine carbonates. Our selected $\lambda_{calcite\text{-}water}$ is lower than some theoretical calculations (0.5253–0.5256; Guo and Zhou, 2019) and synthetic carbonates in other labs (0.5255; Wostbrock et al., 2020a). The cause for this discrepancy is unknown but indicates that careful comparison of $\lambda_{calcite\text{-}water}$ across labs and different material types is needed. We explored the impact of $\lambda_{calcite\text{-}water}$ selection on our interpretations further in Section 2.7.2, but we note here that using higher $\lambda_{calcite\text{-}water}$ values (≅0.5255) would yield $\Delta'^{17}O_{rfw}$ values ~26 per meg lower than waters in the Lake Junín region, which we consider unrealistic (Table S2.14; Figure S2.2). Raw data are provided in Table S2.7 to facilitate future recalculation using different $\lambda_{calcite\text{-}water}$ values.

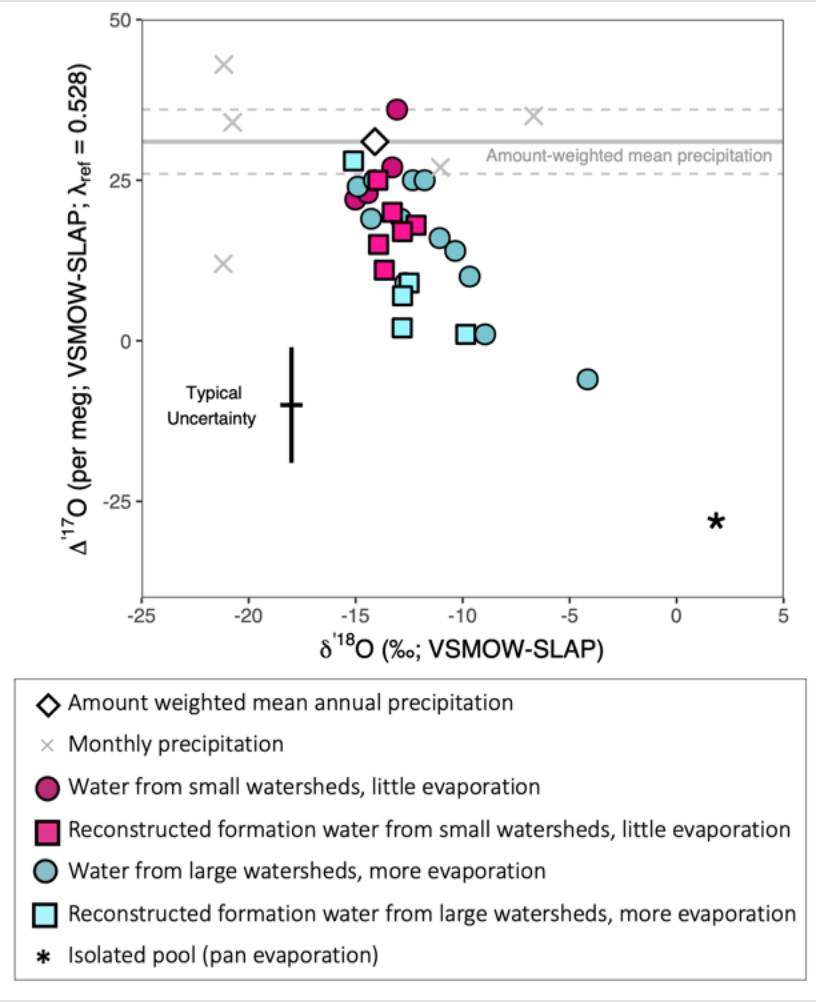

Figure 2.4: Triple oxygen isotope data of surface waters and carbonate formation waters from the Lake Junín region. Mehcocha and Pumacocha are categorized as small watersheds and Yanacocha and Lake Junín are categorized as large watersheds (see Section 2.4.1). Solid and dashed horizontal grey lines represent amount-weighted annual precipitation $\Delta'^{17}O$ and the 1 σ uncertainty, respectively (31 ±5 per meg). The "Typical Uncertainty" is shown as the 1 σ standard deviation for $\Delta'^{17}O$ (=9 per meg) and $\delta'^{18}O$ (=0.5‰) based on the pooled standard deviation of water standards (Table S2.9).

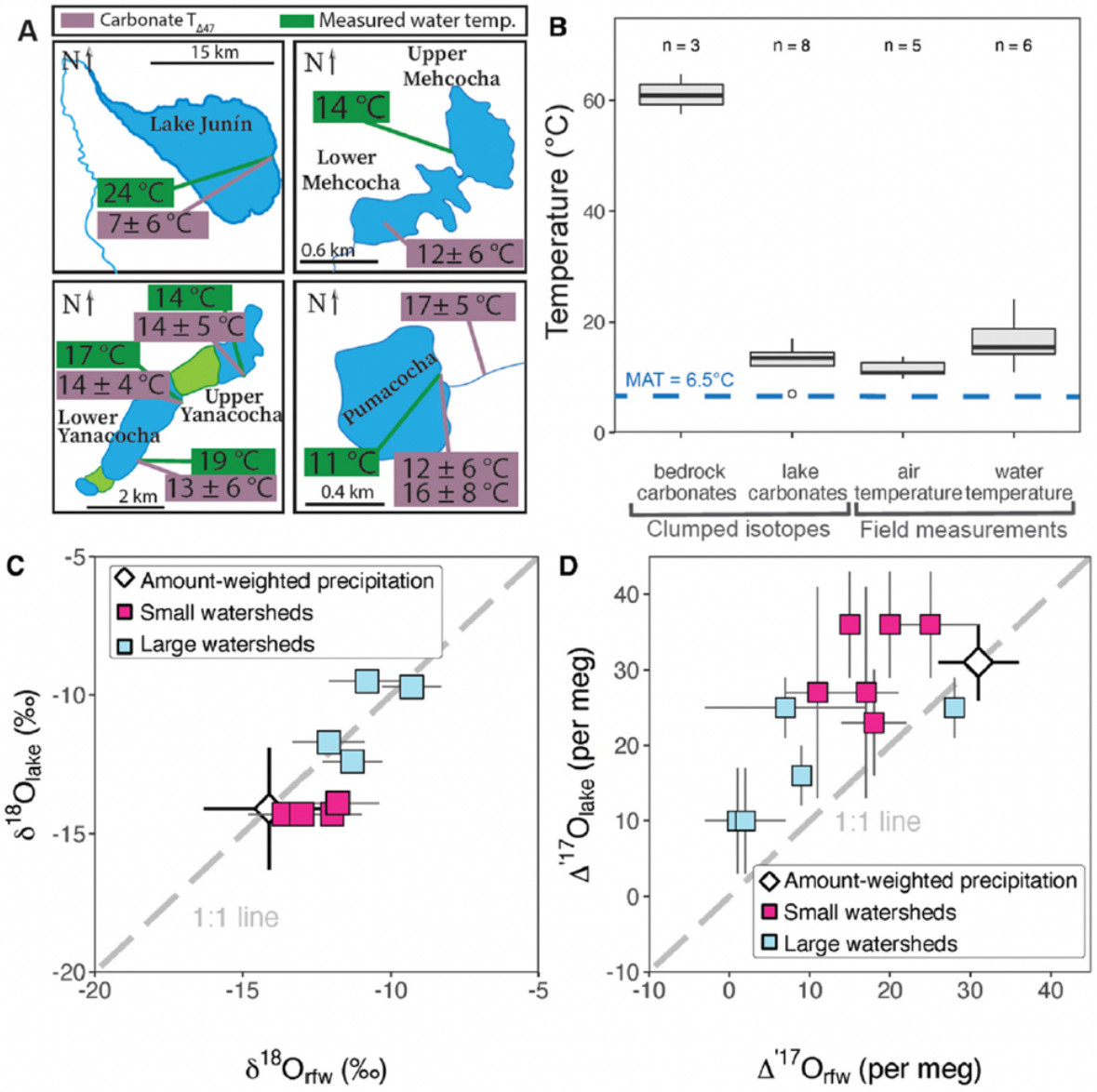

Figure 2.5: Clumped isotope results. (A) Simplified maps of the four lakes illustrating carbonate $T_{\Delta47}$ and surface water temperatures measured at time of sample collection. (B) Box and whisker plots show temperatures for bedrock and lake carbonate derived from clumped isotopes, and measurements of air and water temperatures taken at the time of sample collection in May 2019. The central line of the box illustrates population medians; upper and lower hinges mark quantile boundaries; outliers are represented by open circles. A dashed horizontal line indicates mean annual temperature (MAT= 6.5°C) for reference. (C) $\delta^{18}O$ values of reconstructed carbonate formation waters ($\delta^{18}O_{rfw}$) versus lake waters ($\delta^{18}O_{lake}$) collected at the same locations. (D) $\Delta'^{17}O$ values of reconstructed carbonate formation waters ($\Delta'^{17}O_{rfw}$) versus lake water $\Delta'^{17}O$ ($\Delta'^{17}O_{lake}$) values from waters collected at the same sampling locations. In C-D, symbols are color coded based on categorization of catchment size (e.g., small = pink; large = blue). Error bars on $\delta^{18}O_{rfw}$, $\Delta'^{17}O_{lake}$, and $\Delta'^{17}O_{rfw}$ represent 1 σ standard deviations of replicate analyses. In panel C, uncertainty on $\delta^{18}O_{lake}$ is long term instrument precision (0.3 ‰) and is smaller than the size of the symbols. In panel D, long term analytical precision of 9 per meg for waters is used when replicate analyses of $\Delta'^{17}O_{lake}$ are unavailable. Data from these plots can be found in Tables 2.2–2.3, S2.2.

2.7 Discussion

2.7.1 Water isotopes

The isotopic composition of Junín precipitation is similar to that of precipitation elsewhere in the Peruvian Andes (Figure 2.3; e.g., Aron et al., 2021b; IAEA/WMO, 2022). In a $\delta^{18}O$-$\delta^{2}H$ plot, precipitation samples collected at Junín and Marcapomacocha (a GNIP station 45 km southwest of Junín) fall on or slightly above the GMWL, suggesting the importance of Rayleigh processes on the isotopic composition of regional precipitation (Dansgaard, 1964). The $\Delta'^{17}O$ value of Junín amount-weighted annual precipitation, 31 ±5 per meg, is within the range of semimonthly precipitation $\Delta'^{17}O$ values in the Peruvian Altiplano (29–55 per meg; Figure 2.3; Aron et al., 2021b). Combining precipitation data from Junín and southern Peru, the regional meteoric water line: $\delta'^{17}O=0.5277\ (\pm0.0003)\times\delta'^{18}O+0.0312\ (\pm0.0031)$, lies between the global meteoric water line reported by Luz and Barkan (2010) and a recently updated compilation (Aron et al., 2021a; Table S2.11). Unfortunately, our precipitation dataset spans too short of a time interval to evaluate seasonal trends in $\Delta'^{17}O$ values at Junín.

Surface water d-excess and $\Delta'^{17}O$ values are positively correlated in the Lake Junín region (Pearson's r= 0.94; Figure 2.3C), consistent with the influence of evaporation. The $\Delta'^{17}O$–d-excess relationship is 1.3 ±0.1 per meg/‰, which is similar to observations from a global compilation of surface waters (r= 0.73; 1.2 ±0.1 per meg/‰; Aron et al., 2021a) and highly evaporated surface waters from the Chilean Altiplano (r= 0.94; 1.2 ±0.1 per meg/‰; Voigt et al., 2021). In contrast, precipitation $\Delta'^{17}O$–d-excess are weakly correlated, both in the Lake Junín region (r= 0.30) and elsewhere (e.g., Aron et al., 2021a). This weak correlation may reflect differences in how moisture source conditions affect oxygen and hydrogen isotopic fractionation (e.g., Aron et al., 2021b;2021a), but systematic, long-term studies of precipitation d-excess and $\Delta'^{17}O$ are needed to understand these relationships in the Andes.

2.7.2 Carbonate isotopes

In the Lake Junín region, $T_{\Delta47}$ values of lake carbonates (7–17°C) overlap in range with surface water temperatures measured during our sampling in May 2019 (11–24°C) (Figures 2.5,S2.3; Table 2.2). The measured water temperatures are more variable than carbonate $T_{\Delta47}$

values and we consider them to represent snapshots of field work conditions (e.g., season, time of day) (Figure S2.3; Section 2.4.2.2). In contrast, carbonate samples integrate time (likely months–years). Average $T_{\Delta47}$ for the Lake Junín region lakes is 13 ±3°C, which is higher than MAT (6.5°C) and consistent with observations globally, where lake water temperatures are commonly elevated relative to mean air temperatures (Hren and Sheldon, 2012). This consideration is important when using lake carbonate $T_{\Delta47}$ to infer paleo-temperatures, as it may be appropriate to consider lake carbonate $T_{\Delta47}$ as a maximum estimate of MAT.

Bedrock carbonates yield high $T_{\Delta47}$ values (61 ±4°C) compared to the lacustrine carbonates (13 ±3°C) (Table 2.2, Figure 2.5B). The high bedrock carbonate temperatures are inconsistent with Earth surface conditions and likely reflect burial conditions (Huntington and Lechler, 2015). Bedrock temperatures of 60°C are consistent with burial of ~3 km based on ~20°C/km temperature gradients observed in boreholes in Peru (Henry and Pollack, 1988). We leverage these distinct temperature groupings to screen for detrital carbonate input into local lakes, as incorporation of detrital carbonate into lake sediments would result in unrealistically high lake carbonate $T_{\Delta47}$ values. Accordingly, low lacustrine $T_{\Delta47}$ values support the interpretation that lake carbonate isotope values record lake conditions, as opposed to a signal inherited from detrital material.

We then compare $\delta^{18}O$ values of reconstructed formation water from lacustrine carbonates ($\delta^{18}O_{rfw}$, derived from Δ_{47} measurements) to measured $\delta^{18}O$ values of lake water ($\delta^{18}O_{lake}$) collected at the same locations (Tables 2.2,S2.2). Paired $\delta^{18}O_{rfw}$-$\delta^{18}O_{lake}$ values are positively correlated (r= 0.82, n= 8) and values fall close to a 1:1 line (Figure 2.5C), which suggests the isotopic composition of these carbonates reflects lake water at the time of carbonate formation. The majority of $\delta^{18}O_{lake}$ and $\delta^{18}O_{rfw}$ values are higher than the $\delta^{18}O$ value of amount-weighted annual precipitation and track with lake hydrology, consistent with the influence of evaporation.

We also compare $\Delta'^{17}O$ of reconstructed formation water ($\Delta'^{17}O_{rfw}$) and measured lake waters ($\Delta'^{17}O_{lake}$) (Figure 2.5D). $\Delta'^{17}O_{rfw}$ values follow the same isotopic distribution as $\Delta'^{17}O_{lake}$ from the same catchments (Figure 2.4). However, $\Delta'^{17}O_{rfw}$ values are offset from paired $\Delta'^{17}O_{lake}$ values by -21 to 3 per meg (average: -11 per meg). We consider two possible explanations for this offset: 1) the selection of $\lambda_{calcite\text{-}water}$ is inappropriate for these carbonates, or 2) the carbonates and waters we collected are sampling different conditions.

Of these scenarios, we consider the first most likely. The value we use for $\lambda_{calcite\text{-}water}$ (0.5250; Section 2.6.2.3) was developed from laboratory-precipitated carbonate and may not represent the isotope effects that occur during lacustrine carbonate precipitation. A lower $\lambda_{calcite\text{-}water}$ value, e.g., 0.5246, would align $\Delta'^{17}O_{lake}$ and $\Delta'^{17}O_{rfw}$ values and is consistent with observed $\lambda_{calcite\text{-}water}$ values reported for some natural carbonates (Figure S2.2; Table S2.14) (Huth et al., 2022). Long-term calibration studies are needed to resolve $\lambda_{calcite\text{-}water}$ in lake systems. A second possibility is that sampled lake water $\Delta'^{17}O$ values do not represent lake water $\Delta'^{17}O$ at the time of carbonate formation. We sampled lakes in May, directly after the rainy season when local waters likely represent an evaporative minimum. This contrasts the dry season when carbonates likely formed and could explain why $\Delta'^{17}O_{lake}$ values are higher than $\Delta'^{17}O_{rfw}$ values. However, in this scenario, we would expect to see both a greater offset (more evaporation) in the larger lakes than the smaller lakes and a corresponding offset in $\delta^{18}O$, neither of which we observe (Figure 2.5C–D).

2.7.3 Reconstructing precipitation $\delta^{18}O$

2.7.3.1 Modeling triple oxygen isotopes in lakes

Previous studies have used both isotope-enabled lake budget models and empirical data to establish the relationships between $\Delta'^{17}O$ values of precipitation, lake water, and paired mineral samples in highly evaporated, arid lake systems where lake water $\Delta'^{17}O$ and $\delta'^{18}O$ values are considerably distinct from input waters (Herwartz et al., 2017; Gázquez et al., 2018; Passey and Ji, 2019). In pursuit of developing triple oxygen isotopes to evaluate evaporative loss from lakes across a broad range of climates, we focus this study on data from modern lake systems in humid conditions with low evaporative loss (X_E) and model these conditions using steady-state lake budget equations.

2.7.3.2 Lake budget models

Using the same approach as Passey and Ji (2019), we apply Monte Carlo re-sampling to evaluate steady-state lake budget equations (Supplemental Script 2). In this mass balance approach, the isotopic composition of different reservoirs and volumetric fluxes and associated

fractionations between reservoirs are used to calculate the isotopic composition of residual, evaporated lake waters (Figure S2.4; e.g., Benson and White, 1994; Passey and Ji, 2019).

In their modeling work, Passey and Ji (2019) restrict humidity to 0.3–0.7 to reflect their study area in the western U.S. (h= 0.42–0.55). For this work, we modeled lake water $\Delta'^{17}O$ under a range of humidity conditions to explore the humidity dependence of λ_{lake} (Figure 2.1). We expand the modeled humidity range to 0.3–0.9 to include the conditions of our study area where humidity is 0.7–0.9 (Tables S2.1,S2.15).

We use a lake budget equation that assumes i) lake waters are well mixed, ii) lake level is constant, iii) water is lost from the lake through a combination of evaporation, outflowing rivers, and/or groundwater, iv) waters entering the lake have a uniform isotopic composition and are relatively unevaporated, and v) evaporated moisture is integrated with atmospheric water vapor (Figure S2.4; Passey and Ji, 2019):

$$R_W = \frac{\alpha_{eq} R_I [\alpha_{diff}(1-h) + h(1-F)] + \alpha_{eq} h X_E R_A F}{X_E + \alpha_{eq}(1-X_E)[\alpha_{diff}(1-h) + h(1-F)]} \quad (8)$$

We randomly sample values of X_E, h (relative humidity normalized to lake surface temperature), F (proportion of water vapor derived from upwind sources versus the lake itself), R_A (isotopic composition of atmospheric water vapor; calculated assuming equilibrium with precipitation), and α_{diff}, where α_{diff}=1.02849Φ+(1-Φ), (Φ is the relative proportion of diffusive transport (Φ= 1) versus turbulent transport (Φ= 0) of water vapor during evaporation and 1.02849 is the $^{18}O/^{16}O$ fractionation for pure molecular diffusion; Merlivat, 1978). Model conditions are listed in Table S2.15 and Supplemental Script 2. R_I (isotopic composition of input water) was defined as amount-weighted annual precipitation at Junín (Section 2.6.2.1) and lake temperature (used to calculate water vapor–liquid water equilibrium fractionation, α_{eq}) is 14°C. Each model simulation is conducted with 1000 random samplings of X_E, h, F, R_A, and Φ to produce unique combinations of modeled lake water $^{18}O/^{16}O$ and $^{17}O/^{16}O$ from which we calculate $\Delta'^{17}O$ and λ_{lake} values. We note that the choice of R_A has the greatest impact on the evaporation slope (λ_{lake}) at high humidity (as shown in plants by Landais et al., 2006); constraining R_A will be important for future refinement of model outputs in high humidity settings.

Before proceeding to discussion of the model output and the role of humidity on $\delta'^{18}O$ and $\Delta'^{17}O$ distributions in lakes, we want to explicitly note the limitation and utility of models. Mass balance models are representations of complex systems which can provide frameworks for evaluating and interpretating empirical observations. We recognize that models inherently simplify complex systems, such that not all model assumptions may always be met in natural environments. This does not preclude the utility of models, but users should exercise caution in selecting appropriate models and input parameters, particularly for ancient systems.

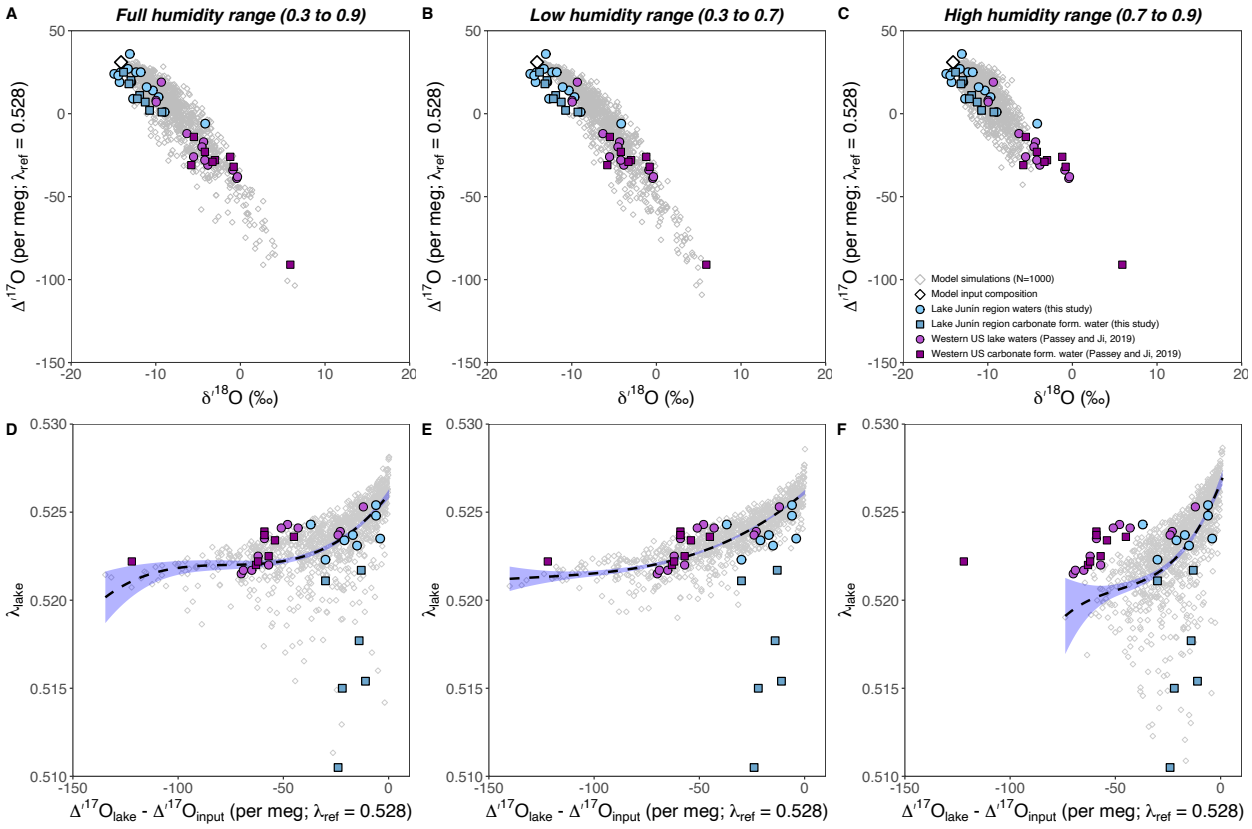

Figure 2.6: Comparison of observed and modeled triple oxygen isotope compositions for modern lakes (see Section 2.7.3.2; Eq. 8; Supplemental Script 2). Panels A-C illustrate 1000 model solutions (grey diamonds) for lake water $\Delta'^{17}O$ and $\delta'^{18}O$ derived from unevaporated input water ($\Delta'^{17}O$= 31 per meg; $\delta'^{18}O$= -14.1‰; represented by a white diamond). Each column represents different inputs for humidity across an X_E (evaporative loss / inputs) range of 0.01 to 1.0 (see Table S2.15 for run parameters). Panels D-F plot modeled $\Delta'^{17}O$ (shown as $\Delta'^{17}O_{lake}$–$\Delta'^{17}O_{input}$) versus modeled λ_{lake} (grey diamonds). A dashed black line shows a third-order polynomial fit for each model dataset and the shaded envelope represents the 95% CI. Note that in Panels D-F the y-axis scale is cropped to 0.510-0.530 to show realistic solutions which fall between equilibrium (λ_{eq}= 0.529; Barkan and Luz, 2005) and diffusive (λ_{diff}= 0.5185; Barkan and Luz, 2007) values. Empirically calculated values of λ_{lake} from lake waters, outflow rivers, and carbonate reconstructed formation waters are superimposed on modeled data (Table S2.12). Note that samples outside the cropped frame are excluded, such that Panels D-F have fewer sample datapoints than Panels A-C. The starting water in our model runs reflects local precipitation and is slightly different than starting water used by Passey and Ji ($\Delta'^{17}O$= 32 per meg and $\delta'^{18}O$= -15‰), however, this does not affect the overall trends in the modeled isotopic distribution for lake water.

2.7.3.3 Model results and the role of humidity

We first compare model outputs to the observed $\delta'^{18}O$ and $\Delta'^{17}O$ values from the arid, western U.S. (Passey and Ji, 2019) and the humid, Lake Junín region (Figure 2.6A). The overlap in distributions of observed and modeled values for both regions makes sense; the isotopic values of unevaporated input waters of these regions are similar and the simulations consider a humidity range that reflects both areas. However, the unique $\Delta'^{17}O$–$\delta^{18}O$ and $\Delta'^{17}O$–λ_{lake} relationships for each study are the result of regional humidity at the two sites. Specifically, humidity is tied to the proportion of kinetic fractionation during evaporation (in turn λ_{lake} is most sensitive to R_A at high humidity; Landais et al., 2006). This highlights a need to explore the influence of humidity on λ_{lake} further before we can effectively leverage λ_{lake} to quantify evaporation widely in different climatic systems.

When modeled humidity is restricted to reflect conditions for specific regions, the model output captures observations for that region. For example, the modeled isotopic composition for lakes in low humidity settings (0.3–0.7) are a good match with observations from the western U.S. (Figure 2.6B), but they fail to capture many of our observations from the Lake Junín region where humidity is high. Correspondingly, the high humidity (0.7–0.9) solution space closely matches our observations in the Lake Junín region but not the observations from the arid western U.S. (Figure 2.6C).

To translate these relationships to ancient systems and use triple oxygen isotopes to reconstruct $\delta^{18}O$ values of unevaporated precipitation, we must also understand how humidity mediates the isotopic relationship between precipitation and lake water, or λ_{lake}, the evaporation slope in $\delta'^{18}O$-$\delta'^{17}O$ space (Figure 2.1C-E) (Passey and Ji, 2019). Currently, our understanding of λ_{lake} relies primarily on highly evaporated systems in arid to hyper-arid environments (Table S2.12) (Herwartz et al., 2017; Surma et al., 2018; Passey and Ji, 2019; Voigt et al., 2021) and other climatic settings and hydrologic systems are under-represented (e.g., Pierchala et al., 2022). Passey and Ji (2019) showed that modeled λ_{lake} varies predictably as a function of $\Delta'^{17}O$ in low humidity (0.3–0.7) such that $\Delta'^{17}O_{lake}$ values can be used to model λ_{lake} for ancient systems. However, for this approach to be widely applicable, we must understand the dependence of triple oxygen evaporation slopes to humidity, which has been explored for plants (e.g., Landais et al., 2006) but not for lake systems, to our knowledge.

To address this gap, we evaluated the modeled relationship between λ_{lake} and $\Delta'^{17}O_{lake}$ with varying humidity. In Figure 2.6D-F we represent $\Delta'^{17}O$ as the difference between lake and input water $\Delta'^{17}O$ values ($\Delta'^{17}O_{lake}$–$\Delta'^{17}O_{input}$) so we can consider data from study regions where input water $\Delta'^{17}O$ might vary. Figure 2.6D-F illustrates the distribution of modeled λ_{lake} values as a function of $\Delta'^{17}O$ for three different ranges of humidity. Our simulations affirm a strong relationship between λ_{lake} and $\Delta'^{17}O$ in all climate settings (Figure 2.6D) and show the potential to refine it where the humidity can be constrained (Figure 2.6E-F). The full humidity (0.3–0.9) model describes all observational data and can be reliably used to estimate λ_{lake}.

However, a simple sensitivity analysis shows that humidity plays an important role on modeled lake water $\Delta'^{17}O$ and λ_{lake} values when all other modeled variables are held constant (Figure S2.5). These results indicate λ_{lake} is most sensitive to humidity when $X_E \cong 0.3$, suggesting that using humidity to refine modeled values of λ_{lake} is most useful in flow-through lakes with a moderate amount of evaporation. Conversely under high evaporation scenarios (X_E >0.7), the difference in modeled λ_{lake} at high and low humidity is minimized. Therefore, when X_E is low, constraining humidity is important for accurate estimates of λ_{lake}, but it is less important when X_E is high (>0.7). λ_{lake} has the largest effect on $\delta'^{18}O_{rucp}$ when the isotopic composition of lake water is very different from input water, as is commonly observed in arid, highly evaporated systems with very low $\Delta'^{17}O_{lake}$ (Figure S2.5C). Uncertainty in λ_{lake} has a smaller effect on reconstructed $\delta'^{18}O_{rucp}$ in humid, less evaporated systems.

We note that our modeled results produce some very low λ_{lake} values (<0.5185, endmember for diffusive vapor transport; Barkan and Luz, 2007) (Figure 2.6D-F). Generally, the very low modeled λ_{lake} values (~4% of solutions) are associated with very high relative humidity (h>0.8), low $\delta'^{18}O_{vapor}$ and $\Delta'^{17}O_{vapor}$ (-26 to -25‰ and 4 to 15 per meg, respectively) and primarily non-lake vapor sources (F>0.9); no clear relationship is observed between low λ_{lake} and Φ or X_E (Figure S2.6). While this combination of conditions could occur in nature, it would be rare. As a result, we expect most realistic λ_{lake} values to be 0.5185–0.529 (Barkan and Luz, 2007; Luz and Barkan, 2010).

We also observe that some carbonates from humid environments produced very low empirical λ_{lake} values (<0.5185). From the model results described above, we cannot rule out the role of climate on these low λ_{lake} values but we also recognize the substantial challenges in

determining a slope (λ_{lake}) between two points (i.e., input water and lake waters) that are very close together in their isotopic composition. In low X_E systems, $\delta^{18}O$ of input water and lake water are often close (<2‰), meaning that the error in selection or measurement of either will result in high uncertainty in the slope between the points (Figure S2.7). In high X_E systems, there is less uncertainty in determining λ_{lake} empirically as $\delta^{18}O$ values of input and lake water differ substantially. Accordingly, observations of λ_{lake} will always have high uncertainty when $\delta^{18}O$ of lake waters and precipitation are similar. This highlights the utility of using modeling approaches to evaluate λ_{lake}, particularly in humid settings (Figures 2.6D-F,S2.5,S2.7).

2.7.3.4 Improving reconstructed precipitation $\delta^{18}O$ estimates

Selection of modeled λ_{lake} is important when reconstructing precipitation $\delta^{18}O$ values ($\delta'^{18}O_{rucp}$) as λ_{lake} values that are too high will yield $\delta'^{18}O_{rucp}$ values that are lower than the true $\delta'^{18}O$ of input waters, while λ_{lake} slopes that are too low produce the opposite effect (Figure 2.1E). We conduct a sensitivity test to evaluate λ_{lake} under each of the three humidity scenarios presented in Section 2.7.3.3. We then use modeled λ_{lake} values to calculate $\delta'^{18}O_{rucp}$ ($\delta'^{18}O_{rucp} = \left[\Delta'^{17}O_{precip} - \Delta'^{17}O_{rfw} + (\lambda_{lake} - \lambda_{ref}) \times \delta'^{18}O_{ref}\right] / \left[\lambda_{lake} - \lambda_{ref}\right]$; Passey and Ji, 2019).

Using the lake budget model, low humidity produces the highest modeled λ_{lake} values and lowest $\delta'^{18}O_{rucp}$ values, high humidity produces the lowest modeled λ_{lake} values and the highest $\delta'^{18}O_{rucp}$ values, and the full humidity model is in the middle (Figure 2.7; Table S2.16). λ_{lake} modeled at high humidity returns $\delta'^{18}O_{rucp}$ values (-15.2 ±2.1‰) that are most similar to amount-weighted annual precipitation (-14.1‰) in the Lake Junín region (Figure 2.7). The full and low humidity models yield lower $\delta'^{18}O_{rucp}$ values (-16.2 ±2.0‰, -17.0 ±2.0‰, respectively). These results highlight the value of considering local humidity (and other parameters in Eq. 8; e.g., R_A, F) when possible to improve accuracy of modeled λ_{lake} and $\delta'^{18}O_{rucp}$ values. The uncertainty in estimated $\delta'^{18}O_{rucp}$ values is a function of both uncertainty in λ_{lake} and $\Delta'^{17}O_{lake}$ (Passey and Ji, 2019), and should be evaluated on a case-to-case basis.

In each humidity scenario, estimated $\delta'^{18}O_{rucp}$ values are lower than $\delta'^{18}O$ values for amount-weighted mean precipitation. Possible explanations include a positive bias in modeled λ_{lake}, selection of $\lambda_{calcite\text{-}water}$ that is too high (Sections 2.6.2.3, 2.7.2), or estimated precipitation $\Delta'^{17}O$ or $\delta'^{18}O$ values that are too high, as also surmised by Passey and Ji (2019). Additional

precipitation and lake water observations in different climate settings will continue to improve our understanding of all of the parameters above.

Notwithstanding continued refinement of λ_{lake} and $\Delta'^{17}O_{precip}$, we show how triple oxygen isotopes in carbonates and waters can be used alongside modeled λ_{lake} values to generate $\delta'^{18}O_{rucp}$ values close to amount-weighted annual precipitation (within ~1–2‰) in both arid and humid environments. In conjunction with other lines of evidence and proxy materials, $\Delta'^{17}O$ can help differentiate between lake systems with different hydrologic states (Figure 2.4), such that we can use $\Delta'^{17}O$ values to evaluate how hydrology influences lacustrine $\delta^{18}O$ records. This is essential for studies that use lakes to reconstruct past climate and hydrology, and for paleoelevation studies that rely on $\delta'^{18}O_{rucp}$ values (e.g., Ibarra et al., 2021; Kelson et al., 2022).

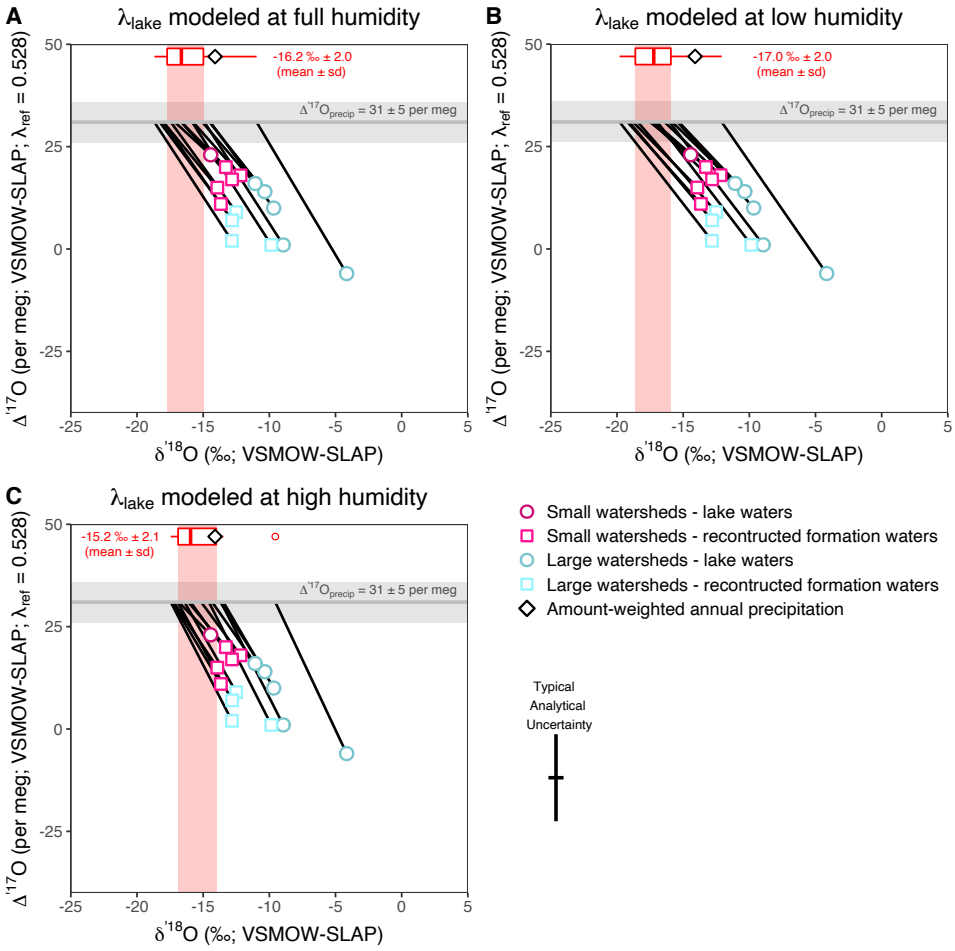

Figure 2.7: Plots of $\Delta'^{17}O$ versus $\delta'^{18}O$ showing the samples used in back projection trajectories (black lines, equivalent to λ_{lake}) for different ranges in humidity: A) full humidity 0.3–0.9, B) low humidity 0.3–0.7, C) high humidity 0.7–0.9. $\delta'^{18}O_{rucp}$ values for each humidity range are represented by the red box and whisker plots. The central line of the box illustrates sample medians; upper and lower hinges illustrate quantile boundaries; outliers are represented by open

circles. A vertical red box demarks the interquartile range in $\delta'^{18}O_{rucp}$ values. $\Delta'^{17}O_{rfw}$ values were calculated using $\lambda_{calcite\text{-}water}$ = 0.5250. Note that we did not calculate $\delta'^{18}O_{rucp}$ values for samples with $\Delta'^{17}O$ values that are indistinguishable from precipitation (31 ±5 per meg, represented by a horizontal grey box).

2.8 Conclusions

In this study, we present new isotope data ($\delta^{18}O$, $\delta^{17}O$, $\delta^{2}H$, Δ_{47}, $\Delta'^{17}O$, d-excess) from precipitation, surface waters, and lake carbonates in the Lake Junín region of Peru. We use these data alongside lake water isotope models run over a broad range of humidity conditions to evaluate and improve the accuracy of precipitation $\delta^{18}O$ reconstructions derived from triple oxygen isotopes. From this work we conclude:

1. Formation water temperatures, derived from modern lake carbonate $T_{\Delta47}$, are elevated compared to MAT, consistent with the growing dataset of Δ_{47} in lakes and analysis of lake temperatures globally.
2. In catchments containing carbonate bedrock influenced by high temperatures, $T_{\Delta47}$ values of lake sediments can be used to screen for detrital inputs.
3. In the Lake Junín region, $\Delta'^{17}O$ values from four lakes reflect the X_E state of each lake, demonstrating that $\Delta'^{17}O$ measurements are effective for evaluating lake hydrology in both humid and arid lake systems.
4. $\delta^{18}O_{precip}$ values reconstructed using triple oxygen isotopic data from lakes are closest to observed mean-weighted $\delta^{18}O_{precip}$ values when humidity is known, but this approach provides accurate $\delta'^{18}O_{rucp}$ estimates even when humidity is unconstrained.

This work solidifies the interpretive framework for using $\Delta'^{17}O$ and Δ_{47} measurements in lake sediments to constrain temperature, lake hydrology, and $\delta^{18}O$ values of precipitation by extending it to humid systems and lakes with little evaporative water loss. Applicability of the $\Delta'^{17}O$ approach for constraining lake water evaporation across climate states and lake types, for either paleoclimate or paleoelevation studies, means that it can widely be applied to geologic archives where climate and/or hydrology may be unconstrained. While our study focuses on carbonate lakes, our results also apply to interpretations of $\Delta'^{17}O$ records from lakes with other mineral precipitates (e.g., silica, gypsum). Future work should focus on applying the $\Delta'^{17}O$

framework to constraining evaporation and $\delta'^{18}O_{rucp}$ values for ancient lake systems, including sediment records from Lake Junín.

Data Availability:

All supplemental files are available at https://doi.org/10.1016/j.epsl.2022.117927. New water isotope data (δ^2H, $\delta^{18}O$, $\Delta'^{17}O$) are available from the University of Utah Water Isotope Database (https://wateriso.utah.edu/waterisotopes/). New carbonate isotope data ($\delta^{18}O$, $\delta^{13}C$, Δ_{47}) are available from the EarthChem database (https://www.earthchem.org/data-access/). Supplemental R Scripts (1–2) are available at https://github.com/sarahakatz/Katz_etal_ModernLakeD17O_SupMat.

Acknowledgements:

The authors gratefully acknowledge the citizen scientists who aided our precipitation and surface water collection efforts. We also thank Union College undergraduates Jordy Herbert, Tshering Lama Sherpa, James Molloy, Mike Kaye, and Laura Piccirillo for assistance with sample collection. Additionally, we thank Drew Gronewold for advice on Monte Carlo modeling; Tyler Huth, Julia Kelson, Natalie Packard, and Nick Ellis for helpful discussions; and Drake Yarian, Emily Beverly, Ryan Horwitz, Elise Pelletier, Jerry Li, and Anouk Verheyden for assistance with analyses. We thank three anonymous reviewers for constructive feedback that improved the quality of this work.

This work was supported financially by a Department of Earth and Environmental Sciences Scott Turner Award, a GSA Graduate Student Research Award, and a GSA Kerry Kelts Research Award to S.A.K.; University of Michigan Departmental Funding and U.S. National Science Foundation funding (EAR-2102843) to N.E.L. and B.H.P.; Union College Funding and U.S. National Science Foundation funding (EAR-1402076) to D.T.R. and D.P.G. The U.S. National Science Foundation funded Union College's isotope ratio mass spectrometer and peripherals (NSF-MRI #1229258).

2.9 Supplementary information

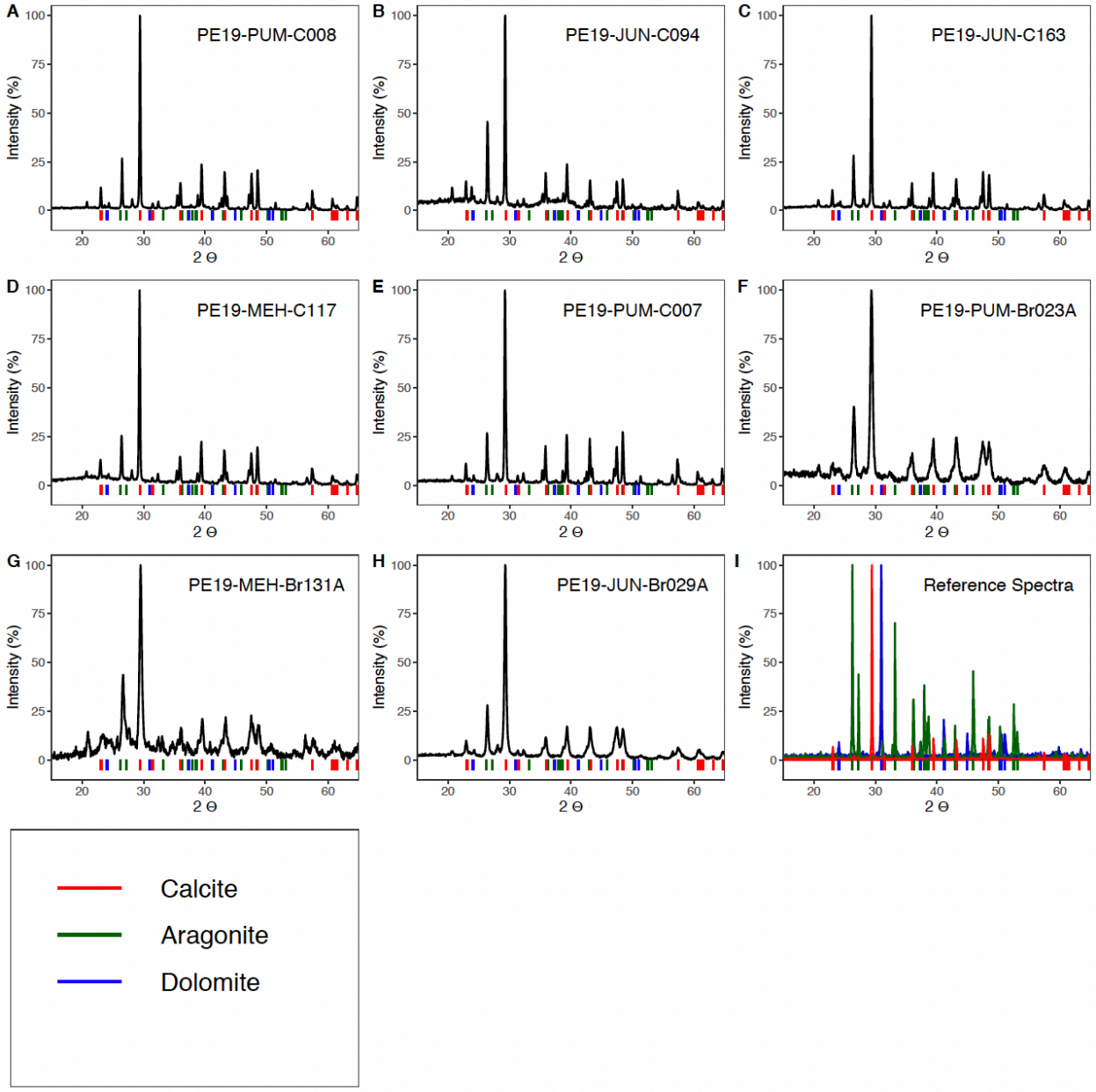

Figure S2.1: XRD spectra for lake carbonates (A-E) and bedrock carbonates (F-H) from the Lake Junín region. Samples were analyzed at a 2 Θ range from 15 to 65° at a 0.05° resolution. Plotted spectra are blank-corrected and normalized by maximum intensity for each sample. The carbonate mineralogy of each sample is entirely calcite based on comparison to reference spectra (I) for calcite (red), aragonite (green), and dolomite (blue). Vertical ticks along the x-axis in each plot indicate 2 Θ peaks for calcite (red), aragonite (green), and dolomite (blue).

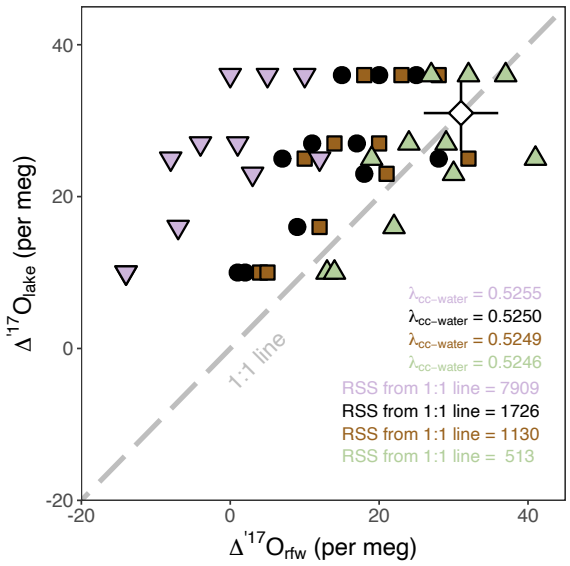

Figure S2.2: As in Figure 2.5D, $\Delta'^{17}O$ values of carbonate formation waters ($\Delta'^{17}O_{rfw}$) versus lake water $\Delta'^{17}O$ ($\Delta'^{17}O_{lake}$) values from waters collected at the same sampling locations. Calculated $\Delta'^{17}O_{rfw}$ is shown for four different $\lambda_{calcite\text{-}water}$ values: 0.5255 (purple, Wostbrock et al. 2020a), 0.5250 (black, Huth et al., 2022), 0.5249 (brown, Kelson et al., 2022), and 0.5246 (green, greatest parity between $\Delta'^{17}O_{rfw}$ and $\Delta'^{17}O_{lake}$ values). RSS: residual sum of squares.

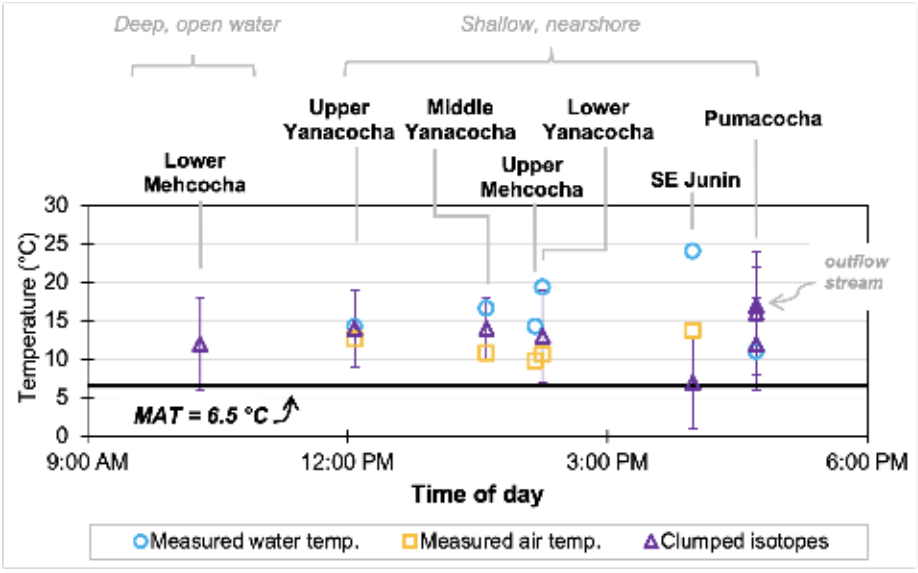

Figure S2.3: Measured air and water temperatures and clumped isotope temperatures plotted versus time of collection. Note that carbonate samples, and air and water temperature measurements were collected over multiple field days from May 5–10, 2019.

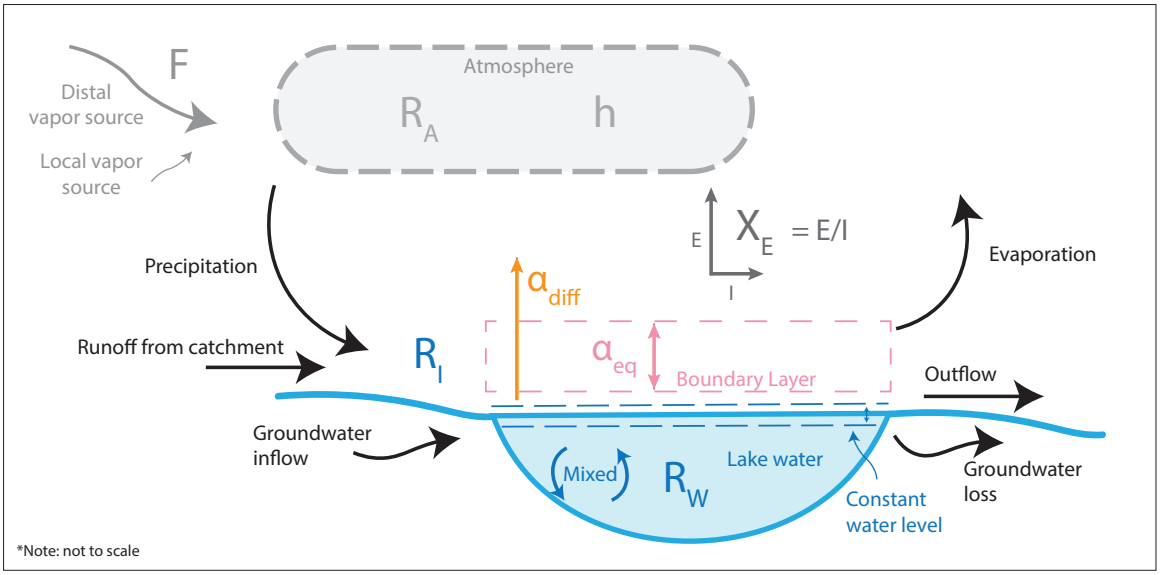

$$R_W = \frac{\alpha_{eq} R_I [\alpha_{diff}(1-h) + h(1-F)] + \alpha_{eq} h X_E R_A F}{X_E + \alpha_{eq}(1-X_E)[\alpha_{diff}(1-h) + h(1-F)]}$$

R_A	Isotopic ratio of atmospheric water vapor.
R_I	Isotopic ratio of unevaporated input waters.
h	Relative humidity normalized to lake surface temperature.
F	Fraction of local vapor derived from non-lake water sources.
α_{eq}	Equilibrium fractionation factor between liquid water and water vapor.
α_{diff}	Kinetic fractionation factor between liquid water and water vapor (relative proportion of diffusive versus turbulent transport).
X_E	Proportion of evaporative losses to inputs (E/I or X_E).

Figure S2.4: Schematic lake balance diagram of an evaporated, flowthrough lake (after Gibson et al., 2016, *QSR*). Black arrows represent volumetric fluxes. Precipitation, runoff, and groundwater inflow are assumed to be relatively unevaporated with respect to lake water. Note that evaporated lake waters that are returned to the atmosphere may affect both over lake humidity (h) and the isotopic composition of atmospheric water vapor (R_A), though this is not explicitly accounted for in Equation 8. The steady state isotopic lake balance equation (Eq. 8) is included below along with a description of each parameter of the equation (see Table S2.15 for additional details). Note: not to scale.

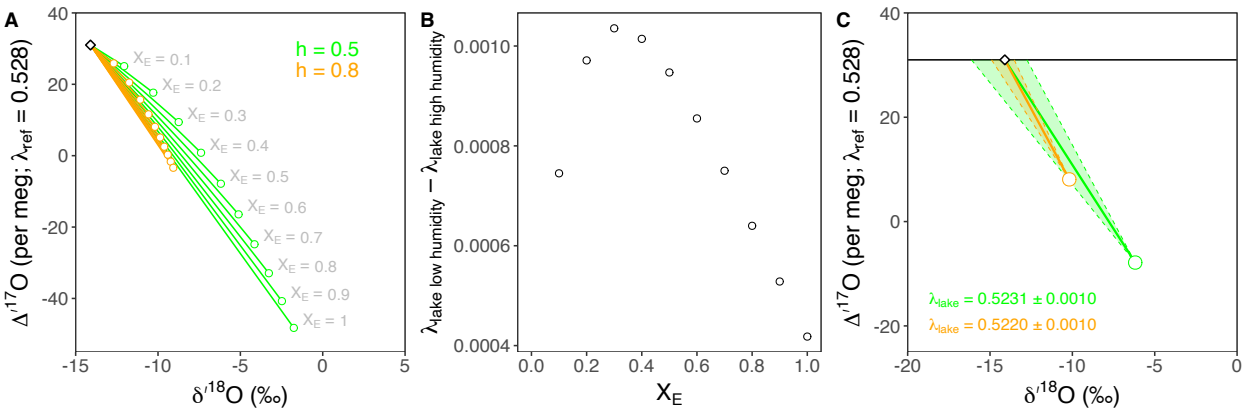

Figure S2.5: Deterministic model output. (A) Modeled results using Equation 8 and the following model conditions: Φ= 0.5; F= 0.9; $\delta'^{18}O_I$= -14.1‰; $\delta'^{18}O_A$= -25.3‰; $\Delta'^{17}O_I$ = 31 per meg; $\Delta'^{17}O_A$= 25 per meg; temperature = 14 °C. The model was run over an X_E range from 0.1 to 1.0 (at intervals of 0.1) for h= 0.5 (arid, green) and h= 0.8 (humid, orange). The white diamond represents the composition of unevaporated input waters. Grey labels indicate X_E for the h= 0.5 scenario; labels are not shown for h= 0.8 for clarity, but follow the same trend as for h= 0.5 (i.e., decreasing $\Delta'^{17}O$ with increasing X_E). Note that the solid lines between each model solution and unevaporated input water are equivalent to λ_{lake} in $\delta'^{17}O$-$\delta'^{18}O$ space and do not represent evaporation trajectories. (B) Difference in λ_{lake} for the two humidity scenarios is shown along the y-axis, versus X_E. The difference in modeled λ_{lake} is highest at relatively low X_E (e.g., 0.2–0.5). (C) As in (A), but showing only the model solutions for X_E= 0.5 at h= 0.5 and 0.8 (green and orange open circles, respectively). Solid colored lines show modeled λ_{lake} for each humidity scenario. Dashed colored lines show λ_{lake} values ±0.0010 to illustrate the effect of λ_{lake} uncertainty on $\delta'^{18}O_{rucp}$. Though the magnitude of λ_{lake} uncertainty is the same for both humidity scenarios, the observed effect on $\delta'^{18}O_{rucp}$ is larger in the low humidity scenario (green shading) when $\Delta'^{17}O$ is more distinct from input $\Delta'^{17}O$.

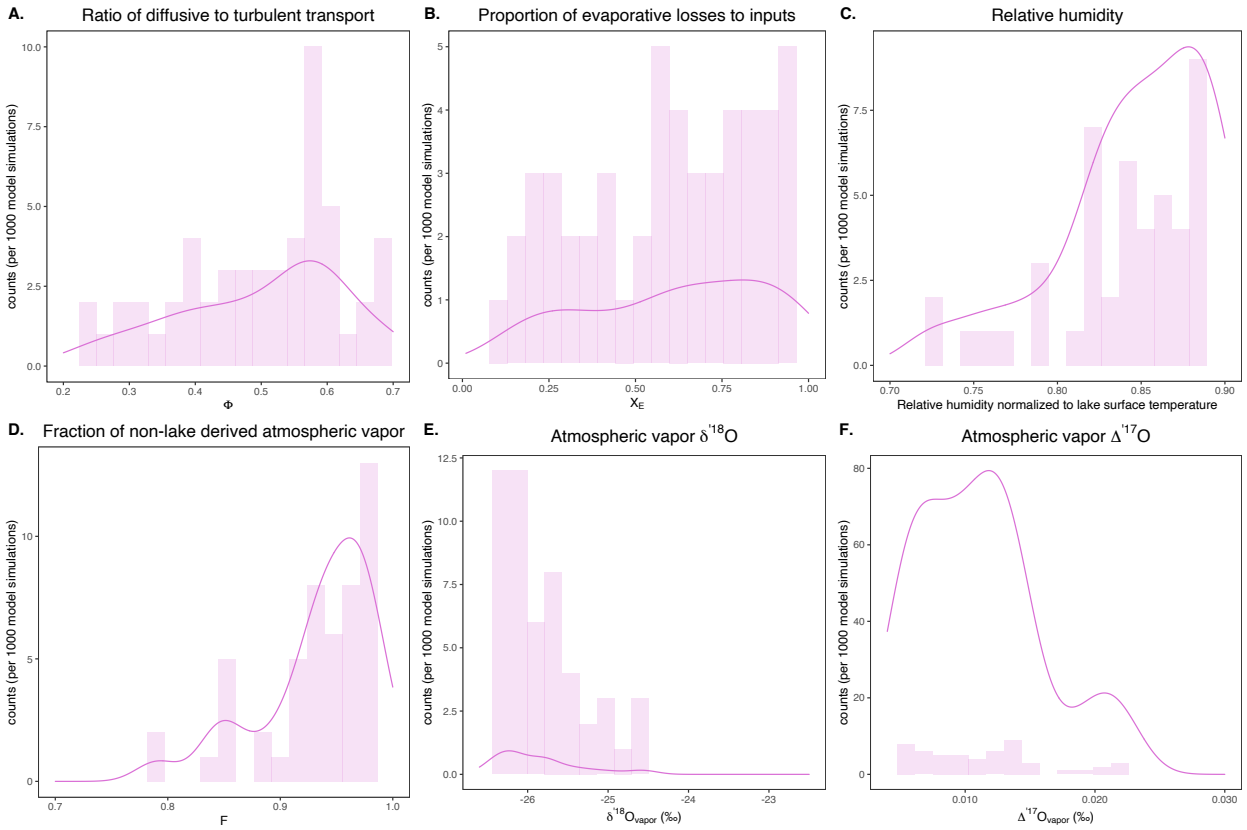

Figure S2.6: Subset of model solutions shown in Figure 2.6F for which λ_{lake} <0.5185. Counts for Φ, X_E, h, F, $\delta'^{18}O_{vapor}$, and $\Delta'^{17}O_{vapor}$ are plotted as histograms; probability density functions are shown as solid lines.

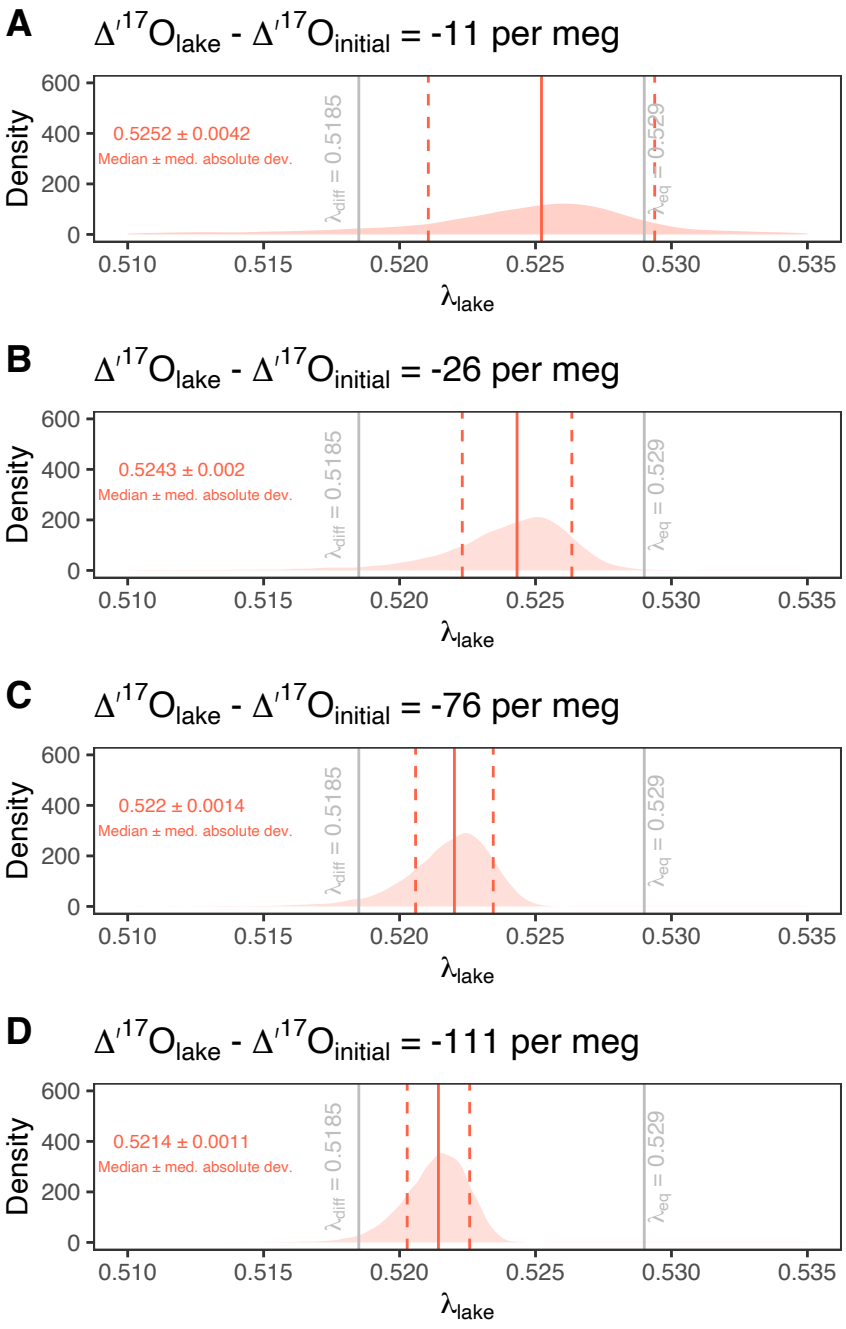

Figure S2.7: Probability density functions illustrating the propagated error for λ_{lake} based on Monte Carlo resampling (n= 10,000) using uncertainty in carbonate $\Delta'^{17}O_{rfw}$ (10 per meg) and $\delta'^{18}O_{rfw}$ (0.957‰), and precipitation $\Delta'^{17}O$ (5 per meg) and $\delta'^{18}O$ (2.2‰). Panels illustrate the dependency of calculated λ_{lake} uncertainty on the magnitude that lake waters have evolved away from input precipitation.

2.10 References

Aron, P.G., Levin, N.E., Beverly, E.J., Huth, T.E., Passey, B.H., Pelletier, E.M., Poulsen, C.J., Winkelstern, I.Z., and Yarian, D.A., 2021a, Triple oxygen isotopes in the water cycle: Chemical Geology, v. 565, p. 1–23, doi:10.1016/j.chemgeo.2020.120026.

Aron, P.G., Poulsen, C.J., Fiorella, R.P., Levin, N.E., Acosta, R.P., Yanites, B.J., and Cassel, E.J., 2021b, Variability and Controls on $\delta^{18}O$, d-excess, and $\Delta'^{17}O$ in Southern Peruvian Precipitation: Journal of Geophysical Research: Atmospheres, v. 126, p. 1–18, doi:10.1029/2020JD034009.

Barkan, E., and Luz, B., 2007, Diffusivity fractionations of $H_2{}^{16}O/H_2{}^{17}O$ and $H_2{}^{16}O/H_2{}^{18}O$ in air and their implications for isotope hydrology: Rapid Communications in Mass Spectrometry, v. 21, p. 2999–3005, doi:10.1002/rcm.3180.

Barkan, E., and Luz, B., 2005, High precision measurements of $^{17}O/^{16}O$ and $^{18}O/^{16}O$ ratios in H_2O: Rapid Communications in Mass Spectrometry, v. 19, p. 3737–3742, doi:10.1002/rcm.2250.

Benson, L. V, and White, J.W.., 1994, Stable Isotopes of Oxygen and Hydrogen in the Truckee River Pyramid Lake Surface-Water System .1. Data-Analysis and Extraction of Paleoclimatic Information: Limnology and Oceanography, v. 39, p. 344–355.

Bird, B.W., Abbott, M.B., Rodbell, D.T., and Vuille, M., 2011a, Holocene tropical South American hydroclimate revealed from a decadally resolved lake sediment $\delta^{18}O$ record: Earth and Planetary Science Letters, v. 310, p. 192–202, doi:10.1016/J.EPSL.2011.08.040.

Bird, B.W., Abbott, M.B., Vuille, M., Rodbell, D.T., Stansell, N.D., and Rosenmeier, M.F., 2011b, A 2,300-year-long annually resolved record of the South American summer monsoon from the Peruvian Andes: Proceedings of the National Academy of Sciences, v. 108, p. 8583–8588, doi:10.1073/pnas.1003719108.

Bonifacie, M., Calmels, D., Eiler, J.M., Horita, J., Chaduteau, C., Vasconcelos, C., Katz, A., Passey, B.H., and Ferry, J.M., 2017, Experimental calibration of the dolomite clumped isotope thermometer from 25 to 350°C, and implications for the temperature estimates for all (Ca, Mg, Fe) CO_3 carbonates digested at high temperature: Geochimica et Cosmochimica Acta, v. 200, p. 255–279, doi:10.1016/j.gca.2016.11.028.

Cobbing, J., Quispesivana, L.Q., and Paz, M.M., 1996, Geologia de los cuadrangulos de Ambo, Cerro de Pasco y Ondores. Boletin N77 Serie A: Carta Geológica Nacinonal.

Dansgaard, W., 1964, Stable isotopes in precipitation: Tellus, v. 16, p. 436–468, doi:10.3402/tellusa.v16i4.8993.

Dennis, K.J., Affek, H.P., Passey, B.H., Schrag, D.P., and Eiler, J.M., 2011, Defining an absolute

reference frame for "clumped" isotope studies of CO_2: Geochimica et Cosmochimica Acta, v. 75, p. 7117–7131, doi:10.1016/j.gca.2011.09.025.

Eiler, J.M., 2007, "Clumped-isotope" geochemistry-The study of naturally-occurring, multiply-substituted isotopologues: Earth and Planetary Science Letters, v. 262, p. 309–327, doi:10.1016/j.epsl.2007.08.020.

Eiler, J.M., 2011, Paleoclimate reconstruction using carbonate clumped isotope thermometry: Quaternary Science Reviews, v. 30, p. 3575–3588, doi:10.1016/j.quascirev.2011.09.001.

Flusche, M.A., Seltzer, G., Rodbell, D., Siegel, D., and Samson, S., 2005, Constraining water sources and hydrologic processes from the isotopic analysis of water and dissolved strontium, Lake Junin, Peru: Journal of Hydrology, v. 312, p. 1–13, doi:10.1016/j.jhydrol.2005.02.021.

Gázquez, F., Morellón, M., Bauska, T., Herwartz, D., Surma, J., Moreno, A., Staubwasser, M., Valero-Garcés, B., Delgado-Huertas, A., and Hodell, D.A., 2018, Triple oxygen and hydrogen isotopes of gypsum hydration water for quantitative paleo-humidity reconstruction: Earth and Planetary Science Letters, v. 481, p. 177–188, doi:10.1016/j.epsl.2017.10.020.

Guo, W., and Zhou, C., 2019, Triple oxygen isotope fractionation in the DIC-H_2O-CO_2 system: A numerical framework and its implications: Geochimica et Cosmochimica Acta, v. 246, p. 541–564, doi:10.1016/j.gca.2018.11.018.

Henry, S.G., and Pollack, H.N., 1988, Terrestrial heat flow above the Andean subduction zone in Bolivia and Peru: Journal of Geophysical Research, v. 93, p. 153–162, doi:10.1029/jb093ib12p15153.

Herwartz, D., Surma, J., Voigt, C., Assonov, S., and Staubwasser, M., 2017, Triple oxygen isotope systematics of structurally bonded water in gypsum: Geochimica et Cosmochimica Acta, v. 209, p. 254–266, doi:10.1016/j.gca.2017.04.026.

Horton, T.W., Defliese, W.F., Tripati, A.K., and Oze, C., 2016, Evaporation induced ^{18}O and ^{13}C enrichment in lake systems: A global perspective on hydrologic balance effects: Quaternary Science Reviews, v. 131, p. 365–379, doi:10.1016/j.quascirev.2015.06.030.

Hren, M.T., and Sheldon, N.D., 2012, Temporal variations in lake water temperature: Paleoenvironmental implications of lake carbonate $\delta^{18}O$ and temperature records: Earth and Planetary Science Letters, v. 337–338, p. 77–84, doi:10.1016/j.epsl.2012.05.019.

Hulston, J.R., and Thode, H.G., 1965, Variations in the S^{33}, S^{34}, and S^{36} contents of meteorites and their relation to chemical and nuclear effects: Journal of Geophysical Research, v. 70, p. 3475–3484, doi:10.1029/JZ070i014p03475.

Huntington, K.W., and Lechler, A.R., 2015, Carbonate clumped isotope thermometry in continental tectonics: Tectonophysics, v. 647–648, p. 1–20, doi:10.1016/j.tecto.2015.02.019.

Huntington, K.W., Saylor, J., Quade, J., and Hudson, A.M., 2015, High late Miocene-Pliocene elevation of the Zhada Basin, southwestern Tibetan Plateau, from carbonate clumped isotope thermometry: Bulletin of the Geological Society of America, v. 127, p. 181–199, doi:10.1130/B31000.1.

Huntington, K.W., Wernicke, B.P., and Eiler, J.M., 2010, Influence of climate change and uplift on Colorado Plateau paleotemperatures from carbonate clumped isotope thermometry: Tectonics, v. 29, p. 1–19, doi:10.1029/2009TC002449.

Huth, T.E., Passey, B.H., Cole, J.E., Lachniet, M.S., McGee, D., Denniston, R.F., Truebe, S., and Levin, N.E., 2022, A framework for triple oxygen isotopes in speleothem paleoclimatology: Geochimica et Cosmochimica Acta, v. 319, p. 191–219, doi:10.1016/j.gca.2021.11.002.

IAEA/WMO, 2022, Global Network of Isotopes in Precipitation (GNIP):, https://www.iaea.org/services/networks/gnip.

Ibarra, D.E., Kukla, T., Methner, K.A., Mulch, A., and Chamberlain, C.P., 2021, Reconstructing Past Elevations From Triple Oxygen Isotopes of Lacustrine Chert: Application to the Eocene Nevadaplano, Elko Basin, Nevada, United States: Frontiers in Earth Science, v. 9, p. 1–19, doi:10.3389/feart.2021.628868.

Kelson, J.R., Petersen, S. V., Niemi, N.A., Passey, B.H., and Curley, A.N., 2022, Looking upstream with clumped and triple oxygen isotopes of estuarine oyster shells in the early Eocene of California, USA: Geology, doi:10.1130/G49634.1.

Kim, S.-T., and O'Neil, J.R., 1997, Equilibrium and nonequilibrium oxygen isotope effects in synthetic carbonates: Geochimica et Cosmochimica Acta, v. 61, p. 3461–3475, doi:10.1016/S0016-7037(97)00169-5.

Landais, A., Barkan, E., Yakir, D., and Luz, B., 2006, The triple isotopic composition of oxygen in leaf water: Geochimica et Cosmochimica Acta, v. 70, p. 4105–4115, doi:10.1016/j.gca.2006.06.1545.

Leng, M.J., and Marshall, J.D., 2004, Palaeoclimate interpretation of stable isotope data from lake sediment archives: Quaternary Science Reviews, v. 23, p. 811–831, doi:10.1016/J.QUASCIREV.2003.06.012.

Luz, B., and Barkan, E., 2010, Variations of $^{17}O/^{16}O$ and $^{18}O/^{16}O$ in meteoric waters: Geochimica et Cosmochimica Acta, v. 74, p. 6276–6286, doi:10.1016/j.gca.2010.08.016.

Merlivat, L., 1978, Molecular diffusitivies or $H_2{}^{16}O$, $HD^{16}O$, and $H_2{}^{18}O$ in gases: The Journal of Chemical Physics, v. 69, doi:10.1063/1.436884.

Miller, M.F., and Pack, A., 2021, Why Measure ^{17}O? Historical Perspective, Triple-Isotope Systematics and Selected Applications: Reviews in Mineralogy and Geochemistry, v. 86, p. 1–34, doi:10.2138/rmg.2021.86.01.

Passey, B.H., Hu, H., Ji, H., Montanari, S., Li, S., Henkes, G.A., and Levin, N.E., 2014, Triple oxygen isotopes in biogenic and sedimentary carbonates: Geochimica et Cosmochimica Acta, v. 141, p. 1–25, doi:10.1016/j.gca.2014.06.006.

Passey, B.H., and Ji, H., 2019, On the use of triple oxygen isotopes in lake waters and carbonates for reconstructing $\delta^{18}O$ of unevaporated precipitation: a case study from the Western United States: Earth and Planetary Science Letters, v. 518, p. 1–12, doi:10.1016/j.epsl.2019.04.026.

Passey, B.H., Levin, N.E., Cerling, T.E., Brown, F.H., and Eiler, J.M., 2010, High-temperature environments of human evolution in East Africa based on bond ordering in paleosol carbonates: Proceedings of the National Academy of Sciences, v. 107, p. 11245–11249, doi:10.1073/pnas.1001824107.

Petersen, S.V. V. et al., 2019, Effects of Improved ^{17}O Correction on Inter-Laboratory Agreement in Clumped Isotope Calibrations, Estimates of Mineral-Specific Offsets, and Temperature Dependence of Acid Digestion Fractionation: Geochemistry, Geophysics, Geosystems, v. 20, p. 3495–3519, doi:10.1029/2018GC008127.

Petryshyn, V.A., Lim, D., Laval, B.L., Brady, A., Slater, G., and Tripati, A.K., 2015, Reconstruction of limnology and microbialite formation conditions from carbonate clumped isotope thermometry: Geobiology, v. 13, p. 53–67, doi:10.1111/gbi.12121.

Pierchala, A., Rozanski, K., Dulinski, M., and Gorczyca, Z., 2022, Triple-isotope mass balance of mid-latitude, groundwater controlled lake: Science of The Total Environment, v. 814, p. 1–11, doi:10.1016/j.scitotenv.2021.151935.

Schauble, E.A., Ghosh, P., and Eiler, J.M., 2006, Preferential formation of $^{13}C–^{18}O$ bonds in carbonate minerals, estimated using first-principles lattice dynamics: Geochimica et Cosmochimica Acta, v. 70, p. 2510–2529, doi:10.1016/j.gca.2006.02.011.

Schoenemann, S.W., Schauer, A.J., and Steig, E.J., 2013, Measurement of SLAP2 and GISP $\delta^{17}O$ and proposed VSMOW-SLAP normalization for $\delta^{17}O$ and $^{17}O_{excess}$: Rapid Communications in Mass Spectrometry, v. 27, p. 582–590, doi:10.1002/rcm.6486.

Seltzer, G., Rodbell, D., and Burns, S., 2000, Isotopic evidence for late Quaternary climatic change in tropical South America: Geology, v. 28, p. 35–38.

SENAMHI, 2022, Datos Hidrometeorológicos a nivel nacional:, https://www.senamhi.gob.pe/?&p=estaciones (accessed November 2019).

Surma, J., Assonov, S., Herwartz, D., Voigt, C., and Staubwasser, M., 2018, The evolution of ^{17}O-excess in surface water of the arid environment during recharge and evaporation: Scientific Reports, v. 8, p. 4972, doi:10.1038/s41598-018-23151-6.

Voigt, C., Herwartz, D., Dorador, C., and Staubwasser, M., 2021, Triple oxygen isotope systematics of evaporation and mixing processes in a dynamic desert lake system: Hydrology and Earth System Sciences, v. 25, p. 1211–1228, doi:10.5194/hess-25-1211-

2021.

Wang, Z., Schauble, E.A., and Eiler, J.M., 2004, Equilibrium thermodynamics of multiply substituted isotopologues of molecular gases: Geochimica et Cosmochimica Acta, v. 68, p. 4779–4797, doi:10.1016/j.gca.2004.05.039.

Wostbrock, J.A.G., Brand, U., Coplen, T.B., Swart, P.K., Carlson, S.J., Brearley, A.J., and Sharp, Z.D., 2020a, Calibration of carbonate-water triple oxygen isotope fractionation: Seeing through diagenesis in ancient carbonates: Geochimica et Cosmochimica Acta, v. 288, p. 369–388, doi:10.1016/j.gca.2020.07.045.

Wostbrock, J.A.G., Cano, E.J., and Sharp, Z.D., 2020b, An internally consistent triple oxygen isotope calibration of standards for silicates, carbonates and air relative to VSMOW2 and SLAP2: Chemical Geology, p. 1–9, doi:10.1016/j.chemgeo.2019.119432.

Young, E.D., Galy, A., and Nagahara, H., 2002, Kinetic and equilibrium mass-dependent isotope fractionation laws in nature and their geochemical and cosmochemical significance: Geochimica et Cosmochimica Acta, v. 66, p. 1095–1104.

Chapter 3 Holocene Temperature And Water Stress In The Peruvian Andes: Insights From Lake Carbonate Clumped And Triple Oxygen Isotopes[2]

3.1 Abstract

Global climate during the Holocene was relatively stable compared to the late Pleistocene. However, evidence from lacustrine records in South America suggests that tropical latitudes experienced significant water balance variability during the Holocene, rather than quiescence. For example, a tight coupling between insolation and carbonate $\delta^{18}O$ records from central Andean lakes (e.g., Lakes Junín, Pumacocha) suggest water balance is tied directly to South American summer monsoon (SASM) strength. However, lake carbonate $\delta^{18}O$ records also incorporate information about temperature and evaporation. To overcome this ambiguity, clumped and triple oxygen isotope records can provide independent constraints on temperature and evaporation. Here, we use clumped and triple oxygen isotopes to develop Holocene temperature and evaporation records from three central Andean lakes, Lakes Junín, Pumacocha, and Mehcocha, to build a more complete picture of regional water balance (*P–E*). We find that Holocene water temperatures at all three lakes were stable and slightly warmer than during the latest Pleistocene. These results are consistent with global data assimilations and records from the foothills and Amazon basin. In contrast, evaporation was highly variable and tracks SASM intensity. The hydrologic response of each lake to SASM depends greatly on the physical characteristics of the lake basin, but they all record peak evaporation in the early to mid-Holocene (11,700 to 4,200 years BP) when regional insolation was relatively low and the SASM was weak. These results corroborate other central Andean records and suggest synchronous, widespread water stress tracks insolation-paced variability in SASM strength.

[2] In review as: Katz, S.A., Levin, N.E., Abbott, M.B., Rodbell, D.T., Passey, B.H., DeLuca, N.M., Larsen, D.J, Woods, A. Holocene temperature and water stress in the Peruvian Andes: insights from lake carbonate clumped and triple oxygen isotopes, *Paleoceanography and Paleoclimatology*.

3.2 Introduction

During the Holocene, the central Andes witnessed ecological turnover (e.g., Hansen et al., 1994; Rozas-Davila et al., 2023; Schiferl et al., 2023), net loss of mountain glaciers (e.g., Rodbell et al., 2008, 2009; Stansell et al., 2013, 2017; Palacios et al., 2020), and expansion of pre-Columbian societies (e.g., Rademaker et al., 2014; de Souza et al., 2019; Riris and Arroyo-Kalin, 2019). Water plays a crucial role in these dynamics, such that hydrologic records from the Holocene (11,700 years before present (i.e., "years BP") to present day) provide insights into the rise of modern environments and the sensitivity of these regions to global climate change (Thompson et al., 1995; Cruz et al., 2005; Rodbell et al., 2022). Many studies have documented the relationship between global climate and the central Andean water cycle during the Holocene (e.g., Seltzer et al., 2000; Woods et al., 2020), as global insolation and high latitude feedbacks control the position of the intertropical convergence zone and the convective strength of the South American summer monsoon (SASM) (e.g., Vuille et al., 2012; McGee et al., 2014; Liu and Battisti, 2015; Woods et al., 2020). However, few studies document how local water balance ($P–E$) has changed in response to SASM variability, such that we lack information about how local $P–E$ relates to global climate change (e.g., Ward et al., 2019; Woods et al., 2020).

The SASM is the primary atmospheric system in the tropical and subtropical latitudes of South America (10 °N–30 °S) and conveys moist air masses from the Atlantic westward over the Amazon basin and central Andes (Lenters and Cook, 1999; Vera et al., 2006; Garreaud et al., 2009; Marengo et al., 2012). Convective intensity (i.e., SASM "strength") and geographic position are controlled by meridional temperature gradients in the Atlantic, such that precession-paced changes in insolation drive rainfall trends in the core monsoon region on millennial–orbital timescales (Figure 3.1a) (Cruz et al., 2005; Liu and Battisti, 2015). SASM strength is greatest when southern hemisphere summer (Dec–Feb) insolation is highest (i.e., the late Holocene) and weakest when local summer insolation is low (i.e., the early Holocene) (Figure 3.1a) (Laskar et al., 2004; McGee et al., 2014).

Oxygen isotopes ($\delta^{18}O$) of precipitation are a common tool used to explore water cycle processes, including SASM dynamics, because isotopes integrate information about atmospheric and terrestrial conditions (Craig, 1961; Dansgaard, 1964; Rozanski et al., 1993). For example, in the monsoon region, the $\delta^{18}O$ value of rainfall can be explained by Rayleigh distillation, whereby

precipitation $\delta^{18}O$ values reflect the degree of rainout at upwind sites. In South America, this leads to a predictable, continental-scale pattern of decreasing precipitation $\delta^{18}O$ values from east to west, corresponding to progressive loss of the heavier isotopes. Under weak SASM conditions during the early Holocene (e.g., 11,700 to 8,200 years BP), the continental $\delta^{18}O$ gradient is weaker compared to a relatively steep gradient under stronger SASM conditions during the late Holocene (e.g., 4,200 years BP to present) (note, Holocene subepoch boundaries follow Cohen et al. 2013, 2023) (Vuille and Werner, 2005; Vuille et al., 2012; Liu and Battisti, 2015). Accordingly, proxy records that reflect precipitation $\delta^{18}O$ values such as ice cores and speleothems have been used extensively to reconstruct the strength and geographic footprint of SASM over the Holocene. For example, in the central Andes, ice core $\delta^{18}O$ records from Huascaran ice cap (9 °S; Figure 3.1b,3.2) (Thompson et al., 1995) and speleothem calcite $\delta^{18}O$ from Huagapo cave (11 °S; Figure 3.1b,3.2) (Kanner et al., 2013) closely track 11 °S insolation during the Holocene (Laskar et al., 2004), with the least negative $\delta^{18}O$ values (weakest SASM) corresponding with the early-Holocene summer insolation minimum and the most negative $\delta^{18}O$ values (strongest SASM) corresponding with peak summertime insolation in the late Holocene.

Precipitation $\delta^{18}O$ values in the tropics have also been interpreted as reflecting rainfall amount (i.e., the "amount effect") at the collection site, where there is an inverse relationship between precipitation amount and $\delta^{18}O$ value (Dansgaard, 1964). Although recent papers discuss the challenges with invoking the amount effect to interpret precipitation $\delta^{18}O$ values in the tropics (e.g., Konecky et al., 2019), for sites proximal to the Atlantic, there is some basis for relating local $\delta^{18}O$ to precipitation amount (Cruz et al., 2009; Liu and Battisti, 2015; Ward et al., 2019). However, this mechanism is not well-established in the central Andes despite modeling efforts (Vuille and Werner, 2005; Liu and Battisti, 2015), extensive modern precipitation data (Aron et al., 2021b), and paleoclimate records (Ward et al., 2019; Woods et al., 2020). Instead, some studies suggest SASM strength through the Holocene may have been decoupled from local moisture availability in the central Andes (Vuille and Werner, 2005; Ward et al., 2019; Woods et al., 2020). Therefore, in the central Andes, precipitation $\delta^{18}O$ values do not offer strong, quantitative evidence of past precipitation amount variations and provide little clarity as to how local *P–E* responds to global climate change.

Developing local *P–E* histories depends on records that are sensitive to changes in water balance, for example, lake levels and hydrology (e.g., Abbott et al., 1997; Placzek et al., 2006), glacier extent (e.g., Stansell et al., 2013, 2017; Sagredo et al., 2014) and faunal assemblages (e.g., Hansen et al., 1994; Rozas-Davila et al., 2023). One region that has been extensively studied is the Lake Junín region in the central Andes (approximately 10.5–11.5 °S; 75.5–76.5 °W; Figure 3.2). Specifically, pollen and sedimentological records from Lake Junín provide evidence of a shift from relatively dry conditions at the start of the Holocene (11,700 BP) to wet in the present (Hansen et al., 1994; Weidhaas, 2017; Woods, 2021; Rozas-Davila et al., 2023; Schiferl et al., 2023). Other studies have relied on isotopic records from Lake Junín to address *P–E* (Seltzer et al., 2000), as lake water $\delta^{18}O$ values increase with respect to precipitation $\delta^{18}O$ values under evaporated conditions and this signature is recorded by lake carbonate (e.g., Leng and Marshall, 2004; Gibson et al., 2016). In a widely cited study, Seltzer et al. (2000) compared the carbonate $\delta^{18}O$ from Lake Junín to the Huascaran ice core $\delta^{18}O$ record (which they interpret to more directly reflect precipitation $\delta^{18}O$) (Thompson et al., 1995) to estimate evaporative loss and observed a maximum offset between the two records in the early Holocene followed by a steady convergence towards present (Figure 3.1b). The authors attributed these results to a reduction in evaporative losses from the lake over the Holocene and increasingly wet conditions under strengthening SASM (Figure 3.1). Later studies replicate this approach by comparing the Lake Junín carbonate $\delta^{18}O$ record to a speleothem $\delta^{18}O$ record from Huagapo cave (Kanner et al., 2013) and to Pumacocha, a hydrologically open lake (Bird et al., 2011a), with similar interpretations of the Lake Junín $\delta^{18}O$ record across all three studies (Figure 3.1,3.2).

Although the Lake Junín $\delta^{18}O$ record is one of a handful of datasets frequently used as evidence of *P–E* change in the central Andes, interpretations based on $\delta^{18}O$ values rely on two assumptions. The first is that the Lake Junín carbonate $\delta^{18}O$ record reflects only changes in precipitation $\delta^{18}O$ values and evaporation, not other factors like temperature and hydrology, which are also known to affect carbonate $\delta^{18}O$ values (e.g., Leng and Marshall, 2004). Without methods to independently constrain temperature and lake water evaporation, the influence of these factors on carbonate $\delta^{18}O$ has never been directly tested. The second assumption is that $\delta^{18}O$ records from Huascaran ice core, Huagapo cave, and Pumacocha lake carbonates reflect only changes in precipitation $\delta^{18}O$ values and that differences in site location, elevation, and archive type are

negligible. Studies that directly compare the different depositional settings could help establish the relationship between $\delta^{18}O$ values recorded by lacustrine, cave, and ice archives, but parallel campaigns to monitor site conditions and/or proxy system modeling (e.g., Dee et al., 2015, 2018) have not yet been established. As a result, the timing and magnitude of *P–E* change in the Lake Junín region remains unclear.

In this study, we develop a framework to evaluate *P–E* change from lake records using carbonate clumped (Δ_{47}) and triple oxygen ($\Delta'^{17}O$) isotopes, which are proxies for the temperature of carbonate formation and degree of lake evaporation, respectively. We present new estimates of Holocene lake water evaporative states and temperature from Lake Junín in order to test longstanding interpretations of the carbonate $\delta^{18}O$ record. We also present evaporation and temperature records from Lakes Pumacocha and Mehcocha, two small, hydrologically open lakes today, which are assumed to track precipitation $\delta^{18}O$ values across the Holocene. Finally, using a lake water isotope mass balance model, we estimate hydrologic change in the three lakes and offer new insights into the Holocene *P–E* balance of the central Andes.

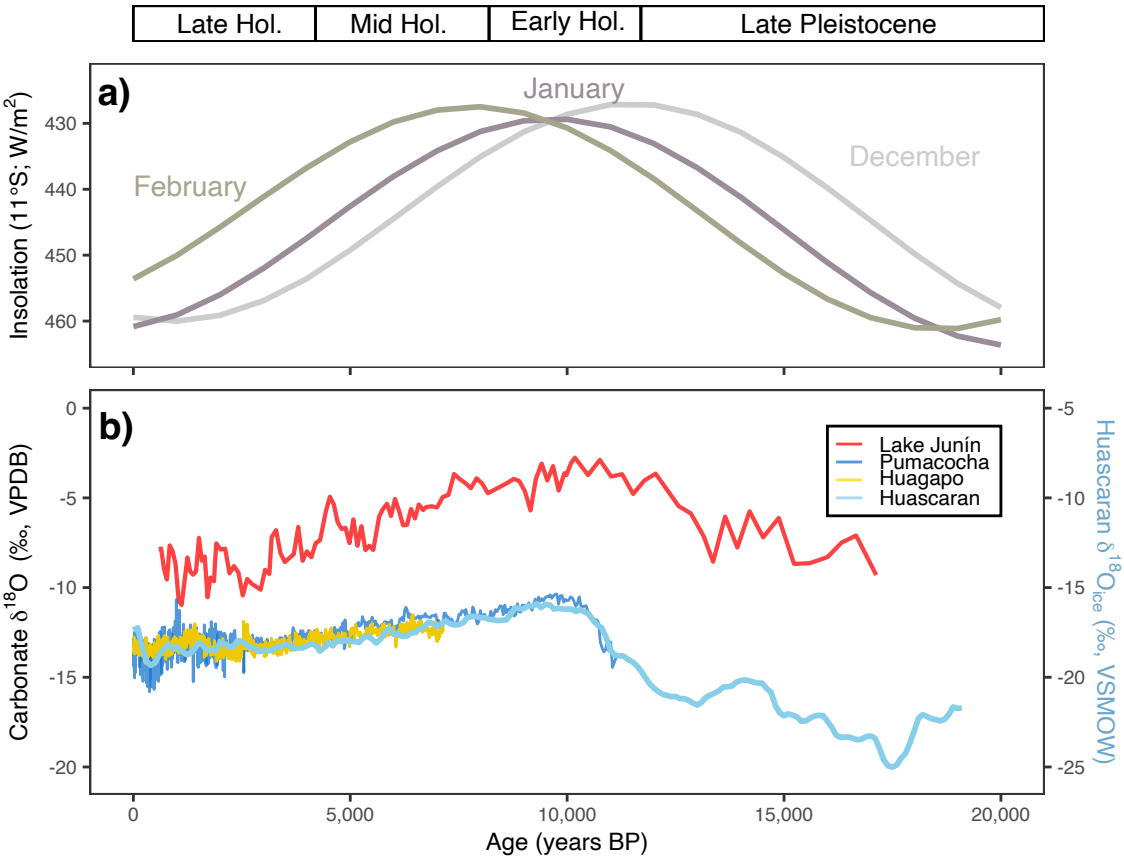

Figure 3.1: Summer insolation and hydroclimate records from the Lake Junín region and Cordillera Blanca (9–11 °S). (a) Summer (Dec–Feb) insolation at 11 °S calculated based on orbital solutions of Laskar et al. (2004) using the R

package *palinsol* (Crucifix, 2016), with y-axis scale reversed. (b) Carbonate $\delta^{18}O$ records from Lake Junín (Seltzer et al., 2000), Lake Pumacocha (Bird et al., 2011a, 2011b), and Huagapo cave (Kanner et al., 2013). The Huascaran ice core $\delta^{18}O$ record is plotted on the right-hand y-axis (Thompson et al., 1995). Epoch and subepoch boundaries follow Cohen et al. (2013, 2023).

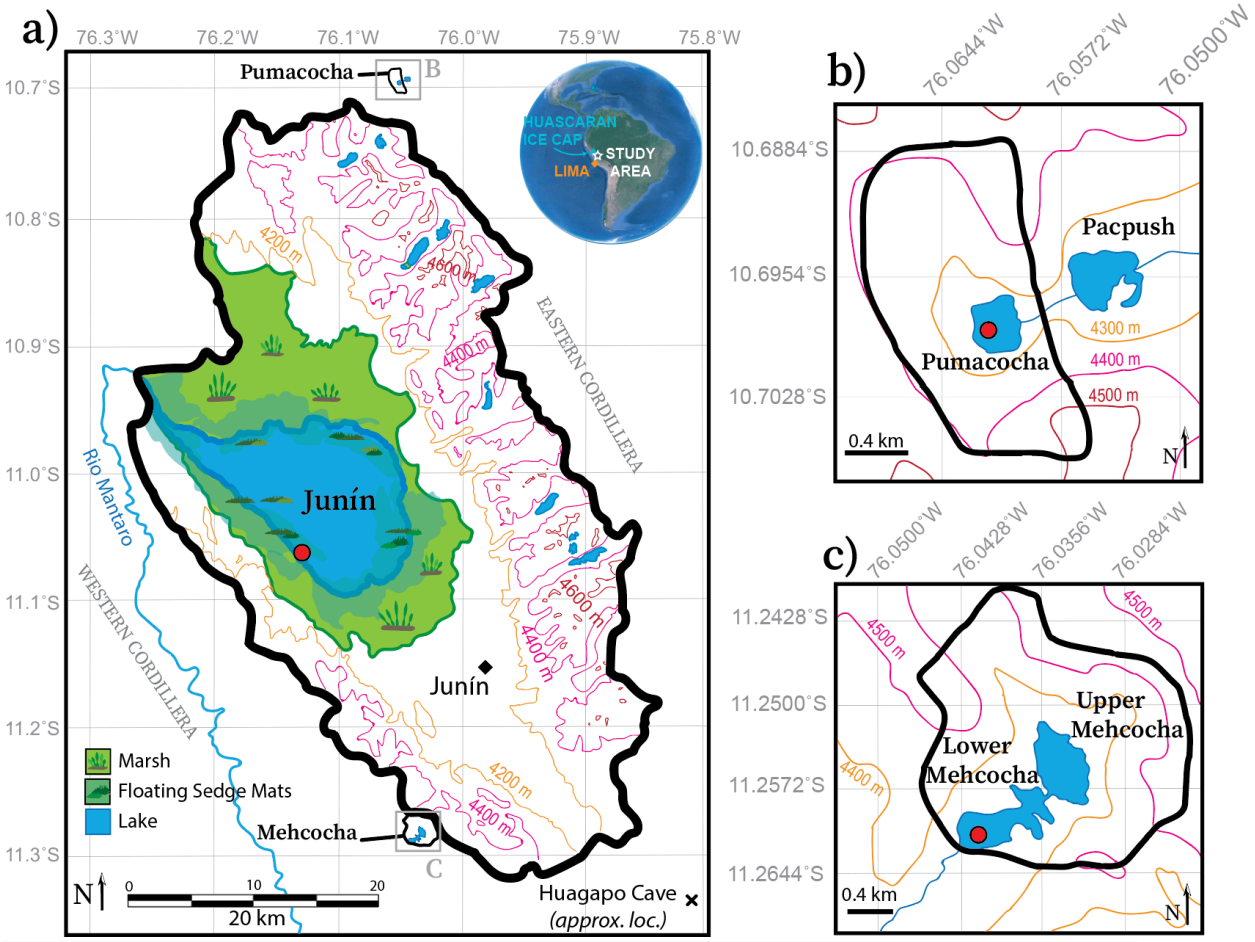

Figure 3.2: Maps of the three lake basins discussed in this study: (a) Junín, (b) Pumacocha, and (c) Mehcocha. Elevation contours shown at 200 m (a) and 100 m (b,c) intervals and thick black outlines denote the watershed boundaries. Red circles in each panel show the approximate coring location at each lake. Inset map in (a), modified from Google Earth, shows the location of the study area and other locations discussed in the text (Google LLC, 2022). Modified from Fig. 2 of Katz et al. (2023) and reprinted with permission of Elsevier.

3.3 Isotope Notation

Isotope ratios are reported with respect to a standard in either "delta" (Eq. 1) or "delta prime" (Eq. 2) notation:

$$\delta^{X}O = ({}^{X}R_{sample}/{}^{X}R_{standard} - 1) \quad \text{Eq. 1}$$

$$\delta'^{X}O = \ln({}^{X}R_{sample}/{}^{X}R_{standard}) \quad \text{Eq. 2}$$

Where R represents the measured ratio of heavy to light isotopes and X is the atomic mass number of the heavy isotope. Both delta and delta prime values are reported in units of "per mil," ‰, where Equations 1 and 2 are multiplied by 10^3.

In a two-isotope system (e.g., $^{18}O/^{16}O$) fractionation between forms or phases (i.e., A, B) that contain the element of interest is expressed with the fractionation factor, α:

$$^{18}\alpha_{A-B} = \frac{^{18}R_A}{^{18}R_B} \quad \text{Eq. 3}$$

In a three-isotope system (e.g., $^{18}O/^{16}O$, $^{17}O/^{16}O$) fractionation factors among isotopologues are related by a power law (Matsuhisa et al., 1978; Young et al., 2002):

$$^{17}\alpha_{A-B} = \left(^{18}\alpha_{A-B}\right)^{\theta} \quad \text{Eq. 4}$$

Where θ represents a fractionation exponent for a discrete process such as water vapor diffusion (θ_{diff}) or equilibrium exchange (θ_{eq}). For processes that may be a combination of discrete fractionation steps, e.g., lake water evaporation, the term λ is used instead of θ (e.g., λ_{lake}).

The term $\Delta'^{17}O$ is defined as:

$$\Delta'^{17}O = \delta'^{17}O - \lambda_{ref} * \delta'^{18}O \quad \text{Eq. 5}$$

and commonly reported in units of "per meg" where Equation 5 is multiplied by 10^6. In hydrologic studies, the reference slope in $\delta'^{18}O$–$\delta'^{17}O$ space, λ_{ref}, is commonly defined as 0.528 (Luz and Barkan, 2010). This definition is useful in hydrologic studies because the liquid water–water vapor equilibrium fractionation exponent, $\theta_{eq} = 0.529$ (Luz and Barkan, 2005), is similar to λ_{ref}, such that λ_{ref} closely approximates the slope of Rayleigh processes and the slope of the Global Meteoric Water Line (≈ 0.528) (Luz and Barkan, 2010; Terzer-Wassmuth et al., 2023). Other processes, such as diffusion of water vapor through air, follow a shallower slope in $\delta'^{18}O$–$\delta'^{17}O$ space where $\theta_{diff} = 0.5185$ (Barkan and Luz, 2007). Evaporation involves both diffusion of water vapor and equilibrium liquid water–water vapor exchange, and the distinct θ_{diff} value leads to modification of the $\Delta'^{17}O$ values in water bodies that have experienced evaporative losses.

In carbonate materials formed in equilibrium with formation waters, the fractionation factor between water and calcite, $^{18}\alpha_{calcite\text{-}water}$, is temperature dependent (Kim and O'Neil, 1997). Carbonate "clumped isotopes" provide carbonate formation temperatures and can be used to constrain $\delta^{18}O$ values of formation water. The stochastic abundance of random "clumps," or bonds between two heavy isotopes, e.g., ^{13}C–^{18}O, can be predicted based on sample $\delta^{13}C$ and $\delta^{18}O$ values.

However, in line with thermodynamic predictions, the measured abundance of "clumps" exceeds the stochastic abundance at Earth's surface conditions (Wang et al., 2004; Schauble et al., 2006). This difference, Δ_{47}, is inversely proportional to formation temperature and independent of sample $\delta^{13}C$ and $\delta^{18}O$ values. Δ_{47} can be defined as:

$$\Delta_{47} = \left[\left(\frac{R47}{R47^*} - 1\right) - \left(\frac{R46}{R46^*} - 1\right) - \left(\frac{R45}{R45^*} - 1\right)\right] \quad \text{Eq. 6}$$

where stochastic ratios are marked with "*". Clumped isotopes have been used to infer formation temperatures, $T\Delta_{47}$, from various types of natural carbonates, including lake carbonates spanning a broad range of climatic settings and hydrologic configurations (Huntington et al., 2010, 2015; Hren and Sheldon, 2012; Horton et al., 2016; Passey and Ji, 2019; Santi et al., 2020; Fetrow et al., 2022; Katz et al., 2023).

3.4 Foundation and interpretive framework

3.4.1 Lake water balance

The water balance of lakes can be described as the volumetric proportion of inputs and losses to the lake basin. In most lakes, direct precipitation and catchment runoff constitute the primary inputs (I), while evaporation (E) and outflow (O) constitute the major losses (Figure 3.3).

Over a time interval of interest, the mass-balance of lakes can be described as a "steady state" system if the volumetric ratio of inputs equals losses:

$$I = E + O \quad \text{Eq. 7}$$

Likewise, steady state conditions also conserve the isotopic mass balance of lakes (Criss, 1999):

$$IR_{\mathrm{I}} = ER_{\mathrm{E}} + OR_{\mathrm{O}} \quad \text{Eq. 8}$$

In a well-mixed lake, it is assumed that the isotopic composition of lake water, R_{lw}, equals R_{O}.

In this study, we group lakes into two hydrologic categories, open and closed, differentiated by the proportion of water loss via evaporation, relative to the total incoming water (Figure 3.3). The proportion of evaporation to inputs can be expressed numerically as X_{E}:

$$X_{\mathrm{E}} = \frac{E}{I} \quad \text{Eq. 9}$$

Under this definition, closed basin lakes have X_E values of 1, reflecting a hydrologic endmember where all losses are via evaporation. Open lakes have X_E values <1 and have a portion of their water loss via outflow; they can be further differentiated as outflow-only ($X_E = 0$), outflow-dominated ($0 < X_E < 0.5$), and evaporation-dominated ($0.5 < X_E < 1$) (Figure 3.3).

Within a region of uniform climate conditions, lakes can exist along a hydrologic spectrum due to variability in basin (e.g., size, topography) and lake (e.g., surface area, depth) characteristics. Over time, changes in regional water balance will also drive hydrologic change among lakes; under more positive water balance conditions (i.e., "wetter") lakes will shift towards a greater proportion of inflow (lower X_E), whereas in negative water balance conditions lakes will shift towards a decreasing proportion of outflow (i.e., "drier," higher X_E).

The isotopic composition of lake water, R_{lw}, is highly sensitive to lake hydrology (i.e., X_E) (Herwartz et al., 2017; Gázquez et al., 2018; Passey and Ji, 2019) and can be calculated as:

$$R_{lw} = \frac{\alpha_{eq} R_I [\alpha_{diff}(1-h)+h(1-F)] + \alpha_{eq} h X_E R_A F}{X_E + \alpha_{eq}(1-X_E)\,[\alpha_{diff}(1-h)+h(1-F)]} \quad \text{Eq. 10}$$

Equation 10 (e.g., Benson and White, 1994; Passey and Ji, 2019) describes a steady state lake where α_{eq} is the temperature-dependent equilibrium exchange between water at the lake surface and atmospheric water vapor (Majoube, 1971) and α_{diff} is "diffusion" of lake water into the unsaturated atmosphere. For $^{18}O/^{16}O$, $^{18}\alpha_{diff}$ values can range between 1 (for non-fractionating, turbulent conditions) and 1.02849 (for molecular diffusion; Merlivat, 1978). Therefore, $^{18}\alpha_{diff}$ can be calculated as $^{18}\alpha_{diff} = 1.02849\Phi + (1 - \Phi)$, where Φ is the relative proportion of diffusive to turbulent transport of water vapor during evaporation (Passey and Ji, 2019). Relative humidity normalized to lake surface temperature is represented by h and F is the fraction of atmospheric vapor derived from distal sources versus the lake itself (where 1 and 0 represent exclusively distal and lake-derived sources of atmospheric vapor, respectively). Assuming that R_A, the isotopic ratio of atmospheric vapor, is in equilibrium with R_I, α_{eq} can be used to calculate R_A. However, note that this approach does not explicitly account for the effect of evaporation on R_A when $F < 1$, nor does it account for the possibility that atmospheric water vapor was derived from a different source or a mixture of sources (e.g., Aggarwal et al., 2016; Aron et al., 2021b).

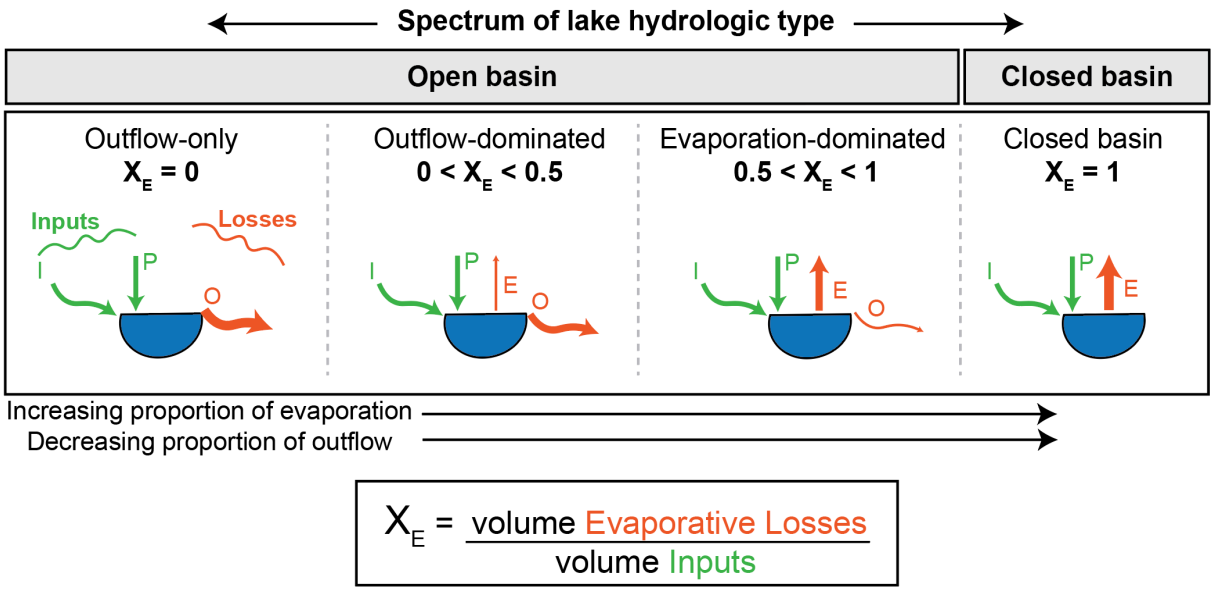

Figure 3.3: Schematic showing the spectrum of lake hydrology from open basin lakes to closed basin lakes. From left to right, the proportion of loss via evaporation and outflow increases and decreases, respectively. X_E is the volumetric proportion of evaporation (E) over inputs (I), see Equation 9 and associated text for more information.

3.4.2 A system for interpreting lake carbonate isotope records

Lake carbonate $\delta^{18}O$ records have been used to build hydroclimate records for many decades. However, the process of translating carbonate proxy data into information about past environmental conditions is rarely straightforward because carbonate $\delta^{18}O$ values can be influenced by precipitation dynamics, moisture source variation, lake water evaporation, and mineralization temperatures (Figure 3.4) (Leng and Marshall, 2004; Horton et al., 2016; Gibson et al., 2016). In this study, we explicitly account for lake temperature and evaporation using a multi-proxy isotope approach (i.e., Δ_{47}, $\Delta'^{17}O$; see Figure 3.4). This coupled hydrologic and isotope mass balance approach allows regional rainfall processes to be decoupled from local water balance (i.e., *P–E*) and temperature.

Figure 3.4a illustrates the two primary controls on the isotopic composition of lake waters: the isotopic composition of water entering the lake ($\delta^{18}O_I$) and evaporation (Leng and Marshall, 2004; Horton et al., 2016; Gibson et al., 2016). The relationship of these two variables to lake water $\delta^{18}O$ ($\delta^{18}O_{lw}$) values is shown by Equation 10 ($\delta^{18}O_{lw} = {}^{18}R_{lw}/{}^{18}R_{SMOW} - 1$). Logically, it makes sense that $\delta^{18}O_I$ values strongly influence $\delta^{18}O_{lw}$ values and that changing $\delta^{18}O_I$ values will translate to a corresponding change in $\delta^{18}O_{lw}$ values (Figure 3.4b). Principally, $\delta^{18}O_I$ reflects water cycle processes on a regional scale and is strongly related to upwind processes including Rayleigh

distillation or conditions at the moisture source (Dansgaard, 1964; Gat, 1996). Unlike $\delta^{18}O$, Rayleigh distillation has little effect on $\Delta'^{17}O$ values of precipitation (Figure 3.4b) (Aron et al., 2021a).

Lake waters can also experience evaporation, which selectively removes light isotopes into the unsaturated atmosphere while heavy isotopes become concentrated in the remaining lake water (Figure 3.4c). As a result, evaporated $\delta^{18}O_{lw}$ values are higher compared to $\delta^{18}O_I$ values (Figure 3.4c) (Leng and Marshall, 2004; Horton et al., 2016; Gibson et al., 2016). Lake water $\Delta'^{17}O$ values become lower compared to input water as the slope of evaporation in $\delta'^{18}O$–$\delta'^{17}O$ space is lower than λ_{ref} (e.g., Gázquez et al., 2018; Passey and Ji, 2019). In hydrologically open lakes where X_E approaches 0 and evaporation is not a significant water balance component, $\delta^{18}O_{lw}$ values will be close to $\delta^{18}O_I$. As the role of evaporation increases (i.e., as X_E increases), so too will the isotopic offset of $\delta^{18}O_{lw}$ and $\delta^{18}O_I$ (Figure 3.4c). Similarly, $\Delta'^{17}O_{lw}$ is closest to $\Delta'^{17}O_I$ when X_E approaches 0 and is much lower than $\Delta'^{17}O_I$ when $X_E >> 0$ (Figure 3.4c) (Gázquez et al., 2018; Katz et al., 2023).

For ancient lake systems, we often lack information about $\delta^{18}O_I$ and/or evaporation, so it is difficult to understand how each component individually contributes to $\delta^{18}O_{lw}$ values (Leng and Marshall, 2004). However, because $\Delta'^{17}O$ is highly sensitive to evaporation but is relatively insensitive to Rayleigh processes (Figure 3.4b,c), it is an ideal tool to constrain lake hydrologic balance and has been successfully applied to a number of modern and paleo lake systems (Herwartz et al., 2017; Gázquez et al., 2018; Passey and Ji, 2019; Ibarra et al., 2021; Voigt et al., 2021; Katz et al., 2023).

Another challenge in studying ancient lake systems is that ancient lake water cannot be measured directly, therefore, we must instead rely on isotope records from authigenic minerals that track changes in $\delta^{18}O_{lw}$ values (Figure 3.4). Carbonate $\delta^{18}O$ ($\delta^{18}O_C$) values are related to $\delta^{18}O_{lw}$ values by the temperature dependent fractionation factor ($^{18}\alpha_{calcite\text{-}water}$) (Kim and O'Neil, 1997) which can be determined from carbonate clumped isotope formation temperatures ($T\Delta_{47}$) (Figure 3.4d). Together, the combination of $\delta^{18}O_C$ and $T\Delta_{47}$ can be used to constrain $\delta^{18}O_{lw}$ values and to develop surface temperature records from lacustrine sediments (Huntington et al., 2010, 2015; Hren and Sheldon, 2012; Horton et al., 2016; Passey and Ji, 2019; Santi et al., 2020; Fetrow et al., 2022; Katz et al., 2023).

When used in tandem, $\delta^{18}O$, $T\Delta_{47}$, and $\Delta'^{17}O$ can be used to develop more robust hydroclimate records that improve upon interpretations based only on carbonate $\delta^{18}O$ values (Figure 3.4) (Passey and Ji, 2019; Katz et al., 2023). In Sections 3.8.1 and 3.8.2, we apply new $T\Delta_{47}$ and $\Delta'^{17}O$ data to this framework to evaluate the temperature and hydrologic influences on carbonate $\delta^{18}O$ records from Lakes Junín, Pumacocha, and Mehcocha.

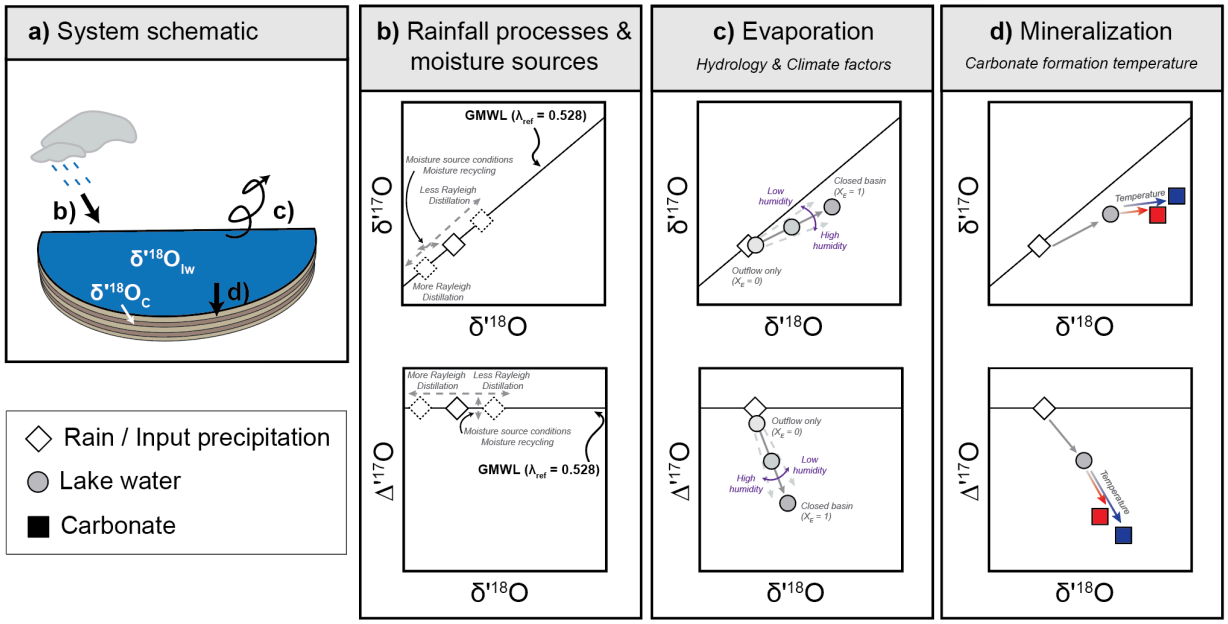

Figure 3.4: (a) Schematic representing three important processes that influence the isotopic compositions of lake water ($\delta'^{18}O_{lw}$) and carbonates ($\delta'^{18}O_C$): (b) rainfall processes and moisture source conditions, (c) evaporation, and (d) mineralization. Note: not to scale.

3.5 Study area

3.5.1 Regional climate and geologic overview

The Lake Junín region in the Andean Cordillera sits at an elevation of >4,000 meters above sea level (masl) (Figure 3.2). Mean annual air temperature in the region is 6.5 °C and diurnal temperature swings (ca. 0–15 °C) greatly exceed variations in average monthly temperatures. Modern precipitation is highly seasonal; ~70% of annual precipitation (900–1,000 mm) occurs in October–April during the strengthened phase of the SASM (Garreaud et al., 2009; Marengo et al., 2012; SENAMHI, 2023). Annual potential evapotranspiration is 525–550 mm/year and relative humidity is consistently 70–90% (SENAMHI, 2023; Katz et al., 2023). The three study lakes are

all located in the upper headwaters of the Amazon Basin. Outflow from Lakes Junín and Mehcocha enter Rio Mantaro, and Pumacocha feeds Rio Huachón (Figure 3.2); eventually, these rivers converge in the Andean foothills and feed the Amazon River in northeast Peru.

Bedrock in the Lake Junín region is primarily Triassic–Jurassic aged marine carbonate from the Pucará Group with some exposure of Permian sandstones (Mitu Group) and Carboniferous carbonates and sandstones (Tarma and Ambo Groups; Ministerio de Energia y Minas, 1979b, 1979a, 1979c; Cobbing et al., 1996). High bicarbonate concentrations in surface waters results in carbonate production in many lakes throughout the region (Flusche et al., 2005).

3.5.2 Lake Junín

Lake Junín is located north of Junín, Peru on a high elevation plateau (4,080 masl, Figure 3.2a). Alluvial fans and glacial outwash form the northern boundary of the basin and prominent Pleistocene glacial moraines are present east of the lake (Hansen et al., 1994; Seltzer et al., 2000; Smith et al., 2005; Woods et al., 2020; Rodbell et al., 2022).

Lake Junín covers a large, ~300 km^2, surface area that represents approximately one third of the total catchment area (Seltzer et al., 2000; Woods et al., 2020). Maximum water depth is 8-12 m, such that the lake surface area to volume ratio is high (~125:1). Accordingly, the lake is highly sensitive to both evaporative water losses and outflow via the Rio Mantaro (Figure 3.2–3.3,3.4c). Precipitation, runoff from the catchment, and groundwater springs along the southwest shore constitute the major volumetric inputs to Lake Junín (Flusche et al., 2005). Directly downstream of Lake Junín, a hydroelectric dam has modified natural lake hydrology since the 1930s, however, we expect that under modern precipitation and climate conditions, lake hydrology would remain open throughout the year, though could become seasonally closed basin during the winter dry season. Despite these fluctuations, the lake can be considered in steady-state on interannual timescales.

The sediment core used in this study was collected from Lake Junín in 1996 at the western margin of the lake (Figure 3.2a). The top 11 meters of the core are composed of laminated marl which was analyzed for carbonate $\delta^{18}O$ by Seltzer et al., (2000) and reflects continuous sedimentation over the last 21,200 years, based on radiocarbon dating.

3.5.3 Lake Pumacocha

Pumacocha is located ~40 km northeast of Junín in the eastern Andean Cordillera. The small, deep lake (Figure 3.2a,b; surface area: 0.1 km^2; depth: 23.5 m; elevation: 4,300 masl) fills a glacial cirque. Pumacocha's lake surface area to volume ratio, ~42:1, is much lower than at Lake Junín. The major water balance components of the lake are precipitation, catchment runoff, and outflow. Today the ratio of evaporation to inputs in this system is very low (Bird et al., 2011b, 2011a), such that X_E is close to 0 and the lake is hydrologically open basin (Figure 3.3, see Section 3.4.1, 3.5.5).

Sediment cores from Pumacocha were collected between 2005–2008 and analyzed for carbonate $\delta^{18}O$ values by Bird et al. (2011b, 2011a). Core age models date the base of the core to ~10,000 years BP and were determined by a combination of ^{137}Cs, varve counting, and radiocarbon dates (Bird et al., 2011b, 2011a). Authigenic carbonate and bands of organic material are present throughout the core and glacial clays are present at the base, representing the formation of the lake post-Holocene deglaciation (Bird et al., 2011a).

3.5.4 Lake Mehcocha

The formal name for this lake is Catucana, but we use an informal name, "Mehcocha," here for consistency with prior studies (e.g., Katz et al., 2023). Mehcocha is located ~12 km southwest of Junín in the western Andean Cordillera (elevation: 4,355 masl). The catchment is composed of two sub-basins which are connected by a narrow straight (Figure 3.2c). The total surface area for both sub-basins is 0.2 km^2 and maximum water depths are 25.5 m and 12.4 m in the upper and lower sub-basins, respectively. Similar to Pumacocha, Mehcocha has a low surface area to volume ratio at ~50:1. The primary water balance components are precipitation, catchment runoff, and outflow; evaporation is low and the lake is an open basin with X_E near 0 (Figure 3.3, see Section 3.4.1). Construction of a road during historical times modified the natural lake outflow, but we assume this had negligible impacts to lake hydrology.

In 2015, stratigraphically overlapping sediment cores were collected from two locations in the lower sub-basin using a lance-driven piston corer deployed from a floating platform on the lake surface. We focus our analyses on core C-15, which was collected from a water depth of 12.4 m, spans 10.1 m of stratigraphy, and terminates on a gravelly-clay glacial till unit that confirms complete recovery of the postglacial sequence. Holocene sediments at this site are predominantly low density (~0.2 g/cm^3), organic-rich (organic matter weight percent values from ~20% to ~60%),

dark brown to brown, banded muds with intervening units of coarse carbonate sand and shell fragments.

3.5.5 Prior hydroclimate interpretations based on carbonate $\delta^{18}O$

The three lakes in this study represent a range of open basin hydrologic configurations, as defined in Section 3.4.1, from outflow-only at Pumacocha and Mehcocha to outflow-dominated at Lake Junín (Figure 3.3). Consistent with the framework outlined in Section 3.4.2, the modern lake water isotope composition reflects both the isotopic composition of input waters and hydrology (i.e., X_E; Figure 3.4). Specifically, input and lake water isotope values are most similar under low evaporation conditions and become dissimilar as evaporation leads to enrichment of heavy isotopes in lake water. Modern lake waters at Pumacocha and Mehcocha have $\delta^{18}O$ and $\Delta'^{17}O$ values identical to mean annual precipitation, consistent with outflow-only lakes as shown in Figure 3.4b,c (Bird et al., 2011b, 2011a; Katz et al., 2023). Lake Junín lake water $\delta^{18}O$ and $\Delta'^{17}O$ values are higher and lower, respectively, than mean annual precipitation due to evaporation (Figure 3.4c) (Flusche et al., 2005; Katz et al., 2023).

Previous workers have leveraged these differences in modern hydrology when interpreting the Holocene carbonate $\delta^{18}O$ records from these lakes. At Pumacocha, carbonate $\delta^{18}O$ values decreased steadily from ca -10 ‰ in the early Holocene to ca -15 ‰ (VPDB) in the late Holocene ($\delta^{18}O_{late}$–$\delta^{18}O_{early}$ = -5 ‰; Figure 3.5b) (Bird et al., 2011b, 2011a). This trend is interpreted as a decrease in $\delta^{18}O_I$ values by the same magnitude caused by an insolation-driven increase in SASM strength over the last 10,000 years (Bird et al., 2011a). To a first order, this interpretation is consistent with the steady decrease in $\delta^{18}O$ values observed both at the nearby Huagapo Cave (from -14 to -11 ‰ VPDB; $\delta^{18}O_{late}$–$\delta^{18}O_{early}$ = -3 ‰) (Kanner et al., 2013) and Huascaran ice core (from -19 to -16 ‰, VSMOW; $\delta^{18}O_{late}$–$\delta^{18}O_{early}$ = -3 ‰) (Thompson et al., 1995), which reflects increasing SASM convective activity (Figure 3.1). Lake hydrology and temperature are not thought to influence the carbonate $\delta^{18}O$ trend (Figure 3.4), and it is assumed Pumacocha remained open basin through the Holocene (Figure 3.3,3.4). However, these assumptions have not been tested by isotopic approaches that can independently resolve changes in lake hydrology, temperature, and input $\delta^{18}O$ values (i.e., Section 3.4.2, Figure 3.4).

Unlike Pumacocha, the influence of evaporation on both modern lake water balance and isotopic composition is well-documented at Lake Junín (Section 3.4; Figure 3.3,3.4) (Flusche et al., 2005; Katz et al., 2023). Compared to the Holocene records from Pumacocha, the Lake Junín carbonate $\delta^{18}O$ record is higher by +7 ‰ in the early Holocene before steadily decreasing to +2 ‰ higher in the late Holocene (Figure 3.5b) (Seltzer et al., 2000; Bird et al., 2011b, 2011a). In previous studies, the offset was entirely attributed to a decreasing proportion of evaporative loss from the lake and increasingly positive water balance (i.e., *P–E*) associated with increasing SASM strength over the Holocene (Figure 3.3,3.4) (Seltzer et al., 2000; Bird et al., 2011b, 2011a; Kanner et al., 2013). Accordingly, this interpretation implies local water balance is in-sync with global climate drivers (i.e., insolation). However, these interpretations have relied on the assumption that the $\delta^{18}O$ offset between Lake Junín and other records only reflects changes in local *P–E* and they hypothesize that other factors that can affect carbonate or ice $\delta^{18}O$ values, including temperature or local basin dynamics, were minimal relative to the effects of evaporation (Figure 3.4) (Kanner et al., 2013; Bird et al. 2011; Seltzer et al., 2000), which is sometimes at odds with the original interpretation of the records (Thompson et al., 1995).

3.6 Laboratory methods and data processing

3.6.1 Radiocarbon dating and age models

We present an updated Bayesian age model for the Lake Junín core (Figure S3.1–S3.2; Table S3.1–S3.3) based on a combination of the radiocarbon dates presented by Seltzer et al. (2000) and 11 new radiocarbon dates. We also present radiometric dates (Table S3.4) and a Bayesian age model (Figure S3.3–S3.4; Table S3.5–S3.6) for the Mehcocha sediment core. Additional methodological information related to radiocarbon dating and age models is provided in Section 3.10.1.

3.6.2 Analytical preparation for Δ_{47} and $\Delta^{17}O$ analysis

We sampled the lake cores from Lakes Junín, Pumacocha, and Mehcocha at approximately 1,000–1,200 year intervals from the start of the Holocene (11,700 years BP) to the present (Table 3.1). Two additional samples were selected from Lake Junín during the latest Pleistocene (17,210 and 12,870 years BP; Table 3.1). To the greatest degree possible, the Holocene samples were

collected from contemporaneous time intervals to facilitate direct comparison among the three lakes.

Bulk sediment samples were treated overnight with 7% hydrogen peroxide to remove organic matter via oxidation. Sediment was then rinsed through a 63 μm mesh, retaining the <63 μm size fraction for isotopic analysis. Samples were dried at 50 °C for several days. A mortar and pestle were used to homogenize sediment prior to analysis. The processed material is light colored (ranging from white to light grey) and void of macroscopic shell or plant materials. In some samples, the process yielded insufficient carbonate material for analysis.

3.6.3 Isotope analysis

3.6.3.1 Carbonate clumped isotopes

Carbonate clumped isotope measurements were made at the University of Michigan (UM) Isotopologue Paleosciences Lab (IPL). We follow the approach described by Passey et al. (2010). To summarize this procedure, carbonate first is digested in a common acid bath containing >100 wt% phosphoric acid at 90 °C, producing CO_2 and H_2O. The latter is trapped cryogenically (via a water trap held at -78 °C) and after passing through this first trap, CO_2 is collected in a second trap held at liquid nitrogen temperature (-180 °C). After isolating the purified CO_2, the sample is thawed and passed through a gas chromatograph held at ca. -20 °C (via a He carrier gas) to further purify the sample before recollection on a final trap held at liquid nitrogen temperature. The high purity CO_2 gas is then introduced to a Nu Perspectives isotope ratio mass spectrometer for analysis in dual inlet mode. Sample gas was measured 40 times (50 second integration; *m/z* 44–49) and laboratory working gas was measured before and after each sample measurement. From these measurements, we calculate $\delta^{13}C$, $\delta^{18}O$ and Δ_{47} values versus laboratory working gas using Brand/IUPAC parameters (Petersen et al., 2019).

Data corrections are performed using a mixed correction of both equilibrium CO_2 gases and carbonate standards run within the same analytical session as samples. Equilibrium gas standards of two distinct $\delta^{13}C$ and $\delta^{18}O$ compositions were introduced to the same sample prep line as used for carbonate samples. Low temperature equilibrated gases were thermally equilibrated in a 30 °C water bath. High temperature equilibrated (i.e., “heated”) gases were generated “on-line” from the same equilibrated gas reservoirs, but with the gases being passed

through a furnace held at 1000 °C immediately prior to analysis (upstream of the gas chromatograph cleanup step) to produce a stochastic distribution of ^{13}C-^{18}O bonds. We also analyzed carbonate ETH (ETH1-4) and IAEA (IAEA-C1 and IAEA-603) standards using the same in-line sample preparatory line and following the same procedure as for samples. Carbonate $\delta^{13}C$ and $\delta^{18}O$ values were standardized to the VPDB reference frame using known values of ETH1-4 (Bernasconi et al., 2018) and IAEA reference materials (assuming IAEA-C1 is isotopically identical to IAEA-603) (Assonov et al., 2020). Measured Δ_{47} data were projected to absolute values ($\Delta_{47\ ICDES90}$) following the approach of Daëron et al. (2016) using measurements of equilibrium gases and ETH1-3 carbonate standards. Finally, we plotted residual Δ_{47} values of ETH4, IAEA-C1, and IAEA-603 from accepted values to assess and correct for in-session offsets and drift.

3.6.3.2 Triple oxygen isotopes

Triple oxygen isotope measurements were made at the UM IPL. We use a three-step process to convert carbonate to O_2 as outlined by Passey et al. (2014) and Ellis and Passey (2023). First, carbonate is digested in H_3PO_4 in a common acid bath at 90 °C and resultant CO_2 is purified using the same approach as described above for clumped isotopes (e.g., digestion biproducts are removed cryogenically and by passage through a GC column) (Passey et al., 2010). Next, CO_2 undergoes methanation to produce H_2O. This is accomplished by reacting CO_2 with excess H_2 over an Fe catalyst held at 560 °C. Lastly, the H_2O is transferred via He carrier gas through a cobalt trifluoride reactor (CoF_3, 360 °C). The O_2 analyte produced by fluorination is purified via gas chromatography and cryogenic separation prior to introduction to a Nu Perspective isotope ratio mass spectrometer. Sample analysis consists of 40 measurements of sample and reference gas, with each gas measurement consisting of a 50 second integration over an *m/z* range of 32–36.

Samples were analyzed concurrently with water standards VSMOW2 and SLAP2, and carbonate standards IAEA-C1 and an in-house groundwater carbonate standard (102-GC-AZ01). Data normalization is carried out over the lifetime of each cobalt trifluoride reactor (replaced every ~200 analyses) with VSMOW2 and SLAP2 typically run in the beginning, middle, and end of each reactor. Sample data are first normalized to the VSMOW-SLAP scale as outlined by Schoenemann et al. (2013; $\delta^{18}O_{VSMOW}$= 0.000 ‰; $\delta^{18}O_{SLAP2}$= -55.500 ‰; $\Delta'^{17}O_{VSMOW}$ and $\Delta'^{17}O_{SLAP2}$ = 0 per meg) and a linear drift correction is applied across the reactor. This yields normalized values for an O_2 analyte. To determine $\Delta'^{17}O$ values of carbonate, we assign $\Delta'^{17}O$ values of IAEA-C1 to the

values reported by Wostbrock et al. (2020) (-100 per meg) following methods outlined in Huth et al. (2022).

3.7 Results

Mehcocha carbonate $\delta^{13}C$ and $\delta^{18}O$ values range from -3.4 to 0.6 ‰ and -14.1 to -9.8 ‰, respectively (VPDB) (Table S3.6, Figure 3.5, S3.3–S3.4).

Carbonate clumped isotope data, $\delta^{13}C$, $\delta^{18}O$, Δ_{47}, are reported in Tables 3.1 and S3.7. Carbonate $\delta^{18}O$ data are also shown in Figure 3.5b. Clumped isotope formation temperatures ($T\Delta_{47}$ values) were calculated from Δ_{47} values using Equation 1 of Anderson et al. (2021) and range from 3.7 to 14.9 °C across all lakes (Table 3.1, S3.7; Figure 3.5c).

Carbonate triple oxygen isotope data, $\delta'^{17}O$, $\delta'^{18}O$, $\Delta'^{17}O$, are reported in Tables 3.1 and S3.8. Carbonate $\delta'^{18}O$ and $\Delta'^{17}O$ values at Pumacocha and Mehcocha range from 16.5 to 19.7 ‰ and -88 to -63 per meg (VSMOW-SLAP) and at Lake Junín range from 19.0 to 28.2 ‰ and -82 to -107 per meg (VSMOW-SLAP), respectively.

We also calculated reconstructed lake water $\delta'^{18}O$ and $\Delta'^{17}O$ ($\delta'^{18}O_{rlw}$; $\Delta'^{17}O_{rlw}$) values (Table 3.1, S3.7). $\delta'^{18}O_{rlw}$ values were calculated from carbonate $\delta^{18}O$ values using $^{18}\alpha_{calcite\text{-}water}$ (Kim and O'Neil, 1997) and temperatures derived from Δ_{47} values. $\delta'^{18}O_{rlw}$ values at Pumacocha and Mehcocha range from -14.9 to -11.7 ‰ and at Lake Junín range from -12.1 to -3.9 ‰ (VSMOW; Figure 3.5d). $\Delta'^{17}O_{rlw}$ values were calculated using a $\lambda_{calcite\text{-}water}$ value of 0.5250 (Huth et al., 2022). $\Delta'^{17}O_{rlw}$ values at Pumacocha and Mehcocha are 6 to 30 per meg and at Lake Junín are -13 to 11 per meg (VSMOW-SLAP; Table 3.1; Figure 3.5e).

Propagated uncertainty was calculated for both $\delta'^{18}O_{rlw}$ and $\Delta'^{17}O_{rlw}$ values using a Monte Carlo resampling approach. For $\delta'^{18}O_{rlw}$ values, the average and 1 σ standard error of $\delta^{18}O_C$ and $T\Delta_{47}$ values (calculated from replicate analyses) were used to resample 10,000 values for both populations; new $^{18}\alpha_{calcite\text{-}water}$ values were calculated from $T\Delta_{47}$ values and applied to $\delta^{18}O_C$ values to determine $\delta'^{18}O_{rlw}$ values. The 1 σ standard deviation of the resampled $\delta'^{18}O_{rlw}$ population is reported in Table 3.1. The propagated uncertainty for $\Delta'^{17}O_{rlw}$ was calculated similarly using the $\Delta'^{17}O_C$ and $\delta'^{18}O_C$ values from triple oxygen isotope analyses and $T\Delta_{47}$ values (Table 3.1; Figure 3.5E).

Table 3.1: Sample information and summarized carbonate isotope data from Lakes Junín, Pumacocha, and Mehcocha.

				Derived from clumped isotopes										Derived from triple oxygen isotopes							
Sample ID	**Comp Depth (cm)**	**Age (yr BP)**	**No. rep. Δ_{47} / $\Delta'^{17}O$ anal.**	**$\delta^{13}C_C$ (‰, VPDB)**	**$\delta^{13}C_C$ 1σ SD (‰)**	**$\delta^{18}O_C$ (‰, VPDB)**	**$\delta^{18}O_C$ 1σ SD (‰)**	**Δ_{47} ICDES90 (‰)**	**Δ_{47} ICDES90 1σ SD (‰)**	**$T\Delta_{47}$ (°C) †**	**$T\Delta_{47}$ 1σ SD (°C)**	**$\delta'^{18}O_{rlw}$ ‡ (‰, VSMOW)**	**$\delta'^{18}O_{rlw}$ # 1σ SD (‰)**	**$\delta'^{17}O_C$ (‰, VSMOW -SLAP)**	**$\delta'^{17}O_C$ 1σ SD (‰)**	**$\delta'^{18}O_C$ (‰, VSMOW -SLAP)**	**$\delta'^{18}O_C$ 1σ SD (‰)**	**$\Delta'^{17}O_C$ (per meg; VSMOW -SLAP)**	**$\Delta'^{17}O_C$ 1σ SD (per meg)**	**$\Delta'^{17}O_{rlw}$ & (per meg; VSMOW -SLAP)**	**$\Delta'^{17}O_{rlw}$ * 1σ SD (per meg)**
Junín (11.05 °S, 76.12 °W, 4080 masl)																					
Junín D4 10.0-15.0 cm	110	1134	3 / 2	4.760	0.054	-10.812	0.026	0.637	0.008	11.4	2.4	-11.361	0.307	9.943	0.504	18.986	0.962	-82	4	11	3
Junín D5 30.0-35.0 cm	230	2299	4 / 2	5.317	0.111	-9.343	0.049	0.651	0.016	7.4	4.4	-10.790	0.505	10.862	0.070	20.749	0.132	-93	0	2	2
Junín D6 10.0-15.0 cm	310	3322	4 / 2	7.022	0.100	-7.362	0.050	0.657	0.016	5.6	4.6	-9.201	0.532	12.526	0.073	23.913	0.121	-100	9	-3	7
Junín D7 8.0-13.0 cm	408	4536	3 / 2	11.023	0.064	-5.476	0.053	0.638	0.018	11.1	5.1	-6.050	0.650	13.427	0.145	25.633	0.263	-107	6	-14	5
Junín D8 30.0-35.0 cm	530	5923	4 / 2	11.398	0.137	-5.963	0.059	0.650	0.021	7.8	6.0	-7.303	0.686	13.272	0.013	25.333	0.029	-104	2	-9	3
Junín D9 30.0-35.0 cm	630	7241	4 / 2	13.212	0.062	-4.793	0.047	0.649	0.015	7.9	4.3	-6.098	0.491	13.750	0.194	26.245	0.379	-108	5	-12	4
Junín D10 7.0-12.0 cm	724	8762	3 / --	13.710	0.115	-4.243	0.028	0.643	0.016	9.6	4.5	-5.159	0.583	--	--	--	--	--	--	--	--
Junín D10 78.0-83.0 cm	795	9912	4 / 2	14.149	0.103	-3.597	0.044	0.634	0.017	12.4	5.1	-3.886	0.559	13.995	0.592	26.704	1.117	-105	2	-13	2
Junín D11 10.0-15.0 cm	810	10276	4 / 1	15.510	0.171	-2.906	0.055	0.646	0.023	9.0	6.6	-3.959	0.734	14.792	--	28.211	--	-104	--	-9	--
Junín D11 88.0-93.0 cm	888	12873	3 / 2	11.912	0.039	-5.253	0.092	0.664	0.009	3.7	2.3	-7.536	0.313	13.020	0.314	24.852	0.598	-102	2	-4	2
Junín D12 91.0-96.0 cm	991	17214	3 / 2	3.792	0.017	-10.350	0.042	0.655	0.010	6.1	2.7	-12.104	0.359	11.025	0.052	21.054	0.104	-92	2	5	2
Pumacocha (10.699 °S, 76.061 °W, 4300 masl)																					
Pumacocha A-05 D2 38.75 cm	124.25	1243	3 / 4	-3.186	0.009	-13.864	0.107	0.636	0.010	11.8	2.9	-14.365	0.370	8.643	0.150	16.487	0.288	-63	5	30	3
Pumacocha A-05 D3 49.65 cm	195.85	2495	2 / 2	-3.253	0.000	-13.362	0.148	0.640	0.007	10.4	2.0	-14.173	0.327	9.120	0.876	17.400	1.658	-67	1	26	1
Pumacocha A-05 D5 26.25 cm	283.35	3522	3 / 2	-3.220	0.026	-13.110	0.108	0.649	0.009	7.9	2.6	-14.476	0.343	9.328	0.192	17.791	0.353	-66	6	30	4
Pumacocha A-05 D6 11 cm	340.70	4528	3 / 3	-3.119	0.015	-13.017	0.133	0.633	0.006	12.6	1.8	-13.338	0.241	9.092	0.579	17.361	1.099	-75	11	17	6
Pumacocha E-06 D3 38.75 cm	398.45	5892	4 / 3	-2.600	0.059	-12.502	0.076	0.638	0.021	11.1	6.2	-13.145	0.675	9.719	0.307	18.551	0.588	-75	4	18	3
Pumacocha E-06 D3 76.75 cm	436.45	7133	3 / 4	-2.221	0.024	-11.903	0.054	0.625	0.007	14.9	2.0	-11.707	0.250	9.825	0.238	18.768	0.452	-84	8	6	4
Pumacocha E-06 D4 59.25 cm	515.55	9363	4 / 3	-2.232	0.050	-10.682	0.064	0.648	0.016	8.4	4.6	-11.919	0.521	10.306	0.166	19.658	0.309	-73	4	21	3

Table 3.1, continued.

				Derived from clumped isotopes										Derived from triple oxygen isotopes							
Sample ID	**Comp Depth (cm)**	**Age (yr BP)**	**No. rep. Δ_{47} / $\Delta'^{17}O$ anal.**	**$\delta^{13}C_C$ (‰, VPDB)**	**$\delta^{13}C_C$ 1σ SD (‰)**	**$\delta^{18}O_C$ (‰, VPDB)**	**$\delta^{18}O_C$ 1σ SD (‰)**	**Δ_{47} ICDES90 (‰)**	**Δ_{47} ICDES90 1σ SD (‰)**	**$T\Delta_{47}$ (°C) †**	**$T\Delta_{47}$ 1σ SD (°C)**	**$\delta'^{18}O_{rlw}$ ‡ (‰, VSMOW)**	**$\delta'^{18}O_{rlw}$ # 1σ SD (‰)**	**$\delta'^{17}O_C$ (‰, VSMOW -SLAP)**	**$\delta'^{17}O_C$ 1σ SD (‰)**	**$\delta'^{18}O_C$ (‰, VSMOW -SLAP)**	**$\delta'^{18}O_C$ 1σ SD (‰)**	**$\Delta'^{17}O_C$ (per meg; VSMOW -SLAP)**	**$\Delta'^{17}O_C$ 1σ SD (per meg)**	**$\Delta'^{17}O_{rlw}$ & (per meg; VSMOW -SLAP)**	**$\Delta'^{17}O_{rlw}$ * 1σ SD (per meg)**
Mehcocha (11.255 °S, 76.035 °W, 4355 masl)																					
Mehcocha C-15 D2 15 cm	115	1238	3 / 2	-2.728	0.232	-13.756	0.028	0.641	0.013	10.2	3.8	-14.624	0.484	8.662	0.098	16.543	0.196	-73	6	21	4
Mehcocha C-15 D4 33 cm	333	3524	3 / 2	-2.085	0.051	-13.732	0.074	0.646	0.009	8.9	2.6	-14.897	0.337	8.722	0.060	16.653	0.105	-70	4	24	3
Mehcocha C-15 D6 23 cm	523	5884	3 / 2	-1.619	0.202	-12.484	0.032	0.644	0.017	9.3	4.8	-13.532	0.616	9.307	0.048	17.781	0.091	-81	1	13	2
Mehcocha C-15 D7 55 cm	655	7101	-- / 1	--	--	--	--	--	--	--	--	--	--	8.943	--	17.103	--	-88	--	7 §	--
Mehcocha C-15 D8 35 cm	735	9350	-- / 2	--	--	--	--	--	--	--	--	--	--	9.724	0.126	18.560	0.229	-76	5	18 §	--

† Calculated using Anderson et al., 2021, Equation 1.

‡ Calculated from $\delta^{18}O_C$ and $^{18}\alpha_{calcite\text{-}water}$ derived from $T\Delta_{47}$ from Kim and O'Neil, 1997.

Propagated uncertainty based on clumped isotope $\delta^{18}O_C$ and $T\Delta_{47}$ values.

& Calculated from $\delta^{18}O_C$ and $\delta^{17}O_C$ values derived from triple oxygen isotope analysis and using $\lambda_{calcite\text{-}water} = 0.5250$ (Huth et al., 2022).

§ Calculated assuming a formation temperature of 9 °C.

* Propagated uncertainty based on $\Delta'^{17}O_C$ and $T\Delta_{47}$ values.

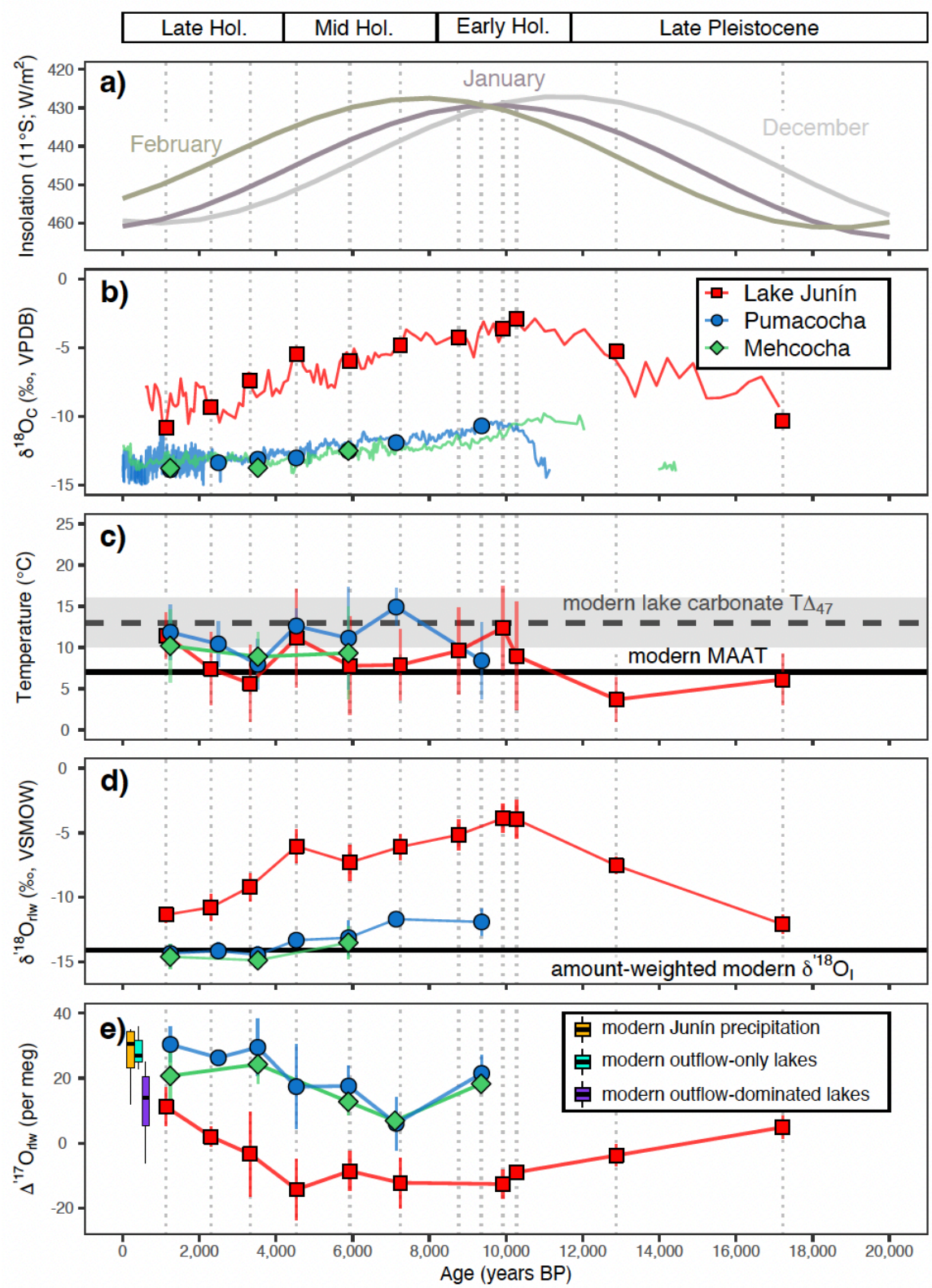

Figure 3.5: Clumped and triple oxygen isotope results.As in Figure 3.1a, Summer (Dec–Feb) insolation at 11 °S (Laskar et al., 2004; Crucifix, 2016), with y-axis scale reversed. (b) As in Figure 3.1b, carbonate $\delta^{18}O$ records from Lakes Junín (red; Seltzer et al., 2000), Pumacocha (blue; Bird et al., 2011a,b), Mehcocha (green). Symbols represent carbonate $\delta^{18}O$ values derived from Δ_{47} analysis. (c) Reconstructed formation temperatures from lake carbonate Δ_{47}

values. Error bars represent 2σ SE of replicate analyses. Solid black and dashed grey horizontal lines, respectively, show mean annual air temperature (MAAT; 6.5 °C) and modern lake carbonate $T\Delta_{47}$ values for these lakes (13 ± 3 °C), for reference (Katz et al., 2023). (d) Reconstructed lake water $\delta'^{18}O$ ($\delta'^{18}O_{rlw}$) derived from carbonate clumped isotope $\delta^{18}O$ and $T\Delta_{47}$ values; error bars represent 2σ SD propagated uncertainty. Black horizontal line shows modern $\delta'^{18}O$ inputs ("amount-weighted modern $\delta'^{18}O_I$"; Katz et al., 2023) from local amount-weighted mean annual precipitation, for reference. (e) Reconstructed lake water $\Delta'^{17}O$ calculated from carbonate $\Delta'^{17}O$, $T\Delta_{47}$, and $\lambda_{calcite\text{-}water}$ = 0.5250, Huth et al. (2022); error bars represent 2σ SD propagated uncertainty. Box and whisker plots (in the style of Tukey) show the $\Delta'^{17}O$ range of modern precipitation (yellow), outflow-only lakes (teal; Pumacocha and Mehcocha), and outflow-dominated lakes (purple; Lake Junín) in the Lake Junín region (water data from Katz et al., 2023). Note, some samples were unable to be analyzed for both Δ_{47} and $\Delta'^{17}O$ due to limited material, such that more points are shown in panel (e) than in panels (b)–(d). In panels (a)–(e), dotted grey vertical lines align with sample dates to facilitate comparison between plots. Data from Table 3.1.

3.8 Discussion

3.8.1 Lake water temperatures and the influence on carbonate $\delta^{18}O$ values

The results of our clumped isotope analysis show that the reconstructed Holocene water temperature records are indistinguishable among the three lakes within analytical precision (Figure 3.5c). Water temperatures (10 ± 2 °C, n = 19) were stable over the Holocene and are similar to water temperatures derived from clumped isotopes of modern lacustrine carbonates from the same lakes (13 ± 3 °C; Figure 3.5c; Table 3.1) (Katz et al., 2023). Carbonate $T\Delta_{47}$ values from Lake Junín in the latest Pleistocene (17,210 and 12,870 years BP) are 5 ± 2 °C (n = 2), and suggest that water temperatures were cooler by ~5 °C (Figure 3.5c; Table 3.1). This may suggest that local air temperatures were lower during the latest Pleistocene or that cool glacial melt waters were entering the lake from the surrounding catchment.

The relatively constant $T\Delta_{47}$ values indicate that changes in Holocene water temperature is not the primary driver of the observed carbonate $\delta^{18}O$ trend at any of the lakes. Additionally, temperature changes are not responsible for the offsets observed among the different records (Figure 3.5b). $\delta^{18}O_{rlw}$ values for each of the three lakes thus show similar patterns to carbonate $\delta^{18}O$ values (Figure 3.5b,d). This suggests that, consistent with prior interpretations of these records (see Section 3.5.5), effects other than temperature, for example, changes in input rainfall $\delta^{18}O$ values (Figure 3.4b) and/or evaporation (Figure 3.4c), drive the decrease in carbonate $\delta^{18}O$ at all three lakes over the Holocene.

3.8.2 Hydrologic interpretations based on $\Delta'^{17}O$

Evaporation is one of several processes that influence the isotopic composition of lake waters (e.g., Leng and Marshall, 2004; Gibson et al., 2016) and can be used to infer local *P–E* conditions through its link to lake water balance (Eq. 9,10; Section 3.4.2; Figures 3.3,3.4). In this section, we use reconstructed lake water $\Delta'^{17}O$ ($\Delta'^{17}O_{rlw}$) values from Lakes Junín, Pumacocha, and Mehcocha to first establish the role of evaporation on the $\delta^{18}O_{rlw}$ records from these lakes following our interpretive framework described in Section 3.4.2. Then we use $\Delta'^{17}O_{rlw}$ values to model changes in lake water balance (i.e., X_E). Finally, we show that when the $\Delta'^{17}O$–derived water balance records from these lakes are considered in unison, they illuminate changes in local *P–E* during the Holocene.

3.8.2.1 Pumacocha and Mehcocha

Based on prior interpretation of the Pumacocha record and the similarity of the Mehcocha $\delta^{18}O$ record and basin characteristics (see Section 3.5.5) (Bird et al., 2011b, 2011a), we expect that both lakes maintained an open, outflow-only hydrology through the Holocene and that $\Delta'^{17}O_{rlw}$ values from these lakes will be similar to $\Delta'^{17}O$ values of modern day precipitation in the region (31 ± 5 per meg; Figure 3.4a,b) (Katz et al., 2023). $\Delta'^{17}O_{rlw}$ values at Pumacocha and Mehcocha are consistent with these expectations during the late Holocene, with average values of 29 (± 2 per meg; $n = 3$) and 24 per meg (± 3 per meg; $n = 2$), respectively (Figure 3.5e). These results suggest that both lakes did maintain open hydrologic conditions (X_E close to 0) and that $\delta^{18}O_{rlw}$ values reflect $\delta^{18}O_I$ values in the late Holocene (4,200 years BP to present).

However, throughout the early and mid-Holocene (11,700–4,200 years BP), $\Delta'^{17}O_{rlw}$ values were significantly lower at both Pumacocha (16 ± 6 per meg, $n = 4$) and Mehcocha (12 ± 6 per meg, $n = 3$) (Figure 3.5e, Table 3.1). These data suggest that both lakes maintained open hydrology, but experienced greater evaporation in the early and mid-Holocene than the late Holocene. Three lines of reasoning support this interpretation: First, the two lake records match each other exceptionally well and show simultaneous, identical changes in $\Delta'^{17}O_{rlw}$ values (Figure 3.5e). Given the hydrologic similarities of the two lakes today, it makes sense that water balance of these lakes would respond similarly to climatic pressures in the past, such as local *P–E* changes. Secondly, the lowest $\Delta'^{17}O$ values correspond with the highest $\delta'^{18}O$ values (Figure S3.6), which

is consistent with evaporative enrichment of waters (Figure 3.4b). Third, there is substantial evidence (isotopic and non-isotopic) that the central Andes was highly water-stressed in the early and mid-Holocene (discussed further in Section 3.8.3), and therefore it is unsurprising that lakes in this region would experience hydrologic change during this period. With respect to the $\delta^{18}O_{rlw}$ values at Pumacocha and Mehcocha throughout the early and mid-Holocene (Figure 3.5d), our $\Delta'^{17}O$ results suggest that $\delta^{18}O_{rlw}$ may be slightly higher than local $\delta^{18}O_I$ values at this time.

An alternative explanation for the low $\Delta'^{17}O_{rlw}$ values observed in the early and mid-Holocene is that $\Delta'^{17}O_I$ values were lower than the present (31 ± 5 per meg) (Katz et al., 2023). For global precipitation datasets today, there is a very small negative correlation between $\Delta'^{17}O$ and $\delta'^{18}O$ values (Terzer-Wassmuth et al., 2023); if such trends applied during the early to mid-Holocene, a 3‰ increase in $\delta'^{18}O_I$ values would correspond with $\Delta'^{17}O_I$ values <5 per meg lower. Other processes, such as sub-cloud evaporation or a change in the seasonality of precipitation could also result in slightly lower $\Delta'^{17}O_I$ values ($\leq$ 10 per meg lower) (Aron et al., 2023; Terzer-Wassmuth et al., 2023). However, this change in $\Delta'^{17}O_I$ is insufficient to explain the full magnitude of $\Delta'^{17}O_{rlw}$ change observed at Pumacocha and Mehcocha, so lake water evaporation must contribute to at least part of the $\Delta'^{17}O_{rlw}$ trend. For the remainder of our analysis, we assume that local $\Delta'^{17}O_I$ values remained at 31 per meg throughout the Holocene. However, changes in $\Delta'^{17}O_I$ must be considered and we address this in Section 3.8.2.3.

Together, these $\Delta'^{17}O$ data suggest that both Pumacocha and Mehcocha maintained open hydrologic conditions throughout the Holocene, consistent with previous interpretations. However, during the early to mid-Holocene, local *P–E* conditions were drier and waters from both lakes experienced greater evaporation, contrasting with how isotopic records from these lakes were previously interpreted (Bird et al., 2011b, 2011a).

3.8.2.2 Lake Junín

The influence of evaporation on Lake Junín's water budget is well-established, both in the present (e.g., Flusche et al., 2005; Katz et al., 2023) and throughout the Holocene (Figure 3.3; see Section 3.5.5) (Seltzer et al., 2000). Accordingly, we expect that Holocene $\Delta'^{17}O_{rlw}$ values will be lower than modern precipitation in the region (31 ± 5 per meg) (Katz et al., 2023) and will be the

lowest in the early Holocene (11,700 to 8,200 years BP) when SASM was weakest and carbonate $\delta^{18}O$ values are highest (Figure 3.5a,b).

Our results show that all $\Delta'^{17}O_{rlw}$ values from Lake Junín are lower than modern precipitation $\Delta'^{17}O$ values (Figure 3.5e). Compared to Pumacocha and Mehcocha, the Lake Junín $\Delta'^{17}O_{rlw}$ record follows the same trend with time, though the $\Delta'^{17}O_{rlw}$ values are lower and exhibit a larger amplitude of change at Lake Junín (Figure 3.5e). This suggests that evaporation has always been a significant water balance component at Lake Junín (i.e., in agreement with the original carbonate $\delta^{18}O$ interpretation by Seltzer et al. (2000)), and that Pumacocha and Mehcocha maintained less-evaporated states, even as all three lakes responded to the same climate pressures. This is consistent with the differences in basin configuration among the lakes, as Lake Junín is the largest and shallowest of the three lakes, therefore water balance/lake hydrology is most likely to vary significantly with local climate.

The highest $\Delta'^{17}O_{rlw}$ values at Lake Junín are observed at 1,130 years BP (11 per meg) and 17,210 years BP (5 per meg) while the lowest $\Delta'^{17}O_{rlw}$ values (-14 to -9 per meg) are observed from 10,280 to 4,540 years BP (Figure 3.5e, Table 3.1). Variation in $\Delta'^{17}O_{rlw}$ values track the $\delta^{18}O_{rlw}$ values closely (Figure 3.5d,e); the strong negative correlation between $\Delta'^{17}O_{rlw}$ and $\delta^{18}O_{rlw}$ values (Figure S3.6) suggests that evaporation is the primary driver of the low $\Delta'^{17}O_{rlw}$ values at Lake Junín (Figure 3.4c). These data indicate that following peak evaporative conditions through the early and mid-Holocene (11,700 to 4,200 years BP), water balance began to steadily increase during the late Holocene before reaching an evaporative minimum in the present (Figure 3.4,3.5e).

We can evaluate the influence of evaporation on $\delta^{18}O_{rlw}$ values by comparing them to reconstructed unevaporated $\delta^{18}O_I$ values that we calculate from $\Delta'^{17}O_{rlw}$ and $\delta^{18}O_{rlw}$ values, using the approach of Passey and Ji (2019) as also done by others (Ibarra et al., 2021; Kelson et al., 2022; Katz et al., 2023; see Section 3.10.2). This approach allows us to assess whether changes in the degree of lake water evaporation accompanied changes in $\delta^{18}O_I$ values (i.e., due to changes in the SASM). The large differences in $\delta^{18}O_{rlw,}$ compared to reconstructed $\delta^{18}O_I$ values, shows that most of the variation in $\delta^{18}O_{rlw}$ values (and by extension $\delta^{18}O_C$ values) is due to evaporation (Figure S3.7; Table S3.9). However, we note that evaporation does not explain all the variation in reconstructed $\delta^{18}O_I$ values; the reconstructed $\delta^{18}O_I$ values are highest in the early to mid-Holocene when summer insolation is low and they reach minima when summer insolation is high, suggesting

a connection to the SASM, consistent with interpretation of other $\delta^{18}O$ records from the region (e.g., Kanner et al., 2013). These data also indicate that the influence of evaporation on $\delta^{18}O_{rlw}$ values was greatest when SASM was weak (during the early to mid-Holocene), and vice versa, pointing to a probable connection between SASM and water balance, which was previously hypothesized (Seltzer et al., 2000), but couldn't be independently shown prior to this study. These results highlight the power of $\Delta'^{17}O$ for resolving evaporative histories in a way that cannot be accomplished by $\delta'^{18}O$ values alone.

3.8.2.3 Estimating lake water balance from $\Delta'^{17}O$ values and implications for P–E

The $\Delta'^{17}O_{rlw}$ results from Lakes Junín, Pumacocha, and Mehcocha record variable lake water evaporation over the Holocene that accompanied changes in the hydrology (X_E) of each lake. To investigate the potential relationship between hydrologic change and local *P–E*, we use a deterministic approach to model the relationship between X_E and $\Delta'^{17}O_{rlw}$ values using Equation 10 (e.g. Benson and White, 1994; Passey and Ji, 2019) and the parameters listed in Table 3.2.

In Figure 3.6, we depict the modeled solution space under a normalized relative humidity (h) range of 0.1–0.9. We express $\Delta'^{17}O$ as the difference between lake water and input $\Delta'^{17}O$ values (i.e., $\Delta'^{17}O_{rlw} - \Delta'^{17}O_I$) and assume $\Delta'^{17}O_I$ is 31 per meg, consistent with modern precipitation in this region. Due to the multivariate nature of Equation 10, the modeled results create a wedge-like structure where $\Delta'^{17}O_{rlw}$ is closely related to both X_E and h (Figure 3.6) (e.g., Gázquez et al., 2018; Passey and Ji, 2019; Katz et al., 2023). We note that while altering the exact parameter values used in the model would induce some minor changes in the solution space, the overall trends between h, X_E, and $\Delta'^{17}O$ are conserved and this does not have a significant effect on our results. We provide code in the Supplemental Materials so that users can tailor model input values to match other study locations.

We use this model to estimate water balance during two intervals: the late Holocene and the early through mid-Holocene (Figure 3.6). Late Holocene average $\Delta'^{17}O_{rlw}$ values are calculated for Pumacocha and Mehcocha over the last 4,200 years when $\Delta'^{17}O_{rlw}$ values were relatively high and stable, and evaporation was at a minimum. For Lake Junín, $\Delta'^{17}O_{rlw}$ values are more variable during the late Holocene, so we only averaged $\Delta'^{17}O_{rlw}$ values over the last 2,500 years (e.g. the youngest two samples analyzed) to assess X_E during a relative evaporative minimum. Early to mid-

Holocene $\Delta'^{17}O_{rlw}$ values are calculated as the average $\Delta'^{17}O_{rlw}$ from 4,200 to 11,700 years BP for each of the lakes when evaporation was at a maximum. Assuming that local humidity in the late Holocene was similar to present (0.7–0.83), we estimate X_E at Lake Junín was 0.4–0.7, reflecting an outflow or evaporation-dominated lake system, whereas both Pumacocha and Mehcocha functioned as outflow-only lakes, similar to today (Figure 3.3,3.6a). However, during the early and mid-Holocene (Figure 3.6b), X_E was between 0.5–1 at Lake Junín, indicative of evaporation-dominated hydrology or potentially closed basin conditions if humidity was similar to modern (~0.75). At Pumacocha and Mehcocha, X_E was between 0.2–0.3, suggesting these lakes maintained an outflow-dominated hydrology, but also experienced significant evaporation of up to 30% loss by volume (Figure 3.6b). Accounting for the sensitivity of X_E to $\Delta'^{17}O_I$, our conclusions are not substantially altered when a slightly lower $\Delta'^{17}O_I$ value is considered (see Section 3.8.2.1; Figure S3.8).

Evaluating lake hydrology across the Holocene, it is clear that all three lakes experienced a synchronous shift towards less evaporated conditions beginning during the late Holocene (after 4,200 years BP). The fact that this shift occurs concurrently at all three sites suggests it does not merely reflect the dynamics of a single lake, rather it likely reflects a regional shift towards more positive (i.e., wetter) *P–E* conditions. These results unambiguously point to the importance of *P–E* change on regional hydroclimate and on the $\delta^{18}O$ records from each of these lakes.

Table 3.2 Values used in deterministic modeling of Equation 10.

Variable	Value	Notes
$^{18}\alpha_{eq}$	1.010328	Calculated from Eq. 1 of Majoube (1971) and a temperature of 14 °C
$^{17}\alpha_{eq}$	1.00545	Calculated from $^{18}\alpha_{eq}$ using $\theta_{eq} = 0.529$
$^{18}\alpha_{diff}$	1.014245	Calculated using $\Phi = 0.5$
$^{17}\alpha_{diff}$	1.007361	Calculated from $^{18}\alpha_{diff}$ using $\theta_{diff} = 0.5185$
F	0.9	Estimated based on typical F estimates used for other lakes; selecting the higher end of the range used for the Great Lakes (0.6–0.9), assuming the smaller fetch of the Junín region lakes would lead to higher F values (Jasechko et al., 2014)
$^{18}R_I$	0.001977125	Calculated assuming $\delta'^{18}O_I = -14.1$ ‰
$^{17}R_I$	0.0003770939	Calculated from $^{18}R_I$ assuming a $\Delta'^{17}O_I$ value of 31 per meg
$^{18}R_A$	0.001954931	Calculated using $^{18}\alpha_{eq}$ and assuming vapor is in equilibrium with water of $\delta'^{18}O = -15$ ‰
$^{17}R_A$	0.0003748506	Calculated from $^{18}R_A$ assuming vapor is in equilibrium with water of $\Delta'^{17}O$ = 35 per meg

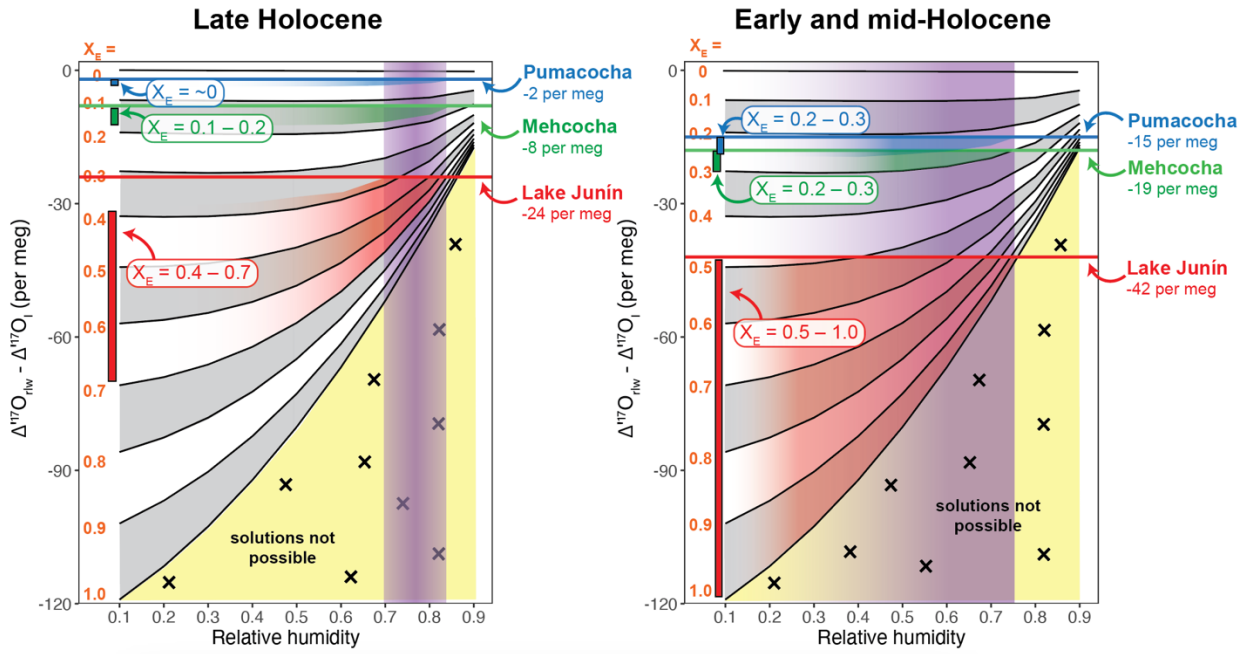

Figure 3.6: Deterministic model of Equation 10 using the values given in Table 3.2 under an X_E range from 0–1 and an h range of 0.1–0.9. $\Delta'^{17}O$ is shown as the difference between reconstructed lake water ($\Delta'^{17}O_{rlw}$) and input waters ($\Delta'^{17}O_I$ =31 per meg) where lower values correspond to greater evaporation. Orange text indicates modeled X_E and alternating white/grey wedges are shown to illustrate how $\Delta'^{17}O_{rlw}$–$\Delta'^{17}O_I$ and h vary over X_E increments of 0.1. Panels (a) and (b) show measured $\Delta'^{17}O_{rlw}$–$\Delta'^{17}O_I$ values as colored horizontal lines and X_E estimates as colored vertical bars for Lakes Junín (red), Pumacocha (blue), and Mehcocha (green) during the late Holocene and early through mid-Holocene, respectively. In (a), the vertical purple box shows the typical humidity range for this region in the present day (~0.7–0.83; SENHAMI, 2023; Katz et al., 2023). In (b), the purple box indicates the humidity range possible given both the model space and $\Delta'^{17}O_{rlw}$–$\Delta'^{17}O_I$ values for Lake Junín. The region shaded yellow indicates a $\Delta'^{17}O_{rlw}$–$\Delta'^{17}O_I$ and h space where solutions are not possible under the model conditions.

3.8.3 Placing local hydroclimate variability within a regional–global context

3.8.3.1 Holocene and late Pleistocene temperatures

South American temperature estimates from the Holocene are relatively sparce, but evidence from groundwater noble gases in the Amazon basin (Stute et al., 1995), pollen assemblages in the Bolivian foothills (Punyasena et al., 2008), and glacial equilibrium line elevations in the Junín region (Smith et al., 2005) suggest local temperatures were stable and similar to present. Global temperature estimates have also been derived from marine data assimilations and the reanalysis products suggest global temperature was relatively stable over the last 9,500 years and varied on the order of ~0.5 °C (Figure 3.7) (Osman et al., 2021). In comparison to Holocene temperatures, the marine proxies suggest global mean temperature was ~5–7 °C

cooler during the Last Glacial (Figure 3.7) (Osman et al., 2021). The distribution of glacial features in the central Peruvian Andes also suggests terrestrial temperatures were cooler by ~5 °C during the Last Glacial and latest Pleistocene (Wright, 1983; Smith et al., 2005).

Within the analytical uncertainty of our results, the $T\Delta_{47}$ data from the Lake Junín region are consistent with other proxy records that suggest cooler regional surface temperatures by ~5 °C during the latest Pleistocene (Wright, 1983; Smith et al., 2005; Osman et al., 2021). During the Holocene, relatively constant temperatures that are similar to modern are observed (Figure 3.7) however the analytical uncertainty of our $T\Delta_{47}$ data (~2–5 °C) is large compared to the small magnitude of temperature change modeled for the South American monsoon region during the Holocene (~1 °C; e.g., Hancock et al., 2023) which means that we are unable to definitively assess whether temperature changes of this magnitude (i.e., 1 °C) occurred at our study sites. Low sampling resolution inhibits us from resolving regional temperature change on sub-millennial timescales, however, our data suggest that local temperatures stabilized at near-modern conditions by around 10,000 years BP. Overall, these data suggest South American surface temperatures remained relatively stable throughout the Holocene across different regions, from the Amazon basin and foothills to the high Andes (e.g., Stute et al., 1995; Punyasena et al., 2008). These results broadly agree with the existing narrative of Holocene temperatures in South America and offer a perspective from the central Andes, showing that high elevation sites experienced a similar magnitude of temperature change as other regions across the continent over the last 20,000 years.

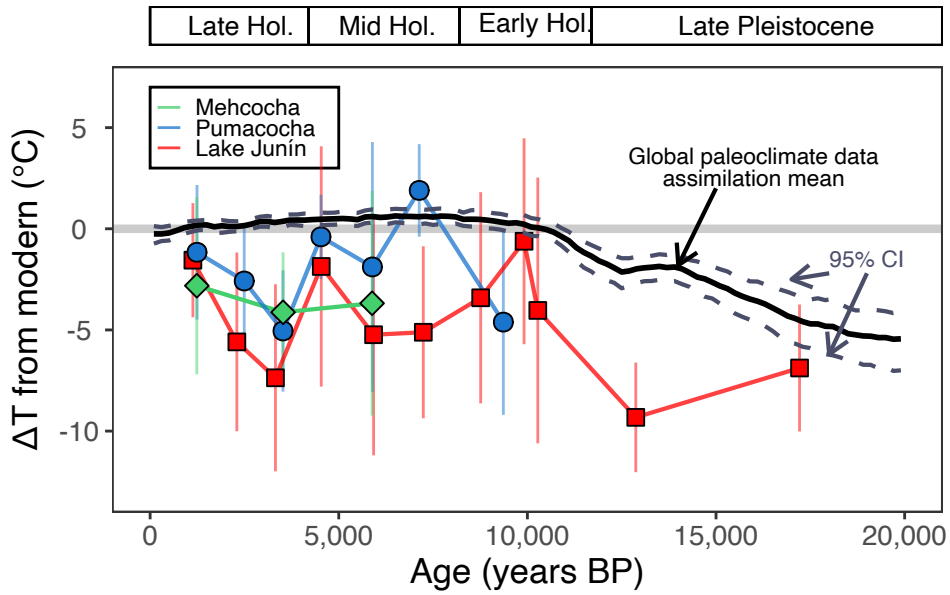

Figure 3.7: Change in temperature (ΔT) from modern lake water temperatures derived from carbonate $T\Delta_{47}$ values for Lakes Junín, Pumacocha, and Mehcocha (where "modern" is defined as 13 °C, Katz et al., 2023). Also shown is a global paleoclimate data assimilation mean (black; and 95% CI, grey dashed line) plotted as the difference from global mean surface temperature (Osman et al., 2021).

3.8.3.2 Holocene P–E in the central Andes

In Section 3.8.2.3, we establish that hydrologic variations at the three study lakes correspond with Holocene *P–E* changes in the Lake Junín region. To explore whether these variations reflect local conditions or are broadly representative of regional conditions in the central Andes, we compare our data to other proxy and modeling studies from the central Andes.

Robust evidence of Holocene *P–E* variations in the central Andes are also recorded by lake level data from Lake Junín (Weidhaas, 2017; Woods, 2021) and changes in clastic sediment flux at glacial lake Yanacocha (Stansell et al., 2015) (Figure 3.8). Lake level records from Lake Junín were derived by correlating changes in sedimentology and shallow water unconformities across a series of sediment cores collected in a lateral transect from shallow to deep waters and provides a useful point of comparison to our isotope data (Figure 3.8a) (Weidhaas, 2017; Woods, 2021). Reconstructed Lake Junín water level data for the last 25,000 years indicate lake level was high and similar (within 2 m) to present during the late Pleistocene until dropping rapidly (by 4 m) at 13,700 years BP, just before the start of the Holocene. After rising briefly by ~2.5 m at 13,100 years BP, a second precipitous drop occurred in the early Holocene with lake level reaching its lowest point at ~7.5 m below modern water level around 9,700 years BP. Following this minimum, lake level increased steadily over the mid-Holocene (8,200 to 4,200 years BP), reaching near-

modern levels at the start of the late Holocene and remained relatively high (within 2.5 m of modern) until present (Figure 3.8a) (Weidhaas, 2017; Woods, 2021). Records of clastic sediment flux at Yanacocha (10.56 °S, 75.93 °W), located 50 km northeast of Lake Junín also record local hydrology, as higher clastic inputs reflect a relatively advanced position of the Huagurucho glacier, whereby glacier advance is closely related to positive local water balance (Figure 3.8b) (Sagredo et al., 2014; Stansell et al., 2015). Similar to the other hydrologic proxies, clastic flux values indicate wet conditions in the late Pleistocene (until around 12,000 years BP), followed by overall dry conditions through the early and mid-Holocene (11,700 to 4,200 years BP), before the return of wetter conditions in the late Holocene (after 4,200 years BP).

Hydroclimate variability in the Holocene has also been approached with model data from CMIP6 (Hancock et al. 2023). CMIP6 model results suggest that annual precipitation amount in the central Andes and core monsoon region was lower at 6,000 years BP (i.e., their "mid-Holocene" time-slice) compared to the pre-Industrial (500 years BP), while the opposite trend is observed in the northern hemisphere. The decrease in annual precipitation reflects large reductions in precipitation during the austral summer, corresponding to weakened SASM during the mid-Holocene (Hancock et al., 2023). These results suggest that reduced summer precipitation may contribute substantially to the *P–E* changes in the central Andes. Conversely, as northern hemisphere monsoons weakened over the Holocene, water balance became more negative (e.g., Haug et al., 2001; Metcalfe et al., 2015; Cheng et al., 2023). The stable lake water temperatures in the Lake Junín region (Figure 3.5c) suggest the influence of temperature on evaporation rates may have been relatively stable over the Holocene. However, calculating quantitative evaporation rates is not possible with our data because, in addition to temperature, evaporation is highly sensitive to changes in other factors that we cannot reliably constrain for these lakes in the Holocene, such as radiation, cloud cover, wind speed, and humidity (e.g., Penman, 1948).

When considering the hydrologic records from the central Andes alongside modeling results, we find it likely that during the early and mid-Holocene (11,700 to 4,200 years BP), hydrologic conditions were drier than present (as reflected by high X_E values among local lakes, low lake levels at Junín, and reduced input of glacial sediment; Figure 3.8) and characterized by diminished summer precipitation and low *P–E*. Interestingly, while the lake levels and lake carbonate $\delta^{18}O$ records closely track southern hemisphere summer insolation changes, the driest conditions recorded by $\Delta'^{17}O_{rlw}$ values slightly lag the southern hemisphere's insolation minimum

(Figure 3.5a,e). This could suggest that either *P–E* changes in the central Andes were delayed compared to the timing of external climate forcings (i.e., orbital factors), or that additional drivers also contributed to *P–E* changes during the Holocene (or some combination of the two). These observations highlight the need for additional well-dated and high-resolution *P–E* records throughout the central Andes which can complement records of SASM variations. Despite the slight temporal offsets, these data suggest that the water balance history of the central Andes reflects a coherent, regional story of water stressed conditions in the early and mid-Holocene (11,700 to 4,200 years BP), followed by wetter, modern hydrologic conditions in the late Holocene (4,200 years BP to present).

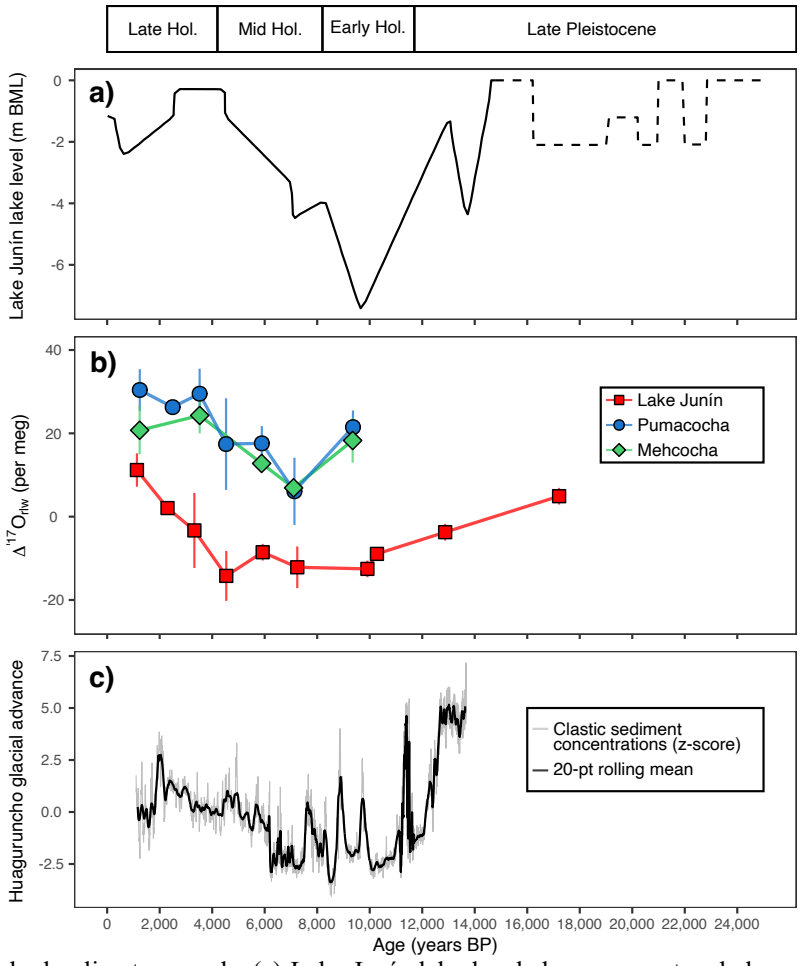

Figure 3.8: Regional hydroclimate records. (a) Lake Junín lake level shown as meters below modern lake level (m BML) (Weidhaas, 2017; Woods, 2021). (b) Reconstructed lake water $\Delta'^{17}O$ ($\Delta'^{17}O_{rlw}$) values for Lake Junín, Pumacocha, and Mehcocha, as in Figure 3.5e. (c) Clastic sediment concentrations from Lake Yanacocha shown as the first principal component of sediment geochemical data, where the first principal component corresponds with glacial flour (z-score; grey line) and a 20-point rolling mean (black line) (Stansell et al., 2015); higher values reflect a more advanced position of the Huaguruncho glacier and positive regional water balance.

3.9 Conclusions

In this study, we present a framework for using clumped and triple oxygen isotopes of lacustrine carbonates to investigate regional temperature and evaporative histories, and to constrain the influence of these factors on lake carbonate $\delta^{18}O$ records. We apply this framework to three lakes in the Peruvian Andes: Lakes Junín, Pumacocha, and Mehcocha. Water temperatures derived from carbonate clumped isotopes were indistinguishable from the present day at all three lakes through the Holocene, suggesting little change in environmental temperatures over the last 11,700 years. Stable temperatures indicate that temperature change was not a factor driving carbonate $\delta^{18}O$ variations at any of the three lakes during the Holocene. Water temperatures during the latest Pleistocene were ~5 °C lower than they were during the Holocene and today. Based on triple oxygen isotope data, we find that each lake experienced changes in hydrology (i.e., X_E) associated with more evaporated conditions throughout the early and mid-Holocene (11,700 to 4,200 years BP). These hydrologic changes co-occurred with weakened SASM strength and dry conditions throughout the central Andes. During the late Holocene, all three lakes became more open, reflecting a positive shift in water balance and wetter conditions. These results confirm that Lake Junín is highly sensitive to regional water balance changes during the Holocene and offer new evidence that Pumacocha and Mehcocha also experienced evaporated conditions through the early and mid-Holocene. This would have led to a positive shift in lake water $\delta^{18}O$ values at Lake Junín compared to precipitation, consistent with previous interpretations of Lake Junín's carbonate $\delta^{18}O$ record. Changes in water balance at these lakes are concurrent with lake level changes and glacial advance from the central Peruvian Andes, suggesting a coherency among regional hydroclimate records. Importantly, we find that hydroclimate change throughout the Holocene is closely linked to summer insolation and SASM dynamics, highlighting the clear connections between Andean water balance and global climate, and how these connections can be illuminated from lake carbonate $\Delta'^{17}O$ and Δ_{47} records.

Open Research:

All new data are provided within the tables of the main text and supporting materials associated with this paper. Clumped and triple oxygen data (replicate level and summarized data for all samples and standards) are available in the dataset Katz et al. (2025) on the Earth Chem repository. Oxygen, carbon, and radiocarbon isotope data, core age models, and summarized

clumped and triple oxygen isotope data are available in the on the NOAA National Centers for Environmental Information repository (www.ncei.noaa.gov/access/paleo-search/study/39181). All supplementary tables are also deposited in the dataset Katz et al., (2024) on the University of Michigan Deep Blue repository (doi.org/10.7302/ct1w-sm35). Supplementary code is available within the supporting materials and at: https://github.com/sarahakatz/HoloceneD17O.

Acknowledgements

We thank Kirsten Andrews, Matthew Salinas, Million Mengesha, Julia Kelson, Natalie Packard, Tyler Huth, Nick Ellis, Nick Weidhaas, and Kristina Brady Shannon for analytical and field assistance. We also thank David Gillikin, Elizabeth Olson, Larry Edwards, Dylan Parmenter, Jungpyo Hong, Laura Lopera, Josef Werne, Pedro Tapia, members of the Isotopologue Paleosciences Lab, and members of UM Paleoclimate seminar for useful discussions that improved the presentation of this work. We thank two anonymous reviewers and Editor Matthew Huber for their constructive comments. We acknowledge the late Herb Wright and Geoff Seltzer for their early work on Lake Junín which was foundational to this study. The authors declare no conflicts of interest.

Funding was provided by: The Geologic Society of America Graduate Student Research Grant (SAK), Scott Turner Award (SAK), Rackham Predoctoral Fellowship (SAK), NSF EAR-2102843 (NEL, BHP), NSF EAR-2102996 (DTR), NSF EAR-2103082 (MBA) and the UM Department of Earth & Environmental Sciences (NEL, BHP, SAK).

3.10 Supplementary information

3.10.1 Radiocarbon analysis and age model generation

Radiocarbon analysis was conducted on terrestrial macrofossils collected from both the Lake Junín and Mehcocha sediment cores. Samples and standards were prepared at the University of Pittsburgh using standard protocols (https://sites.uci.edu/keckams/files/2016/12/aba_protocol.pdf). Samples were dated by accelerator mass spectrometry at the W.M. Keck Carbon Cycle AMS facility at the University of California, Irvine. Uncalibrated radiocarbon ages are reported in Table S3.1 and S3.4 for Lake Junín and Mehcocha, respectively.

Calibrated ages were calculated using IntCal13 (Reimer et al., 2013). The R package, bacon (Blaauw and Christen, 2011), was used to construct age-depth models for both cores using the following settings: *acc.mean* = 20 yr/cm, *acc.shape* = 1.5, *mem.mean* = 0.7, *mem.strength* = 4. Model outputs are shown in Figures S3.1 and S3.3 for Lake Junín and Mehcocha, respectively. Modeled mean, median, and 95% CI intervals are reported every 1 cm in Tables S3.2 and S3.5 for Lake Junín and Mehcocha, respectively.

3.10.2 Decoupling the influence of evaporation and changing input $\delta^{18}O$ values on lake water $\delta^{18}O$ values

Changes in lake water evaporation and/or the $\delta'^{18}O$ value of water entering a lake ($\delta'^{18}O_I$) result in changes to lake water $\delta'^{18}O$ values (see the interpretive framework discussed in Section 3.4.2 for details). To decouple the influence of these two factors on reconstructed lake water $\delta'^{18}O$ ($\delta'^{18}O_{rlw}$) values, a "back projection" method was developed by Passey and Ji (2019) whereby reconstructed lake water $\Delta'^{17}O$ ($\Delta'^{17}O_{rlw}$) values are used to estimate and correct for the influence of lake water evaporation on $\delta^{18}O_{rlw}$ values, leading to estimates of unevaporated $\delta'^{18}O_I$ values. The relationship between $\delta^{18}O_I$, $\Delta'^{17}O_{rlw}$ and $\delta'^{18}O_{rlw}$ can be described as (Passey and Ji, 2019, Equation 7):

$$\delta'^{18}O_I = \frac{\Delta'^{17}O_I - \Delta'^{17}O_{rlw} + (\lambda_{lake} - \lambda_{ref}) \times \delta'^{18}O_{rlw}}{(\lambda_{lake} - \lambda_{ref})}$$

where $\Delta'^{17}O_I$ is the $\Delta'^{17}O$ value of unevaporated input water (given in units of ‰), λ_{lake} is the lake water fractionation exponent, and λ_{ref} = 0.528 (see Section 3.3 for further discussion of λ_{ref} and λ_{lake}).

The values $\Delta'^{17}O_{rlw}$ and $\delta'^{18}O_{rlw}$ can be determined from analytical measurements of carbonates, $\Delta'^{17}O$ values of modern precipitation are used to represent $\Delta'^{17}O_I$ (assuming $\Delta'^{17}O_I$ is conserved through time), and an estimation is made for λ_{lake} (Passey and Ji, 2019; Ibarra et al., 2021; Kelson et al., 2022; Katz et al., 2023). Passey and Ji (2019) showed that λ_{lake} can be estimated from $\Delta'^{17}O_{rlw}$ values under a humidity range of 0.3–0.7 and Katz et al. (2023) extended these estimates to humidity between 0.3–0.9.

Here, we calculate $\delta'^{18}O_I$ values for Lake Junín over the course of the Holocene using the back projection method. We do not present $\delta'^{18}O_I$ values for Lakes Pumacocha or Mehcocha because the relatively small degree of evaporation (i.e., $\Delta'^{17}O_{rlw}$ and $\Delta'^{17}O_I$ values are very similar) results in a high degree of uncertainty in λ_{lake}, and by extension, $\delta'^{18}O_I$ values (see Katz et al., 2023). For Lake Junín, we present $\delta'^{18}O_I$ values determined using three different humidity scenarios for estimating λ_{lake} (low, high and a full range of values), following the approach in Katz et al. (2023) (Figure S3.7; Table S3.9). We can further refine these estimates by selecting what we believe is the most likely humidity scenario for each sample. Our selection is based qualitatively on $\Delta'^{17}O_{rlw}$ values, as we assume there is a relationship between $\Delta'^{17}O_{rlw}$ and humidity. We use these new $\delta'^{18}O_I$ values to calculate the magnitude of evaporative influence on $\delta'^{18}O_{rlw}$ values by subtracting $\delta'^{18}O_I$ from $\delta'^{18}O_{rlw}$ (Figure S3.7d).

The magnitude of lake water evaporation varied over the Holocene and led to lake waters which were ~ +9 ‰ (compared to $\delta'^{18}O_I$) during the early and mid-Holocene, but freshened over the Holocene to ~ +5 ‰ (compared to $\delta'^{18}O_I$) during the late Holocene (Figure S3.7; Table S3.9). To a first order, changes in the magnitude of evaporation track changes in SASM, The combination of these data reveal that, over the Holocene, changes in $\delta'^{18}O_I$ and lake water evaporation were responsible for changes in $\delta'^{18}O_{rlw}$ values (Figure S3.7), with the highest $\delta'^{18}O_I$ values during the early Holocene (~ -12.6 ‰, VSMOW-SLAP) before decreasing through the mid to late Holocene ($\gtrsim$ -16.6 ‰, VSMOW-SLAP). This decreased of ~4 ‰ is similar to the ~3 ‰ change in $\delta'^{18}O_I$ estimated from local speleothem and ice core records (Thompson et al., 1995; Kanner et al., 2013) and supports prior interpretations that $\delta'^{18}O_I$ values at Lake Junín reflect changes in SASM strength over the Holocene.

3.10.3 Supplementary figures

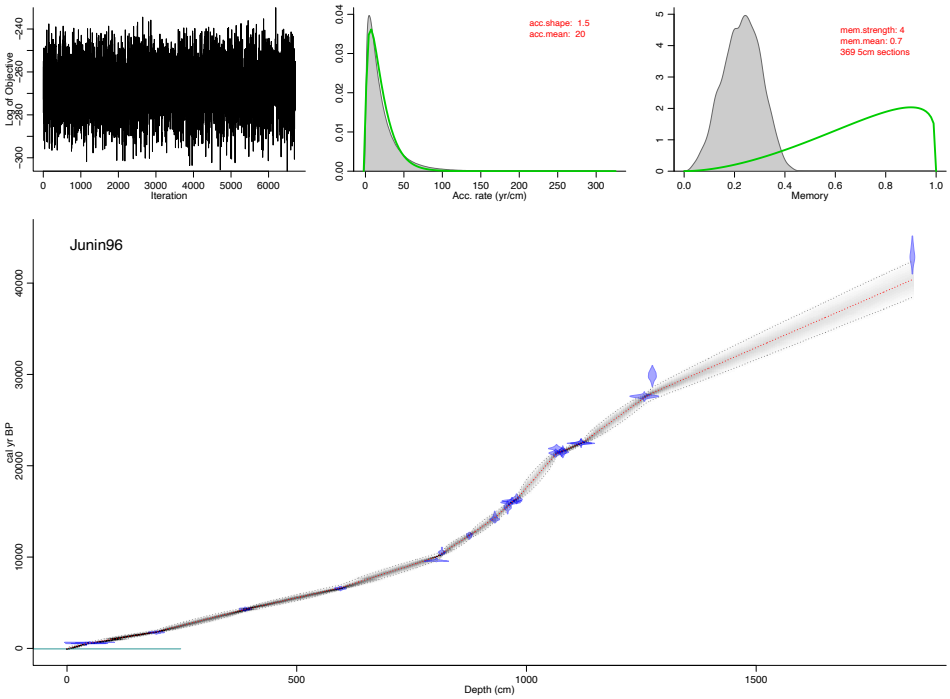

Figure S3.1: Lake Junín age model produced in the R package *bacon* (Blaauw and Christen, 2011) using the IntCal13 calibration curve of Reimer et al. (2013). ^{14}C radiocarbon dates are provided in Table S3.1 and model output is provided in Table S3.2.

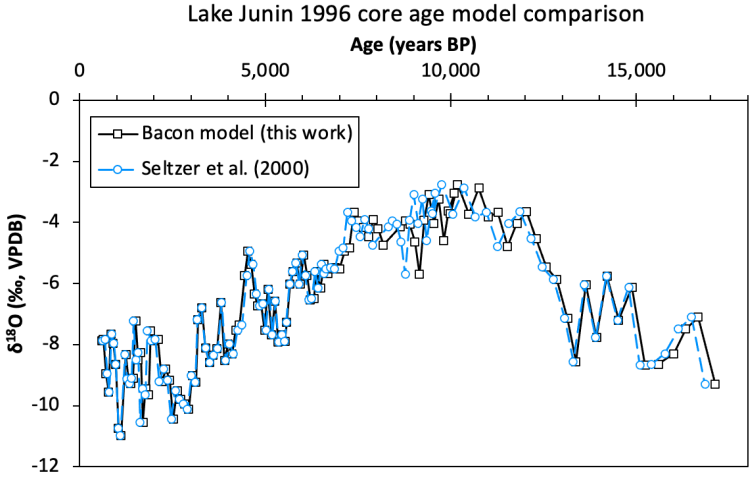

Figure S3.2: Comparison between the original Lake Junín age model from Seltzer et al. (2000) (dashed blue line, Table S3.3) and the revised *bacon* age model (solid black line, Figure S3.1, Table S3.1–S3.3).

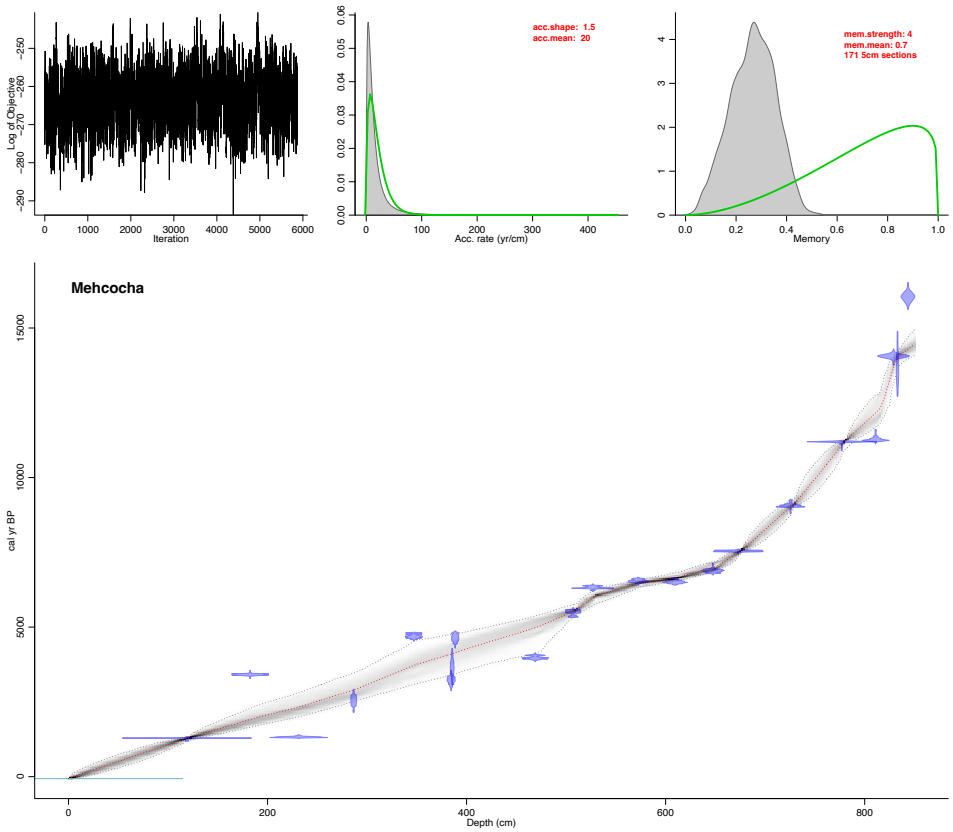

Figure S3.3: Lake Mehcocha age model produced in the R package *bacon* (Blaauw and Christen, 2013) using the IntCal13 calibration curve of Reimer et al. (2013). ^{14}C radiocarbon dates are provided in Table S3.4 and model output is provided in Table S3.5.

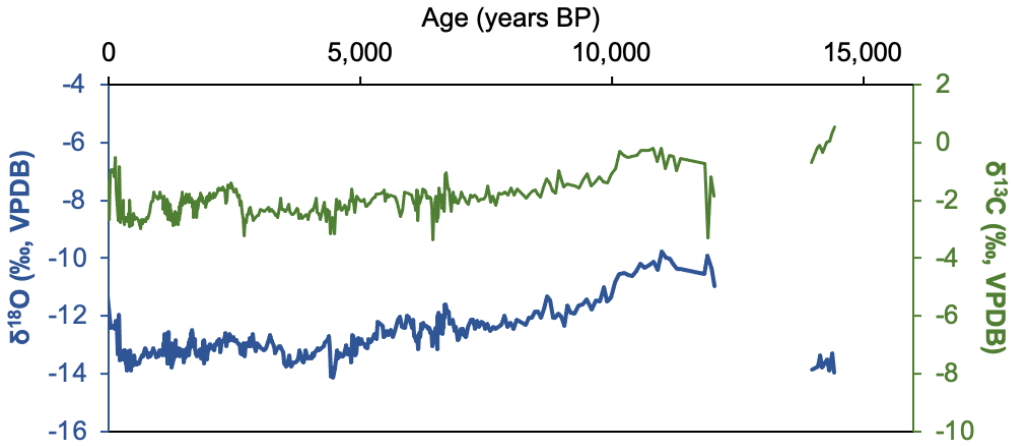

Figure S3.4: Lake Mehcocha $\delta^{13}C$ and $\delta^{18}O$ records (‰, VPDB). Data are provided in Table S3.6.

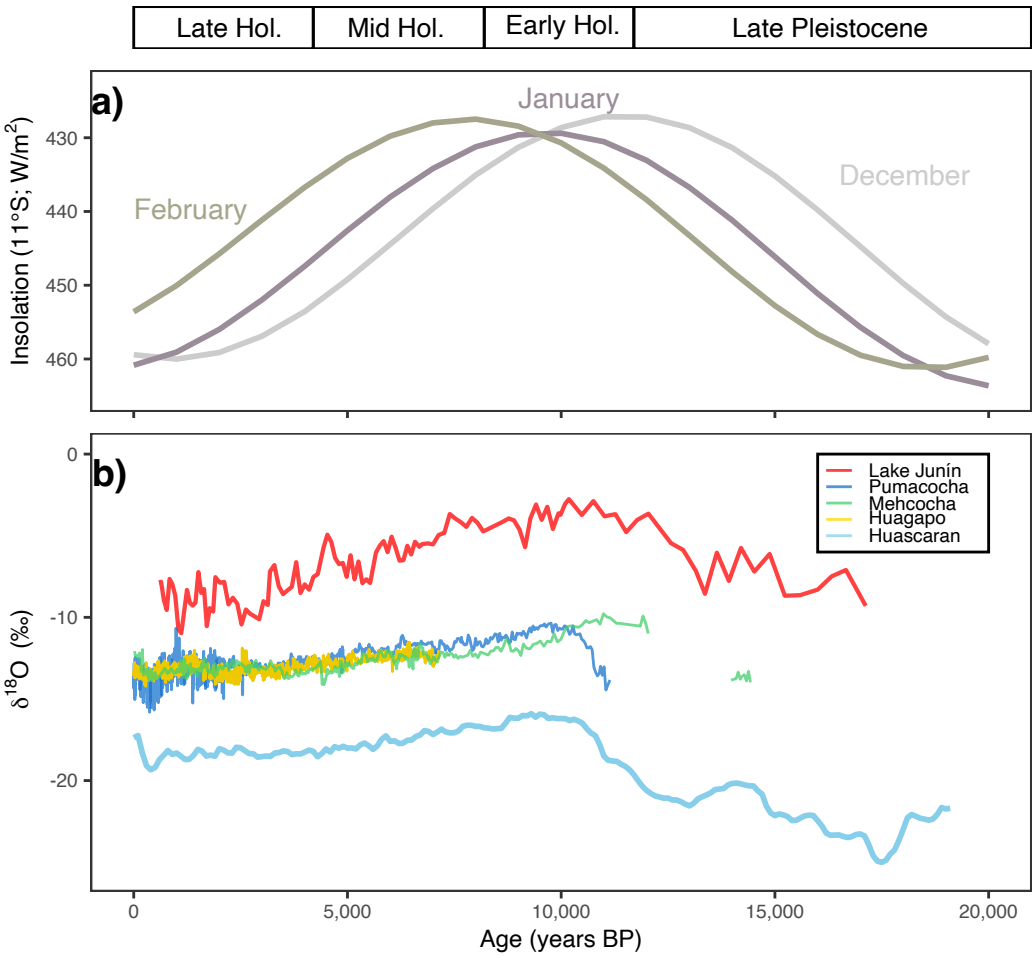

Figure S3.5: Regional insolation and compiled $\delta^{18}O$ records. (a) Dec–Feb. insolation at 11 °S, as in Figure 3.1 (Laskar et al., 2004; Crucifix, 2016). (b) Carbonate $\delta^{18}O$ records from Lakes Junín (Seltzer et al., 2000), Pumacocha (Bird et al., 2011), and Mehcocha (‰, VPDB) shown alongside speleothem $\delta^{18}O$ from Huagapo cave (‰, VPBD) (Kanner et al., 2013) and Huascaran ice core $\delta^{18}O$ (‰, VSMOW) (Thompson et al., 1995). Lake Junín data is shown on the updated *bacon* age model shown in Figure S3.1–S3.2.

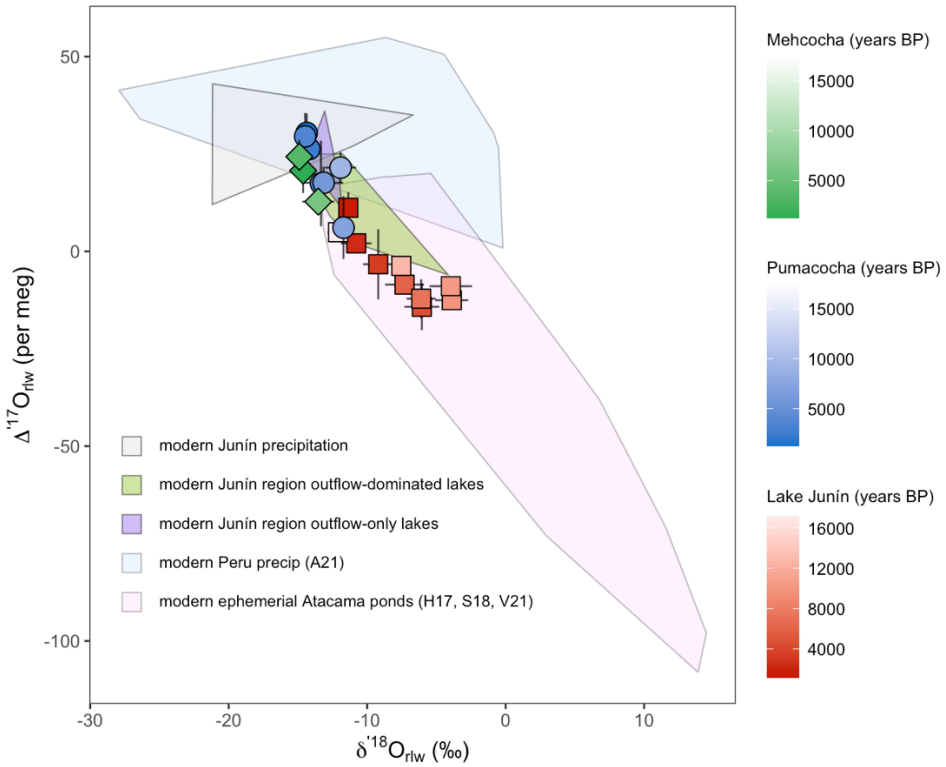

Figure S3.6: Reconstructed formation water $\Delta'^{17}O$ and $\delta'^{18}O$ values for Lake Junín (red squares), Pumacocha (blue circles), and Mehcocha (green diamonds). See Table 3.1 for data. Tinted scale bars and symbol fill correspond to sample age. Shaded polygons represent modern water and reconstructed carbonate formation water $\Delta'^{17}O$ and $\delta'^{18}O$ values for Junín precipitation and lakes (Katz et al., 2023). Also shown are polygons representing the range of modern precipitation $\Delta'^{17}O$ and $\delta'^{18}O$ values observed in Peru (data from Aron et al., 2021) and waters from modern ephemeral ponds in the Atacama (data from Herwartz et al., 2017; Surma et al., 2018; Voigt et al., 2021).

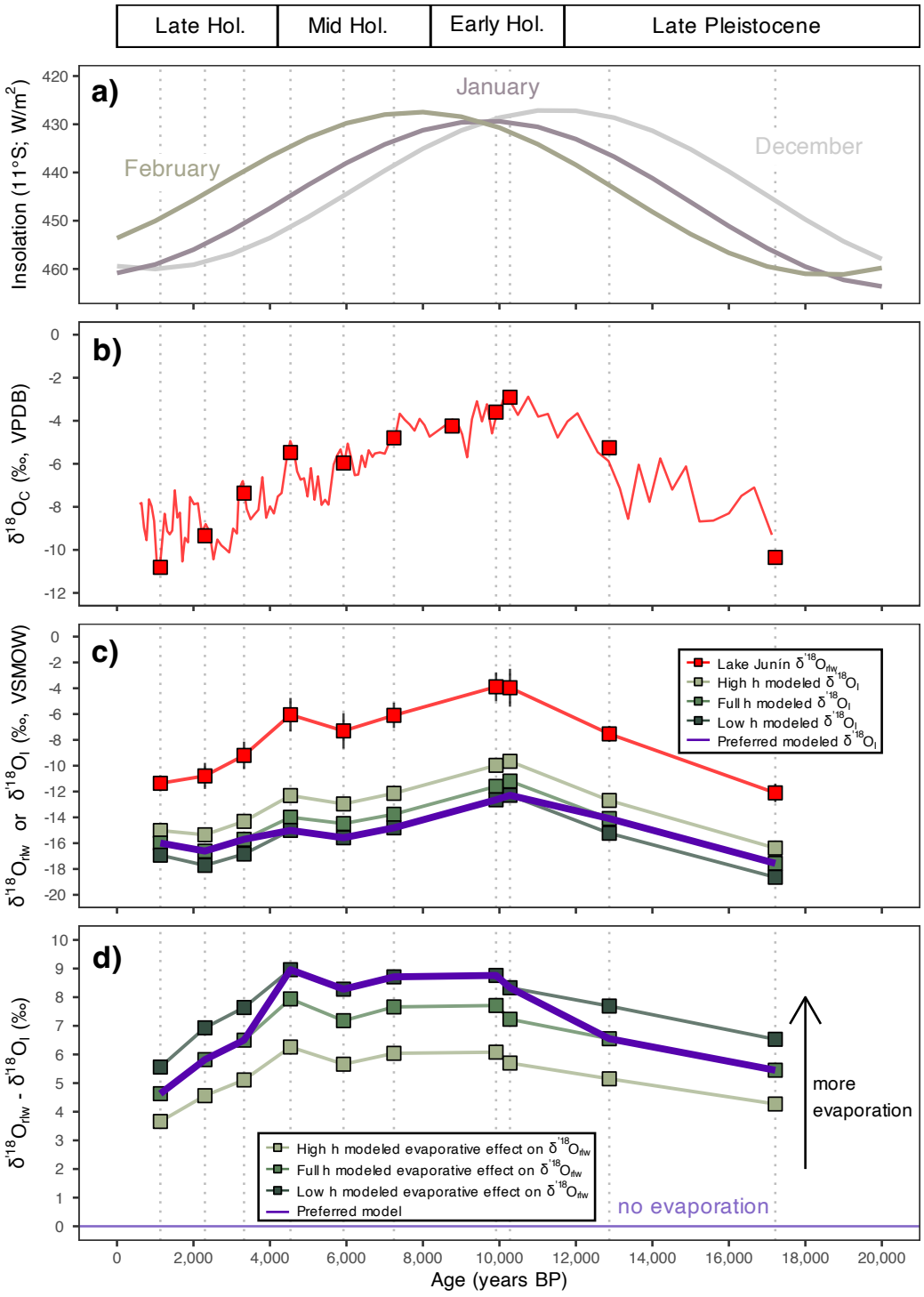

Figure S3.7: The influence of evaporation and changing input $\delta'^{18}O$ values on lake water $\delta^{18}O$ values. (a) Dec–Feb. insolation at 11 °S, as in Figure 3.1 (Laskar et al., 2004; Crucifix, 2016). (b) Carbonate $\delta^{18}O$ record from Lake Junín (Seltzer et al., 2000), with $\delta^{18}O$ measurements from Δ_{47} analysis shown as red squares. (c) As in Figure 3.5, reconstructed lake water $\delta'^{18}O$ ($\delta'^{18}O_{rlw}$) values derived from carbonate clumped isotope $\delta^{18}O$ and $T\Delta_{47}$ values; error bars represent 2σ SD propagated uncertainty. Also shown is reconstructed input water $\delta'^{18}O$ ($\delta'^{18}O_I$) calculated from $\delta'^{18}O_{rlw}$ and $\Delta'^{17}O_{rlw}$ using the back projection approach of Passey and Ji (2019) using three

different humidity scenarios to calculate λ_{lake} (see Katz et al., 2023). (d) The difference between $\delta'^{18}O_{rlw}$ and $\delta'^{18}O_I$ is shown for the three humidity scenarios and represents the magnitude by which $\delta'^{18}O_{rlw}$ values are evaporatively enriched in ^{18}O with respect to $\delta'^{18}O_I$ values. The purple lines in both (c) and (d) show preferred solutions for each sample across the three humidity scenarios; we qualitatively selected the high, full, and low humidity scenarios for $\Delta'^{17}O_{rlw}$ values >20 per meg, -5 to 20 per meg, and <-5 per meg, respectively. See Table S3.9 for the data plotted in both (c) and (d).

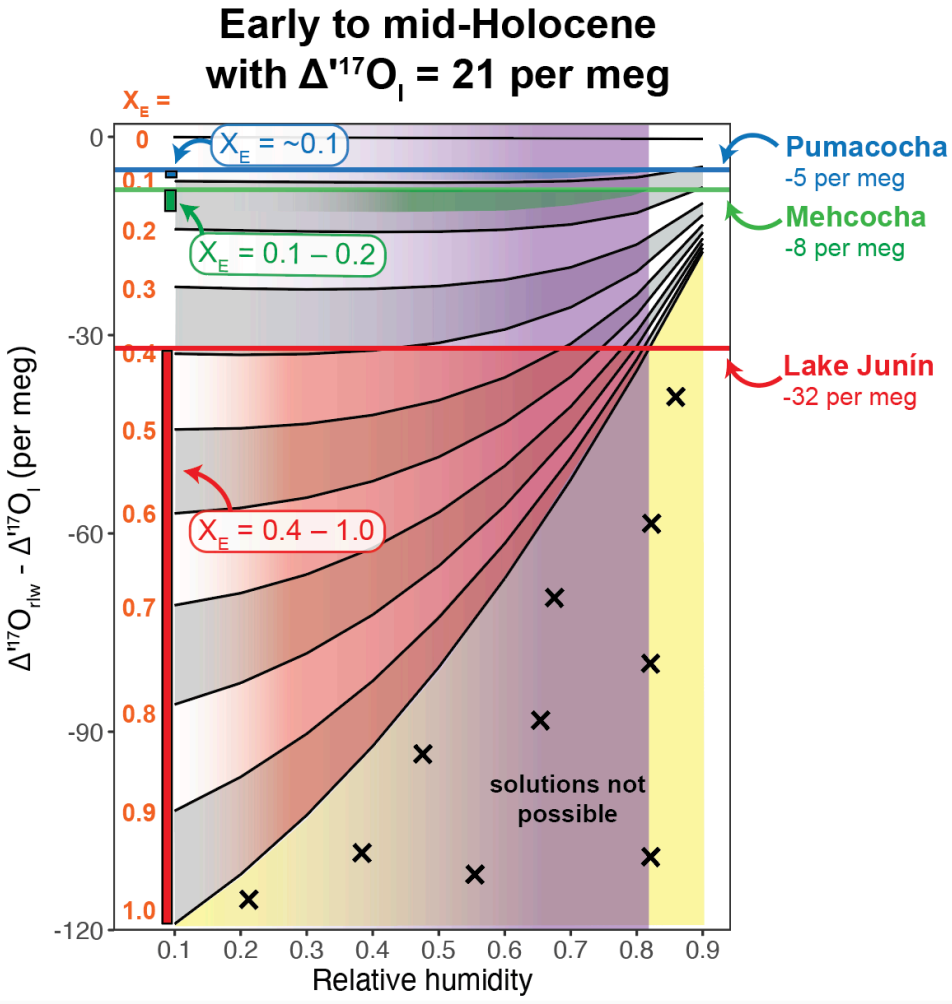

Figure S3.8: X_E estimates for Lakes Junín, Pumacocha, and Mehcocha during the early and mid-Holocene assuming a different $\Delta'^{17}O_I$ value (21 per meg). Model parameters are the same as in Table 3.2.

3.11 References

Abbott, M.B., Binford, M.W., Brenner, M., and Kelts, K.R., 1997, A 3500 ^{14}C yr High-Resolution Record of Water-Level Changes in Lake Titicaca, Bolivia/Peru: Quaternary Research, v. 47, p. 169–180, doi:10.1006/qres.1997.1881.

Aggarwal, P.K., Romatschke, U., Araguas-Araguas, L., Belachew, D., Longstaffe, F.J., Berg, P., Schumacher, C., and Funk, A., 2016, Proportions of convective and stratiform precipitation revealed in water isotope ratios: Nature Geoscience, v. 9, p. 624–629, doi:10.1038/ngeo2739.

Anderson, N.T. et al., 2021, A Unified Clumped Isotope Thermometer Calibration (0.5–1,100°C) Using Carbonate-Based Standardization: Geophysical Research Letters, v. 48, doi:10.1029/2020GL092069.

Aron, P.G., Levin, N.E., Beverly, E.J., Huth, T.E., Passey, B.H., Pelletier, E.M., Poulsen, C.J., Winkelstern, I.Z., and Yarian, D.A., 2021a, Triple oxygen isotopes in the water cycle: Chemical Geology, v. 565, p. 1–23, doi:10.1016/j.chemgeo.2020.120026.

Aron, P.G., Li, S., Brooks, J.R., Welker, J.M., and Levin, N.E., 2023, Seasonal Variations in Triple Oxygen Isotope Ratios of Precipitation in the Western and Central United States: Paleoceanography and Paleoclimatology, v. 38, doi:10.1029/2022PA004458.

Aron, P.G., Poulsen, C.J., Fiorella, R.P., Levin, N.E., Acosta, R.P., Yanites, B.J., and Cassel, E.J., 2021b, Variability and Controls on $\delta^{18}O$, d-excess, and $\Delta'^{17}O$ in Southern Peruvian Precipitation: Journal of Geophysical Research: Atmospheres, v. 126, p. 1–18, doi:10.1029/2020JD034009.

Assonov, S., Groening, M., Fajgelj, A., Hélie, J., and Hillaire-Marcel, C., 2020, Preparation and characterisation of IAEA-603, a new primary reference material aimed at the VPDB scale realisation for $\delta^{13}C$ and $\delta^{18}O$ determination: Rapid Communications in Mass Spectrometry, v. 34, doi:10.1002/rcm.8867.

Barkan, E., and Luz, B., 2007, Diffusivity fractionations of $H_2{}^{16}O/H_2{}^{17}O$ and $H_2{}^{16}O/H_2{}^{18}O$ in air and their implications for isotope hydrology: Rapid Communications in Mass Spectrometry, v. 21, p. 2999–3005, doi:10.1002/rcm.3180.

Benson, L. V, and White, J.W.C., 1994, Stable Isotopes of Oxygen and Hydrogen in the Truckee River Pyramid Lake Surface-Water System .1. Data-Analysis and Extraction of Paleoclimatic Information: Limnology and Oceanography, v. 39, p. 344–355.

Bernasconi, S.M., Müller, I.A., Bergmann, K.D., Breitenbach, S.F.M., Fernandez, A., Hodell, D.A., Jaggi, M., Meckler, A.N., Millan, I., and Ziegler, M., 2018, Reducing Uncertainties in Carbonate Clumped Isotope Analysis Through Consistent Carbonate-Based Standardization: Geochemistry, Geophysics, Geosystems, v. 19, p. 2895–2914, doi:10.1029/2017GC007385.

Bird, B.W., Abbott, M.B., Rodbell, D.T., and Vuille, M., 2011a, Holocene tropical South American hydroclimate revealed from a decadally resolved lake sediment $\delta^{18}O$ record: Earth and Planetary Science Letters, v. 310, p. 192–202, doi:10.1016/J.EPSL.2011.08.040.

Bird, B.W., Abbott, M.B., Vuille, M., Rodbell, D.T., Stansell, N.D., and Rosenmeier, M.F., 2011b, A 2,300-year-long annually resolved record of the South American summer monsoon from the Peruvian Andes: Proceedings of the National Academy of Sciences, v. 108, p. 8583–8588, doi:10.1073/pnas.1003719108.

Blaauw, M., and Christen, J.A., 2011, Flexible paleoclimate age-depth models using an autoregressive gamma process: Bayesian Analysis, v. 6, p. 457–474, doi:10.1214/11-BA618.

Cheng, Y., Zhang, C., Li, Y., Li, X., Liu, W., and Zhao, C., 2023, Increasing lake evaporation over the Holocene revealed by oxygen stable isotope in Indian-monsoon dominated southwestern China: Global and Planetary Change, v. 228, p. 104217, doi:10.1016/j.gloplacha.2023.104217.

Cobbing, J., Quispesivana, L.Q., and Paz, M.M., 1996, Geologia de los cuadrangulos de Ambo, Cerro de Pasco y Ondores:, https://hdl.handle.net/20.500.12544/200 (accessed February 2024).

Cohen, K.M., Finney, S.C., Gibbard, P.L., and Fan, J.-X., 2013, The ICS International Chronostratigraphic Chart: Episodes, v. 36, p. 199–204, doi:10.18814/epiiugs/2013/v36i3/002.

Cohen, K.M., Harper, D.A.T., Gibbard, S.C., and Car, N., 2023, International Chronostratigraphic Chart v2023/09: International Commission on Stratigraphy, www.stratigraphy.org (accessed December 2023).

Craig, H., 1961, Isotopic Variations in Meteoric Waters: Science, v. 133, p. 1702–1703.

Criss, R.E., 1999, Principles of Stable Isotope Distribution: New York, Oxford University Press, 1–254 p.

Crucifix, M., 2016, Insolation for Paleoclimate Studies “palinsol” v0.93:, https://bitbucket.org/mcrucifix/insolhttps://bitbucket.org/mcrucifix/insol (accessed January 2023).

Cruz, F.W., Burns, S.J., Karmann, I., Sharp, W.D., Vuille, M., Cardoso, A.O., Ferrari, J.A., Silva Dias, P.L., and Viana, O., 2005, Insolation-driven changes in atmospheric circulation over the past 116,000 years in subtropical Brazil: Nature, v. 434, p. 63–66, doi:10.1038/nature03365.

Cruz, F.W., Vuille, M., Burns, S.J., Wang, X., Cheng, H., Werner, M., Lawrence Edwards, R., Karmann, I., Auler, A.S., and Nguyen, H., 2009, Orbitally driven east-west antiphasing of South American precipitation: Nature Geoscience, v. 2, p. 210–214, doi:10.1038/ngeo444.

Daëron, M., Blamart, D., Peral, M., and Affek, H.P., 2016, Absolute isotopic abundance ratios and the accuracy of Δ_{47} measurements: Chemical Geology, v. 442, p. 83–96, doi:10.1016/j.chemgeo.2016.08.014.

Dansgaard, W., 1964, Stable isotopes in precipitation: Tellus, v. 16, p. 436–468, doi:10.3402/tellusa.v16i4.8993.

Dee, S., Emile-Geay, J., Evans, M.N., Allam, A., Steig, E.J., and Thompson, D.M., 2015, PRYSM: An open-source framework for PRoxY System Modeling, with applications to oxygen-isotope systems: Journal of Advances in Modeling Earth Systems, v. 7, p. 1220–1247, doi:10.1002/2015MS000447.

Dee, S.G., Russell, J.M., Morrill, C., Chen, Z., and Neary, A., 2018, PRYSM v2.0: A Proxy System Model for Lacustrine Archives: Paleoceanography and Paleoclimatology, v. 33, p. 1250–1269, doi:10.1029/2018PA003413.

Ellis, N.M., and Passey, B.H., 2023, A novel method for high-precision triple oxygen isotope analysis of diverse Earth materials using high temperature conversion–methanation–fluorination and isotope ratio mass spectrometry: Chemical Geology, doi:10.1016/j.chemgeo.2023.121616.

Fetrow, A.C., Snell, K.E., Di Fiori, R. V., Long, S.P., and Bonde, J.W., 2022, How Hot Is Too Hot? Disentangling Mid-Cretaceous Hothouse Paleoclimate From Diagenesis: Paleoceanography and Paleoclimatology, v. 37, doi:10.1029/2022PA004517.

Flusche, M.A., Seltzer, G., Rodbell, D., Siegel, D., and Samson, S., 2005, Constraining water sources and hydrologic processes from the isotopic analysis of water and dissolved strontium, Lake Junin, Peru: Journal of Hydrology, v. 312, p. 1–13, doi:10.1016/j.jhydrol.2005.02.021.

Garreaud, R.D., Vuille, M., Compagnucci, R., and Marengo, J., 2009, Present-day South American climate: Palaeogeography, Palaeoclimatology, Palaeoecology, v. 281, p. 180–195, doi:10.1016/j.palaeo.2007.10.032.

Gat, J.R., 1996, Oxygen and Hydrogen Isotopes in the Hydrologic Cycle: Annual Review of Earth and Planetary Sciences, v. 24, p. 225–262, doi:10.1146/annurev.earth.24.1.225.

Gázquez, F., Morellón, M., Bauska, T., Herwartz, D., Surma, J., Moreno, A., Staubwasser, M., Valero-Garcés, B., Delgado-Huertas, A., and Hodell, D.A., 2018, Triple oxygen and hydrogen isotopes of gypsum hydration water for quantitative paleo-humidity reconstruction: Earth and Planetary Science Letters, v. 481, p. 177–188, doi:10.1016/j.epsl.2017.10.020.

Gibson, J.J., Birks, S.J., and Yi, Y., 2016, Stable isotope mass balance of lakes: A contemporary perspective: Quaternary Science Reviews, v. 131, p. 316–328, doi:10.1016/j.quascirev.2015.04.013.

Google LLC, 2022, Google Earth version 7.3.6.9345:, https://earth.google.com/web/ (accessed December 2023).

Hancock, C.L., McKay, N.P., Erb, M.P., Kaufman, D.S., Routson, C.R., Ivanovic, R.F., Gregoire, L.J., and Valdes, P., 2023, Global Synthesis of Regional Holocene Hydroclimate Variability Using Proxy and Model Data: Paleoceanography and Paleoclimatology, v. 38, doi:10.1029/2022PA004597.

Hansen, B.C.S., Seltzer, G.O., and Wright, H.E., 1994, Late Quaternary vegetational change in the central Peruvian Andes: Palaeogeography, Palaeoclimatology, Palaeoecology, v. 109, p. 263–285, doi:10.1016/0031-0182(94)90179-1.

Haug, G.H., Hughen, K.A., Sigman, D.M., Peterson, L.C., and Röhl, U., 2001, Southward Migration of the Intertropical Convergence Zone Through the Holocene: Science, v. 293, p. 1304–1308, doi:10.1126/science.1059725.

Herwartz, D., Surma, J., Voigt, C., Assonov, S., and Staubwasser, M., 2017, Triple oxygen isotope systematics of structurally bonded water in gypsum: Geochimica et Cosmochimica Acta, v. 209, p. 254–266, doi:10.1016/j.gca.2017.04.026.

Horton, T.W., Defliese, W.F., Tripati, A.K., and Oze, C., 2016, Evaporation induced ^{18}O and ^{13}C enrichment in lake systems: A global perspective on hydrologic balance effects: Quaternary Science Reviews, v. 131, p. 365–379, doi:10.1016/j.quascirev.2015.06.030.

Hren, M.T., and Sheldon, N.D., 2012, Temporal variations in lake water temperature: Paleoenvironmental implications of lake carbonate $\delta^{18}O$ and temperature records: Earth and Planetary Science Letters, v. 337–338, p. 77–84, doi:10.1016/j.epsl.2012.05.019.

Huntington, K.W., Saylor, J., Quade, J., and Hudson, A.M., 2015, High late Miocene-Pliocene elevation of the Zhada Basin, southwestern Tibetan Plateau, from carbonate clumped isotope thermometry: Bulletin of the Geological Society of America, v. 127, p. 181–199, doi:10.1130/B31000.1.

Huntington, K.W., Wernicke, B.P., and Eiler, J.M., 2010, Influence of climate change and uplift on Colorado Plateau paleotemperatures from carbonate clumped isotope thermometry: Tectonics, v. 29, p. 1–19, doi:10.1029/2009TC002449.

Huth, T.E., Passey, B.H., Cole, J.E., Lachniet, M.S., McGee, D., Denniston, R.F., Truebe, S., and Levin, N.E., 2022, A framework for triple oxygen isotopes in speleothem paleoclimatology: Geochimica et Cosmochimica Acta, v. 319, p. 191–219, doi:10.1016/j.gca.2021.11.002.

Ibarra, D.E., Kukla, T., Methner, K.A., Mulch, A., and Chamberlain, C.P., 2021, Reconstructing Past Elevations From Triple Oxygen Isotopes of Lacustrine Chert: Application to the Eocene Nevadaplano, Elko Basin, Nevada, United States: Frontiers in Earth Science, v. 9, p. 1–19, doi:10.3389/feart.2021.628868.

Jasechko, S., Gibson, J.J., and Edwards, T.W.D., 2014, Stable isotope mass balance of the Laurentian Great Lakes: Journal of Great Lakes Research, v. 40, p. 336–346, doi:10.1016/j.jglr.2014.02.020.

Kanner, L.C., Burns, S.J., Cheng, H., Edwards, R.L., and Vuille, M., 2013, High-resolution variability of the South American summer monsoon over the last seven millennia: insights from a speleothem record from the central Peruvian Andes: Quaternary Science Reviews, v. 75, p. 1–10, doi:10.1016/j.quascirev.2013.05.008.

Katz, S.A., Levin, N.E., Rodbell, D.T., Gillikin, D.P., Aron, P.G., Passey, B.H., Tapia, P.M., Serrepe, A.R., and Abbott, M.B., 2023, Detecting hydrologic distinctions among Andean lakes using clumped and triple oxygen isotopes: Earth and Planetary Science Letters, v. 602, p. 117927, doi:10.1016/j.epsl.2022.117927.

Katz, S., Levin, N. E., Abbott, M. B., Rodbell, D. T., Passey, B. H., DeLuca, N. M., Larsen, D. J., Woods, A., 2024. Data associated with "Holocene temperature and water stress in the Peruvian Andes: insights from lake carbonate clumped and triple oxygen isotopes", [Dataset]. Version 1.0. University of Michigan Deep Blue Data. doi.org/10.7302/ct1w-sm35. Accessed 2024-03-20.

Katz, S., Levin, N. E., Abbott, M. B., Rodbell, D. T., Passey, B. H., DeLuca, N. M., Larsen, D. J., Woods, A., 2025. Holocene temperature and water stress in the Peruvian Andes: insights from lake carbonate clumped and triple oxygen isotopes, [Dataset]. Version 1.0. Interdisciplinary Earth Data Alliance (IEDA). https://doi.org/10.60520/IEDA/113158. Accessed 2024-03-20.

Kelson, J.R., Petersen, S. V., Niemi, N.A., Passey, B.H., and Curley, A.N., 2022, Looking upstream with clumped and triple oxygen isotopes of estuarine oyster shells in the early Eocene of California, USA: Geology, doi:10.1130/G49634.1.

Kim, S.-T., and O'Neil, J.R., 1997, Equilibrium and nonequilibrium oxygen isotope effects in synthetic carbonates: Geochimica et Cosmochimica Acta, v. 61, p. 3461–3475, doi:10.1016/S0016-7037(97)00169-5.

Konecky, B.L., Noone, D.C., and Cobb, K.M., 2019, The Influence of Competing Hydroclimate Processes on Stable Isotope Ratios in Tropical Rainfall: Geophysical Research Letters, v. 46, p. 1622–1633, doi:10.1029/2018GL080188.

Laskar, J., Robutel, P., Joutel, F., Gastineau, M., Correia, A.C.M., and Levrard, B., 2004, A long-term numerical solution for the insolation quantities of the Earth: Astronomy & Astrophysics, v. 428, p. 261–285, doi:10.1051/0004-6361:20041335.

Leng, M.J., and Marshall, J.D., 2004, Palaeoclimate interpretation of stable isotope data from lake sediment archives: Quaternary Science Reviews, v. 23, p. 811–831, doi:10.1016/J.QUASCIREV.2003.06.012.

Lenters, J.D., and Cook, K.H., 1999, Summertime Precipitation Variability over South America: Role of the Large-Scale Circulation: Monthly Weather Review, v. 127, p. 409–431, doi:10.1175/1520-0493(1999)127<0409:SPVOSA>2.0.CO;2.

Liu, X., and Battisti, D.S., 2015, The influence of orbital forcing of tropical insolation on the climate and isotopic composition of precipitation in South America: Journal of Climate, v. 28, p. 4841–4862, doi:10.1175/JCLI-D-14-00639.1.

Luz, B., and Barkan, E., 2005, The isotopic ratios $^{17}O/^{16}O$ and $^{18}O/^{16}O$ in molecular oxygen and their significance in biogeochemistry: Geochimica et Cosmochimica Acta, v. 69, p. 1099–1110, doi:10.1016/j.gca.2004.09.001.

Luz, B., and Barkan, E., 2010, Variations of $^{17}O/^{16}O$ and $^{18}O/^{16}O$ in meteoric waters: Geochimica et Cosmochimica Acta, v. 74, p. 6276–6286, doi:10.1016/j.gca.2010.08.016.

Majoube, M., 1971, Fractionnement en oxygène 18 et en deutérium entre l'eau et sa vapeur: Journal de Chimie Physique, v. 68, p. 1423–1436.

Marengo, J.A. et al., 2012, Recent developments on the South American monsoon system: International Journal of Climatology, v. 32, p. 1–21, doi:10.1002/joc.2254.

Matsuhisa, Y., Goldsmith, J.R., and Clayton, R.N., 1978, Mechanisms of hydrothermal crystallization of quartz at 250°C and 15 kbar: Geochimica et Cosmochimica Acta, v. 42, p. 173–182, doi:10.1016/0016-7037(78)90130-8.

McGee, D., Donohoe, A., Marshall, J., and Ferreira, D., 2014, Changes in ITCZ location and cross-equatorial heat transport at the Last Glacial Maximum, Heinrich Stadial 1, and the mid-Holocene: Earth and Planetary Science Letters, v. 390, p. 69–79, doi:10.1016/j.epsl.2013.12.043.

Merlivat, L., 1978, Molecular diffusitivies or $H_2{}^{16}O$, $HD^{16}O$, and $H_2{}^{18}O$ in gases: The Journal of Chemical Physics, v. 69, doi:10.1063/1.436884.

Metcalfe, S.E., Barron, J.A., and Davies, S.J., 2015, The Holocene history of the North American Monsoon: 'known knowns' and 'known unknowns' in understanding its spatial and temporal complexity: Quaternary Science Reviews, v. 120, p. 1–27, doi:10.1016/j.quascirev.2015.04.004.

Ministerio de Energia y Minas, 1979a, Mapa Geologico del Cuadrangulo de Cerro de Pasco: v. Hoja 22-K.

Ministerio de Energia y Minas, 1979b, Mapa Geologico del Cuadrangulo de Ondores: v. Hoja 23-K.

Ministerio de Energia y Minas, 1979c, Mapa Geologico del Cuadrangulo Ulcumajo: v. Hoja 21-I.

Osman, M.B., Tierney, J.E., Zhu, J., Tardif, R., Hakim, G.J., King, J., and Poulsen, C.J., 2021, Globally resolved surface temperatures since the Last Glacial Maximum: Nature, v. 599, p. 239–244, doi:10.1038/s41586-021-03984-4.

Palacios, D. et al., 2020, The deglaciation of the Americas during the Last Glacial Termination: Earth-Science Reviews, v. 203, p. 103113, doi:10.1016/j.earscirev.2020.103113.

Passey, B.H., Hu, H., Ji, H., Montanari, S., Li, S., Henkes, G.A., and Levin, N.E., 2014, Triple oxygen isotopes in biogenic and sedimentary carbonates: Geochimica et Cosmochimica Acta, v. 141, p. 1–25, doi:10.1016/j.gca.2014.06.006.

Passey, B.H., and Ji, H., 2019, On the use of triple oxygen isotopes in lake waters and carbonates for reconstructing $\delta^{18}O$ of unevaporated precipitation: a case study from the Western United States: Earth and Planetary Science Letters, v. 518, p. 1–12, doi:10.1016/j.epsl.2019.04.026.

Passey, B.H., Levin, N.E., Cerling, T.E., Brown, F.H., and Eiler, J.M., 2010, High-temperature environments of human evolution in East Africa based on bond ordering in paleosol carbonates: Proceedings of the National Academy of Sciences, v. 107, p. 11245–11249, doi:10.1073/pnas.1001824107.

Penman, H.L., 1948, Natural evaporation from open water, bare soil and grass: Proceedings of the Royal Society of London. Series A. Mathematical and Physical Sciences, v. 193, p. 120–145, doi:10.1098/rspa.1948.0037.

Petersen, S.V. V. et al., 2019, Effects of Improved ^{17}O Correction on Inter-Laboratory Agreement in Clumped Isotope Calibrations, Estimates of Mineral-Specific Offsets, and Temperature Dependence of Acid Digestion Fractionation: Geochemistry, Geophysics, Geosystems, v. 20, p. 3495–3519, doi:10.1029/2018GC008127.

Placzek, C., Quade, J., and Patchett, P.J., 2006, Geochronology and stratigraphy of late Pleistocene lake cycles on the southern Bolivian Altiplano: Implications for causes of tropical climate change: Bulletin of the Geological Society of America, v. 118, p. 515–532, doi:10.1130/B25770.1.

Punyasena, S.W., Mayle, F.E., and McElwain, J.C., 2008, Quantitative estimates of glacial and Holocene temperature and precipitation change in lowland Amazonian Bolivia: Geology, v. 36, p. 667–670, doi:10.1130/G24784A.1.

Rademaker, K., Hodgins, G., Moore, K., Zarrillo, S., Miller, C., Bromley, G.R.M., Leach, P., Reid, D.A., Álvarez, W.Y., and Sandweiss, D.H., 2014, Paleoindian settlement of the high-altitude Peruvian Andes: Science, v. 346, p. 466–469, doi:10.1126/science.1258260.

Reimer, P.J. et al., 2013, IntCal13 and Marine13 Radiocarbon Age Calibration Curves 0–50,000 Years cal BP: Radiocarbon, v. 55, p. 1869–1887, doi:10.2458/azu_js_rc.55.16947.

Riris, P., and Arroyo-Kalin, M., 2019, Widespread population decline in South America correlates with mid-Holocene climate change: Scientific Reports, v. 9, doi:10.1038/s41598-019-43086-w.

Rodbell, D.T. et al., 2022, 700,000 years of tropical Andean glaciation: Nature, v. 607, p. 301–306, doi:10.1038/s41586-022-04873-0.

Rodbell, D.T., Seltzer, G.O., Mark, B.G., Smith, J.A., and Abbott, M.B., 2008, Clastic sediment flux to tropical Andean lakes: records of glaciation and soil erosion: Quaternary Science Reviews, v. 27, p. 1612–1626, doi:10.1016/j.quascirev.2008.06.004.

Rodbell, D.T., Smith, J.A., and Mark, B.G., 2009, Glaciation in the Andes during the Lateglacial and Holocene: Quaternary Science Reviews, v. 28, p. 2165–2212, doi:10.1016/j.quascirev.2009.03.012.

Rozanski, K., Araguás-Araguás, L., and Gonfiantini, R., 1993, Isotopic Patterns in Modern Global Precipitation, *in* Swart, P.K., Lohmann, K.C., McKenzie, J.M., and Savin, S. eds., Climate Change in Continental Isotopic Records Geophysical Monograph, Geophysical Monograph Series, v. 78, p. 1–36, doi:10.1029/GM078p0001.

Rozas-Davila, A., Rodbell, D.T., and Bush, M.B., 2023, Pleistocene megafaunal extinction in the grasslands of Junín-Peru: Journal of Biogeography, v. 50, p. 755–766, doi:10.1111/jbi.14566.

Sagredo, E.A., Rupper, S., and Lowell, T. V., 2014, Sensitivities of the equilibrium line altitude to temperature and precipitation changes along the Andes: Quaternary Research, v. 81, p. 355–366, doi:10.1016/j.yqres.2014.01.008.

Santi, L.M., Arnold, A.J., Ibarra, D.E., Whicker, C.A., Mering, J.A., Lomarda, R.B., Lora, J.M., and Tripati, A., 2020, Clumped isotope constraints on changes in latest Pleistocene hydroclimate in the northwestern Great Basin: Lake Surprise, California: GSA Bulletin, v. 132, p. 2669–2683, doi:10.1130/B35484.1.

Schauble, E.A., Ghosh, P., and Eiler, J.M., 2006, Preferential formation of ^{13}C–^{18}O bonds in carbonate minerals, estimated using first-principles lattice dynamics: Geochimica et Cosmochimica Acta, v. 70, p. 2510–2529, doi:10.1016/j.gca.2006.02.011.

Schiferl, J. et al., 2023, A neotropical perspective on the uniqueness of the Holocene among interglacials: Nature Communications, v. 14, p. 7404, doi:10.1038/s41467-023-43231-0.

Schoenemann, S.W., Schauer, A.J., and Steig, E.J., 2013, Measurement of SLAP2 and GISP $\delta^{17}O$ and proposed VSMOW-SLAP normalization for $\delta^{17}O$ and $^{17}O_{excess}$: Rapid Communications in Mass Spectrometry, v. 27, p. 582–590, doi:10.1002/rcm.6486.

Seltzer, G., Rodbell, D., and Burns, S., 2000, Isotopic evidence for late Quaternary climatic change in tropical South America: Geology, v. 28, p. 35, doi:10.1130/0091-7613(2000)28<35:IEFLQC>2.0.CO;2.

SENAMHI, 2023, Datos Hidrometeorológicos a nivel nacional:, https://www.senamhi.gob.pe/?&p=estaciones (accessed January 2023).

Smith, J.A., Seltzer, G.O., Farber, D.L., Rodbell, D.T., and Finkel, R.C., 2005, Early Local Last Glacial Maximum in the Tropical Andes: Science, v. 308, p. 678–681, doi:10.1126/science.1107075 ARTICLE.

de Souza, J.G. et al., 2019, Climate change and cultural resilience in late pre-Columbian Amazonia: Nature Ecology and Evolution, v. 3, p. 1007–1017, doi:10.1038/s41559-019-0924-0.

Stansell, N.D., Licciardi, J.M., Rodbell, D.T., and Mark, B.G., 2017, Tropical ocean-atmospheric forcing of Late Glacial and Holocene glacier fluctuations in the Cordillera Blanca, Peru: Geophysical Research Letters, v. 44, p. 4176–4185, doi:10.1002/2016GL072408.

Stansell, N.D., Rodbell, D.T., Abbott, M.B., and Mark, B.G., 2013, Proglacial lake sediment records of Holocene climate change in the western Cordillera of Peru: Quaternary Science Reviews, v. 70, p. 1–14, doi:10.1016/J.QUASCIREV.2013.03.003.

Stansell, N.D., Rodbell, D.T., Licciardi, J.M., Sedlak, C.M., Schweinsberg, A.D., Huss, E.G., Delgado, G.M., Zimmerman, S.H., and Finkel, R.C., 2015, Late Glacial and Holocene glacier fluctuations at Nevado Huaguruncho in the Eastern Cordillera of the Peruvian Andes: Geology, v. 43, p. 747–750, doi:10.1130/G36735.1.

Stute, M., Forster, M., Frischkorn, H., Serejo, A., Clark, J.F., Schlosser, P., Broecker, W.S., and Bonani, G., 1995, Cooling of Tropical Brazil (5°C) During the Last Glacial Maximum: Science, v. 269, p. 379–383, doi:10.1126/science.269.5222.379.

Surma, J., Assonov, S., Herwartz, D., Voigt, C., and Staubwasser, M., 2018, The evolution of ^{17}O-excess in surface water of the arid environment during recharge and evaporation: Scientific Reports, v. 8, p. 4972, doi:10.1038/s41598-018-23151-6.

Terzer-Wassmuth, S., Araguás-Araguás, L.J., Wassenaar, L.I., and Stumpp, C., 2023, Global and local meteoric water lines for $\delta^{17}O/\delta^{18}O$ and the spatiotemporal distribution of $\Delta'^{17}O$ in Earth's precipitation: Scientific Reports, v. 13, p. 19056, doi:10.1038/s41598-023-45920-8.

Thompson, L.G., Mosely-Thompson, E., Davis, M.E., Lin, P.-N., Henderson, K.A., Cole-Dai, J., Bolzan, J.F., and Liu, K. -b., 1995, Late Glacial Stage and Holocene Tropical Ice Core Records from Huascaran, Peru: Science, v. 269, p. 46–50.

Vera, C., Silvestri, G., Liebmann, B., and González, P., 2006, Climate change scenarios for seasonal precipitation in South America from IPCC-AR4 models: Geophysical Research Letters, v. 33, p. L13707, doi:10.1029/2006GL025759.

Voigt, C., Herwartz, D., Dorador, C., and Staubwasser, M., 2021, Triple oxygen isotope systematics of evaporation and mixing processes in a dynamic desert lake system:

Hydrology and Earth System Sciences, v. 25, p. 1211–1228, doi:10.5194/hess-25-1211-2021.

Vuille, M., Burns, S.J., Taylor, B.L., Cruz, F.W., Bird, B.W., Abbott, M.B., Kanner, L.C., Cheng, H., and Novello, V.F., 2012, A review of the South American monsoon history as recorded in stable isotopic proxies over the past two millennia: Climate of the Past, v. 8, p. 1309–1321, doi:10.5194/cp-8-1309-2012.

Vuille, M., and Werner, M., 2005, Stable isotopes in precipitation recording South American summer monsoon and ENSO variability: Observations and model results: Climate Dynamics, v. 25, p. 401–413, doi:10.1007/s00382-005-0049-9.

Wang, Z., Schauble, E.A., and Eiler, J.M., 2004, Equilibrium thermodynamics of multiply substituted isotopologues of molecular gases: Geochimica et Cosmochimica Acta, v. 68, p. 4779–4797, doi:10.1016/j.gca.2004.05.039.

Ward, B.M., Wong, C.I., Novello, V.F., McGee, D., Santos, R. V., Silva, L.C.R., Cruz, F.W., Wang, X., Edwards, R.L., and Cheng, H., 2019, Reconstruction of Holocene coupling between the South American Monsoon System and local moisture variability from speleothem $\delta^{18}O$ and $^{87}Sr/^{86}Sr$ records: Quaternary Science Reviews, v. 210, p. 51–63, doi:10.1016/j.quascirev.2019.02.019.

Weidhaas, N., 2017, A 25,000-year lake level history of Lake Junin, Peru from stratigraphic and oxygen isotope studies [MS Thesis]: University of Pittsburgh.

Woods, A., 2021, A sedimentary perspective from Lake Junín on monsoon strength and glaciation in the tropical Andes over multiple glacial cycles [PhD Thesis]: University of Pittsburgh.

Woods, A. et al., 2020, Andean drought and glacial retreat tied to Greenland warming during the last glacial period: Nature Communications, v. 11, p. 5135, doi:10.1038/s41467-020-19000-8.

Wostbrock, J.A.G., Cano, E.J., and Sharp, Z.D., 2020, An internally consistent triple oxygen isotope calibration of standards for silicates, carbonates and air relative to VSMOW2 and SLAP2: Chemical Geology, p. 1–9, doi:10.1016/j.chemgeo.2019.119432.

Wright, H.E., 1983, Late-Pleistocene glaciation and climate around the Junin Plain, central Peruvian highlands.: Geografiska Annaler, Series A, v. 65 A, p. 35–43, doi:10.1080/04353676.1983.11880072.

Young, E.D., Galy, A., and Nagahara, H., 2002, Kinetic and equilibrium mass-dependent isotope fractionation laws in nature and their geochemical and cosmochemical significance: Geochimica et Cosmochimica Acta, v. 66, p. 1095–1104, doi:10.1016/S0016-7037(01)00832-8.

Chapter 4 Large Swings In South American Tropical Water Balance Driven By Orbital Forcings[3]

4.1 Abstract

Despite the importance of tropical monsoons in controlling the distribution of heat and water on Earth, details about how tropical temperatures and water balance respond to global climate change remain poorly understood. Sediment records at Lake Junín (11 °S) provide an opportunity to explore these connections over the last 650 ka. However, the existing paleoclimate records from the lake reflect glacial extent and pollen assemblages, which are sensitive to both temperature and water balance change, so it is difficult to isolate which factor(s) contribute(s) to changes in the proxy records. While previous studies suggest that changes in the clastic sediment abundance in the core (a proxy of glacial extent) is indicative of major swings in hydrology, attributing these changes to water balance isn't possible without independent controls on temperature. Here, we use the clumped and triple oxygen isotope distributions of lake carbonates to develop temperature and water balance records at Lake Junín. We focus on two interglacials, the Holocene and MIS 15, when the glacial proxy suggests significant and rapid temperature and/or water balance change occurred. We find that water temperatures at Lake Junín during MIS 15 and the Holocene were similar to present day, and do not explain the variability in the glacial proxy. Conversely, lake water evaporation, and, by extension, water balance was highly variable during MIS 15 and Lake Junín alternated between an outflow-only open-basin and a (nearly) closed basin. Curiously, the amplitude of evaporative change was significantly less during the Holocene. While water balance clearly follows a precession pacing during both interglacials and supports a connection to the South American summer monsoon (SASM), precession cannot explain the difference in amplitude of water balance variability between the Holocene and MIS 15. We postulate that orbital eccentricity is responsible for augmenting SASM strength (and Lake Junín's

[3] Coauthors: Naomi E. Levin, Donald T. Rodbell, Mark B. Abbott, Benjamin H. Passey, and Scott Katz. In preparation for submission to *Geology*.

water balance) during the Holocene and MIS 15, leading to greater variability during MIS 15. These results suggest the planetary energy budget and heat distribution are important controls on monsoon intensity and water balance at Lake Junín during interglacials.

4.2 Introduction

The tropics are integral for the global water cycle however, until recently, it was unclear if the tropics followed the same rhythm as global climate. New sedimentological and pollen records from Lake Junín, Peru, span the last 650 ka and definitively show that tropical climate and global glacial cycles were in sync, providing a new opportunity to study the connection between the tropics and global climate forcings (Figure 4.1–4.2; Rodbell et al., 2022; Schiferl et al., 2023).

The sediments in the Lake Junín core reflect the climate history of the central Andes. During glacial intervals, glaciers form in Lake Junín's upper catchment, eroding and transporting sediment to the lake (Smith et al., 2005; Woods et al., 2020; Rodbell et al., 2022). The geochemical signature of the lake's clastic sediments (high Ti/Ca ratios and magnetic susceptibility) is distinct from the authigenic carbonates and peats that characterize the interglacials (Rodbell et al., 2008, 2022). Rodbell et al. (2022) leverage these distinctions and develop a metric called the Junín "Glacial Index" (GI). The GI was originally interpreted as a record of "*clastic sediment flux and the extent of regional ice cover*," which is straightforward during glacials, but is more difficult to interpret during ice-free interglacials when clastic flux was consistently very low (see Figure 4.1). Instead, previous studies have suggested that changes in interglacial sedimentology may reflect differences in water levels and lake hydrology (Woods, 2021; Rodbell et al., 2022). Therefore, we hypothesize that the GI could reflect changes in lake water balance during interglacials, rather than glacial extent or temperature changes.

In the South American low latitudes, the South American summer monsoon (SASM) is the dominant atmospheric feature and transports moisture from the Atlantic across the continent (Vera et al., 2006; Garreaud et al., 2009; Marengo et al., 2012). Speleothem isotope records suggest that changes in SASM over the last ~350 ka follow a precession pacing, consistent with long-term changes in seasonal energy budgets between the northern and southern hemispheres (Cruz et al., 2005; Cheng et al., 2013; Liu and Battisti, 2015; Wang et al., 2017). Accordingly, we hypothesize that if the Lake Junín GI reflects interglacial water balance changes, the timing and magnitude of these changes will relate to changes in the SASM.

To test these hypotheses, we use clumped (Δ_{47}) and triple oxygen ($\Delta'^{17}O$) isotopes of carbonate sediments to reconstruct temperature and water balance histories at Junín during two interglacial periods: Marine Isotope Stage 15 (MIS 15; 621–563 ka), and the Holocene (11.7 ka–present). We focus our analysis on MIS 15 and the Holocene for two reasons; first, GI values during both interglacials are very low (Figure 4.1), suggesting negligible contributions of glacial sediment to the lake; therefore the GI must be reflecting non-glacial factors at these times. Second, these intervals allow us to test our hypothesis that the GI is linked to changes in SASM, as SASM variability over the Holocene is already well-established, and large changes in southern hemisphere summer insolation during MIS 15 suggest the SASM was also variable at this time.

Here we present new Δ_{47} and $\Delta'^{17}O$ data from MIS 15 and combine these data with a recently reported Holocene dataset (Katz et al., *in review*). Our $\Delta'^{17}O$ results indicate that significant variations in regional water balance occurred during both interglacials. Water balance changes track precession and confirm a link to the SASM and the GI. Temperatures during both interglacials were stable and similar to present. The primary difference between the two records is that water balance variations are much larger in amplitude during MIS 15; in our analysis we discuss the role of orbital parameters on monsoon dynamics to explain these observations.

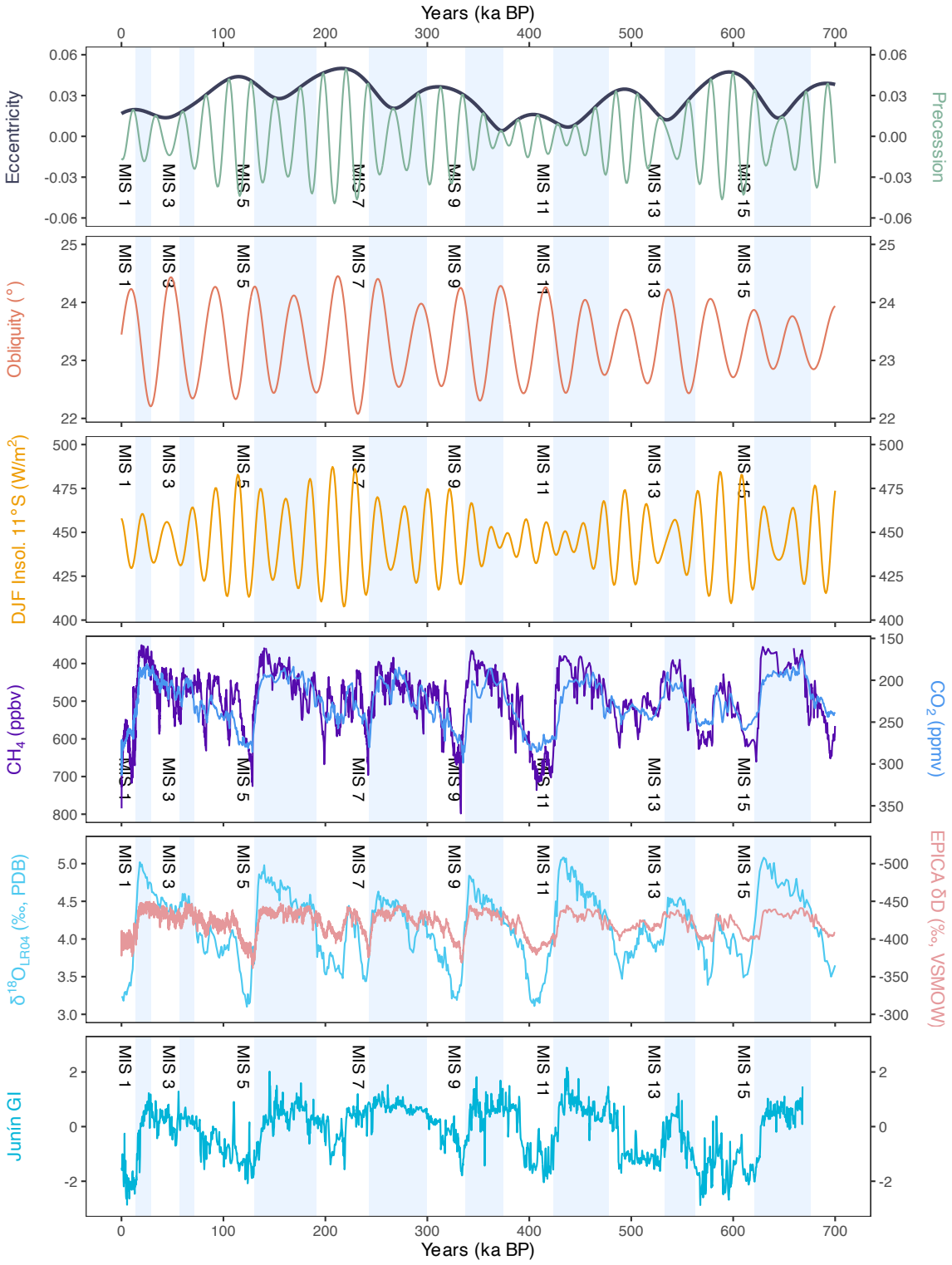

Figure 4.1: Orbital parameters and proxy records over the last 700 ka. (A) Eccentricity, precession (shown as $e\sin(\varpi)$, where e is the eccentricity parameter and ϖ is the true solar longitude of the perihelion), (B) obliquity, and (C) average DJF insolation at 11 °S were calculated from orbital solutions of Laskar et al. (2004) using the R package *palinsol* (Crucifix, 2016). (D) Atmospheric CH_4 (Loulergue et al., 2008) and CO_2 (Bereiter et al., 2015) records from EPICA Dome C (note y-axis scale is reversed). (E) Benthic foraminiferal $\delta^{18}O$ "stack" (Lisiecki and Raymo, 2005) and EPICA

Dome C ice core δD record (Jouzel et al., 2007). (F) Lake Junín Glacial Index (GI) (Rodbell et al., 2022). Glacial intervals are indicated by light blue vertical bars which extend through each panel; interglacials are labeled by Marine Isotope Stages (i.e., "MIS") following boundary dates of Lisiecki and Raymo (2005).

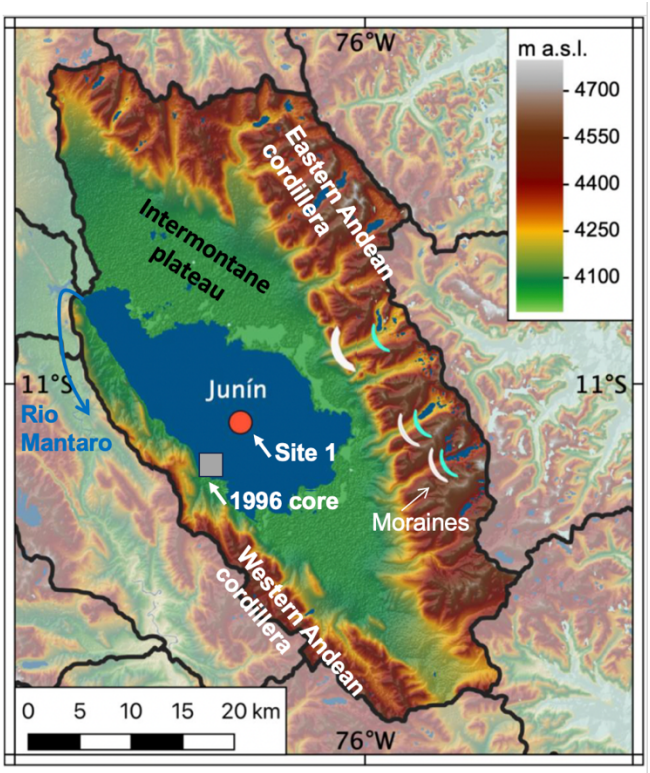

Figure 4.2: Map of the Lake Junín catchment. Thick black lines denote catchment boundaries and the color scale bar reflects elevation in meters above sea level (masl). Dark blue regions represent modern lakes. The red circle and grey square indicate the approximate locations of drilling Site 1 where the MIS 15 cores were collected (Hatfield et al., 2020b, 2020a; Chen et al., 2020; Rodbell et al., 2022) and the 1996 core where Holocene cores were collected (Katz et al. *in review*; Seltzer et al., 2000), respectively. Figure adapted from Woods et al. (2020).

4.3 Study area & background

The Junín region is located on the western extent of the SASM range (Vera et al., 2006; Garreaud et al., 2009; Marengo et al., 2012; Woods et al., 2020) and 70% of annual rainfall (900–1,000 mm) occurs during the extended wet season from October–April when SASM is in the strengthened phase (SENAMHI, 2023).

Lake Junín is a large, shallow lake (>300 km^2 surface area; 8–12 m water depth) situated on a high elevation plateau in Peru (Figure 4.2; 11.0 °S; 76.1 °W; 4080 masl). The lake is bound laterally by the Eastern and Western Andean Cordillera, and to the north by a glacial outwash fan. Bedrock exposed throughout the upper catchment is primarily Jurassic–Triassic marine carbonate with minor outcrops of Carboniferous carbonates and sandstones and Permian to Neogene intrusive units (Cobbing et al., 1996).

The sediment cores used in this study were collected from Lake Junín's depocenter, i.e., "Site 1" (Figure 4.2), from a floating drilling platform in 2015 (Hatfield et al., 2020b). The core chronology for the last 677 ka is based on radiometric dating (^{14}C, U/Th) and paleomagnetic tie points (Hatfield et al., 2020a; Chen et al., 2020; Woods et al., 2020). More recently, Rodbell et al. (2022) tuned the Junín age model to the EPICA Dome C core (Jouzel et al., 2007) using nine tie points; we present data on this age model.

4.4 Sample selection & methods

We selected 18 samples for Δ_{47} and $\Delta'^{17}O$ analysis from intervals of the Lake Junín core that span the full GI range during MIS 15 (Figure S4.1). Samples are >70 wt% carbonate and were treated overnight with 10% hydrogen peroxide and sieved, retaining the <63 μm size fraction for analysis.

Isotope analysis was performed at the University of Michigan Isotopologue Paleosciences Laboratory using a Nu Perspective IRMS (see Supplementary Information (Section 4.8.1–4.8.2) for isotope notation and extended methods). Δ_{47} analysis was conducted on a CO_2 analyte over *m/z* 44–49 following methods of Passey et al. (2010) to produce $\delta^{13}C$, $\delta^{18}O$, and Δ_{47} values. $\Delta'^{17}O$ analysis was conducted on an O_2 analyte produced via an acid digestion-methanation-fluorination process (Passey et al., 2014; Ellis and Passey, 2023). $\delta^{18}O$, $\delta^{17}O$, and $\Delta'^{17}O$ values are calculated from *m/z* 32–36 measurements. For isotope measurements, we report the mean and 1σ standard deviation of replicate analyses and use mean values for all calculations (Table 4.1).

Carbonate formation temperatures (*T*) were calculated from Δ_{47} values and reflect lake water temperature at the time of carbonate formation. *T* values were also used to evaluate oxygen isotope fractionation during carbonate formation, from which we derive past lake water $\delta^{18}O$ ($\delta^{18}O_{LW}$) and $\Delta'^{17}O$ ($\Delta'^{17}O_{LW}$) values from carbonate isotopes (see Supplementary Information (Section 4.8.2.3) for more details).

4.5 Results & Interpretations

The MIS 15 *T* values range from 6 to 14 °C and show no systematic trends over time, indicating that lake water temperatures were stable within analytical uncertainty (Figure S4.2). The average *T* (11 ± 3 °C) is indistinguishable from *T* values derived from both Holocene lake

carbonates at Lake Junín (10 ± 2 °C) and modern lake carbonates in this region (13 ± 3 °C; Figure S4.2; Katz et al., 2023; *in review*), illustrating that Lake Junín water temperatures during MIS 15 were similar to present. This is consistent with modeling studies that suggest temperatures in the South American tropics were similar to present (within –0.5 to 0.2 °C) during both MIS 15 and the Holocene (Berger and Yin, 2012).

Carbonate $\delta^{18}O$ ($\delta^{18}O_C$) values derived from Δ_{47} analysis range from -17.4 to -3.0 ‰ (VPDB). Using paired $\delta^{18}O_C$ and *T* values, we calculate $\delta^{18}O_{LW}$ values ranging from -18.5 to -4.0 ‰ (VSMOW; Figure S4.3). $\Delta'^{17}O_{LW}$ values range from -14 to 43 per meg (VSMOW-SLAP; Figure 4.3). See Table 4.1 for data and Supplementary Information (Section 4.8.2.3) for calculation details.

Both $\Delta'^{17}O_{LW}$ and $\delta'^{18}O_{LW}$ values show a striking ~23 ka cyclicity that matches changes in orbital precession and, by extension, southern hemisphere summer insolation, implying a likely connection with the SASM (Figure 4.3, S4.3). High summer insolation corresponds with low $\delta'^{18}O_{LW}$ values and high $\Delta'^{17}O_{LW}$ values; the reverse is observed when summertime insolation is low (Figure 4.3, S4.3). Importantly, insolation, $\delta'^{18}O_{LW}$, and $\Delta'^{17}O_{LW}$ show a very similar relationship during the Holocene, suggesting that there may be similar forcing mechanisms among the two interglacials.

Commonly, Rayleigh distillation is invoked to explain $\delta^{18}O$ records in the central Andes because enhanced SASM strength is associated with low $\delta^{18}O$ values of local precipitation and this signal is recorded by speleothems and other types of geologic records (e.g., Vuille and Werner, 2005; Bird et al., 2011; Kanner et al., 2013). At first glance, it is tempting to interpret the $\delta'^{18}O_{LW}$ records from Lake Junín as reflecting SASM strength because the $\delta'^{18}O_{LW}$ values are lowest when summer insolation is highest (i.e., strong SASM) and vice versa (Figure S4.3). However, the magnitude of $\delta'^{18}O_{LW}$ change (~15 ‰) is much larger than we observe in South American speleothem records over the last ~250 ka (~5 ‰; e.g., Cruz et al., 2005; Cheng et al., 2013; Wang et al., 2017), suggesting that although changes in Rayleigh distillation probably explain some of the $\delta'^{18}O_{LW}$ trend, this mechanism alone cannot explain the entirety of the $\delta'^{18}O_{LW}$ record. Furthermore, Rayleigh distillation has little influence on precipitation $\Delta'^{17}O$ values in South America today (e.g., Aron et al., 2021b), so this mechanism cannot explain the large $\Delta'^{17}O_{LW}$

trends during MIS 15 or the Holocene. Accordingly, we look to other drivers that can explain the observed $\Delta'^{17}O_{LW}$ and $\delta'^{18}O_{LW}$ records.

Following the framework presented by Katz et al. (*in review*) for Lake Junín during the Holocene, we interpret $\Delta'^{17}O_{LW}$ values as reflecting lake water evaporative state. Under this framework, high $\Delta'^{17}O_{LW}$ values near modern-day precipitation $\Delta'^{17}O$ ($\Delta'^{17}O_P = 31 \pm 5$ per meg; Katz et al., 2023) reflect negligible evaporation in an outflow-dominated lake, while lower $\Delta'^{17}O_{LW}$ values reflect more significant evaporative losses from the lake. Similar to $\Delta'^{17}O_{LW}$, evaporation also causes $\delta'^{18}O_{LW}$ values to be increasingly offset from precipitation $\delta^{18}O$, with $\delta'^{18}O_{LW}$ increasing as a result of evaporative loss. Using a numerical modeling approach, Katz et al. (*in review*) also demonstrate that $\Delta'^{17}O_{LW}$ values can be used to quantify lake water balance (i.e., the volumetric proportion of water entering the lake vs water lost to evaporation), whereby higher $\Delta'^{17}O_{LW}$ values correspond with a more positive water balance compared to low $\Delta'^{17}O_{LW}$ values (e.g., also following Gázquez et al., 2018; Surma et al., 2018; Passey and Ji, 2019). The highest $\Delta'^{17}O_{LW}$ values during MIS 15 (~30 to 43 per meg) are similar to modern $\Delta'^{17}O_P$ in the central Andes (Aron et al., 2021b; Katz et al., 2023) and likely reflect a wet endmember state when evaporation was negligible and outflow dominated the lake's water balance. In contrast, the lowest $\Delta'^{17}O_{LW}$ values during MIS 15 (~ -14 to -9 per meg) indicate significant evaporative losses from the lake (on the order of ~50–100% by volume), indicating the lake basin was (nearly) closed (Katz et al. *in review*). Using this framework in the Discussion (Section 4.6) below, we interpret $\Delta'^{17}O_{LW}$ values as reflecting lake basin evaporative state and, by extension, local water balance.

Table 4.1: MIS 15 samples and summarized isotope data.

				Derived from clumped isotope analysis										Derived from triple oxygen isotope analysis			
Sample ID	**Comp Depth (m)**	**Age (ka BP)**[†]	**No. rep. Δ_{47} / $\Delta'^{17}O$ anal.**	**$\delta^{13}C_C$ (‰, VPDB)**	**$\delta^{13}C$ 1σ sd (‰)**	**$\delta^{18}O_C$ (‰, VPDB)**	**$\delta^{18}O$ 1σ sd (‰)**	**Δ_{47} (‰, ICDES90)**	**Δ_{47} 1σ SD (‰)**	***T*** **(°C)**[‡]	***T*** **1σ sd (°C)**	**$\delta'^{18}O_{LW}$ (‰, VSMOW)**[#]	**$\delta'^{18}O_{LW}$ 1σ sd (‰)**[&]	**$\Delta'^{17}O_C$ (per meg; VSMOW-SLAP)**	**$\Delta'^{17}O_C$ 1σ sd (per meg)**	**$\Delta'^{17}O_{LW}$ (per meg, VSMOW-SLAP)** [*f*]	**$\Delta'^{17}O_{LW}$ 1σ sd (per meg)**[*]
1C-23H-2 41-42 cm	70.734	564.2	2 / 3	1.723	0.122	-14.109	0.028	0.656	0.008	6.0	2.2	-15.930	0.36	-67	8	29	5
1C-23H-2 65-66 cm	70.974	566.6	4 / 4	-0.458	0.043	-14.750	0.024	0.628	0.008	14.0	2.3	-14.780	0.25	-57	5	34	3
1C-23H-2 73-74 cm	71.054	567.3	4 / 2	7.646	0.170	-10.199	0.120	0.639	0.019	10.9	5.6	-10.875	0.62	-76	6	17	5
1E-15H-1 51-52 cm	71.629	573.0	4 / 2	12.964	0.065	-6.717	0.097	0.630	0.024	13.8	7.5	-6.711	0.82	-101	1	-9	3
1E-15H-1 97-98 cm	72.089	577.5	3 / 3	16.466	0.332	-2.969	0.075	0.649	0.006	7.9	1.6	-4.269	0.22	-104	8	-9	5
1E-15H-1 105-106 cm	72.169	578.3	4 / 3	14.872	0.080	-6.075	0.049	0.646	0.019	8.9	5.5	-7.150	0.62	-91	5	4	3
1E-15H-1 119-120 cm	72.309	579.6	2 / 3	3.535	0.024	-12.895	0.082	0.628	0.005	14.0	1.5	-12.897	0.24	-71	9	20	5
1E-15H-1 133-134 cm	72.449	581.0	-- / 3	--	--	--	--	--	--	--	--	--	--	-67 [§]	6	26	--
1E-15H-2 5-6 cm	72.671	583.2	2 / 3	1.403	0.141	-17.331	0.042	0.636	0.008	11.8	2.4	-17.904	0.37	-63	9	30	5
1E-15H-2 7-8 cm	72.691	583.4	3 / 5	0.934	0.203	-17.366	0.247	0.645	0.011	9.1	3.3	-18.526	0.44	-51	9	43	4
1C-24H-1 71-72 cm	72.956	588.1	4 / 2	7.360	0.158	-10.421	0.178	0.629	0.026	14.1	7.8	-10.392	0.85	-77	3	14	3
1C-24H-1 133-134 cm	73.576	599.3	2 / 4	14.195	0.028	-3.033	0.043	0.645	0.010	9.1	3.0	-4.044	0.48	-108	6	-14	3
1C-24H-1 135-136 cm	73.596	599.7	-- / 1	--	--	--	--	--	--	--	--	--	--	-91 [§]	--	2	--
1C-24H-1 145-146 cm	73.696	601.5	4 / 3	7.871	0.066	-11.126	0.065	0.630	0.006	13.6	1.8	-11.214	0.20	-72	2	19	1
1C-24H-2 13-14 cm	73.890	605.0	3 / 4	0.836	0.074	-14.098	0.070	0.641	0.001	10.1	0.2	-14.992	0.05	-72	7	22	4
1C-24H-2 23-24 cm	73.990	606.8	3 / 5	-0.093	0.062	-14.506	0.124	0.640	0.020	10.7	5.7	-15.261	0.72	-67	6	26	3
1C-24H-2 69-70 cm	74.450	615.2	4 / 3	12.439	0.212	-8.575	0.234	0.631	0.018	13.3	5.4	-8.693	0.60	-80	4	11	3
1C-24H-2 95-96 cm	74.710	619.9	4 / 3	14.627	0.345	-4.681	0.061	0.629	0.011	13.9	3.3	-4.645	0.36	-99	2	-8	2

[†] Presented on the age model of Rodbell et al., 2022.

[‡] Calculate from Δ_{47} values using Anderson et al., 2021, Equation 1.

[#] Calculated from $\delta^{18}O_C$ and $^{18}\alpha_{cc\text{-}wt}$ (calculated from *T* and equations from Kim and O'Neil, 1997).

[&] Propagated uncertainty based on clumped isotope $\delta^{18}O_C$ and *T* values.

[§] *T* assumed as 11.3 °C.

[*f*] Calculated from $\delta^{18}O_C$ and $\delta^{17}O_C$ values derived from $\Delta'^{17}O$ analysis and using $\lambda_{cc\text{-}wt} = 0.5250$ (Huth et al., 2022).

[*] Propagated uncertainty based on $\Delta'^{17}O_C$ and *T* values.

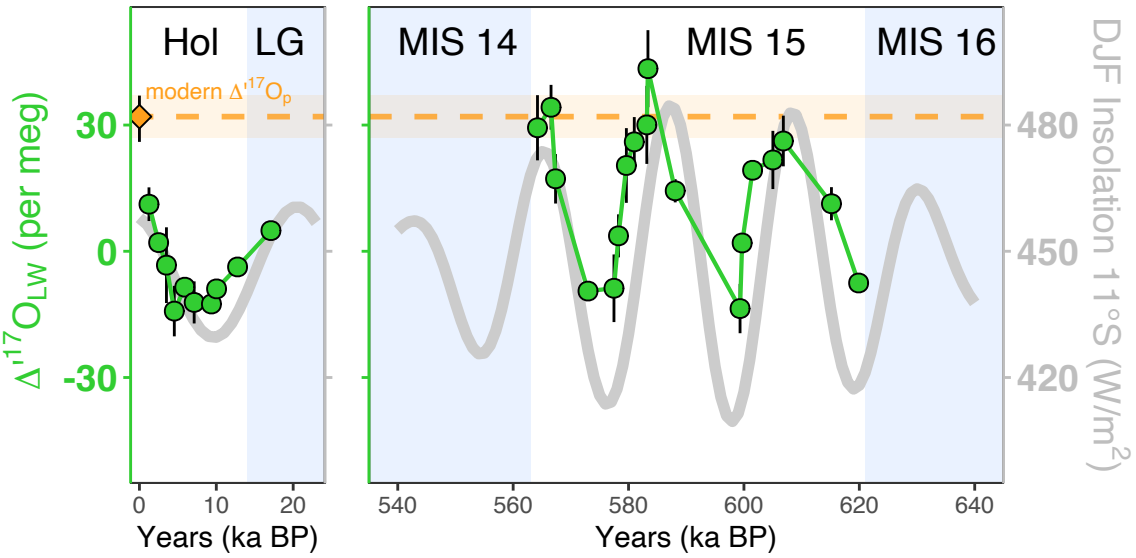

Figure 4.3: Lake Junín $\Delta'^{17}O_{LW}$ values versus insolation. Lake Junín $\Delta'^{17}O_{LW}$ values (means are shown as green circles with 1σ SD) during the Holocene ("Hol" = MIS 1), Last Glacial ("LG"), and MIS 15 versus DJF insolation at 11 °S (grey line). Modern $\Delta'^{17}O_P$ (31 ± 5 per meg; Katz et al., 2023) at Junín is shown for reference (orange diamond at 0 years BP and orange horizontal band). Insolation was calculated from the orbital solutions of Laskar et al. (2004) using the R package *palinsol* (Crucifix, 2016).

4.6 Discussion

4.6.1 The role of orbital forcings on regional water balance

4.6.1.1 Precession

The most striking feature of the Lake Junín $\Delta'^{17}O_{LW}$ and $\delta'^{18}O_{LW}$ records is the ~23 ka pacing during both MIS 15 and the Holocene (Figure 4.3; S4.3). This pacing closely matches precession's influence on austral summer insolation and suggests a connection to the SASM. The highest $\Delta'^{17}O_{LW}$ values are observed when summer insolation is high, suggesting evaporation is low when SASM is strong; the reverse is true when $\Delta'^{17}O_{LW}$ values are low (Figure 4.3). Additionally, $\Delta'^{17}O_{LW}$ and $\delta'^{18}O_{LW}$ values exhibit a strong negative correlation (Pearson's r = -0.96), consistent with evaporated waters from modern systems (Figure S4.4). This makes sense from a hydrologic perspective if we assume that changes in the SASM have a direct impact on the local water cycle. This is not surprising at Lake Junín because the large surface area and shallow water depth mean the lake is extremely sensitive to changes in precipitation and/or evaporative

fluxes. Accordingly, we infer that precession's control on SASM is the dominant factor influencing the pace of water balance variations at Lake Junín during both MIS 15 and the Holocene.

4.6.1.2 Eccentricity

The timing of water balance change at Lake Junín (inferred from $\Delta'^{17}O_{LW}$) can be explained by precession-paced changes in SASM strength; however, we observe a larger amplitude of water balance change during MIS 15 than the Holocene (Figure 4.3), which cannot be explained by precession. The large changes in water balance during MIS 15 were accompanied by high amplitude changes in southern hemisphere summer insolation that are related to orbital eccentricity, which was larger during MIS 15 than the Holocene (Figure 4.1; Laskar et al., 2004).

When the Earth is closest to the sun in its orbital path (i.e., perihelion), the planet receives more solar energy than when the planet is far from the sun (i.e., aphelion), resulting in more solar insolation per unit area. Accordingly, at low orbital eccentricity, planetary insolation is relatively similar over the course of the year, minimizing seasonal insolation differences between the hemispheres (Figure 4.4). Comparatively, when eccentricity is high, the difference in solar energy receipts between perihelion and aphelion are maximized, resulting in differential heating at the top of the atmosphere throughout the year. In this way, eccentricity modulates the role of precession on seasonal insolation (Figure 4.1, 4.4). This directly affects interhemispheric temperature gradients and influences atmospheric dynamics, including the position and overturning of Hadley cells, which directly control monsoon systems (e.g., D'Agostino et al., 2020).

When the austral summer (average of December-February) insolation is calculated during MIS 15 and the Holocene, we observe that eccentricity has a large influence on insolation over a precession cycle. Daily summer insolation at 11 °S during MIS 15 ranges from 411 W/m^2 (599 ka, high eccentricity, high precession) to 484 W/m^2 (588 ka, high eccentricity, low precession), the insolation difference is 73 W/m^2, which is 16% of modern summer insolation (Figure S4.5–S4.6; Laskar et al., 2004). During the Holocene, summer insolation ranges from 431 W/m^2 (11 ka, low eccentricity, high precession) to 458 W/m^2 (0 ka, low eccentricity, low precession), the insolation difference is 27 W/m^2 and 6% of modern summer insolation (Figure S4.5–S4.6; Laskar et al., 2004). Northern hemisphere insolation follows an opposite pattern, such that the interhemispheric thermal gradient is maximized at high eccentricity (Figure S4.6). From these calculations, we infer that the SASM was probably more variable during MIS 15, when variations in eccentricity exerted

a strong influence on insolation, than during the Holocene. Accordingly, the larger SASM changes likely explain why water balance changes were larger in amplitude during MIS 15 (Figure 4.3).

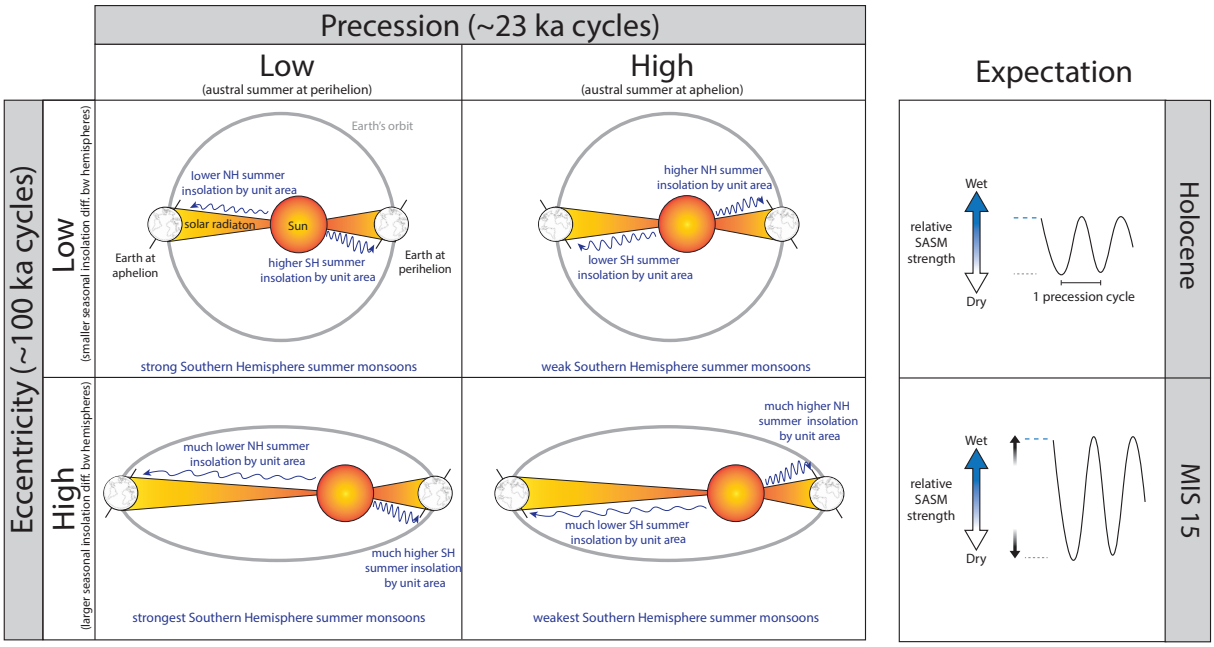

Figure 4.4: Schematic illustrating orbital controls on planetary insolation and expected pattern of hydrologic change. Precession and eccentricity endmembers are shown, note that obliquity (i.e., axial tilt) is constant. "NH" = Northern Hemisphere, "SH" = Southern Hemisphere. Not to scale.

4.6.2 Connecting water balance and the GI

At the outset of this work, we hypothesized that during interglacials, the Lake Junín GI is related to changing water balance, which we can now evaluate using $\Delta'^{17}O_{LW}$ values. Figure 4.5 shows the relationship between $\Delta'^{17}O_{LW}$ and the GI during MIS 15 and the Holocene. The GI is generally low (below 0) for both intervals, consistent with interglacial conditions, but appears to show some structure that matches that of the $\Delta'^{17}O_{LW}$ records. During both interglacials, the lowest GI values are associated with low $\Delta'^{17}O_{LW}$ values, while higher GI values are associated with higher $\Delta'^{17}O_{LW}$ values. This suggests that during MIS 15 and the Holocene, our initial expectation was correct; the GI does reflect changes in lake water balance. It is also relevant to note that water balance changes during both MIS 15 and the Holocene occurred during a period when *T* values were stable, within analytical uncertainty (Figure S4.2). This is consistent with hypotheses from

prior work, that suggest hydroclimate variability in the outer-tropics can occur in the absence of large temperature changes (Woods et al., 2020; Rodbell et al., 2022) and cautions against using the GI record as a metric of interglacial temperature change.

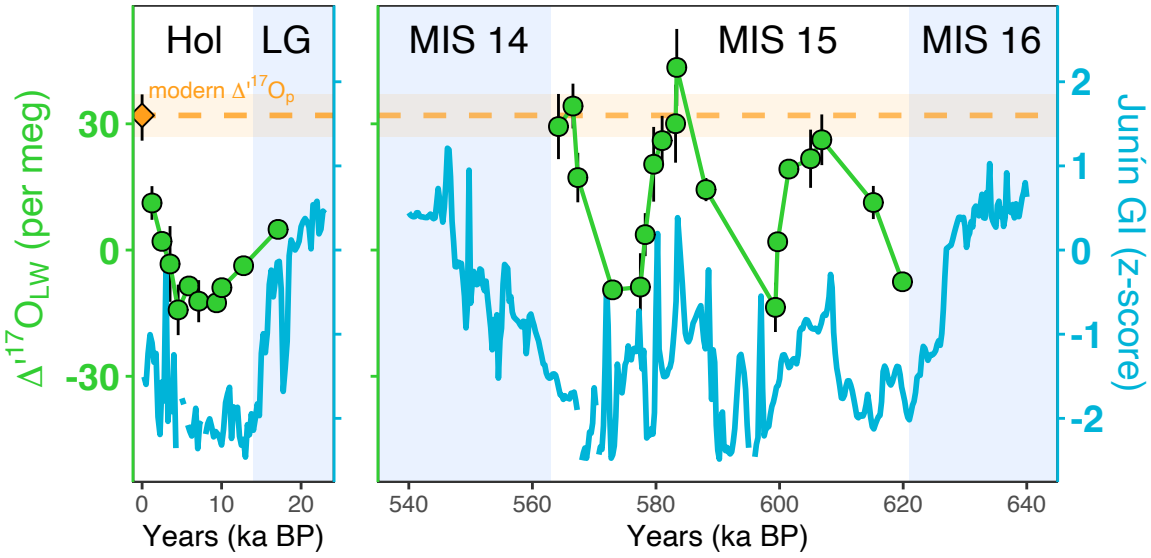

Figure 4.5: As in Figure 4.3 but $\Delta'^{17}O_{LW}$ is shown versus the Junín GI (blue line; Rodbell et al., 2022).

4.7 Conclusions

We present $\Delta'^{17}O$-based evidence of large variations in lake water balance at Lake Junín during MIS 15. The close correspondence between our $\Delta'^{17}O_{LW}$ data and local summertime insolation suggests a link to precession-paced changes in SASM strength and implies that regional water balance also responded to changes in the SASM. Combining these new MIS 15 $\Delta'^{17}O_{LW}$ data with Holocene $\Delta'^{17}O_{LW}$ data from Lake Junín shows that precession controls monsoon and water balance variability during at least two interglacials. However, the amplitude of hydrologic change during MIS 15 is greater than the Holocene, which we attribute to a larger eccentricity parameter and increased SASM variability. These results illustrate the important role of Earth's energy balance on monsoon systems and regional water balance.

Acknowledgements:

We thank Kirsten Andrews, Nick Ellis, Million Mengesha, Julia Kelson, Tyler Huth, Jungpyo Hong, and Jada Langston for analytical and laboratory assistance. Collection of the Lake Junín core was made possible through the efforts of the International Continental Scientific Drilling Program (ICDP). We also thank Elizabeth Olson, David Gillikin, Larry Edwards, Dylan Parmenter, Jungpyo Hong, Laura Lopera, Josef Werne, and Pedro Tapia for useful feedback on the presentation of this work.

Funding:

Funding was provided by the Geological Society of America Student Research Grant (SAK), the University of Michigan Rackham Predoctoral Fellowship (SAK), the University of Michigan Department of Earth and Environmental Sciences (SAK, NEL, BHP) and the National Science Foundation: EAR-2102843 (NEL, BHP), EAR-1402076 (DTR), EAR-2102996 (DTR), EAR-1404113 (MBA) and EAR-2103082 (MBA).

4.8 Supplementary information

4.8.1 Isotope notation

Isotope ratios, ${}^{X}R$, represent the abundance of a rare, heavy isotope to the most abundant isotope of that element, where X represents the heavy isotope mass number. Isotope ratios can be expressed in "delta" (Eq. 1) or "delta prime" (Eq. 2) notation, whereby R values of samples (R_{sample}) are reported with respect to a standard ($R_{standard}$).

$$\delta^{X} = ({}^{X}R_{sample}/{}^{X}R_{standard} - 1) \quad \text{Eq. 1}$$

$$\delta'^{X} = \ln({}^{X}R_{sample}/{}^{X}R_{standard}) \quad \text{Eq. 2}$$

Commonly δ and δ' values are multiplied by 1000 and reported in units of "per mil", ‰.

Mass differences between isotopologues (i.e., molecules with different isotope compositions), cause isotopologues to participate in reactions at different rates (Criss, 1999). This leads to "fractionation," or preferential partitioning of isotopes between different phases or forms

(A and B) (Criss, 1999). The fractionation factor is process-dependent and is parameterized as α:

$$^{x}\alpha_{A-B} = {}^{x}R_A \,/\, {}^{x}R_B \quad \text{Eq. 3}$$

For elements (e.g., O) with more than two stable isotopes (^{16}O, ^{17}O, ^{18}O), fractionation factors are related by a power law:

$$^{17}\alpha_{A-B} = \left(^{18}\alpha_{A-B}\right)^{\theta} \quad \text{Eq. 4}$$

Like α, the value of θ, the fractionation exponent, is process-dependent. For example, diffusion of liquid water into a dry atmosphere follows $\theta_{diff} = 0.5185$ (Barkan and Luz, 2007), while equilibrium exchange between liquid water and water vapor follows $\theta_{eq} = 0.529$ (Barkan and Luz, 2005).

In nature, it is common for multiple fractionation processes to occur concurrently and the nomenclature λ is used instead of θ to parameterize these more complex relationships. In arrays of natural samples, linear regression in $\delta'^{18}O$–$\delta'^{17}O$ space can be used to approximate λ.

The term $\Delta'^{17}O$ is defined by Eq. 5, and reflects a residual from a reference line, λ_{ref}.

$$\Delta'^{17}O = \delta'^{17}O - \delta'^{18}O \times \lambda_{ref} \quad \text{Eq. 5}$$

In hydrologic studies, λ_{ref} is defined as 0.528, which approximates the slope of the meteoric water line (i.e., Rayleigh distillation) in $\delta'^{18}O$–$\delta'^{17}O$ space (Luz and Barkan, 2010; Aron et al., 2021a; Terzer-Wassmuth et al., 2023). Thereby, fractionating processes that follow a different slope than λ_{ref} (e.g., θ_{diff}) will cause $\Delta'^{17}O$ values to diverge from λ_{ref}. $\Delta'^{17}O$ values are commonly reported in units of "per meg" (1 per meg = 10^{-3} ‰).

In addition to single substitutions of a heavy isotope, R values also describe double substitutions, such as ^{47}R values of CO_2, which reflect the abundance of ^{13}C-^{18}O-^{16}O relative to its light counterpart, ^{12}C-$^{16}O_2$. The statistical likelihood of a double substitution, or "clump," is directly related to the ^{13}R and ^{18}R composition of a sample. A stochastic (i.e., random) distribution of "clumps" (based on ^{13}R and ^{18}R) can be denoted as $^{47}R^*$. However, in CO_2 derived from acid digestion of carbonates, measured ^{47}R values are higher than $^{47}R^*$ (note that a correction is made for the ^{12}C-^{18}O-^{17}O isobar, e.g., Petersen et al., 2019). The difference between $^{47}R^*$ and the measured ^{47}R value is defined as Δ_{47}:

$$\Delta_{47} = \left[\left(\frac{^{47}R}{^{47}R*} - 1\right) - \left(\frac{^{46}R}{^{46}R*} - 1\right) - \left(\frac{^{45}R}{^{45}R*} - 1\right)\right] \times 1000 \quad \text{Eq. 6}$$

Theoretical and experimental studies have shown that carbonate Δ_{47} is directly related to mineralization temperature, with higher carbonate Δ_{47} values reflecting cooler formation temperatures (e.g., Wang et al., 2004; Schauble et al., 2006; Eiler, 2007). As such, carbonate clumped isotope paleothermometry can be used to determine carbonate formation temperatures from a variety of geologic materials (Huntington and Petersen, 2023), including inorganically-precipitated lake carbonates (e.g., Huntington et al., 2010; Hren and Sheldon, 2012; Ingalls et al., 2020; Santi et al., 2020; Fetrow et al., 2022).

4.8.2 Extended methods

4.8.2.1 Clumped isotope analysis and data corrections

Clumped isotope analysis was performed at the University of Michigan (UM) Isotopologue Paleosciences Laboratory (IPL). Our laboratory setup, described by Passey et al. (2010), uses a common acid bath (in-line with our preparatory system) to digest carbonate via a 10 minute digestion in >100 wt% phosphoric acid at 90 °C. The resultant CO_2 analyte and H_2O biproduct are passed through a cryogenic trap, held at -80 to -78 °C, via He carrier gas. H_2O is frozen onto the trap while CO_2 passes through and is collected on a second trap held at liquid nitrogen temperature (-178 °C), and He carrier gas is purged from the system. The CO_2 is then passed through a GC column (-25 to -20 °C) before being recollected on a final trap (-178 °C) and subsequent cryogenic transfer to the mass spectrometer.

Carbonate standards were run using the same setup as for samples. In addition to carbonate samples, we also analyzed a suit of four gas standards, which are introduced to the same preparatory line as carbonates, upstream of the GC column. Two CO_2 gas standards of differing $\delta^{13}C$ and $\delta^{18}O$ compositions are held in a 30 °C water bath and represent thermally-equilibrated low temperature endmembers. These same gasses can also be routed through an on-line furnace system (1000 °C) to produce thermally-equilibrated high temperature endmembers that represent a stochastic distribution of ^{13}C–^{18}O bonds.

Analyses were conducted on a Nu Perspective isotope ratio mass spectrometer in dual inlet mode. Following sample introduction to the bellows, both sample and working gas intensities are

set to 40 nA intensity for *m/z* 44. Analysis consists of 40 cycles of working gas and sample gas measurement, followed by a final working gas measurement. Each measurement is made for 50 seconds on *m/z* 44–49. From these measurements, raw $\delta^{13}C$, $\delta^{18}O$, and Δ_{47} values were calculated versus the working gas using Brand/IUPAC parameters, as recommended by Petersen et al. (2019).

Sample data are corrected by "session," whereby a session reflects a time range (typically weeks to months) where run conditions were stable for all samples and standards. A carbonate standard or gas was run on-average every 3-5 samples.

$\delta^{13}C$ and $\delta^{18}O$ values were normalized to the VPDB reference frame using carbonate standards: ETH1–4 (Bernasconi et al., 2018), IAEA-603, and IAEA-C1 values (Assonov et al., 2020; assuming IAEA-C1 is isotopically identical to IAEA-603, after Huth et al., 2022). An in-house groundwater carbonate (102-GC-AZ01) was not included in standardization to serve as an external check. Measured $\delta^{13}C$ and $\delta^{18}O$ values were regressed against accepted values and the resulting linear model was applied to sample data. Residuals were calculated by subtracting accepted $\delta^{13}C$ and $\delta^{18}O$ values from corrected $\delta^{13}C$ and $\delta^{18}O$ values. Residuals do not show a time-dependent trend, so we did not apply a final residual correction for any session.

Δ_{47} corrections were accomplished using a combination of both equilibrated gasses and carbonate standards (ETH1–3). ETH-4 and 102-GC-AZ01 were not included in standardization to serve as external checks. We converted raw Δ_{47} sample values to the ICDES90 reference frame using the approach outlined by Equations 8–9 of Daëron et al. (2016; also used by Bernasconi et al., 2021; Daëron, 2021). Residual Δ_{47} values were calculated for gas standards and ETH1–3 by subtracting accepted Δ_{47} values from measured Δ_{47} values. Residuals were plotted versus the analysis date/time and a time-dependent polynomial function was modeled for each session. Modeled residual were calculated for all analyses and were used to perform a drift correction, producing the Δ_{47} values reported in this text.

4.8.2.2 Triple oxygen isotope analysis and data corrections

Triple oxygen isotope analysis was performed at the UM IPL on an O_2 analyte which was produced from carbonate using a three step conversion process which includes acid digestion, methanation, and fluorination (following methods described by Passey et al., 2014; Ellis and Passey, 2023).

Acid digestion of carbonates in our lab follows the same setup as described for clumped

isotopes. Following purification, CO_2 is introduced to excess H_2 gas in the presence of an Fe catalyst held at 560 °C. This reaction produces H_2O and CH_4, where H_2O is the species of interest and CH_4 is a byproduct. The slow reaction rate requires CO_2 to be passed over the catalytic reactor multiple times to reach full conversion (Ellis and Passey, 2023). Previously this was accomplished in our system using a closed circulating loop and peristaltic pump (H_2O was continuously cryogenically trapped through this process) (Passey et al., 2014). More recently, a series of traps and values was implemented which pass CO_2 through the catalytic reactor multiple times to reach full conversion (Ellis and Passey, 2023).

The final step of gas preparation is fluorination, in which H_2O is introduced to CoF_3 at 360 °C. Note that liquid H_2O can also be directly injected into the CoF_3 reactor, bypassing the acid digestion and methanation steps required for carbonates. We analyze liquid water standards (including VSMOW and SLAP2) via direct injection of the liquid sample into the fluorination reactor. The fluorination process produces O_2 and byproducts CoF_2 and HF. CoF_2, a solid, remains in the reactor column, while O_2 and HF are cryogenically separated by a trap held at liquid nitrogen temperature. HF is collected on this trap, while O_2 is further purified by passing through a GC column containing 5 Å molecular sieve before being collected on a trap packed with silica gel at liquid nitrogen temperature. Further details are provided by Ellis and Passey (2023). The O_2 is then transferred to a Nu Perspective mass spectrometer for analysis.

Triple oxygen isotope analysis on O_2 is performed in dual inlet mode. Both sample and working gas are set to 20 nA intensity for *m/z* 32. Analysis consists of 40 cycles of working gas and sample gas measurement, followed by a final working gas measurement. Each measurement is made for 50 seconds on *m/z* 32–36. From these measurements, raw $\delta^{17}O$, $\delta^{18}O$, and $\Delta'^{17}O$ values were calculated versus the working gas.

Data normalization is performed by CoF_3 reactor, which typically reflects ~200 analyses (commonly several months of analytical time). Water standards, VSMOW and SLAP2, were analyzed in 3–4 replicates at the start of each reactor and again near the end of the rector (approximately 1–2 months later). Note that here "replicates" refer to unique water injection events, rather than reanalysis of a single gas aliquot. In addition to water standards, carbonate standards, IAEA-C1 and 102-GC-AZ01, are also regularly analyzed.

Normalization of $\delta^{17}O$ and $\delta^{18}O$ values to the VSMOW–SLAP scale follows Schoenemann et al. (2013) where $\Delta'^{17}O$ values of SMOW and SLAP are assigned as 0 per meg and $\delta^{18}O_{SMOW} = 0.000$

‰ and $\delta^{18}O_{SLAP}$ = -55.500 ‰. We also apply a linear drift correction based on analytical date/time and VSMOW residual values. This produces $\Delta'^{17}O$ values of O_2, which for waters, is equal to H_2O, while for carbonates we perform a final transformation to account for fractionation during acid digestion. Following Huth et al. (2022) and other studies (e.g., Kelson et al., 2022, 2023; Katz et al., 2023), we perform a one-point correction that pins $\Delta'^{17}O$ values of IAEA-C1 to those reported by Wostbrock et al. (2020) for IAEA-603: $\Delta'^{17}O$ = -100 per meg (assuming both materials are isotopically identical). Finally, we calculated residual $\Delta'^{17}O$ values between measured values and the long-term mean for our lab's in-house carbonate standard (102-GC-AZ01) to assess analytical performance. For the periods when samples were analyzed for this study, 102-GC-AZ01 residuals are within the typical measurement uncertainty for our lab and did not exhibit a time-dependent trend, so we declined to perform a final time-dependent correction.

4.8.2.3 Calculating $\delta^{18}O_{LW}$ and $\Delta'^{17}O_{LW}$ values and assessing uncertainty

Using *T* values, we calculated $^{18}\alpha_{cc\text{-}wt}$, the fractionation factor between calcite and water (Kim and O'Neil, 1997). For samples lacking clumped isotope values (n=2), we assumed the formation temperature was 11.3 °C, reflecting the mean temperature of our dataset. We also calculated $^{17}\alpha_{cc\text{-}wt}$ from $^{18}\alpha_{cc\text{-}wt}$ using a $\lambda_{cc\text{-}wt}$ value of 0.5250 (Huth et al., 2022; Kelson et al., 2022). Reconstructed lake water $\delta'^{18}O$ values ($\delta'^{18}O_{LW}$) from clumped isotope $\delta^{18}O$ values range from -18.5 to -4.0 ‰ (VSMOW) (Table 4.1). Reconstructed lake water $\Delta'^{17}O$ values ($\Delta'^{17}O_{LW}$) range from -14 to +43 per meg (VSMOW-SLAP) (Figure 4.3; Table 4.1).

We calculated the propagated uncertainty in $\delta'^{18}O_{LW}$ and $\Delta'^{17}O_{LW}$ values using a Monte Carlo re-sampling approach. For $\delta'^{18}O_{LW}$, averages and the 1 σ SE of $\delta^{18}O_C$ and *T* were calculated from replicate clumped isotope analyses. We applied the *rnorm()* function in *R* to model the probability density function (PDF) of both $\delta'^{18}O_C$ and *T* and resampled 10,000 values from both populations. From resampled *T* values, we calculated new $^{18}\alpha_{cc\text{-}wt}$ values, which we used along with resampled $\delta'^{18}O_C$ values to calculate $\delta'^{18}O_{LW}$ values. The 1 σ SD of the new $\delta'^{18}O_{LW}$ PDF is reported in Table 4.1. The propagated uncertainty in $\Delta'^{17}O_{LW}$ values was calculated similarly. Averages and the 1 σ SE of $\delta^{18}O_C$ and $\Delta'^{17}O_C$ were calculated from replicate triple oxygen isotope analyses and the *rnorm()* function was used to generate a PDF from which 10,000 resampled values were generated. The $^{17}\alpha_{cc\text{-}wt}$ values were calculated from resampled $^{18}\alpha_{cc\text{-}wt}$ values. The 1 σ SD of

the new $\Delta'^{17}O_{LW}$ PDF is reported in Table 4.1.

4.8.3 Supplementary figures

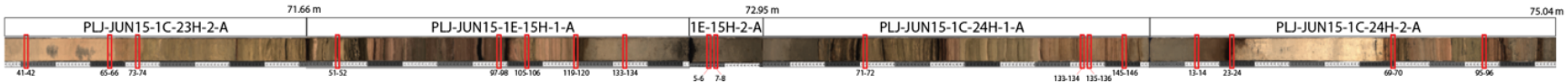

Figure S4.1: High resolution images of the "on-splice" cores covering MIS 15 with sampling locations indicated by red boxes (n = 18). Composite core depths and drive identification are listed along the top. Drive depths are listed along the bottom for each sample. See Table 4.1 for summarized sample information.

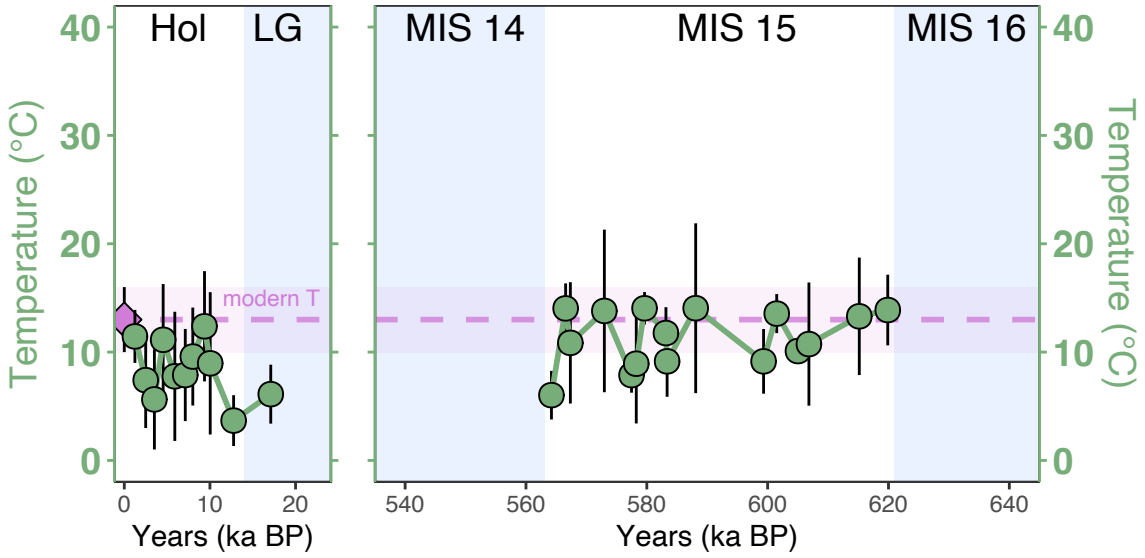

Figure S4.2: Lake Junín water temperatures derived from carbonate Δ_{47} analysis (mean and 1σ SD are shown) during the Holocene ("Hol"), Last Glacial ("LG"), and MIS 15 (using the calibration of Anderson et al., 2021). Modern water temperature derived from Δ_{47} values from lake carbonates in the Junín region (13 ± 3 per meg; Katz et al., 2023) is shown for reference (purple diamond at 0 years BP and purple horizontal band).

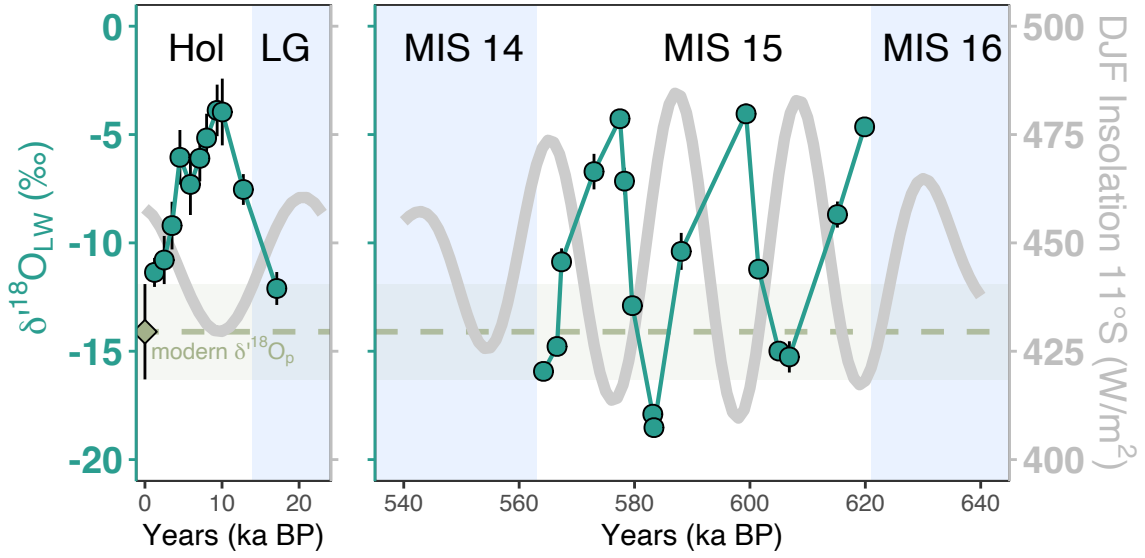

Figure S4.3: Lake Junín MIS 15 $\delta'^{18}O_{LW}$ values (‰; VSMOW) and summer insolation at 11°S. Lake Junín $\delta'^{18}O_{LW}$ values (means are shown as teal circles with 1σ SD, which is sometimes smaller than the symbol) during the Holocene ("Hol" = MIS 1), Last Glacial ("LG"), and MIS 15 versus DJF insolation at 11 °S (grey line). Modern $\delta'^{18}O_P$ (-14.1 ± 2.2 ‰; Katz et al., 2023) at Junín is shown for reference (khaki diamond at 0 years BP and khaki horizontal band). Insolation was calculated from the orbital solutions of Laskar et al. (2004) using the R package *palinsol* (Crucifix, 2016).

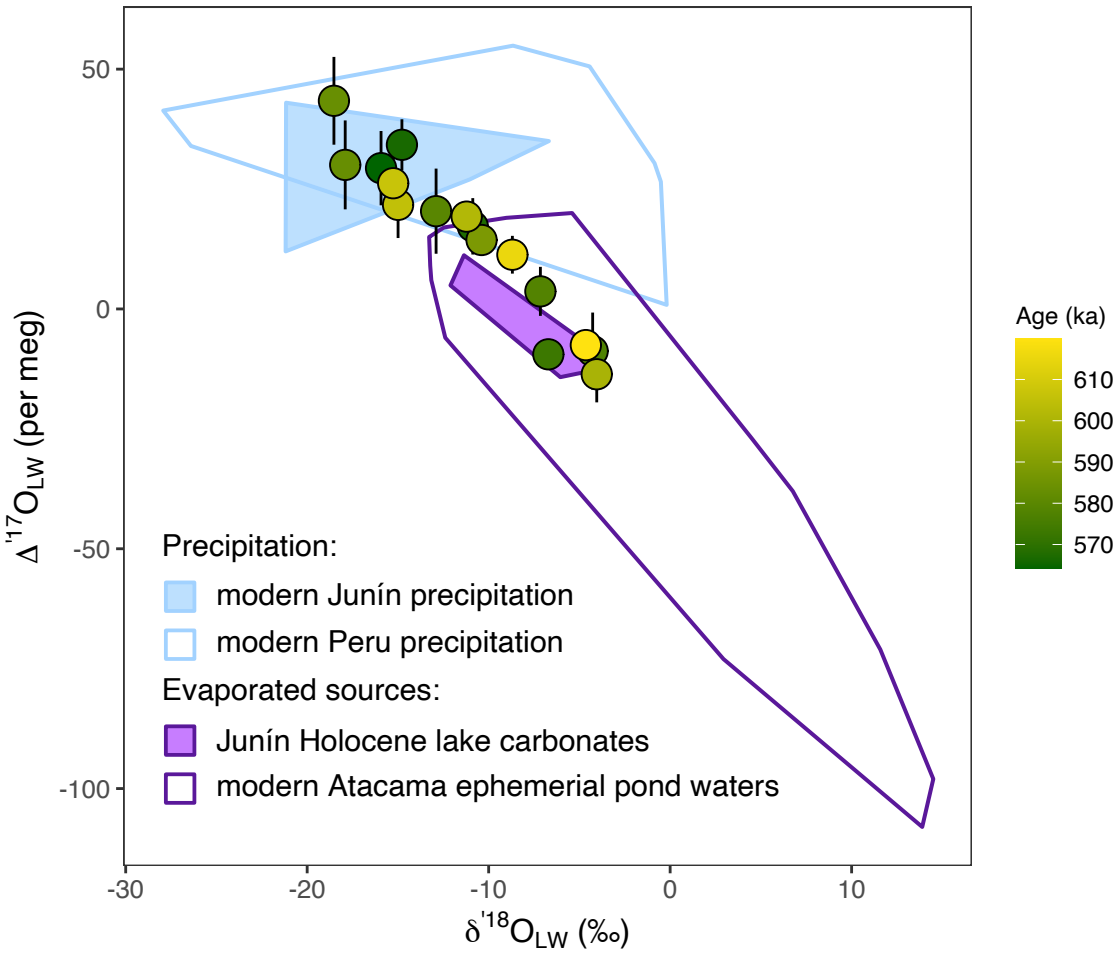

Figure S4.4: $\Delta'^{17}O_{LW}$ and $\delta'^{18}O_{LW}$ values from MIS 15 samples with fill color indicating sample age (Pearson's r = –0.96). Analytical uncertainty is shown as the 1σ SD of replicate analyses. For comparison, polygons show the range of water $\Delta'^{17}O$ and $\delta'^{18}O$ values of modern Peru precipitation (Aron et al., 2021), Junín precipitation (Katz et al., 2023), modern Atacama ephemeral pond waters (Herwartz et al., 2017; Surma et al., 2018; Voigt et al., 2021), and Holocene lake carbonate $\Delta'^{17}O_{LW}$ and $\delta'^{18}O_{LW}$ values from Junín (Katz et al., *in review*).

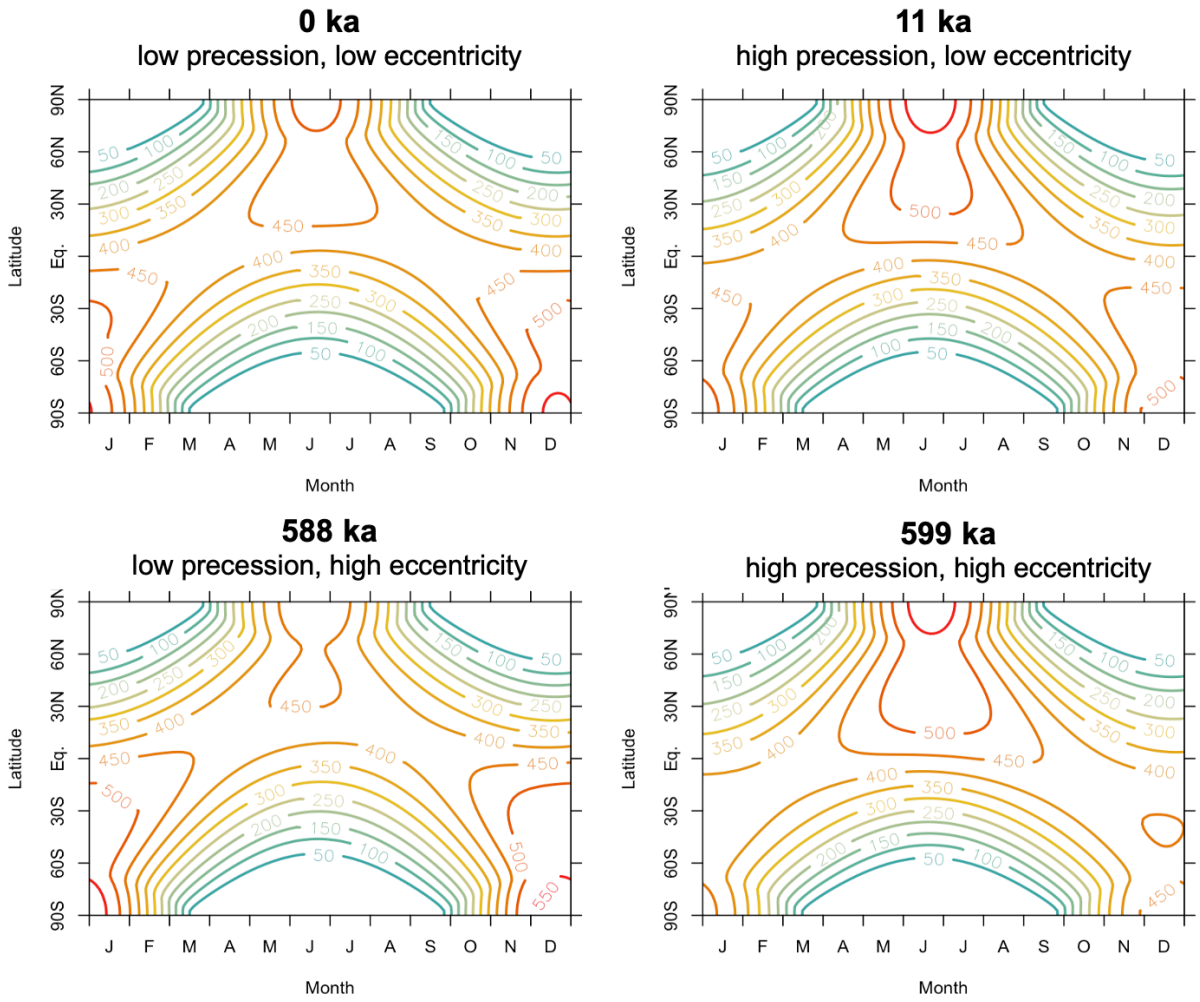

Figure S4.5: Contour graphs showing mean daily insolation at the top of the atmosphere over the course of a year as a function of latitude. Contour interval is 50 W/m^2 and color reflects insolation values from low (blues) to high (reds). Top row shows two time slices from the Holocene reflecting opposite precession values. Bottom row shows the same, but for MIS 15. Calculated from orbital solutions of Laskar et al. (2004) using the R package *palinsol* (Crucifix, 2016).

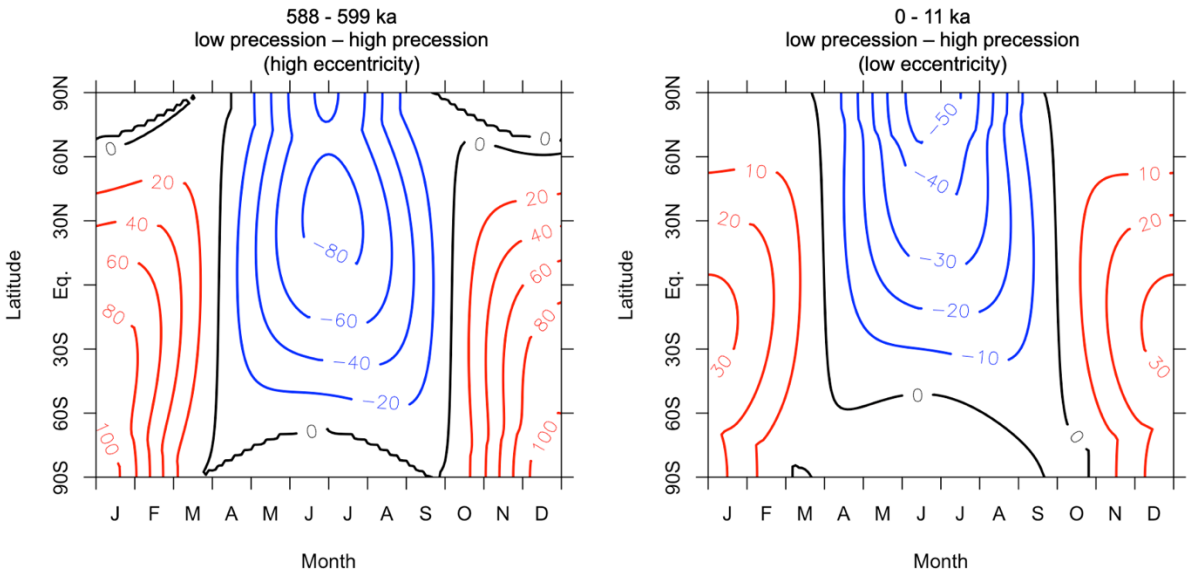

Figure S4.6: As in Figure S4.5, but showing differences during MIS 15 (588–599 ka; left) and the Holocene (0–11 ka; right). Contour interval is 50 W/m^2 and colors reflect positive (red) and negative (blue) insolation differences between the time slices. Note that the positive insolation differences during DJF in the Southern Hemisphere are expected to reflect stronger SASM conditions at 588 ka and 0 ka (compared to 599 ka and 11 ka, respectively). Calculated from orbital solutions of Laskar et al. (2004) using the R package *palinsol* (Crucifix, 2016).

4.9 References

Anderson, N.T. et al., 2021, A Unified Clumped Isotope Thermometer Calibration (0.5–1,100°C) Using Carbonate-Based Standardization: Geophysical Research Letters, v. 48, doi:10.1029/2020GL092069.

Aron, P.G., Levin, N.E., Beverly, E.J., Huth, T.E., Passey, B.H., Pelletier, E.M., Poulsen, C.J., Winkelstern, I.Z., and Yarian, D.A., 2021a, Triple oxygen isotopes in the water cycle: Chemical Geology, v. 565, p. 1–23, doi:10.1016/j.chemgeo.2020.120026.

Aron, P.G., Poulsen, C.J., Fiorella, R.P., Levin, N.E., Acosta, R.P., Yanites, B.J., and Cassel, E.J., 2021b, Variability and Controls on $\delta^{18}O$, d-excess, and $\Delta'^{17}O$ in Southern Peruvian Precipitation: Journal of Geophysical Research: Atmospheres, v. 126, p. 1–18, doi:10.1029/2020JD034009.

Assonov, S., Groening, M., Fajgelj, A., Hélie, J., and Hillaire-Marcel, C., 2020, Preparation and characterisation of IAEA-603, a new primary reference material aimed at the VPDB scale realisation for $\delta^{13}C$ and $\delta^{18}O$ determination: Rapid Communications in Mass Spectrometry, v. 34, doi:10.1002/rcm.8867.

Barkan, E., and Luz, B., 2007, Diffusivity fractionations of $H_2{}^{16}O/H_2{}^{17}O$ and $H_2{}^{16}O/H_2{}^{18}O$ in air and their implications for isotope hydrology: Rapid Communications in Mass Spectrometry, v. 21, p. 2999–3005, doi:10.1002/rcm.3180.

Barkan, E., and Luz, B., 2005, High precision measurements of $^{17}O/^{16}O$ and $^{18}O/^{16}O$ ratios in H_2O: Rapid Communications in Mass Spectrometry, v. 19, p. 3737–3742, doi:10.1002/rcm.2250.

Bereiter, B., Eggleston, S., Schmitt, J., Nehrbass-Ahles, C., Stocker, T.F., Fischer, H., Kipfstuhl, S., and Chappellaz, J., 2015, Revision of the EPICA Dome C CO_2 record from 800 to 600 kyr before present: Geophysical Research Letters, v. 42, p. 542–549, doi:10.1002/2014GL061957.

Berger, A., and Yin, Q., 2012, Modelling the Past and Future Interglacials in Response to Astronomical and Greenhouse Gas Forcing, *in* The Future of the World's Climate, Elsevier, p. 437–462, doi:10.1016/B978-0-12-386917-3.00015-4.

Bernasconi, S.M. et al., 2021, InterCarb: A Community Effort to Improve Interlaboratory Standardization of the Carbonate Clumped Isotope Thermometer Using Carbonate Standards: Geochemistry, Geophysics, Geosystems, v. 22, doi:10.1029/2020GC009588.

Bernasconi, S.M., Müller, I.A., Bergmann, K.D., Breitenbach, S.F.M., Fernandez, A., Hodell, D.A., Jaggi, M., Meckler, A.N., Millan, I., and Ziegler, M., 2018, Reducing Uncertainties in Carbonate Clumped Isotope Analysis Through Consistent Carbonate-Based Standardization: Geochemistry, Geophysics, Geosystems, v. 19, p. 2895–2914, doi:10.1029/2017GC007385.

Bird, B.W., Abbott, M.B., Rodbell, D.T., and Vuille, M., 2011, Holocene tropical South American hydroclimate revealed from a decadally resolved lake sediment $\delta^{18}O$ record: Earth and Planetary Science Letters, v. 310, p. 192–202, doi:10.1016/J.EPSL.2011.08.040.

Chen, C.Y. et al., 2020, U-Th dating of lake sediments: Lessons from the 700 ka sediment record of Lake Junín, Peru: Quaternary Science Reviews, v. 244, p. 106422, doi:10.1016/j.quascirev.2020.106422.

Cheng, H., Sinha, A., Cruz, F.W., Wang, X., Edwards, R.L., d'Horta, F.M., Ribas, C.C., Vuille, M., Stott, L.D., and Auler, A.S., 2013, Climate change patterns in Amazonia and biodiversity: Nature Communications, v. 4, p. 1411, doi:10.1038/ncomms2415.

Cobbing, J., Quispesivana, L.Q., and Paz, M.M., 1996, Geologia de los cuadrangulos de Ambo, Cerro de Pasco y Ondores. Boletin N77 Serie A: Carta Geológica Nacinonal:, https://hdl.handle.net/20.500.12544/200 (accessed February 2024).

Criss, R.E., 1999, Principles of Stable Isotope Distribution: New York, Oxford University Press, 1–254 p.

Crucifix, M., 2016, Insolation for Paleoclimate Studies "palinsol" v0.93:, https://bitbucket.org/mcrucifix/insolhttps://bitbucket.org/mcrucifix/insol (accessed January 2023).

Cruz, F.W., Burns, S.J., Karmann, I., Sharp, W.D., Vuille, M., Cardoso, A.O., Ferrari, J.A., Silva Dias, P.L., and Viana, O., 2005, Insolation-driven changes in atmospheric circulation over

the past 116,000 years in subtropical Brazil: Nature, v. 434, p. 63–66, doi:10.1038/nature03365.

Daëron, M., 2021, Full Propagation of Analytical Uncertainties in Δ_{47} Measurements: Geochemistry, Geophysics, Geosystems, v. 22, doi:10.1029/2020GC009592.

Daëron, M., Blamart, D., Peral, M., and Affek, H.P., 2016, Absolute isotopic abundance ratios and the accuracy of Δ_{47} measurements: Chemical Geology, v. 442, p. 83–96, doi:10.1016/j.chemgeo.2016.08.014.

Eiler, J.M., 2007, "Clumped-isotope" geochemistry-The study of naturally-occurring, multiply-substituted isotopologues: Earth and Planetary Science Letters, v. 262, p. 309–327, doi:10.1016/j.epsl.2007.08.020.

Ellis, N.M., and Passey, B.H., 2023, A novel method for high-precision triple oxygen isotope analysis of diverse Earth materials using high temperature conversion–methanation–fluorination and isotope ratio mass spectrometry: Chemical Geology, doi:10.1016/j.chemgeo.2023.121616.

Fetrow, A.C., Snell, K.E., Di Fiori, R. V., Long, S.P., and Bonde, J.W., 2022, How Hot Is Too Hot? Disentangling Mid-Cretaceous Hothouse Paleoclimate From Diagenesis: Paleoceanography and Paleoclimatology, v. 37, doi:10.1029/2022PA004517.

Garreaud, R.D., Vuille, M., Compagnucci, R., and Marengo, J., 2009, Present-day South American climate: Palaeogeography, Palaeoclimatology, Palaeoecology, v. 281, p. 180–195, doi:10.1016/j.palaeo.2007.10.032.

Gázquez, F., Morellón, M., Bauska, T., Herwartz, D., Surma, J., Moreno, A., Staubwasser, M., Valero-Garcés, B., Delgado-Huertas, A., and Hodell, D.A., 2018, Triple oxygen and hydrogen isotopes of gypsum hydration water for quantitative paleo-humidity reconstruction: Earth and Planetary Science Letters, v. 481, p. 177–188, doi:10.1016/j.epsl.2017.10.020.

Hatfield, R.G., Stoner, J.S., Solada, K.E., Morey, A.E., Woods, A., Chen, C.Y., McGee, D., Abbott, M.B., and Rodbell, D.T., 2020a, Paleomagnetic Constraint of the Brunhes Age Sedimentary Record From Lake Junín, Peru: Frontiers in Earth Science, v. 8, p. 1–18, doi:10.3389/feart.2020.00147.

Hatfield, R.G., Woods, A., Lehmann, S.B., Weidhaas, N., Chen, C.Y., Kück, J., Pierdominici, S., Stoner, J.S., Abbott, M.B., and Rodbell, D.T., 2020b, Stratigraphic correlation and splice generation for sediments recovered from a large-lake drilling project: an example from Lake Junín, Peru: Journal of Paleolimnology, v. 63, p. 83–100, doi:10.1007/s10933-019-00098-w.

Herwartz, D., Surma, J., Voigt, C., Assonov, S., and Staubwasser, M., 2017, Triple oxygen isotope systematics of structurally bonded water in gypsum: Geochimica et Cosmochimica Acta, v. 209, p. 254–266, doi:10.1016/j.gca.2017.04.026.

Hren, M.T., and Sheldon, N.D., 2012, Temporal variations in lake water temperature: Paleoenvironmental implications of lake carbonate $\delta^{18}O$ and temperature records: Earth and Planetary Science Letters, v. 337–338, p. 77–84, doi:10.1016/j.epsl.2012.05.019.

Huntington, K.W., and Petersen, S. V., 2023, Frontiers of Carbonate Clumped Isotope Thermometry: Annual Review of Earth and Planetary Sciences, v. 51, doi:10.1146/annurev-earth-031621-085949.

Huntington, K.W., Wernicke, B.P., and Eiler, J.M., 2010, Influence of climate change and uplift on Colorado Plateau paleotemperatures from carbonate clumped isotope thermometry: Tectonics, v. 29, p. 1–19, doi:10.1029/2009TC002449.

Huth, T.E., Passey, B.H., Cole, J.E., Lachniet, M.S., McGee, D., Denniston, R.F., Truebe, S., and Levin, N.E., 2022, A framework for triple oxygen isotopes in speleothem paleoclimatology: Geochimica et Cosmochimica Acta, v. 319, p. 191–219, doi:10.1016/j.gca.2021.11.002.

Ingalls, M., Frantz, C.M., Snell, K.E., and Trower, E.J., 2020, Carbonate facies-specific stable isotope data record climate, hydrology, and microbial communities in Great Salt Lake, UT: Geobiology, v. 18, p. 566–593, doi:10.1111/gbi.12386.

Jouzel, J. et al., 2007, Orbital and Millennial Antarctic Climate Variability over the Past 800,000 Years: Science, v. 317, p. 793–796, doi:10.1126/science.1141038.

Kanner, L.C., Burns, S.J., Cheng, H., Edwards, R.L., and Vuille, M., 2013, High-resolution variability of the South American summer monsoon over the last seven millennia: insights from a speleothem record from the central Peruvian Andes: Quaternary Science Reviews, v. 75, p. 1–10, doi:10.1016/j.quascirev.2013.05.008.

Katz, S.A., Levin, N.E., Abbott, M.B., Rodbell, D.T., Passey, B.H., DeLuca, N.M., Larsen, D.J., and Woods, A. Holocene temperature and water stress in the Peruvian Andes: insights from lake carbonate clumped and triple oxygen isotopes: Paleoceanography and Paleoclimatology, *in review*.

Katz, S.A., Levin, N.E., Rodbell, D.T., Gillikin, D.P., Aron, P.G., Passey, B.H., Tapia, P.M., Serrepe, A.R., and Abbott, M.B., 2023, Detecting hydrologic distinctions among Andean lakes using clumped and triple oxygen isotopes: Earth and Planetary Science Letters, v. 602, p. 117927, doi:10.1016/j.epsl.2022.117927.

Kelson, J.R. et al., 2023, Triple oxygen isotope compositions of globally distributed soil carbonates record widespread evaporation of soil waters: Geochimica et Cosmochimica Acta, doi:10.1016/j.gca.2023.06.034.

Kelson, J.R., Petersen, S. V., Niemi, N.A., Passey, B.H., and Curley, A.N., 2022, Looking upstream with clumped and triple oxygen isotopes of estuarine oyster shells in the early Eocene of California, USA: Geology, doi:10.1130/G49634.1.

Kim, S.-T., and O'Neil, J.R., 1997, Equilibrium and nonequilibrium oxygen isotope effects in synthetic carbonates: Geochimica et Cosmochimica Acta, v. 61, p. 3461–3475, doi:10.1016/S0016-7037(97)00169-5.

Laskar, J., Robutel, P., Joutel, F., Gastineau, M., Correia, A.C.M., and Levrard, B., 2004, A long-term numerical solution for the insolation quantities of the Earth: Astronomy & Astrophysics, v. 428, p. 261–285, doi:10.1051/0004-6361:20041335.

Lisiecki, L.E., and Raymo, M.E., 2005, A Pliocene-Pleistocene stack of 57 globally distributed benthic $\delta^{18}O$ records: Paleoceanography, v. 20, doi:10.1029/2004PA001071.

Liu, X., and Battisti, D.S., 2015, The influence of orbital forcing of tropical insolation on the climate and isotopic composition of precipitation in South America: Journal of Climate, v. 28, p. 4841–4862, doi:10.1175/JCLI-D-14-00639.1.

Loulergue, L., Schilt, A., Spahni, R., Masson-Delmotte, V., Blunier, T., Lemieux, B., Barnola, J.-M., Raynaud, D., Stocker, T.F., and Chappellaz, J., 2008, Orbital and millennial-scale features of atmospheric CH_4 over the past 800,000 years: Nature, v. 453, p. 383–386, doi:10.1038/nature06950.

Luz, B., and Barkan, E., 2010, Variations of $^{17}O/^{16}O$ and $^{18}O/^{16}O$ in meteoric waters: Geochimica et Cosmochimica Acta, v. 74, p. 6276–6286, doi:10.1016/j.gca.2010.08.016.

Marengo, J.A. et al., 2012, Recent developments on the South American monsoon system: International Journal of Climatology, v. 32, p. 1–21, doi:10.1002/joc.2254.

Passey, B.H., Hu, H., Ji, H., Montanari, S., Li, S., Henkes, G.A., and Levin, N.E., 2014, Triple oxygen isotopes in biogenic and sedimentary carbonates: Geochimica et Cosmochimica Acta, v. 141, p. 1–25, doi:10.1016/j.gca.2014.06.006.

Passey, B.H., and Ji, H., 2019, On the use of triple oxygen isotopes in lake waters and carbonates for reconstructing $\delta^{18}O$ of unevaporated precipitation: a case study from the Western United States: Earth and Planetary Science Letters, v. 518, p. 1–12, doi:10.1016/j.epsl.2019.04.026.

Passey, B.H., Levin, N.E., Cerling, T.E., Brown, F.H., and Eiler, J.M., 2010, High-temperature environments of human evolution in East Africa based on bond ordering in paleosol carbonates: Proceedings of the National Academy of Sciences, v. 107, p. 11245–11249, doi:10.1073/pnas.1001824107.

Petersen, S.V. V. et al., 2019, Effects of Improved ^{17}O Correction on Inter-Laboratory Agreement in Clumped Isotope Calibrations, Estimates of Mineral-Specific Offsets, and Temperature Dependence of Acid Digestion Fractionation: Geochemistry, Geophysics, Geosystems, v. 20, p. 3495–3519, doi:10.1029/2018GC008127.

Rodbell, D.T. et al., 2022, 700,000 years of tropical Andean glaciation: Nature, v. 607, p. 301–306, doi:10.1038/s41586-022-04873-0.

Rodbell, D.T., Seltzer, G.O., Mark, B.G., Smith, J.A., and Abbott, M.B., 2008, Clastic sediment flux to tropical Andean lakes: records of glaciation and soil erosion: Quaternary Science Reviews, v. 27, p. 1612–1626, doi:10.1016/j.quascirev.2008.06.004.

Santi, L.M., Arnold, A.J., Ibarra, D.E., Whicker, C.A., Mering, J.A., Lomarda, R.B., Lora, J.M., and Tripati, A., 2020, Clumped isotope constraints on changes in latest Pleistocene hydroclimate in the northwestern Great Basin: Lake Surprise, California: GSA Bulletin, v. 132, p. 2669–2683, doi:10.1130/B35484.1.

Schauble, E.A., Ghosh, P., and Eiler, J.M., 2006, Preferential formation of $^{13}C–^{18}O$ bonds in carbonate minerals, estimated using first-principles lattice dynamics: Geochimica et Cosmochimica Acta, v. 70, p. 2510–2529, doi:10.1016/j.gca.2006.02.011.

Schiferl, J. et al., 2023, A neotropical perspective on the uniqueness of the Holocene among interglacials: Nature Communications, v. 14, p. 7404, doi:10.1038/s41467-023-43231-0.

Schoenemann, S.W., Schauer, A.J., and Steig, E.J., 2013, Measurement of SLAP2 and GISP $\delta^{17}O$ and proposed VSMOW-SLAP normalization for $\delta^{17}O$ and $^{17}O_{excess}$: Rapid Communications in Mass Spectrometry, v. 27, p. 582–590, doi:10.1002/rcm.6486.

Seltzer, G., Rodbell, D., and Burns, S., 2000, Isotopic evidence for late Quaternary climatic change in tropical South America: Geology, v. 28, p. 35, doi:10.1130/0091-7613(2000)28<35:IEFLQC>2.0.CO;2.

SENAMHI, 2023, Datos Hidrometeorológicos a nivel nacional:, https://www.senamhi.gob.pe/?&p=estaciones (accessed January 2023).

Smith, J.A., Seltzer, G.O., Farber, D.L., Rodbell, D.T., and Finkel, R.C., 2005, Early Local Last Glacial Maximum in the Tropical Andes: Science, v. 308, p. 678–681, doi:10.1126/science.1107075 ARTICLE.

Surma, J., Assonov, S., Herwartz, D., Voigt, C., and Staubwasser, M., 2018, The evolution of ^{17}O-excess in surface water of the arid environment during recharge and evaporation: Scientific Reports, v. 8, p. 4972, doi:10.1038/s41598-018-23151-6.

Terzer-Wassmuth, S., Araguás-Araguás, L.J., Wassenaar, L.I., and Stumpp, C., 2023, Global and local meteoric water lines for $\delta^{17}O/\delta^{18}O$ and the spatiotemporal distribution of $\Delta'^{17}O$ in Earth's precipitation: Scientific Reports, v. 13, p. 19056, doi:10.1038/s41598-023-45920-8.

Vera, C. et al., 2006, Toward a Unified View of the American Monsoon Systems: Journal of Climate, v. 19, p. 4977–5000, doi:10.1175/JCLI3896.1.

Voigt, C., Herwartz, D., Dorador, C., and Staubwasser, M., 2021, Triple oxygen isotope systematics of evaporation and mixing processes in a dynamic desert lake system: Hydrology and Earth System Sciences, v. 25, p. 1211–1228, doi:10.5194/hess-25-1211-2021.

Vuille, M., and Werner, M., 2005, Stable isotopes in precipitation recording South American summer monsoon and ENSO variability: Observations and model results: Climate Dynamics, v. 25, p. 401–413, doi:10.1007/s00382-005-0049-9.

Wang, X., Edwards, R.L., Auler, A.S., Cheng, H., Kong, X., Wang, Y., Cruz, F.W., Dorale, J.A., and Chiang, H.W., 2017, Hydroclimate changes across the Amazon lowlands over the past 45,000 years: Nature, v. 541, p. 204–207, doi:10.1038/nature20787.

Wang, Z., Schauble, E.A., and Eiler, J.M., 2004, Equilibrium thermodynamics of multiply substituted isotopologues of molecular gases: Geochimica et Cosmochimica Acta, v. 68, p. 4779–4797, doi:10.1016/j.gca.2004.05.039.

Woods, A., 2021, A sedimentary perspective from Lake Junín on monsoon strength and glaciation in the tropical Andes over multiple glacial cycles [PhD Thesis]: University of Pittsburgh.

Woods, A. et al., 2020, Andean drought and glacial retreat tied to Greenland warming during the last glacial period: Nature Communications, v. 11, p. 5135, doi:10.1038/s41467-020-19000-8.

Wostbrock, J.A.G., Cano, E.J., and Sharp, Z.D., 2020, An internally consistent triple oxygen isotope calibration of standards for silicates, carbonates and air relative to VSMOW2 and SLAP2: Chemical Geology, p. 1–9, doi:10.1016/j.chemgeo.2019.119432.

Chapter 5 Conclusion

This dissertation presents new data and conceptual models that represent significant contributions in the fields of stable isotope geochemistry and South American paleoclimatology (Chapters 2–4). In this chapter, I highlight the major conclusions from this dissertation. I end by summarizing my reflections on the current state of the field and look ahead to promising directions of future work.

5.1 Landscape of the field at the outset of this dissertation

The outset of this dissertation coincided with two events which were important in shaping my research directions: i) the collection of the Lake Junín sediment record, and ii) the expansion of clumped (Δ_{47}) and triple oxygen ($\Delta'^{17}O$) isotopes in modern hydrology and paleoclimate applications

Collection of the Lake Junín record was a complex process requiring the efforts of many people to plan and execute. In particular, the vision and logistical coordination by Dr. Don Rodbell (Union College, USA), Dr. Mark Abbott (University of Pittsburgh, USA), Dr. Pedro Tapia (Instituto Nacional De Investigacion En Glaciares Y Ecosistemas De Montaña, Peru), and the International Continental Scientific Drilling Program (ICDP) crew were instrumental to the exhumation of this record (e.g., Rodbell et al., 2012). Furthermore, robust age models are key for meaningful paleoclimate interpretations, and age dating of the Lake Junín core was accomplished by a novel suite of approaches, including radiocarbon dating, U/Th dating on lake carbonates, and radiometric tie points (Hatfield et al., 2020a; Chen et al., 2020; Woods et al., 2020). The exceptional duration and the reliable, independent age controls quickly catapulted the Lake Junín record to a preeminent position among South American climate records. During the course of my dissertation, studies began to emerge which highlighted the paleoclimate information preserved by the core's geochemical and pollen records (Woods et al., 2020; Rodbell et al., 2022; Rozas-Davila et al., 2023; Schiferl et al., 2023). However, oxygen isotope records from the core have been slow to emerge because carbonate $\delta^{18}O$ values at Lake Junín are driven by a complex combination of

controls (e.g., precipitation $\delta^{18}O$, water temperature, and lake water evaporation) which makes these records difficult to interpret (Seltzer et al., 2000; Flusche et al., 2005).

At the same time, carbonate Δ_{47} was becoming a well-established proxy of carbonate formation temperature in many natural systems (including lake systems), while $\Delta'^{17}O$ was emerging as a reliable hydrologic tracer. The field of triple oxygen isotopes was in its infancy at the start of this dissertation but has expanded rapidly in the last six years (e.g., Aron et al., 2021a; Xia et al., 2023; Terzer-Wassmuth et al., 2023), with $\Delta'^{17}O$ showing exceptional promise for constraining kinetic processes, including evaporation (e.g., Barkan and Luz, 2007; Surma et al., 2015). In 2019, Passey and Ji presented the first study to use a combination of Δ_{47} and $\Delta'^{17}O$ measurements on lacustrine carbonates to determine the influence of both temperature and evaporation on carbonate $\delta^{18}O$ values across four lakes in the western United States (Passey and Ji, 2019). This work demonstrated that improved climate interpretations could be achieved by joining Δ_{47} and $\Delta'^{17}O$, and this set the stage for numerous studies, including my dissertation work (e.g., Ibarra et al., 2021; Beverly et al., 2021; Kelson et al., 2022, 2023; Katz et al., 2023, *in review*).

5.2 Major contributions & the current state of the field

As a body of work, this dissertation joins new techniques in isotope geochemistry with sediment records from Lake Junín to advance our understanding of South American paleoclimate. Chapter 2 is a modern calibration study in which we presented $\Delta'^{17}O$ data from precipitation, lake waters, and carbonates, and Δ_{47} from carbonates across four lakes in the Junín region of central Peru. Chapters 2 and 3 combine data with conceptual models leading to the development of a conceptual and numerical framework for interpreting carbonate Δ_{47} and $\Delta'^{17}O$ values in lake systems. Chapters 3 and 4 present lake carbonate Δ_{47} and $\Delta'^{17}O$ records during two interglacial periods (the Holocene and MIS 15) from lakes in the Lake Junín region and discuss the role of global climate forcings on tropical hydroclimate.

Synthesizing the most important findings across these studies, two main themes emerge: i) advances in application of new isotope techniques (e.g., Δ_{47} and $\Delta'^{17}O$) in lake systems, and ii) advances in South American paleoclimate. Both are explored further below.

This dissertation significantly contributes to the quantity of Δ_{47} and $\Delta'^{17}O$ data collected from lacustrine systems and greatly improves our ability to interpret these data. In Chapter 2, we

show that, in humid settings, $\Delta'^{17}O$ values of lake waters and carbonates reflect evaporation, which had previously only been established in arid systems. As in more arid settings (e.g., Passey and Ji, 2019; Voigt et al., 2021), the magnitude of evaporation in humid systems is recorded by $\Delta'^{17}O$ values and reflects lake hydrology (Chapters 2 and 3). Importantly, even within a single climatic setting (i.e., the Junín region), $\Delta'^{17}O$ values are different at lakes that represent different lake hydrologic conditions spanning from open, outflow-only basins to evaporation-dominated or closed basins. Combining the empirical data from Chapter 2 with deterministic modeling of steady state lake water balance equations (e.g., Criss, 1999; Surma et al., 2015; Passey and Ji, 2019), Chapters 2 and 3 present a comprehensive framework for interpreting lake carbonate Δ_{47} and $\Delta'^{17}O$ values. This advance has been paramount for using $\Delta'^{17}O$ as a proxy of evaporation in paleoclimate applications (e.g., Chapters 3 and 4). The framework developed in these chapters can also be applied to lakes across a range of environments and hydrologic types and provides a robust basis for modern and paleoclimate interpretations; we recommend this framework be used as a starting point for future studies that join Δ_{47} and $\Delta'^{17}O$ data in lake systems.

The second major contribution of this work was made in the field of South American tropical paleoclimatology. The first studies to have emerged from the Lake Junín record have led to important new hypotheses that tropical hydroclimate experienced large changes as a result of global climate forcings over the last 700 ka (e.g., Rodbell et al., 2022). However, existing geochemical and pollen datasets were not able to definitively determine whether changes in temperature, water balance, or some combination of the two contributed to these changes (Woods et al., 2020; Rodbell et al., 2022; Schiferl et al., 2023). In this dissertation, I develop new temperature and water balance records using lake carbonate Δ_{47} and $\Delta'^{17}O$ values to directly address these uncertainties (Chapters 3 and 4). A major finding of this work is that temperatures in the Andes during two interglacial periods (e.g., the Holocene and MIS 15) were similar to present day and stable over the course of both records. This suggests global climate forcings had a negligible influence on tropical temperatures during both interglacials. Conversely, lake water balance was highly variable during both interglacials. The pacing and amplitude suggests orbital forcing (i.e., precession and eccentricity) were the dominant controls on the South American summer monsoon (SASM). More broadly, changes in the SASM are linked to regional water balance, suggesting other regions in the SASM range may have experienced similar hydrologic change to the Lake Junín region. Together, the results of Chapters 3 and 4 provide new,

independent constraints on Andean temperature and water balance over two interglacial periods and imply a strong connection between regional hydroclimate and global forcings, affirming the Lake Junín record as an exceptional archive of tropical climate.

This dissertation uses exciting advances in isotope geochemistry to provide new insights into South American hydroclimate. Below, I reflect on the current state of the field and summarize research directions where future studies can make valuable scientific contributions.

5.3 Final reflections and a look forward

1) **Models provide an important basis for proxy studies.** In this dissertation, I use new conceptual and numerical models (which are ground-truthed by a modern calibration study) to develop a framework for interpreting carbonate Δ_{47} and $\Delta'^{17}O$ values in lacustrine systems. Models are valuable because they provide a clear set of expectations upon which to scaffold data interpretations. This is especially valuable when applied to emergent proxy systems, such as triple oxygen isotopes. For practitioners in this rapidly expanding field, conceptual and numerical models should be viewed as assets for illuminating insights into climatic, hydrologic, and/or biological processes.

   The chapters in this dissertation present an example of how models and data can be effectively integrated as a best-practice in paleoclimate applications. However, multiple directions of future research persist. First, models are often ground-truthed to some degree by modern datasets to ensure that these simplified representations of complex systems capture key processes. Modern Δ_{47} and $\Delta'^{17}O$ data from lakes has increased significantly in recent years, however, building out modern datasets from lakes across a wider range of water balance and climate settings remains an important research objective. Specifically, more data from under-sampled types of lake systems (i.e., closed basin lakes in humid settings or outflow-dominated lakes in arid settings). Additionally, most studies to-date reflect samples collected opportunistically and/or assume samples collected from 1–2 locations are reflective of an entire catchment (e.g., Passey and Ji, 2019; Katz et al., 2023); studies that employ a more extensive and careful sampling/monitoring campaign are obvious next steps (e.g., Pierchala et al., 2022).

Furthermore, advances in the next generation of lake models would be an asset and could include adaptation of existing water balance models to a Bayesian framework, addition of an isotopic turnover component, and/or proxy systems modeling.

2) **A multiproxy approach often gleans more information than a single proxy system, but technological advances are needed to increase the accessibility of specialized analytical methods.** Time and time again, this dissertation points to the power of a multi-proxy approach ($\delta^{18}O$, Δ_{47}, $\Delta'^{17}O$) for gleaning more precise climate information than can be achieved by a single proxy system (e.g., $\delta^{18}O$). While Δ_{47} and $\Delta'^{17}O$ analyses are becoming more routine, both approaches remain time-consuming and require access to high-precision mass spectrometers for analysis and complex front-end chemistry to prepare samples. For now, faster, cheaper, $\delta^{18}O$ analyses remain the backbone of many studies, with Δ_{47} and $\Delta'^{17}O$ analyses commonly only performed on a subset of samples and guided by existing $\delta^{18}O$ datasets. Recent technological advances in laser-based analytical systems for measuring waters and CO_2 evolved from acid digestion of carbonates (e.g., from Picarro, Los Gatos, and TILDAS) seem promising and could result in Δ_{47} and $\Delta'^{17}O$ analyses that require less time, less lab space, and systems that are easier to run (e.g., Berman et al., 2013; Prokhorov et al., 2019; Wang et al., 2020; Yanay et al., 2022; Perdue et al., 2022; Hare et al., 2022; Hutchings and Konecky, 2023). However, despite some initial comparative studies between these analytical approaches, it is not yet clear if data from laser-based studies and mass spectrometers are fully intercomparable (Berman et al., 2013; Steig et al., 2014; Wassenaar et al., 2021).

I identify two directions of future work within this theme. First, reference materials (e.g., waters, carbonates) are needed that have $\Delta'^{17}O$ values that are agreed-upon by the community and which can be used to standardize data across different laboratories. In the absence of agreed-upon $\Delta'^{17}O$ values for common water and carbonate reference materials (e.g., USGS waters, NBS-19, IAEA standards), it is difficult (or impossible) for comparison of $\Delta'^{17}O$ measurements across various laboratories and analytical techniques. Second, given that very few labs have published $\Delta'^{17}O$ data from carbonates, no systematic interlaboratory comparison studies have been conducted, to date. Compounded by the lack

of agreed-upon reference material $\Delta'^{17}O$ values, it remains difficult to compare carbonate $\Delta'^{17}O$ data across different labs. Further, because of recent advances measuring $\Delta'^{17}O$ on CO_2 gas (evolved from carbonates via acid digestion), a surge in $\Delta'^{17}O$ data from carbonates is likely; systematic comparison of data produced via laser systems and mass spectrometers will be urgently needed over the next couple of years.

3) **A wealth of paleoclimate information remains untapped in the Lake Junín record.** This dissertation only touches on two of seven interglacial periods recorded at Lake Junín; detailed study of the remaining intervals using Δ_{47} and $\Delta'^{17}O$ remains an active and exciting avenue of work. Furthermore, this dissertation does not establish new glacial temperature and water balance records because the core sections that record these intervals lack suitable carbonate sediments for Δ_{47} and $\Delta'^{17}O$ analysis (Hatfield et al., 2020b; Chen et al., 2020; Rodbell et al., 2022). Ongoing biomarker work by collaborators at the University of Pittsburgh will provide new, quantitative information about hydroclimate during glacial periods which will complement the results from interglacials presented in this dissertation. Together, the combination of these datasets will contribute to a more complete understanding of Andean hydroclimate over the last 650 ka.

4) **We still don't have a complete understanding of precipitation $\Delta'^{17}O$ variability.** The $\Delta'^{17}O$ value of precipitation guides both modern water cycle and paleo-hydroclimate interpretations. However, capturing spatial and temporal variations of precipitation $\Delta'^{17}O$ values requires long (multi-year) records that are collected at a high temporal resolution (ideally event-scale to bimonthly) and represent a global sample set. The first regional and global datasets with these qualities are emerging (Luz and Barkan, 2010; Aron et al., 2021b, 2023; Terzer-Wassmuth et al., 2023), but significant gaps remain in sample coverage, particularly in high elevation regions, which is especially relevant for paleoclimate research at Junín. Furthermore, regional studies have suggested precipitation $\Delta'^{17}O$ values can reflect a diverse range of processes which are not yet fully understood from global data compilations but deserve further study. These include seasonality (Landais et al., 2012; Tian et al., 2018; Aron et al., 2023), raindrop re-evaporation (Landais et al., 2010; Kaseke et al., 2018), moisture source and oceanic conditions (Landais et al.,

2008; Uechi and Uemura, 2019; Sha et al., 2023), convective activity (Landais et al., 2010), and moisture recycling. While we are beginning to piece together what precipitation $\Delta'^{17}O$ looks like on a global scale, more work is certainly needed on a regional basis.

Additionally, while a handful of studies now report precipitation $\Delta'^{17}O$ values over multiple years, we do not understand how precipitation $\Delta'^{17}O$ values at a single site vary on decadal timescales and longer, which is highly relevant for paleoclimate studies. Future work developing $\Delta'^{17}O$ records from ice cores and speleothems could represent an avenue for developing precipitation $\Delta'^{17}O$ records that cover a much longer duration than the instrumental record (e.g., Landais et al., 2008; Affolter et al., 2015; Sha et al., 2023).

5) **A complex relationship exists between tropical and global climate.** At the outset of this dissertation, I motivated our study of South American paleoclimate as a means to gather insights into how the tropics respond to global climate change. Unsurprisingly, the findings in this dissertation confirm that global climate has a complex and multifaceted relationship with regional climate. One of the most coherent findings in this new body of research is that changes in the Andean water cycle appear highly sensitive to global climate through the influence of the South American summer monsoon (SASM) on continental-scale rainfall patterns and regional water balance. However, the SASM response to ongoing climate change (particularly rising atmospheric greenhouse gas (GHG) concentrations) remains an outstanding question. Two avenues for future research which could illuminate these connections include climate modeling studies that test the role of GHGs on atmospheric dynamics in the tropics and paleoclimate studies designed to assess SASM changes under a range of ancient atmospheric GHG conditions.

5.4 References

Affolter, S., Häuselmann, A.D., Fleitmann, D., Häuselmann, P., and Leuenberger, M., 2015, Triple isotope (δD, $\delta^{17}O$, $\delta^{18}O$) study on precipitation, drip water and speleothem fluid inclusions for a Western Central European cave (NW Switzerland): Quaternary Science Reviews, v. 127, p. 73–89, doi:10.1016/j.quascirev.2015.08.030.

Aron, P.G., Levin, N.E., Beverly, E.J., Huth, T.E., Passey, B.H., Pelletier, E.M., Poulsen, C.J., Winkelstern, I.Z., and Yarian, D.A., 2021a, Triple oxygen isotopes in the water cycle: Chemical Geology, v. 565, p. 1–23, doi:10.1016/j.chemgeo.2020.120026.

Aron, P.G., Li, S., Brooks, J.R., Welker, J.M., and Levin, N.E., 2023, Seasonal Variations in Triple Oxygen Isotope Ratios of Precipitation in the Western and Central United States: Paleoceanography and Paleoclimatology, v. 38, doi:10.1029/2022PA004458.

Aron, P.G., Poulsen, C.J., Fiorella, R.P., Levin, N.E., Acosta, R.P., Yanites, B.J., and Cassel, E.J., 2021b, Variability and Controls on $\delta^{18}O$, d-excess, and $\Delta'^{17}O$ in Southern Peruvian Precipitation: Journal of Geophysical Research: Atmospheres, v. 126, p. 1–18, doi:10.1029/2020JD034009.

Barkan, E., and Luz, B., 2007, Diffusivity fractionations of $H_2{}^{16}O/H_2{}^{17}O$ and $H_2{}^{16}O/H_2{}^{18}O$ in air and their implications for isotope hydrology: Rapid Communications in Mass Spectrometry, v. 21, p. 2999–3005, doi:10.1002/rcm.3180.

Berman, E.S.F., Levin, N.E., Landais, a, Li, S.N., and Owano, T., 2013, Measurement of $\delta^{18}O$, $\delta^{17}O$, and ^{17}O-excess in Water by Off-Axis Integrated Cavity Output Spectroscopy and Isotope Ratio Mass Spectrometry: Analytical Chemistry, v. 85, p. 10392–10398, doi: 10.1021/Ac402366t.

Beverly, E.J., Levin, N.E., Passey, B.H., Aron, P.G., Yarian, D.A., Page, M., and Pelletier, E.M., 2021, Triple oxygen and clumped isotopes in modern soil carbonate along an aridity gradient in the Serengeti, Tanzania: Earth and Planetary Science Letters, v. 567, p. 1–13, doi:10.1016/j.epsl.2021.116952.

Chen, C.Y. et al., 2020, U-Th dating of lake sediments: Lessons from the 700 ka sediment record of Lake Junín, Peru: Quaternary Science Reviews, v. 244, p. 106422, doi:10.1016/j.quascirev.2020.106422.

Criss, R.E., 1999, Principles of Stable Isotope Distribution: New York, Oxford University Press, 1–254 p.

Flusche, M.A., Seltzer, G., Rodbell, D., Siegel, D., and Samson, S., 2005, Constraining water sources and hydrologic processes from the isotopic analysis of water and dissolved strontium, Lake Junin, Peru: Journal of Hydrology, v. 312, p. 1–13, doi:10.1016/j.jhydrol.2005.02.021.

Hare, V.J., Dyroff, C., Nelson, D.D., and Yarian, D.A., 2022, High-Precision Triple Oxygen Isotope Analysis of Carbon Dioxide by Tunable Infrared Laser Absorption Spectroscopy: Analytical Chemistry, v. 94, p. 16023–16032, doi:10.1021/acs.analchem.2c03005.

Hatfield, R.G., Stoner, J.S., Solada, K.E., Morey, A.E., Woods, A., Chen, C.Y., McGee, D., Abbott, M.B., and Rodbell, D.T., 2020a, Paleomagnetic Constraint of the Brunhes Age Sedimentary Record From Lake Junín, Peru: Frontiers in Earth Science, v. 8, p. 1–18, doi:10.3389/feart.2020.00147.

Hatfield, R.G., Woods, A., Lehmann, S.B., Weidhaas, N., Chen, C.Y., Kück, J., Pierdominici, S., Stoner, J.S., Abbott, M.B., and Rodbell, D.T., 2020b, Stratigraphic correlation and splice generation for sediments recovered from a large-lake drilling project: an example from

Lake Junín, Peru: Journal of Paleolimnology, v. 63, p. 83–100, doi:10.1007/s10933-019-00098-w.

Hutchings, J.A., and Konecky, B.L., 2023, Optimization of a Picarro L2140-i cavity ring-down spectrometer for routine measurement of triple oxygen isotope ratios in meteoric waters: Atmospheric Measurement Techniques, v. 16, p. 1663–1682, doi:10.5194/amt-16-1663-2023.

Ibarra, D.E., Kukla, T., Methner, K.A., Mulch, A., and Chamberlain, C.P., 2021, Reconstructing Past Elevations From Triple Oxygen Isotopes of Lacustrine Chert: Application to the Eocene Nevadaplano, Elko Basin, Nevada, United States: Frontiers in Earth Science, v. 9, p. 1–19, doi:10.3389/feart.2021.628868.

Kaseke, K.F., Wang, L., Wanke, H., Tian, C., Lanning, M., and Jiao, W., 2018, Precipitation Origins and Key Drivers of Precipitation Isotope (^{18}O, ^{2}H, and ^{17}O) Compositions Over Windhoek: Journal of Geophysical Research: Atmospheres, v. 123, p. 7311–7330, doi:10.1029/2018JD028470.

Katz, S.A., Levin, N.E., Abbott, M.B., Rodbell, D.T., Passey, B.H., DeLuca, N.M., Larsen, D.J., and Woods, A. Holocene temperature and water stress in the Peruvian Andes: insights from lake carbonate clumped and triple oxygen isotopes: Paleoceanography and Paleoclimatology, *in review*.

Katz, S.A., Levin, N.E., Rodbell, D.T., Gillikin, D.P., Aron, P.G., Passey, B.H., Tapia, P.M., Serrepe, A.R., and Abbott, M.B., 2023, Detecting hydrologic distinctions among Andean lakes using clumped and triple oxygen isotopes: Earth and Planetary Science Letters, v. 602, p. 117927, doi:10.1016/j.epsl.2022.117927.

Kelson, J.R. et al., 2023, Triple oxygen isotope compositions of globally distributed soil carbonates record widespread evaporation of soil waters: Geochimica et Cosmochimica Acta, doi:10.1016/j.gca.2023.06.034.

Kelson, J.R., Petersen, S. V., Niemi, N.A., Passey, B.H., and Curley, A.N., 2022, Looking upstream with clumped and triple oxygen isotopes of estuarine oyster shells in the early Eocene of California, USA: Geology, doi:10.1130/G49634.1.

Landais, A., Barkan, E., and Luz, B., 2008, Record of $\delta^{18}O$ and ^{17}O-excess in ice from Vostok Antarctica during the last 150,000 years: Geophysical Research Letters, v. 35, p. 1–5, doi:10.1029/2007GL032096.

Landais, A., Ekaykin, A., Barkan, E., Winkler, R., and Luz, B., 2012, Seasonal variations of ^{17}O-excess and d-excess in snow precipitation at Vostok station, East Antarctica: Journal of Glaciology, v. 58, p. 725–733, doi:10.3189/2012JoG11J237.

Landais, A., Risi, C., Bony, S., Vimeux, F., Descroix, L., Falourd, S., and Bouygues, A., 2010, Combined measurements of $^{17}O_{excess}$ and d-excess in African monsoon precipitation: Implications for evaluating convective parameterizations: Earth and Planetary Science Letters, v. 298, p. 104–112, doi:10.1016/j.epsl.2010.07.033.

Luz, B., and Barkan, E., 2010, Variations of $^{17}O/^{16}O$ and $^{18}O/^{16}O$ in meteoric waters: Geochimica et Cosmochimica Acta, v. 74, p. 6276–6286, doi:10.1016/j.gca.2010.08.016.

Passey, B.H., and Ji, H., 2019, On the use of triple oxygen isotopes in lake waters and carbonates for reconstructing $\delta^{18}O$ of unevaporated precipitation: a case study from the Western United States: Earth and Planetary Science Letters, v. 518, p. 1–12, doi:10.1016/j.epsl.2019.04.026.

Perdue, N., Sharp, Z., Nelson, D., Wehr, R., and Dyroff, C., 2022, A rapid high-precision analytical method for triple oxygen isotope analysis of CO_2 gas using tunable infrared laser direct absorption spectroscopy: Rapid Communications in Mass Spectrometry, v. 36, doi:10.1002/rcm.9391.

Pierchala, A., Rozanski, K., Dulinski, M., and Gorczyca, Z., 2022, Triple-isotope mass balance of mid-latitude, groundwater controlled lake: Science of The Total Environment, v. 814, p. 1–11, doi:10.1016/j.scitotenv.2021.151935.

Prokhorov, I., Kluge, T., and Janssen, C., 2019, Optical clumped isotope thermometry of carbon dioxide: Scientific Reports, v. 9, p. 4765, doi:10.1038/s41598-019-40750-z.

Rodbell, D.T. et al., 2022, 700,000 years of tropical Andean glaciation: Nature, v. 607, p. 301–306, doi:10.1038/s41586-022-04873-0.

Rodbell, D.T., Abbott, M.B., and ICDP, L.J.W.G., 2012, Workshop on Drilling of Lake Junin, Peru: Potential for Development of a Continuous Tropical Climate Record: Scientific Drilling, v. 13, p. 58–60, doi:10.2204/iodp.sd.13.10.2011.

Rozas-Davila, A., Rodbell, D.T., and Bush, M.B., 2023, Pleistocene megafaunal extinction in the grasslands of Junín-Peru: Journal of Biogeography, v. 50, p. 755–766, doi:10.1111/jbi.14566.

Schiferl, J. et al., 2023, A neotropical perspective on the uniqueness of the Holocene among interglacials: Nature Communications, v. 14, p. 7404, doi:10.1038/s41467-023-43231-0.

Seltzer, G., Rodbell, D., and Burns, S., 2000, Isotopic evidence for late Quaternary climatic change in tropical South America: Geology, v. 28, p. 35, doi:10.1130/0091-7613(2000)28<35:IEFLQC>2.0.CO;2.

Sha, L. et al., 2023, Variations in triple oxygen isotope of speleothems from the Asian monsoon region reveal moisture sources over the past 300 years: Communications Earth & Environment, v. 4, p. 384, doi:10.1038/s43247-023-01043-6.

Steig, E.J., Gkinis, V., Schauer, A.J., Schoenemann, S.W., Samek, K., Hoffnagle, J., Dennis, K.J., and Tan, S.M., 2014, Calibrated high-precision ^{17}O-excess measurements using cavity ring-down spectroscopy with laser-current-tuned cavity resonance: Atmos. Meas. Tech, v. 7, p. 2421–2435, doi:10.5194/amt-7-2421-2014.

Surma, J., Assonov, S., Bolourchi, M.J., and Staubwasser, M., 2015, Triple oxygen isotope signatures in evaporated water bodies from the Sistan Oasis, Iran: Geophysical Research Letters, v. 42, p. 8456–8462, doi:10.1002/2015GL066475.

Terzer-Wassmuth, S., Araguás-Araguás, L.J., Wassenaar, L.I., and Stumpp, C., 2023, Global and local meteoric water lines for $\delta^{17}O/\delta^{18}O$ and the spatiotemporal distribution of $\Delta'^{17}O$ in Earth's precipitation: Scientific Reports, v. 13, p. 19056, doi:10.1038/s41598-023-45920-8.

Tian, C., Wang, L., Kaseke, K.F., and Bird, B.W., 2018, Stable isotope compositions ($\delta^{2}H$, $\delta^{18}O$ and $\delta^{17}O$) of rainfall and snowfall in the central United States: Scientific Reports, v. 8, p. 1–15, doi:10.1038/s41598-018-25102-7.

Uechi, Y., and Uemura, R., 2019, Dominant influence of the humidity in the moisture source region on the ^{17}O-excess in precipitation on a subtropical island: Earth and Planetary Science Letters, v. 513, p. 20–28, doi:10.1016/j.epsl.2019.02.012.

Voigt, C., Herwartz, D., Dorador, C., and Staubwasser, M., 2021, Triple oxygen isotope systematics of evaporation and mixing processes in a dynamic desert lake system: Hydrology and Earth System Sciences, v. 25, p. 1211–1228, doi:10.5194/hess-25-1211-2021.

Wang, Z., Nelson, D.D., Dettman, D.L., McManus, J.B., Quade, J., Huntington, K.W., Schauer, A.J., and Sakai, S., 2020, Rapid and Precise Analysis of Carbon Dioxide Clumped Isotopic Composition by Tunable Infrared Laser Differential Spectroscopy: Analytical Chemistry, v. 92, p. 2034–2042, doi:10.1021/acs.analchem.9b04466.

Wassenaar, L., Terzer-Wassmuth, S., and Douence, C., 2021, Progress and challenges in dual- and triple-isotope ($\delta^{18}O$, $\delta^{2}H$, $\Delta^{17}O$) analyses of environmental waters: An international assessment of laboratory performance: Rapid Communications in Mass Spectrometry, v. 35, doi:10.1002/rcm.9193.

Woods, A. et al., 2020, Andean drought and glacial retreat tied to Greenland warming during the last glacial period: Nature Communications, v. 11, p. 5135, doi:10.1038/s41467-020-19000-8.

Xia, Z., Surma, J., and Winnick, M.J., 2023, The response and sensitivity of deuterium and ^{17}O-excess parameters in precipitation to hydroclimate processes: Earth-Science Reviews, v. 242, doi:10.1016/j.earscirev.2023.104432.

Yanay, N. et al., 2022, Rapid and precise measurement of carbonate clumped isotopes using laser spectroscopy: Science Advances, v. 8, doi:10.1126/sciadv.abq0611.